**UNIVERSITY OF SOUTHAMPTON**
FACULTY OF PHYSICAL SCIENCES AND ENGINEERING
SCHOOL OF ELECTRONICS AND COMPUTER SCIENCE

# Coherent and Non-coherent Coded Modulation for Cooperative Communications

by

*Dandan Liang*
*B. Eng., MSc.*

A doctoral thesis report submitted in partial fulfilment of
the requirements for the award of Doctor of Philosophy
at the University of Southampton

June 2013

SUPERVISOR:
*Dr. Soon Xin Ng*
PhD, SMIEEE, MIET, CEng, FHEA
and
*Professor Lajos Hanzo*
FREng, FIEEE, FIEE, DSc, EIC IEEE Press
Chair of Communications, Signal Processing and Control Group
Department of Electronics and Computer Science
University of Southampton
Southampton SO17 1BJ
United Kingdom

Dedicated to my family

UNIVERSITY OF SOUTHAMPTON

ABSTRACT

FACULTY OF PHYSICAL SCIENCES AND ENGINEERING
SCHOOL OF ELECTRONICS AND COMPUTER SCIENCE

Doctor of Philosophy

**Coherent and Non-coherent Coded Modulation For Cooperative Communications**

by Dandan Liang

The design trade-offs of coherent versus non-coherent coded modulation conceived for cooperative communications are explored. More specifically, coherent versus non-coherent coded modulation designed for traditional point-to-point communications is investigated first, before we extend the application of coded modulation to cooperative communications.

Firstly, we focus our attention on coherent coded modulation, when communicating over Additive White Gaussian Noise (AWGN) and uncorrelated Rayleigh fading channels, followed by the investigation of the adaptive coded modulation (ACM), when transmitting over both quasi-static as well as over shadow-and-fast Rayleigh fading channels. Furthermore, soft-decision aided non-coherent coded modulation designed both for fixed modes and adaptive modes is proposed. More specifically, we conceive soft-decision aided Differential Amplitude and Phase-Shift Keying (DAPSK) for low-complexity wireless communications, since it dispenses with high-complexity channel estimation. We commence by designing soft-decision based demodulation for 16-level DAPSK, or l6-level Star Quadrature Amplitude Modulation, which is then invoked for iterative detection aided Bit-Interleaved Coded Modulation (BICM-ID). It is shown that the proposed 16-DAPSK based BICM-ID scheme achieves a coding gain of approximately 14 dBs in comparison to the identical-throughput 16-level Differential Phase-Shift Keying (16DPSK) assisted BICM scheme at a Bit Error Ratio (BER) of $10^{-6}$. Then, we derive the soft-output probability formulas required for a soft-decision based demodulation of high-order DAPSK, in order to facilitate iterative detection by exchanging extrinsic information with an outer Turbo Code (TC). Furthermore, when the TC block size is increased, the system operates closer to the channel capacity. Offset DAPSK is also considered in order to facilitate the employment of a less stringent linear power amplifier specification at the transmitter. Compared to the identical-throughput TC assisted 64-ary Differential Phase-Shift Keying (64-DPSK) scheme, the 4-ring based TC assisted 64-ary DAPSK arrangement has a power-efficiency improvement of 4.2 dB at a BER of $10^{-5}$. Furthermore, when the TC block size is increased, the system operates closer to the channel capacity. More specifically, when using a TC block length of 400 modulated symbols, the 64 DAPSK(4, 16) scheme is 11.25 dB away from its capacity curve, while it operates within 2.7 dB of the capacity, when using a longer TC block length of 40 000 symbols. Furthermore, for the sake of an improved energy efficiency, we proposed the adaptive modes for non-coherent coded modulation.

Then, we considered coded modulation schemes designed for cooperative communications.

Firstly, an attractive hybrid method of mitigating the effects of error propagation that may be imposed by the relay node (RN) on the destination node (DN) is proposed in Chapter 4. We select the most appropriate RN location for achieving a specific target BER at the relay and signalled the RN-BER to the DN. The knowledge of this BER is then exploited by the decoder at the destination. Our simulation results show that when the BER encountered at the RN is low, we do not have to activate the RN-BER aided decoder at the DN. However, when the RN-BER is high, significant system performance improvements may be achieved by activating the proposed RN-BER based decoding technique at the DN. For example, a power-reduction of up to about 19 dB is recorded at a DN BER of $10^{-4}$. Secondly, the basic principle of ACM invoked for cooperative communications is detailed in the context of three main structures: single RN aided ACM, twin RN aided ACM and single RN aided ACM additionally combined with the source-to-destination (SD) link at the DN. Then we propose an adaptive TTCM (ATTCM) aided Distributed Space-Time Trellis Coding (STTC) scheme for cooperative communication over quasi-static Rayleigh fading channels. Specifically, an ATTCM scheme is employed by the source node during the first transmission period for reliably conveying the source bits to $N$ RNs by appropriately adjusting the code-rate and modulation mode according to the near-instantaneous channel conditions. It is shown that the proposed ATTCM-DSTTC scheme requires 12 dBs less transmission power in comparison to a standard TTCM scheme when aiming for a Frame Error Ratio (FER) of $10^{-3}$.

Finally, we focus our attention on non-coherent coded modulation conceived for cooperative communications. Firstly, we investigate a 16-StQAM-TC assisted NC scheme relying on the popular butterfly network topology. As expected, the achievable BER performance is affected by the location of the RN. More specifically, when the transmit powers at the SNs and RN are identical, the RN located at the centre of the butterfly network topology achieves the best performance. However, when the appropriately designed power sharing approach is invoked in Section 5.2.1.2, the optimum RN location is closer to the DNs, and another 1 dB of power gain can be attained. Then, the NC capacity was quantified and the simulation results of Figure 5.5 showed that the achievable capacity of the NC scenario is improved compared to the single-link scenario. Secondly, as a novel application example, our soft-decision M-DAPSK scheme is incorporated into an AF based cooperative communication system. We found that an AF based cooperative communication system obtains a 4.5 dB SNR improvement for a TC block length of 40 000 modulated symbols, compared to that of the traditional point-to-point transmission. Finally, we propose a low-complexity amalgamated cooperative wireless and optical-fiber communication scheme for uplink communication in a FFR based multicell, multiuser system. The FFR principle is invoked for improving the cell-edge performance without reducing the throughput of the cell-center. Each cell is illuminated with the aid of six Remote Antennas (RAs), which are connected to the central base-station with the aid of realistically modelled imperfect optical-fiber links. When a Mobile Station (MS) is located at the cell-edge, the two nearest RAs can be invoked for detecting and forwarding the user's signal to the base-station, based on the Single-Input Multiple-Output (SIMO) principle. Furthermore, we employ both the Digital Fiber Optic (DFO) and Analogue Radio-over-Fiber (AROF)

principles for the optical fiber link. We then design a Turbo Coded (TC) 16-level Star-Quadrature Amplitude Modulation (StQAM) scheme for supporting optical-fiber-aided cooperative wireless transmissions, where the receiver does not have to estimate the channel state information. Hence, a lower detection complexity can be achieved, when compared to coherently detected schemes, albeit naturally, at a 3 dB power-loss. We also investigate the effect of phase-rotations imposed by imperfect optical-fiber links. Our non-coherent TC-StQAM scheme is robust to both wireless and optical-fiber imperfections. More explicitly, the proposed TC-StQAM-SIMO scheme is capable of removing 6 out of 12 BER peaks at the cell-edge, despite dispensing with CSI for both the wireless and optical-fiber links. As a further improvement, the adaptive turbo-coded soft-decision aided differential detection (ATSDD) scheme is employed by the Mobile Station (MS) for reliably conveying the source bits to a pair of nearby Remote Antennas (RAs) by appropriately adjusting the modulation mode according to the near-instantaneous wireless and AROF channel condition. The ATSDD switching thresholds are specifically adjusted for ensuring that the BER remains below $10^{-5}$. We also investigated the effect of phase-rotations routinely imposed by practical imperfect Radio-over-fiber (ROF) links. We demonstrate that our ATSDD scheme is robust to both wireless and optical-fiber imperfections.

# Declaration of Authorship

I, **Dandan Liang**, declare that the thesis entitled **Coherent and Non-coherent Coded Modulation for Cooperative Communications** and the work presented in it are my own and has been generated by me as the result of my own original research. I confirm that:

- This work was done wholly or mainly while in candidature for a research degree at this University;
- Where any part of this thesis has previously been submitted for a degree or any other qualification at this University or any other institution, this has been clearly stated;
- Where I have consulted the published work of others, this is always clearly attributed;
- Where I have quoted from the work of others, the source is always given. With the exception of such quotations, this thesis is entirely my own work;
- I have acknowledged all main sources of help;
- Where the thesis is based on work done by myself jointly with others, I have made clear exactly what was done by others and what I have contributed myself;
- Parts of this work have been published.

Signed: ..... Date: .....

# Acknowledgements

I would like to express my heartfelt gratitude to Dr. Soon Xin Ng and Professor Lajos Hanzo for their outstanding supervision and support throughout my research. Thank Dr. Ng for his kindness guidance and help. Without his patient instruction, insightful criticism and expert guidance, my research would not have been done easily, meanwhile he gives me that “Tomorrow will be able to be better”. Thank Prof. Hanzo for not only offering me valuable suggestions in the academic studies but also teaching me the attitude of “step by step”. In a word, their guidance, inspiration and encouragement have greatly benefited me not only in work but also in life. Most importantly, I would like to thank them for their invaluable friendship.

Many thanks also to my colleagues and the staff of the Communications Group, both past and present, for their support, help and discussions throughout my research. Special thanks to my colleagues, Professor Sheng Chen, Professor Lie-Liang Yang, Dr. Rob Maunder, Dr. Mohammed El-Hajjar, Dr. Rong Zhang, Dr. Muhammad Fasih, Chao Xu, Dr. Li Wang, Xinyi Xu, Meng Song, Varghese Antony Thomas, Li Li, Yongkai Huo and Chuyi Qian for their kindly provided technical support and collaborative work. Thanks to my friends I have during my PhD years, too numerous to mention here explicitly. Also thanks to Denise Harvey and Lauren J Dampier for their help in the adiministratvie matters.

I would also like to express my appreciation to my parents Zhaosheng Liang and Guangmei Liu, to my elder sister and brother-in-law Yan Liang and Junhua Hu, as well as to my parents-in-law Yanqun Zhong and Yanjun Chen for their love and support. Furthermore, thanks also to my husband Dr. Shida Zhong for his love, support and care for me.

# List of Publications

## Journals:

1. **D. Liang**, S. X. Ng and L. Hanzo, "Soft-decision Star-QAM aided BICM-ID", IEEE Signal Processing Letters, vol.18, no.3, pp.169-172, 2011.

2. **D. Liang**, S. X. Ng and L. Hanzo, "Near-Capacity Turbo Coded Soft-decision Aided DAPSK/Star-QAM for Amplify-and-forward based Cooperative Communications", IEEE Transactions on Communications, vol.61, no.3, pp.1080-1087, 2013.

3. C. Xu, **D. Liang**, S. X. Ng and L. Hanzo, "Reduced-Complexity Non-coherent Soft-Decision-Aided M-DAPSK Dispensing with Channel Estimation", IEEE Transactions on Vehicular Technology, vol.61, no.4, pp.1415 - 1425, 2013..

4. C. Xu, **D. Liang**, S. Sugiura, S. X. Ng and L. Hanzo, "Reduced-Complexity Approx-Log-MAP and Max-Log-MAP Soft PSK/QAM Detection Algorithms", IEEE Transactions on Communications, IEEEXplore Early Access Articles, 2013.

5. **D. Liang**, V. A. Thomas, X. Xu, S. X. Ng, M. El-Hajjar and L. Hanzo, "Adaptive Soft-decision aided Differential Modulation for Cooperative Wireless and Optical-Fiber Communications", *submitted to* IEEE Signal Processing Letters, 2013.

6. L. Wang, L. Li, C. Xu, **D. Liang**, S. X. Ng and L. Hanzo, "Multiple-Symbol Joint Signal Processing for Differentially Encoded Single- and Multi-Carrier Communications: Principles, Designs and Applications", *submitted to* IEEE Communications Surveys & Tutorial.

## Conferences:

1. S. X. Ng, C. Qian, **D. Liang** and L. Hanzo, "Adaptive Turbo Trellis Coded Modulation Aided Distributed Space-Time Trellis Coding for Cooperative Communications", Proceedings of IEEE Vehicular Technology Conference (VTC) Spring, 16-19 May 2010, Taipei, Taiwan.

2. **D. Liang**, S. X. Ng and L. Hanzo, "Relay-Induced Error Propagation Reduction for Decode-and-Forward Cooperative Communications ", Proceedings of IEEE GLOBECOM 2010, 6-10 December 2010, Miami, Florida, USA.

3. **D. Liang**, S. X. Ng and L. Hanzo, "Near-Capacity Turbo Coded Soft-decision Aided DAPSK/Star-QAM", Proceedings of IEEE Vehicular Technology Conference (VTC) Fall, 5-8 September 2011, San Francisco, USA.

4. **D. Liang**, M. Song, S. X. Ng and L. Hanzo, "Turbo Coded and Cooperative Network Coded Non-Coherent Soft-Decision Star-QAM Dispensing with Channel Estimation", Proceeding of IEEE GLOBECOM 2011, Houston, TX, USA.

5. C. Xu, **D. Liang**, S. Sugiura, S. X. Ng and L. Hanzo, “Reduced-Complexity Soft-Decision Aided PSK Detection”, Proceeding of IEEE Vehicular Technology Conference (VTC) Fall, 3-6 September 2012, Qubec City, Canada.

6. C. Xu, **D. Liang**, S. Sugiura, S. X. Ng and L. Hanzo, “Reduced-complexity Soft STBC detection”, Proceeding of IEEE GLOBECOM, 3-7 December 2012, Anaheim, USA.

7. **D. Liang**, X. Xu, S. X. Ng and L. Hanzo, “Turbo-coded star-QAM for cooperative wireless and optical-fiber communications”, Proceeding of IEEE 3rd International Conference on Photonics, Penang, Malaysia, 01 - 03 Oct 2012, pp. 267-271.

# Contents

# Glossary

| | |
|---|---|
| **ACM** | Adaptive Coded Modulation |
| **AF** | Amplify-and-Forward |
| **APP** | *A Posteriori* Probability |
| **AROF** | Analogue ROF |
| **ATSDD** | Adaptive Turbo-coded Soft-decision aided Differential Detection |
| **AWGN** | Additive White Gaussian Noise |
| | |
| **BER** | Bit Error Ratio |
| **BICM** | Bit-Interleaved Coded Modulation |
| **BICM-ID** | Bit-Interleaved Coded Modulation with Iterative Decoding |
| **BMIAD** | Bit Metric of Iterative *a posteriori* probability Decoders |
| **BPS** | Bits Per Symbol |
| | |
| **CCMC** | Continuous-Input Continuous-Output Memoryless Channel |
| **CM** | Coded Modulation |
| **CRDED** | Correcting the Relay's Decoding Errors at the Destination |
| **CSI** | Channel State Information |
| | |
| **DAPSK** | Differential Amplitude and Phase-Shift Keying |
| **DCMC** | Discrete-Input Continuous-Output Memoryless Channel |
| **DF** | Decode-and-forward |
| **DFDD** | Decision-Feedback Differential Detection |
| **DFO** | Digital Fiber Optic |
| **DMC** | Discrete Memoryless Channel |
| **DPSK** | Differential Phase Shift Keying |
| **DSTTC** | Distributed STTC |
| | |
| **EXIT** | Extrinsic Information Transfer |

**FED** Free Euclidean distance
**FER** Frame Error Ratio
**FFR** Fractional Frequency Reuse

**LPDD** Linear Prediction aided Differential Detection
**LTE** Long-Term Evolution

**MAP** Maximum-A-Posteriori
**MI** Mutual information
**MLSE** maximum likelihood sequence estimation
**MSDD** Multi-Symbol Differential Detection
**MSDSD** Multiple-Symbol Differential Sphere Detection

**NC** Networking Coding

**PDF** Probability Density Function

**RDRPLR** Reduced-Distance-Related Pathloss Reduction
**RDRPLR** reduced-distance-related pathloss reduction
**RN**$_1$ the first RN
**RN**$_2$ the second RN
**RNSPA** RN Selection or Power Allocation
**RNSPA** Relay Node Selection or Power Allocation
**ROF** Radio-over-Fiber
**RSC** Recursive Systematic Convolutional

**SER** Symbol Error Ratio
**SIMO** Single-Input Multiple-Output
**SISO** Single-Input Single-Output
**SNR** Signal-to-Noise Ratio
**SNR**$_r$ received SNR
**StQAM** Star-QAM

**TCM** Trellis-Coded Modulation
**TTCM** Turbo-Trellis Coded Modulation
**TuCM** Turbo Coding aided BICM

**UFR** Unity Frequency Reuse

**VA** Viterbi Algorithm

**WiMAX** Wordwide interoperability for Microwave Access

# List of Symbols

## Special symbols

| | |
|---|---|
| $a_k$: | The amplitude of the PSK ring. |
| $b_i$: | The $i$th coded bit of the symbol. |
| $b_a$: | The most significant bit of the encoded symbol. |
| $b_\theta$: | The coded bits of the symbol for the DPSK bit-to-symbol mapper. |
| $\boldsymbol{b}$: | A symbol vector, or combination, representing one of the possible transmited symbol sequence. |
| $c_k$: | The coded symbol of the encoder at instance $k$. |
| $c_k^i$: | The original coded bits. |
| $\Delta c_k^i$: | The decoding errors. |
| C: | The Channel Capacity. |
| $C_{CCMC}$: | Capacity of the Continuous-Input Continuous-Output Memoryless Channel. |
| $C_{DMC}$: | Capacity of Discrete Memoryless Channel Capacity. |
| $C_{DCMC}$: | Capacity of Discrete-Input Continuous-Output Memoryless Channel |
| $d_{free}$: | The minimum free Euclidean distance. |
| $D$: | The delay due to one register stage. |
| $E_b$: | Bit energy. |
| $E_b/N_0$: | Ratio of bit energy to noise power spectral density. |
| $E_s$: | Symbol energy. |
| $E_s/N_0$: | Ratio of symbol energy to noise power spectral density. |

$E[k]$: The expected value of $k$.

$f_d$: The Doppler frequency.

$G(D)$: The generator polynomials matrix for Convolutional codes.

$\mathsf{G}$: The reduced-distance-related pathloss reduction factor.

$h$: The channel's coefficient.

$H^i(D)$: The coefficients of the generator polynomials for bit $i$ in TCM codes.

$I$: The mutual information.

$I_t$: The iterations number.

$k$: The symbol index.

$m$: The decision feedback equaliser's feed forward order.

$m_a$: The number of bits of amplitudes.

$m_p$: The number of bits of phases.

$M$: The number of levels of a multi-level modulation scheme, PSK or QAM.

$M_a$: The number of amplitudes.

$M_p$: The number of phases.

$\tilde{\mathsf{m}}$: The number of information bits in a modulated symbol.

$\tilde{\mathsf{m}}$: The number of encoded information bits in a modulated symbol.

$\mathsf{m}$: The number of bits in a modulated symbol.

$M$: The number of levels of a multi-level modulation scheme, PSK or QAM.

$N$: The number of symbols produced in each transmission interval, or the number of symbols per JD block.

$N_m$: The window size for MMSD.

$n(t)$: AWGN added to the transmitted signal.

$N_0$: Single-sided power spectral density of white noise.

$p_k$: The amplitude ratio.

$P(c_k^i; O)$: The *extrinsic a pOsteriori* probability of the original coded bits.

$P(\hat{c}_k^i; O)$: The joint probability.

$P(\Delta c_k^i)$: The probability of decoding errors.

$P^a(b_i)$: The *a priori* bit probabilities.

$P^e(b_i)$: The extrinsic bit probability.

$q_k^i$: The $i$th bit of the $k$th symbol.

$R_c$: Convolution coding rate.

$R_m$: Number of bits per modulated symbol.

$R_o$: Overall throughput.

$R_s$: Overall system's normalised throughput.

$\mathsf{SNR}_{min}$: The minimum SNR.

$\mathsf{SNR}_r$: The received SNR.

$\mathsf{SNR}_t$: The transmit SNR.

$\overline{SNR_t}$: The average transmit SNR.

$\mathsf{SNR}_{t,R}$: The transmit SNR at the RN.

$\mathsf{SNR}_{t,S_1}$: The transmit SNR at the $SN_1$.

$\mathsf{SNR}_{t,S_2}$: The transmit SNR at the $SN_2$.

$T$: Symbol transmission period.

$u_k$: The input symbol to the encoder at instance $k$.

$v_k$: The $k$th differentially encoded symbol.

$w_k$: The $k$th PSK symbol.

$x_k$: The transmitted symbol at instance $k$.

$y_k$: The received symbol at instance $k$.

$\aleph$: The pathloss exponent.

$\alpha$: The forward variable of a MAP decoder.

$\beta$: The backward variable of a MAP decoder.

$\tilde{\beta}_f$: The RN amplify factor.

$\beta_f$: The average amplify factor.

$\chi(i,b)$: The subset that contains all the phasors for which the position $i$ of the phasor has the binary value $b$, $b \in \{0,1\}$.

$\chi(i,b)$: The set of constellation points having the $i$th bit set to $b$.

$\delta$: The maximum phase difference considered.

$\delta_{SR}$: Different transmission SNR between SN and RN in log-domain form.

$\Delta$: Different transmission SNR between to nodes.

$\gamma$: The branch transition metric of a MAP decoder.

$\gamma_r$: The received SNR in log-domain form.

$\gamma_t$: The transmitted SNR in log-domain form.

$\nu$: The code memory.

$\pi$: Interleaver.

$\pi^{-1}$: Deinterleaver.

$\sigma^2$: The noise variance per dimension

$\triangle\phi_k$: The phase differences.

Chapter 1

# Introduction

## 1.1 Mutual Information

Mutual information (MI) constitutes one of the first information theoretic measures defined as early as 1948 by Shannon [1]. While MI provides a general quantitative measure of information, with applications in numerous fields of research, such as in physics, statistics, economics and so on, it is most commonly encountered in the context of communications engineering. It may be interpreted as the amount of information a random variable contains about another [1,2]. In this section, the MI will be investigated in the context of channel capacity in Section 1.1.1 and Extrinsic Information Transfer (EXIT) charts in Section 1.1.2.

### 1.1.1 Channel Capacity

The Channel Capacity ($C$) quantifies the maximum achievable transmission rate ($C^*$) of a system communicating over a band-limited channel. The unit of channel capacity $C$ is bit per symbol, which may be normalized by the symbol-duration, yielding the transmission rate $C^*$ in bit per second, i.e. we have $C^* = \frac{C}{T}$, where $T$ is the symbol period. Shannon quantified the capacity of a Single-Input Single-Output (SISO) Additive White Gaussian Noise (AWGN) channel in 1948 [1]. Following this, the main research-objective was to find practical coding schemes that were capable of approaching the channel capacity of the AWGN channel. This goal proved to be challenging, but not impossible. Initially, most work on channel coding has been focussed on finding powerful binary codes, following by the practical breakthrough by Ungerböck, which led to the invention of Trellis-Coded Modulation (TCM) [3], constituted by joint coding and modulation, also referred to as coded modulation (CM). Below the basic concept of channel capacity will be briefly introduced.

Let us assume that the input and output of the Discrete Memoryless Channel (DMC) [4] can be expressed as $X$ and $Y$, respectively, where $X$ may be one of $K$ discrete-amplitude values, while $Y$ may be one of $J$ legitimate discrete-amplitude values. Furthermore, let us consider the assignment

of $x = a_k$ and $y = b_j$. Then the probability of occurrence for each event can be expressed as:

$$p(k) = P(x = a_k), \tag{1.1}$$

$$p(j) = P(y = b_j). \tag{1.2}$$

Additionally, the probability of receiving $y = b_j$, provided that $x = a_k$ was transmitted can be expressed as:

$$p(j \mid k) = P(y = b_j \mid x = a_k). \tag{1.3}$$

The mutual information [5] between the event $y = b_j$ and the event $x = a_k$ may be expressed as:

$$I_{X;Y}(a_k; b_j) = \log_2 \left[ \frac{p(k|j)}{p(k)} \right] \text{[bit]}. \tag{1.4}$$

Moreover, the average mutual information, $I(X;Y)$, which is the expectation [6] of $I_{X;Y}(a_k; b_j)$, can be expressed as:

$$I(X;Y) = \sum_{k=1}^{K} \sum_{j=1}^{J} p(k,j) \log_2 \left[ \frac{p\,(k|j)}{p(k)} \right] \text{[bit/symbol]}. \tag{1.5}$$

Furthermore, with the aid of Bayes' rule [7], we have:

$$p(x|y) = \frac{p(y|x)p(x)}{p(y)}, \;\; p(x,y) = p(y|x)p(x), \tag{1.6}$$

where the average mutual information can be rewritten as:

$$I(X;Y) = \sum_{k=1}^{K} \sum_{j=1}^{J} p(j|k)p(k) \log_2 \left[ \frac{p(k|j)}{p(k)} \right] \quad \text{[bit/symbol]}. \tag{1.7}$$

The channel capacity is the highest possible average mutual information, which can be found by selecting the specific set of input symbol probability assignments, $\{p(k); k = 1, ..., K\}$. The DMC [5] capacity can be expressed as:

$$C_{DMC} = \max_{\{p(k);k=1...,K\}} \sum_{k=1}^{K} \sum_{j=1}^{J} p(j|k)p(k) \log_2 \left[ \frac{p(j|k)}{p(j)} \right] \quad \text{[bit/symbol]}. \tag{1.8}$$

In practice, the probability of the channel's input symbols cannot be controlled, therefore, the channel capacity cannot be approached. A relative of the DMC is the Continuous-Input Continuous-Output Memoryless Channel (CCMC) [4], and the corresponding continuous-valued discrete-time coefficients of $x$ and $y$ may be written as:

$$x[n] \in [-\infty, +\infty], \tag{1.9}$$

$$y[n] \in [-\infty, +\infty], n = 1, ..., N, \tag{1.10}$$

while the capacity of the CCMC may be written as:

$$C_{CCMC} = \max_{p(\mathbf{x})} \int_{-\infty}^{\infty} ... \int_{-\infty}^{\infty} p(\mathbf{y}|\mathbf{x})p(\mathbf{x}) \log_2 \left[ \frac{p(\mathbf{y}|\mathbf{x})}{p(\mathbf{y})} \right] d\mathbf{x} d\mathbf{y} \text{[bit/symbol]}, \tag{1.11}$$

where $\mathbf{x} = (x_m[1], ..., x_m[N])$ and $\mathbf{y} = (y[1], ..., y[N])$ are $N$-dimensional signals at the channel's input and output, respectively. Discrete-Input Continuous-Output Memoryless Channel (DCMC) [4] is another relative of the DMC, where the channel's input belongs to the discrete set of $M$-ary values:

$$\mathbf{x} \in \{\mathbf{x}_m : m = 1, ..., M\}, \tag{1.12}$$

while the channel's output $y$ has the continuous-valued coefficients:

$$y[n] \in [-\infty, +\infty], n = 1, ..., N. \tag{1.13}$$

The capacity of the DCMC channel can be expressed as:

$$C_{DCMC} = \max_{p(\mathrm{X}_1)...p(\mathrm{X}_M)} \sum_{m=1}^{M} \int_{-\infty}^{\infty} ... \int_{-\infty}^{\infty} p(y|\mathrm{X}_m) p(\mathrm{X}_m) \log_2 \left[ \frac{p(y|\mathrm{X}_m)}{p(y)} \right] d\mathbf{y} [\text{bit/symbol}], \tag{1.14}$$

where $\mathbf{x}_m = (x_m[1], ..., x_m[N])$ is the $N$-dimensional $M$-ary symbol at the channel's input, while $\mathbf{y} = (y[1], ..., y[N])$ is the $N$-dimensional signal at the channel's output.

#### 1.1.1.1 Capacity of the AWGN Channel

The capacity of a continuous-input continuous-output AWGN channel or the Shannon bound of an AWGN channel can be formulated as follows. The channel's input $x(t)$ can be modelled by band-limited Gaussian noise. The samples of both the noise sources $x(t)$ and $n(t)$ are generated at the Nyquist rate. Hence, they are independent identically distributed Gaussian random variables with zero mean having a variance of $\sigma^2$ for $x(t)$ and $N_0/2$ for $n(t)$. If the Probability Density Functions (PDFs) of $p(x)$, $p(y)$ and $p(y \mid x)$ are Gaussian, the CCMC capacity can be formulated as:

$$C_{CCMC}^{AWGN} = WT \log_2(1+\gamma) \, [\text{bit/symbol}], \tag{1.15}$$

$$= \frac{N}{2} \log_2(1+\gamma) \, [\text{bit/symbol}], \tag{1.16}$$

where $W$ is the bandwidth, which is limited by an ideal low-pass or bandpass filtering of the waveform, $T$ is the time interval and $\gamma$ is the Signal-to-Noise Ratio (SNR). It is worth noting that the capacity of the CCMC is an unrestricted bound, since the capacity is only restricted by $\gamma$ and by the bandwidth $W$. For the DCMC capacity formulated for the transmission of $N$-dimensional $M$-ary signals, we have:

$$p(\mathbf{x_m}) = \frac{1}{M}, m = 1, ..., M, \tag{1.17}$$

if the $M$-ary signals are uniformly distributed. The conditional probability of receiving $y$ given that $x$ was transmitted may be expressed as:

$$p(\mathbf{y}|\mathbf{x_m}) = \prod_{n=1}^{N} \frac{1}{\sqrt{\pi N_0}} e^{\left( \frac{-(y_n - x_{mn})^2}{N_0} \right)}, \tag{1.18}$$

where $N_0/2$ is the noise variance per dimension. Based on Eq. 1.18, the DCMC capacity [8, 9] may be written as:

$$C_{DCMC}^{AWGN} = \log_2(M) - \frac{1}{M(\sqrt{\pi})^N} \cdot \sum_{m=1}^{M} \int_{-\infty}^{\infty} \ldots \int_{-\infty}^{\infty} e^{-|\mathbf{t}|^2} \log_2 \left[ \sum e^{(-2\mathbf{t}\cdot\mathbf{d}_{\mathrm{mi}} - |\mathbf{d}_{\mathrm{mi}}|^2)} \right] d\mathbf{t} \left[ \mathrm{bit}/\mathrm{symbol} \right] \tag{1.19}$$

where $\mathbf{d}_{\mathrm{mi}} = (\mathbf{x}_m - \mathbf{x}_i)/\sqrt{N_0}$ and $\mathbf{t} = (t[1], ..., t[N])$ is an integration variable. Furthermore, the $N$-dimensional AWGN channel can be presented as $\mathbf{n} = (n[1], ..., n[N])$. The average SNR [10] can be expressed as:

$$\gamma = \frac{\mathrm{E}[x_m^2(t)]}{\mathrm{E}[n^2(t)]} = \frac{\frac{1}{M}\sum_{n=1}^{N} |\mathbf{x}_m|^2}{\sum_{n=1}^{N} \mathrm{E}[n^2(t)]} = \frac{E_s}{NN_0/2}, \tag{1.20}$$

where $E_s$ is the average energy of the $N$-dimensional $M$-ary symbol $X_m$ and $NN_0/2$ is the average energy of the $N$-dimensional AWGN $n$. Furthermore, the capacity of the DCMC for two-dimensional $M$-ary input signal may be expressed as [10]:

$$C_{DCMC}^{AWGN} = \log_2(M) - \frac{1}{M} \sum_{m=1}^{M} \mathrm{E} \left[ \log_2 \sum_{i=1}^{M} e^{\left( \frac{-|\mathbf{x}_m + \mathbf{n} - \mathbf{x}_i|^2 + |\mathbf{n}|^2}{N_0} \right)} \right] \text{[bit/symbol]}, \tag{1.21}$$

where $n$ is the AWGN having a variance of $N_0/2$ per dimension.

#### 1.1.1.2 Capacity of the Uncorrelated Rayleigh Fading Channel

The complex-valued Rayleigh fading coefficient can be defined as: $h = h_i + j \cdot h_q$, where $j = \sqrt{-1}$, while $h_i$ and $h_q$ are the in-phase and quadrature-phase coefficients, respectively. More specifically, $h_i$ and $h_q$ are zero-mean independent identical distributed Gaussian random variables when considering an uncorrelated Rayleigh fading channel. The resultant complex-valued coefficient $\chi_2^2$ of the Rayleigh fading channel is a chi-squared distributed random variable with two degrees of freedom. The corresponding PDF [4] can be expressed as:

$$p(\chi_2^2) = \frac{1}{2\sigma_r^2} e^{\left( -\frac{\chi_2^2}{2\sigma_r^2} \right)}. \tag{1.22}$$

The capacity of continuous-input continuous-output uncorrelated (memoryless) Rayleigh fading channels [11, 12] can be expressed as:

$$C_{CCMC}^{RAY} = E \left[ \frac{N}{2} \log_2(1 + \chi_2^2 \gamma) \right] [bits/symbol]. \tag{1.23}$$

The DCMC capacity for $N = 2$-dimensional $M$-ary complex signals, can be formulated as [4]:

$$C_{DCMC}^{RAY} = \log_2(M) - \frac{1}{M} \sum_{m=1}^{M} E \left[ \log_2 \sum_{i=1}^{m} e^{(\Phi_i^m)} \right] [bits/symbol], \tag{1.24}$$

where the exponent is given by [4]:

$$\begin{aligned} \Phi_i^m &= \frac{-|h(\mathrm{X}_m - \mathrm{X}_i) + n|^2 + |n|^2}{N_0} \\ &= \frac{-\left|\chi_2^2(\mathrm{X}_m - \mathrm{X}_i) + \Omega\right|^2 + |\Omega|^2}{\chi_2^2 N_0}. \end{aligned} \tag{1.25}$$

For complex-valued $M$-ary signals having $N \geq 2$ dimensions, we arrive at [13, 14]:

$$\Phi_i^m = \sum_{n=1}^{N} \frac{-\left|\chi_2^2[n]\left(x_m[n] - x_i[n]\right) + \Omega[n]\right|^2 + |\Omega[n]|^2}{\chi_2^2[n] N_0}, \tag{1.26}$$

where $\chi_2^2[j] = \chi_2^2[j+1]$ for $j \in \{1, 3, 5...\}$ has two dimensions for a complex-valued channel, while $\Omega[n]$ is the $d$th dimension of the N-dimensional AWGN, which has a zero mean and a variance of $\chi_2^2[n] N_0/2$ per dimension.

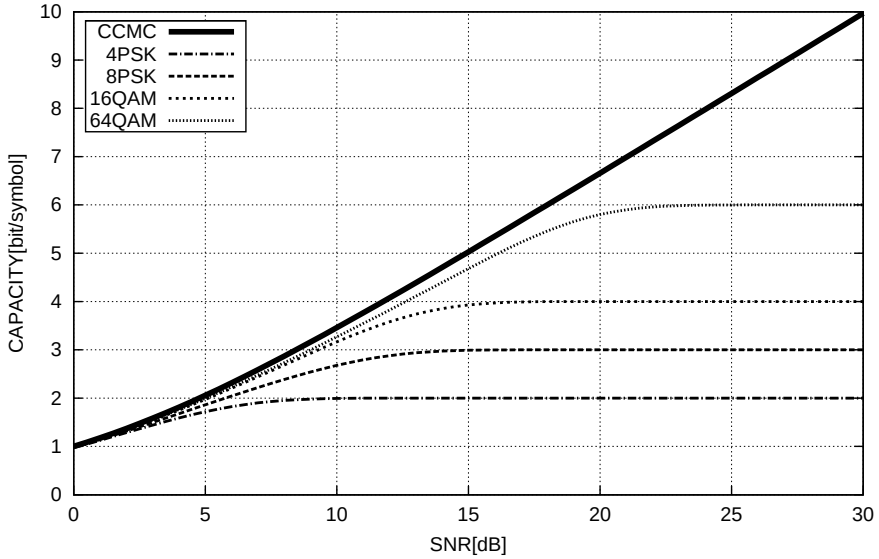


Figure 1.1: Capacity versus SNR (dB) for the CCMC and DCMC for transmissions over the AWGN channel.

Figure 1.1 shows the comparison of the DCMC capacity for 4PSK, 8PSK, 16QAM and 64QAM as well as the CCMC capacity. More specifically, the asymptotic DCMC capacity is 2 for 4PSK, 3 for 8PSK, 4 for 16QAM and 6 for 64QAM. Based on the channel capacity, we can design Adaptive Coded Modulation (ACM) schemes activating the appropriate SNR-dependent coding rate and modulation modes. For example, 8PSK modulation may be employed at an SNR of 5 dB, while if the SNR is improved to 15 dB, 64QAM may be adopted.

Figure 1.2 presents the CCMC and DCMC capacity versus SNR performance for transmission over uncorrelated Rayleigh fading channels. Compared to Figure 1.1, it can be seen that although the channel capacity is also 2 Bits Per Symbol (BPS) for 4PSK, 3 BPS for 8PSK, 4 BPS for 16QAM, and 6 BPS for 64QAM, the SNR required for transmission over uncorrelated Rayleigh fading channels is higher than that necessitated for transmission over an AWGN channel. More specifically, approaching the channel capacity at 2 BPS requires an SNR of about 10 dB for 4PSK over an AWGN channel and 20 dB over uncorrelated Rayleigh fading channels.

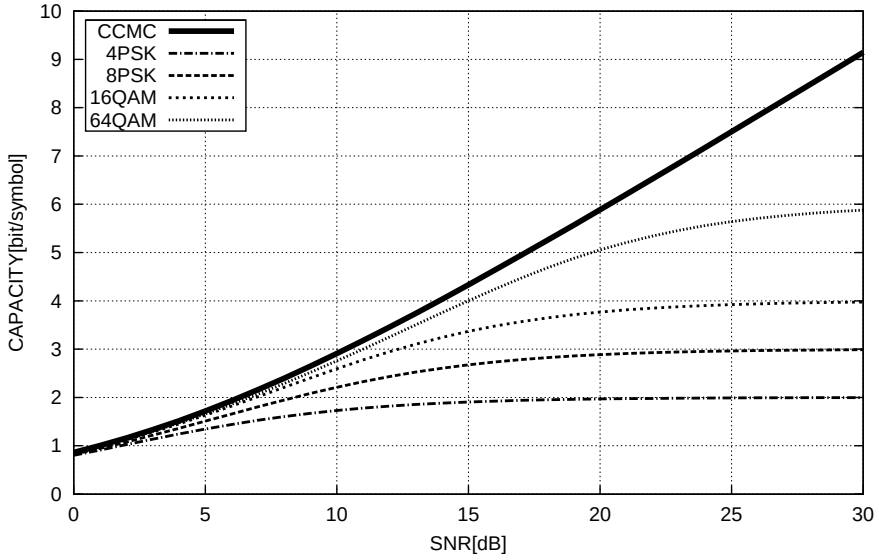


Figure 1.2: Capacity versus SNR (dB) for CCMC and DCMC for transmission over uncorrelated Rayleigh fading channels.

### 1.1.2 Extrinsic Information Transfer Characteristics

Extrinsic Information Transfer (EXIT) charts have been regarded as a useful tool conceived for analyzing the convergence behaviour of iterative decoding, when the transmission block length is sufficiently long [15]. This subsection will briefly introduce the concept of symbol-based EXIT charts based on [16, 17]. Then, the efficient computation of EXIT functions is discussed in the context of non-binary iterative decoding, such as Turbo-Trellis Coded Modulation (TTCM) for example [18].

#### 1.1.2.1 Brief Introduction to EXIT Charts

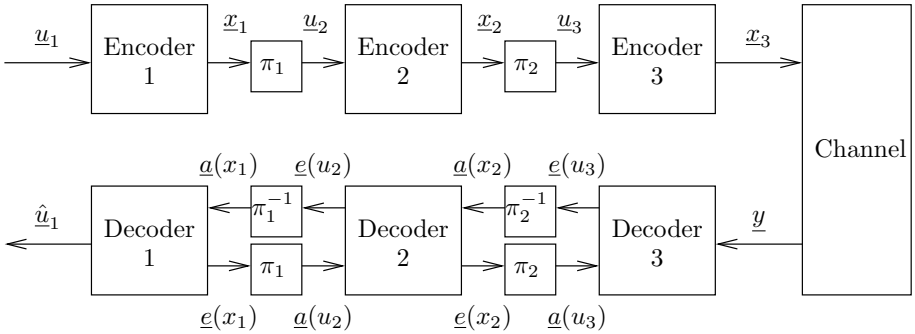


Figure 1.3: The schematic of a 3-stage serially concatenated coding scheme [19]. Note that $\pi$ and $\pi^{-1}$ represents the interleaver and deinterleaver, respectively.

Recently, the convergence analysis of iterative decoding algorithms has attracted much attention, since it is capable of predicting the achievable code performance during the code de-

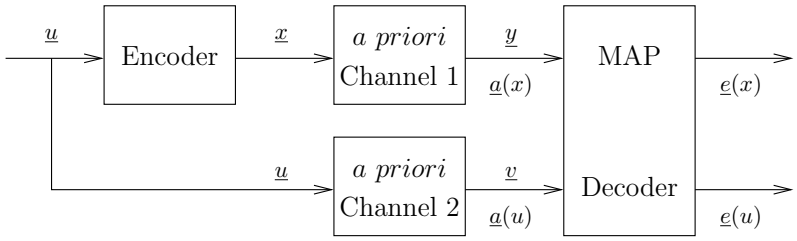


Figure 1.4: Modelling the encoding and decoding of an intermediate encoder [19].

sign without Monte-Carlo simulations [15, 18, 20, 21]. More explicitly, EXIT charts allow us to avoid time-consuming decoding simulations, when designing near-capacity codes with guaranteed convergence. EXIT charts can also be used for determining the decoding convergence of the two-component TTCM scheme. This is achieved by visualizing the input/output MI characteristics of the symbol-based constituent Recursive Systematic Convolutional (RSC) Maximum-A-Posteriori (MAP) decoders [20]. Figure 1.4 shows the simplified model of the three-stage concatenated scheme of Figure 1.3, where $\underline{u}$ represents the input symbols and $\underline{x}$ represents the output symbols of the encoder, while the *a priori* channels are employed for modelling the outer and inner decoders of Figure 1.3. Furthermore, the per-symbol average mutual information used in the EXIT chart may be expressed as follows [15, 18, 20]:

1. the average per-symbol mutual information between $\underline{u}$ and $\underline{a}(u)$ of Figure 1.4 is:

$$I_A(u) = \frac{1}{N_u} \sum_{k=1}^{N_u} I[u_k; a(u_k)], \tag{1.27}$$

2. the average per-symbol mutual information between $\underline{x}$ and $\underline{a}(x)$ of Figure 1.4 is:

$$I_A(x) = \frac{1}{N_x} \sum_{k=1}^{N_x} I[x_k; a(x_k)], \tag{1.28}$$

3. the average per-symbol mutual information between $\underline{u}$ and $\underline{e}(u)$ of Figure 1.4:

$$I_E(u) = \frac{1}{N_u} \sum_{k=1}^{N_u} I[u_k; e(u_k)], \tag{1.29}$$

4. the average per-symbol mutual information between $\underline{x}$ and $\underline{e}(u)$ of Figure 1.4:

$$I_E(x) = \frac{1}{N_x} \sum_{k=1}^{N_x} I[x_k; e(x_k)], \tag{1.30}$$

where the number of symbols in the sequences $\underline{u}$ and $\underline{x}$ are given by $N_u$ and $N_x$, respectively. Based on Equation 1.27−1.30, we observe that the intermediate decoder is associated with four MI transfers. Hence, for the three-stage architecture of Figure 1.3, three-dimensional EXIT charts are required for visualizing the MI exchange between the intermediate and the outer decoder as well as between the intermediate and the inner decoder.

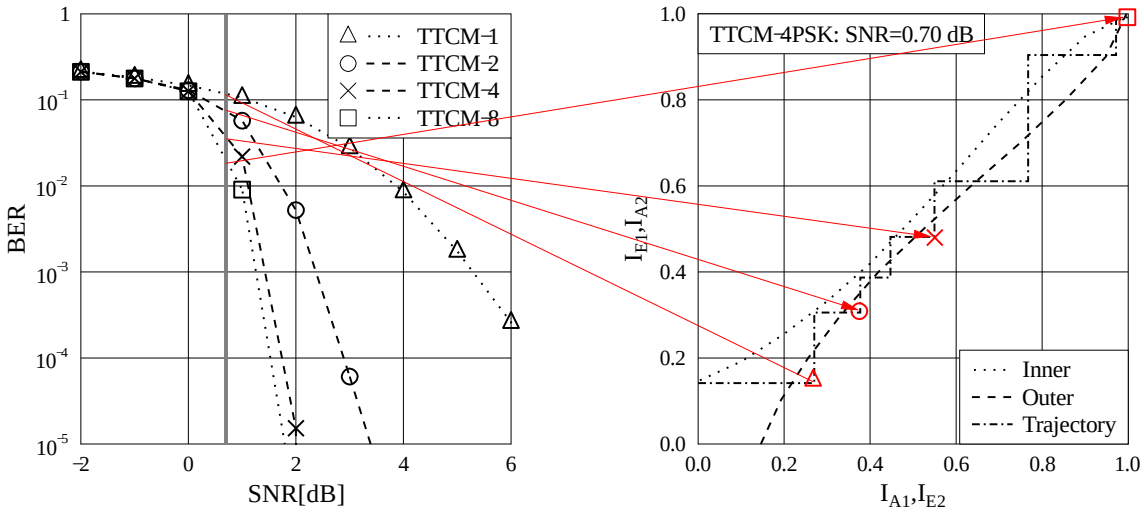


Figure 1.5: The relationship between the BER and EXIT charts.

Figure 1.5 portrays the stylized relationship between the BER and EXIT charts, when we consider the example of TTCM-4PSK having 1 200 symbols per block for transmission over an AWGN channel. Observe in Figure 1.5 that the EXIT chart recorded at the SNR of 0.7 dB has an open tunnel and again the arrows illustrate the relationship between the BER and the MI visualized by the EXIT charts. More specifically, as seen in Figure 1.5, the BER curve is gradually shifted to the left, while the decoding trajectory is approaching to the point of $(1, 1)$ of convergence towards a low vanishingly BER. Hence, the EXIT charts constitute effective semi-analytical tools of designing iterative detection aided techniques.

## 1.2 Coded Modulation

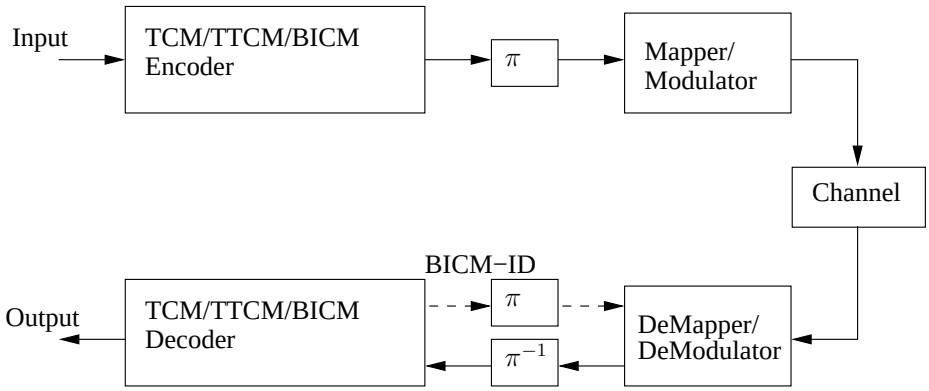


Figure 1.6: The simplified schematic of coded modulation schemes [22]. Note that $\pi$ and $\pi^{-1}$ represents the interleaver and deinterleaver, respectively.

Coded Modulation (CM) constitutes a bandwidth-efficient communication scheme that com-

bines the functions of coding and modulation by absorbing the channel-coded bits with the aid of extending the symbol-constellation [6, 22]. CM schemes can be designed by employing relatively high-rate channel coding schemes in conjunction with multidimensional or relatively high-level modulation schemes. A coding gain may be achieved without bandwidth expansion. Figure 1.6 presents the simplified schematic of CM schemes. At the transmitter, the source node generates random information bits, which are encoded by one of the TCM, TTCM, or Bit-Interleaved Coded Modulation (BICM) encoders. Then the coded bits are appropriately interleaved and they are used for modulating the waveforms based on the various bit-to-symbol mapping rules. At the receiver, the demodulator is followed by a deinterleaver and a TCM/TTCM/BICM decoder. It worth noting that the channel decoder's output is appropriately interleaved and fed back to the demodulator input in Bit-Interleaved Coded Modulation with Iterative Decoding (BICM-ID) schemes. In this thesis, a variety of CM assisted systems will be proposed and investigated.

### 1.2.1 History of Coded Modulation

The history of coded modulation dates back to Shannon's pioneering work [1], which founded information theory and motived the search for codes that are capable of producing an arbitrarily low probability of error, despite operating in the vicinity of the capacity. The evolution of CM research over the past 60 years following Shannon's legendary contribution [1] can been seen in Table 1.1 and Table 1.2. More specifically, Table 1.1 and Table 1.2 shows the important milestones, exciting discoveries, their inventors and specific contributions.

### 1.2.2 History of Adaptive Coded Modulation

The vision of a communication system that provides ubiquitous high-speed access to information has led to widespread research on information transmission over multipath fading channels. An attractive technique of achieving robust and spectrally efficient communication over multipath fading channels is to adapt the transmission scheme to the current channel characteristics by signalling the channel quality estimates available at the receiver back to the transmitter. Unlike nonadaptive schemes, which are designed for worst-case channel conditions for the sake of achieving an acceptable performance, adaptive signalling methods take advantage of favourable near-instantaneous channel conditions by allocating the transmit power judiciously.

Adaptive modulation can be invoked for duplex communication between the Mobile Station (MS) and Base Station (BS), where the modes have to be adapted and signalled between them, in order to allow channel quality estimates and signalling to take place [72–74]. The modulation mode adaptation is the action of the transmitter in response to time-varying channel conditions. In order to efficiently react to the changes in channel quality, the following steps have to be taken:

- *channel quality estimation*: In order to appropriately select the transmission parameters to be employed for the next transmission, a reliable estimation of the channel transfer function

| Year | Author(s) | Contribution |
|---|---|---|
| 1948 | Shannon [1] | Information theory and capacity |
| 1949 | Shannon [23] | Gaussian channel capacity, the sampling theorem and a geometric signal space theory |
| 1950 | Hamming [24] | Hamming codes were discovered |
| 1954 | Reed [25] | Reed-Muller (RM) codes |
| 1955 | Elias [26] | Convolutional codes |
| 1962 | Gallager [27]<br>Forney *et al.* [28] | Low-density parity-check (LDPC) codes<br>2400 BPS modem commercially available (4PSK) |
| 1967 | Forney *et al.* [28] | 4800 BPS modem commercially available (8PSK) |
| 1971 | Forney *et al.* [28] | 9600 BPS modem commercially available (16-QAM) |
| 1972 | Bahl *et al.* [29] | Maximum A-Posteriori (MAP) algorithm |
| 1974 | Bahl *et al.* [30] | The symbol based MAP algorithm |
| 1975 | Sugiyama *et al.* [31] | Euclidean algorithm for decoding |
| 1977 | MacWilliams [32]<br>Imai and Hirawaki [33] | Monograph on the theory of error correcting codes<br>Bandwidth-efficient MultiLevel Coding (MLC) |
| 1978 | Wolf [34] | Trellis-decoding of block codes |
| 1980 | Forney *et al.* [28] | 14,400 BPS modem commercially available (64-QAM) |
| 1982 | Ungerböck [3] | Trellis-Coded Modulation (TCM) |
| 1984 | Forney *et al.* [28] | 14,400 BPS modem commercially available (128-QAM) |
| 1987 | Wei [35] | Rotationally invariant differentially encoded multidimensional constellation for the design of TCM |
| 1988 | Blahut [36] | Multiple trellis-coded modulation |
| 1989 | Pottie and Taylor [37]<br>Calderbank [38] | Multilevel codes based on partitioning<br>Multilevel codes and multistage decoding |
| | Hagenauer *et al.* [39] | Soft-Output Viterbi Algorithm (SOVA) |
| 1990 | Koch and Baier [40] | Classic Log-MAP algorithm and sub-optimal Max-Log-MAP algorithm |
| 1991 | Webb *et al.* [41] | Hard-decision Star QAM/Differential Amplitude Phase Shift Keying (DAPSK) |
| 1992 | Zehavi [42] | Bit-Interleaved Coded Modulation (BICM) |
| 1993 | Berrou [43] | Turbo codes |
| 1994 | Kofman *et al.* [44]<br>Huber and Wachsmann [45]<br>Le Goff *et al.* [46] | Performances of a multilevel coded modulation<br>Capacity of equivalent channels of multilevel coding<br>BICM-based Trubo Coded Modulation (TuCM) |
| 1995 | Robertson *et al.* [47] | Approx-Log-MAP algorithm |
| 1996 | Raphaeli [48] | Noncoherent coded modulation |

Table 1.1: Milestones in Coded Modulation (1948-1996).

| Year | Author(s) | Contribution |
|---|---|---|
| 1997 | Li and Ritcey [49] | Bit-Interleaved Coded Modulation with Iterative Decoding (BICM-ID) |
| | Chen *et al.* [50, 51] | Soft Viterbi decoding metrics for DAPSK |
| 1998 | Robertson and Worz [52] | Turbo trellis-coded modulation (TTCM) |
| | Li and Ritcey [49] | BICM-ID using soft feedback |
| | Caire *et al.* [53] | The theoretical error bound of BICM |
| | ten Brink *et al.* [54, 55] | Soft-decision demodulation techniques |
| 1999 | Li and Ritcey [56] | Combining TCM with BICM-ID |
| 2000 | Morelos-Zaragoza *et al.* [57] | Multilevel coded modulation (symmetric constellation) |
| | Isaka *et al.* [58] | Multilevel coded modulation (asymmetric constellation) |
| 2001 | Chindapol and Ritcey [59] | Bit-to-symbol mapping for BICM-ID |
| | Örmeci *et al.* [60] | Adaptive BICM using outdated channel information |
| 2004 | Hanzo *et al.* [6] | TCM, TTCM, BICM and BICM-ID schemes |
| | Hou and Lee [61] | Multilevel LDPC code design for semi-BICM |
| | Lampe *et al.* [62] | Multilevel coding for multiple-antenna transmission |
| 2005 | Ishibashi *et al.* [63] | Soft-decision-aided DAPSK |
| 2006 | Nana *et al.* [64] | Improved decoding of LDPC coded modulations |
| 2009 | Ng *et al.* [65] | Distributed turbo trellis coded modulation for Cooperative communications |
| 2010 | Yang *et al.* [66] | Labelling optimization for BICM-ID systems |
| 2011 | Nguyen and Lampe [67] | BICM with mismatched decoding metrics |
| | Islam *et al.* [68] | Analysis and design of cooperative BICM-OFDM systems |
| 2012 | Cheng *et al.* [69] | Improve the performance of the LTE turbo-coded modulation by irregular mapping |
| | Andalibi *et al.* [70] | Analysing BICM in multiple-input multiple-output systems with channel estimation error |
| 2013 | Tran *et al.* [71] | Precoding and symbol grouping for non-orthogonal amplify-and-forward relaying in BICM systems |

Table 1.2: Milestones in Coded Modulation (1997-2013).

during the next active transmit timeslot is necessary.

- *Choice of the appropriate parameters for the next transmission*: Based on the prediction of the channel conditions for the next timeslot, the transmitter has to select the appropriate modulation and channel coding modes for the subcarriers.

- *Signalling or blind detection of the employed parameters*: The receiver has to be informed, as to which demodulator parameters to employ for the received packet. This information can either be explicitly conveyed within the transmission frame, or it may be detected by the remote transmitter by means of blind detection mechanisms [73].

  The milestones of ACM are shown in Tables 1.3–1.4.

## 1.3 Outline of the Thesis

The organization of the report is listed bellow with reference to Figure 1.7:

**Chapter 1:** The concept of MI is introduced and the channel capacity is quantified, followed a rudimentary portrayal of Extrinsic Information Transfer (EXIT) charts. The chapter is concluded by a brief historical perspective on both coded modulation and adaptive coded modulation.

**Chapter 2:** In this chapter, the family of coherent coded modulation schemes is introduced. In Section 2.2.2, we first discuss a number of powerful coherent-detection-aided joint coding and modulation schemes, namely TCM, TTCM, BICM and BICM/ID for 4PSK, 8PSK, 16QAM and 64QAM. Then in Section 2.2.5 their performance is characterized for transmission over both Gaussian and Rayleigh fading channels. Finally, in Section 2.3 near-instantaneous adaptive coded modulation schemes are proposed and their BER, BPS and mode selection probability is characterized for transmission over quasi-static Rayleigh fading as well as shadow-and-fast Rayleigh fading channels.

**Chapter 3:** Following the study of coherent coded modulation in Chapter 2 in Section 2.2.2, we proposed low complexity, near-capacity soft-decision aided DAPSK schemes based on BICM, BICM-ID and TuCM codes. In Section 3.2, the fixed modes based on BICM, BICM-ID and TuCM were investigated in the context of soft-decision aided M-DAPSK. Then in Section 3.3 the related adaptive schemes were characterized for transmission over quasi-static Rayleigh fading channels and shadow-and-slow Rayleigh fading channels.

**Chapter 4:** Based on the discussion of Chapter 2 in Section 2.2.2 and Section 2.3, we employed the coherent coded modulation schemes for cooperative communications. Firstly, in Section 4.2 the relay-induced error propagation of decode-and-forward based cooperative communications was mitigated. Then in Section 4.3 adaptive coded modulation schemes were

| Year | Author(s) | Contribution |
|---|---|---|
| 1968 | Hayes [75] | Envisioned an adaptive receiver and a feedback channel |
| 1972 | Cavers [76] | Variable-rate transmission for Rayleigh fading channels |
| 1974 | Hentinen [77] | Adaptive transmission schemes for fading channels |
| 1991 | Steele and Webb [78] | Adaptive star QAM (QAM) constellations |
| 1995 | Otsuki *et al.* [79] | Adaptive square QAM constellations |
| 1996 | Torrance and Hanzo [80] | Optimisation of switching levels for adaptive modulation in slow Rayleigh fading |
| 1997 | Goldsmith and Chua [81] | Variable-rate, variable-power MQAM for fading channels |
| 1997 | Chua and Goldsmith [82] | Adaptive Coded Modulation (ACM) for fading channels |
| 1998 | Goeckel [83] | Adaptive coding for fading channels using outdated channel estimates |
| | Lim and Jeong [84] | Adaptive modulation using multipath fading compensation |
| 1999 | Alouini and Goldsmith [85] | Capacity of different adaptive transmission and diversity-combining techniques |
| | Wong and Hanzo [86] | Upper-bound performance of a wideband burst-by-burst adaptive modem |
| 2000 | Duel-Hallen [87] | Long-range channel quality prediction techniques |
| | Hole *et al.* [88] | Adaptive multidimensional coded modulation over flat fading channels |
| | Lau *et al.* [89] | Adaptive bit interleaved TCM for Rayleigh fading channels |
| 2001 | Choi and Hanzo [90] | Optimum mode-switching assisted adaptive modulation |
| | Ng, Wong and Hanzo [91] | Burst-by-burst adaptive decision feedback equalized TCM, TTCM, BICM and BICM-ID |
| | Liu *et al.* [92] | Bandwidth-efficient, low-latency ACM for time-varying channels |
| 2003 | Zhang *et al.* [93] | OFDM-based adaptive TCM schemes in both single- and multi-user environments |
| 2005 | Zhou *et al.* [94] | Adaptive modulation aided MIMO systems with perfect and imperfect channel state information |
| 2006 | Duong [95] | ACM with receive antenna diversity and imperfect channel knowledge at the receiver and transmitter |

Table 1.3: Milestone of Adaptive Coded Modulation (1968-2006).


Figure 1.7: The outline of thesis.

| Year | Author(s) | Contribution |
|---|---|---|
| 2007 | Caire [96] | Information theoretic foundations of ACM |
| 2008 | Duong *et al.* [97] | Analysis and Optimization of ACM in spatially correlated SIMO Rayleigh fading channels |
| 2011 | Brown [98] | Adaptive demodulation in differentially coherent phase systems |
| | Clemente *et al.* [99] | Closed-form analysis of ACM over Rician shadow-fading channels |
| 2012 | Tao and Duel-Hallen [100] | Adaptive BICM for OFDM systems assisted by fading prediction |

Table 1.4: Milestone of Adaptive Coded Modulation (2007-2012).

designed for cooperative communication. Finally, in Section 4.4 adaptive TTCM aided distributed STTCs were proposed for cooperative communications.

**Chapter 5:** The non-coherent coded modulation schemes of Chapter 3 designed for cooperative communications were further exploited in this chapter. Firstly, in Section 5.2 Star-QAM aided turbo coded network coding dispensing with channel estimation was conceived, which was then combined with soft-decision aided DAPSK in the context of AF cooperative communications. Finally, combined cooperative wireless and optical-fiber communications systems were studied.

## 1.4 Novel Contributions of the Thesis

Based on the following publications [101–107], the novel contributions of the thesis are summarised as follows:

1. The Relay Node Selection or Power Allocation (RNSPA) concept conceived for reducing the error-propagation is proposed. In the context of this technique we either select a RN near the desired location, or allocate the most appropriate transmit power to the RN in order to maintain the target SNR at the DN. Naturally, a beneficial amalgam of these techniques is expected to have a better end-to-end performance than the above-mentioned two methods in isolation [102].

2. Then we propose an effective solution for mitigating the lack of temporal diversity, when communicating over quasi-static Rayleigh fading channels. On one hand, the ATTCM scheme effectively exploits the full-potential of various TTCM schemes, when communicating over the source-to-relay links, where the error propagation imposed by the DAF-aided relay nodes is minimised. On the other hand, the DSTTC scheme offers spatial diversity for the relay-to-destination links for the sake of assisting the STTC-TTCM decoder at the destination node

in minimizing the probability of decoding errors [101].

3. We derive the soft-decision demodulation formula for 16-StQAM. Then the performance benefits of using this new formula are demonstrated in the context of BICM and BICM-ID schemes invoked for communications over correlated Rayleigh fading channels [103].

4. The performance benefits of using our proposed soft-decision demodulation formula for 16-StQAM are quantified in the context of a TC aided 16-StQAM scheme, when communicating over correlated Rayleigh fading channels. Then, we employ the 16-StQAM aided TC based physical layer scheme for assisting a butterfly topology based Network Coding (NC) system. A power sharing mechanism is also proposed for further reducing the overall transmit power requirement of the network [106].

5. We use the existing Bit Metric of Iterative *a posteriori* probability Decoders (BMIAD) 16-DAPSK (2,8) scheme as a benchmark for our proposed 16-DAPSK (2,8) schemes. We derive the soft-decision demodulation probability formulas for M-DAPSK ($M_a$,$M_p$) schemes, which have more than two concentric PSK rings. We quantify the EXIT-chart-based throughput of M-DAPSK ($M_a$,$M_p$) systems and show that our TC-aided M-DAPSK ($M_a$,$M_p$) schemes are capable of approaching the achievable channel capacity. We then conceive a novel soft-decision DAPSK aided AF based cooperative system, which completely dispenses with channel estimation [107].

6. We investigate the uplink performance of FFR based multicell multiuser schemes, as a complement of the corresponding downlink investigation. We further extend the SISO based non-coherent 16StQAM scheme to a Single-Input Multiple-Output (SIMO) system. We investigate both the Turbo-Coded 16StQAM and 16QAM schemes in the multicell, multiuser uplink system considered, when imperfect DFO or AROF links are considered [108]. Furthermore, the a novel adaptive turbo-coded soft-decision aided differential detection system is designed for wireless-optical communications over imperfect optic fiber links in the AROF principle [109].

Chapter 2

# Coherent Coded Modulation

## 2.1 Introduction

In Chapter 1 we have reviewed the history of Coded Modulation (CM) and Adaptive Coded Modulation (ACM). Let us now investigate further both the principles and the attainable performance of coherent CM and ACM schemes in this chapter.

One of the most important objectives in the design of digital cellular systems is the efficient exploitation of the available spectrum in order to accommodate the ever-increasing traffic demands. The design of CM schemes is affected by a variety of criteria, such as: implementation complexity, coding/interleaving delay, the effective throughput and so on [6]. The Trellis-Coded Modulation (TCM) scheme employing symbol-based channel interleaving combined with Set Partitioning (SP) assisted signal labelling was proposed by Ungerböck [110]. A joint coding and modulation scheme, namely Turbo Trellis-Coded Modulation (TTCM) was proposed by Robertson [52], which has a similar structure to turbo codes, but employs TCM schemes as component codes. The TTCM arrangement employs symbol-based channel interleaving combined with SP assisted signal labelling. Both TCM and TTCM using SP assisted signal labelling were proposed for achieving a higher Free Euclidean Distance (FED) between the unprotected bits of the constellation, so that parallel trellis transitions can be associated with the unprotected information bits, which reduced the decoding complexity. Another powerful CM scheme utilising bit-based channel interleaving in conjunction with Gray signal labelling, which is referred to as Bit–Interleaved Coded Modulation (BICM), was proposed by Zehavi [42]. An iterative joint decoding and demodulation assisted BICM (BICM-ID) arrangement using SP based signal labelling was proposed by Li [49], which increased the Euclidean distance of conventional BICM and exploited the full advantage of bit interleaving with the aid of soft-decision feedback based iterative decoding.

In order to counteract the time-varying nature of the mobile radio channels, near-instantaneous ACM schemes have been proposed [84, 86, 111], where a higher-rate and/or a higher-order modulation mode is employed, when the instantaneous estimated channel quality is high in order to

increase the number of Bits Per Symbol (BPS) transmitted. Conversely, a more robust lower-rate code and/or a lower-order modulation mode is employed, when the instantaneous channel quality is low, in order to improve the Bit Error Ratio (BER) performance. When communicating over quasi-static Rayleigh fading channels, each transmission frame effectively experiences an AWGN channel associated with a received SNR ($SNR_r$) determined by the ratio of the constant fading coefficient and the noise power. By contrast, each transmission frame effectively experiences an uncorrelated Rayleigh fading channel having $SNR_r$ determined by the constant fading coefficient and the noise power, when communicating over 'shadow-and-fast' Rayleigh fading channels.

A number of powerful joint coding and coherent modulation schemes, namely TCM, TTCM, BICM and BICM/ID for 4PSK, 8PSK, 16QAM and 64QAM are introduced in Section 2.2, while the corresponding fixed CM modes' performance is characterized in Section 2.2.5. Furthermore, a near-instantaneous ACM scheme is invoked in Section 2.3 and the corresponding simulation results are shown in Section 2.3.2. The chapter is concluded in Section 2.4.

## 2.2 Fixed Mode

CM constitutes a bandwidth efficient scheme [22] that combines the functions of channel coding and modulation. In this section, the coherent TCM, TTCM, BICM and BICM-ID schemes relying on 4PSK, 8PSK, 16QAM and 64QAM will be introduced. Furthermore, SP and the Maximum A Posteriori MAP algorithm are also discussed. Finally, the corresponding simulation results will be presented in Section 2.2.5.

### 2.2.1 Rate and SNR

Let us consider a system, where the channel encoder has a coding rate of:

$$R_c = \frac{k}{n}, \tag{2.1}$$

and an $M$-ary modulation scheme transmitting $m$ BPS is used, where:

$$R_m = \log_2(M) = \mathrm{m}. \tag{2.2}$$

The overall throughput of the scheme may be expressed as:

$$R_o = R_c \cdot R_m = \frac{k}{n}\mathrm{m}. \tag{2.3}$$

The ratio of the symbol energy to the spectral density of the noise ratio determines the SNR which can be expressed as:

$$\gamma = \frac{E_s}{N_0}, \tag{2.4}$$

while the ratio of the information bit energy to the noise spectral density can be calculated as:

$$\frac{E_b}{N_0} = \frac{1}{R}\frac{E_s}{N_0} = \frac{\gamma}{R}. \tag{2.5}$$

The noise variance per dimension is given by $\sigma^2 = N_0/2$. Therefore, at a given SNR or $E_b/N_0$ value, the corresponding noise variance per dimension can be formulated as:

$$\sigma^2 = \frac{RE_b}{2(\frac{E_s}{N_0})} = \frac{E_s}{2R(\frac{E_b}{N_0})}. \tag{2.6}$$

### 2.2.2 Fading Channel

Fading appears due to attenuation of the radio signal, when it passes through objects on its way from the transmitter to the receiver, as well as due to reflection and scattering of the transmitted signal. Furthermore, the received signal power is reduced in proportion to the distance between the antennas, which can be compensated by increasing the transmit power with the aid of power-control. When designing coded modulation, it is important to know the correlation of the fading over both time and frequency. Figure 2.1 represents an overview of diverse fading channel manifestations. Let us commence with the two basic types of fading effects, namely large-scale and small-scale fading: [1]

- *Large-scale fading* arises due to path loss as a function of distance and shadowing imposed by large objects, such as large-bodied vehicles, buildings and hills. This occurs as the mobile moves across the terrain, and it is typically frequency independent.
- *Small-scale fading* is due to the constructive and destructive interference of the multiple signal paths between the transmitter and receiver. This occurs at a spatial scale, which is of the order of the carrier wavelength and it is frequency dependent.

Furthermore, large-scale fading is more relevant to cell-site planning, while small-scale fading is more relevant to the design of reliable and efficient communications links. Hence, small-scale fading constitutes the focus of the thesis.

### 2.2.3 Turbo Trellis-Coded Modulation

Trellis-Coded Modulation (TCM) may be invoked as the constituent component code employed in the TTCM structure. Hence, it is worth describing the basic principle of TCM, before introducing TTCM. The TCM scheme was introduced by Ungerböck in [3, 110]. Compared to conventional uncoded modulation schemes, a simple four-state TCM scheme is capable of improving the robustness of digital transmission against additive noise, which may be quantified in terms of the required SNR. This is achieved without decreasing the data rate or expending the bandwidth [110], albeit at the cost of an increased detection complexity. Upon using more complex schemes, the coding

[1] Small-scale fading often obeys *Rayleigh fading*, because if the multiple reflective paths are large in number and there is no line-of-sight signal component, the envelope of the received signal is statistically described by a Rayleigh Probability Density Function (PDF). When there is a dominant non-fading signal component, such as a line-of-sight propagation path, the small-scale fading envelope is described by a Rician PDF [112].

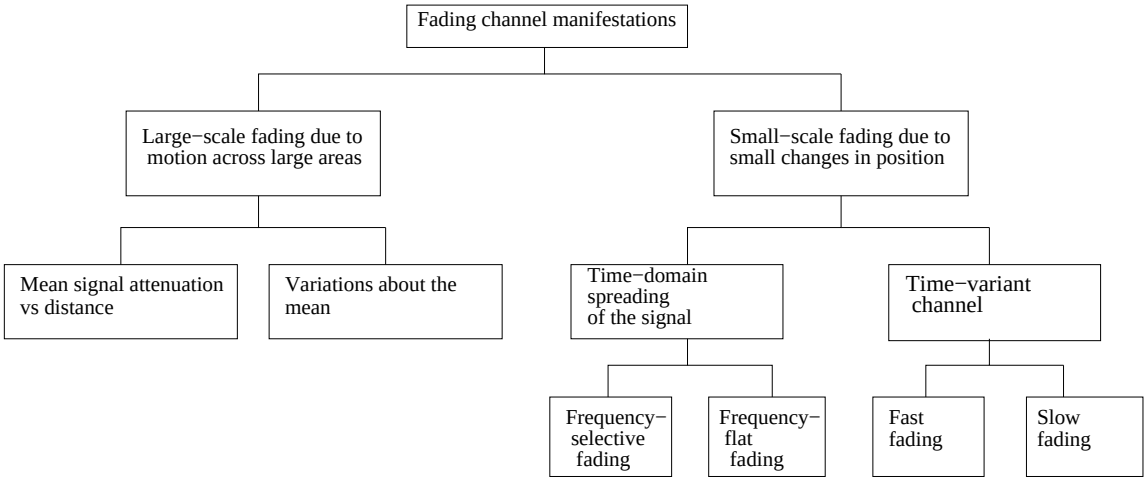


Figure 2.1: Fading channel manifestations [113, 114].

gain may be increased to a degree. The TCM schemes may be described by their state transition diagram, which is similar to the trellis diagrams of binary convolutional codes [115]. More specially, the redundant non-binary symbols represented by the constellation phasors are employed for labelling the trellis branches of the TCM scheme, rather than using the binary code symbols, as in binary convolutional codes.

#### 2.2.3.1 TCM Principle

Ungerböck's TCM encoder is constituted by a Recursive Systematic Convolutional (RSC) encoder and a modulator [10]. Figure 2.2 shows the TCM encoder having an eight-state Ungerböck

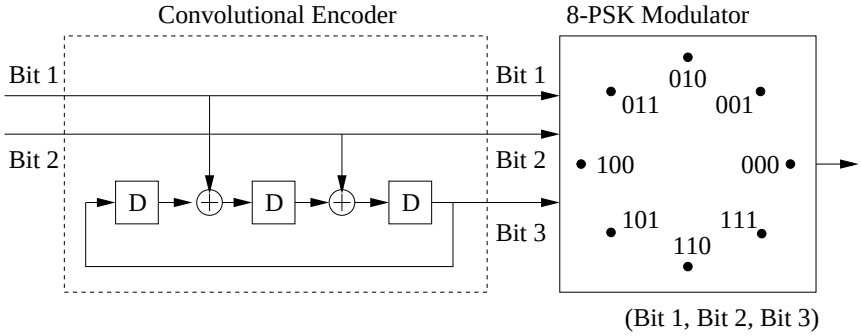


Figure 2.2: The basic 8PSK TCM encoder using Ungerböck's RSC encoder and modulator [116].

code [10], which has a high Free Euclidean distance (FED) for the sake of attaining a high performance gain, when communicating over Additive White Gaussian Noise (AWGN) channels. The 2-bit input binary sequence produces 3-bit codewords, which are then interleaved by a symbol interleaver for dispersing the bursty symbol errors generated by the fading channel. Finally, these 3-bit codewords are modulated to one of the 8 ($2^3$) possible constellation points of an 8PSK modulator.

The generator polynomials, which define the connections between the information bits and adders can be represented as:

$$H^j(D) = h_\nu^j.D^\nu + h_{\nu-1}^j.D^{\nu-1} + ... + h_1^j.D + h_0^j, \tag{2.7}$$

where $D$ denotes the delay due to a register stage and $h_i^j$ equals 1 in the scenario, when there is a connection at a specific encoder stage, while $h_i^j$ is 0, if there is no connection. Furthermore $H^j(D)$ for $j \geq 1$ is the generator polynomial associated with the $j$th information bit. Ungerböck [10] suggested that all feedback polynomials must have coefficients of $h_\nu^0 = h_0^0 = 1$. Hence, the parity bit should be the same for these transitions, when two paths diverge from or merge into a common state in the trellis, otherwise the other bits of the symbols differ in at least one bit position [10]. The design of coded modulation schemes is affected by a variety of factors, such as the cost and complexity. A high FED is required for transmission over AWGN channels, while a high *effective code length* and a high minimum product distance are required for transmission over fading channels [117].

#### 2.2.3.2 Set Partitioning

The SP technique was proposed by Ungerböck for ensuring such that parallel transitions are assigned to constellation points exhibiting a high Euclidean distance for the sake of having a low error probability. Additionally, the signal set can be partitioned into various subsets. More specifically, the minimum Euclidean distance of the signal points in the new subset is increased at every partitioning step [115]. Figure 2.3 shows the SP of 16QAM. Conventional TCM schemes are typically decoded/demodulated with the aid of the appropriately modified Viterbi Algorithm (VA), which is a maximum likelihood sequence estimation (MLSE) algorithm [118]. Nonetheless, a performance close to the minimum Symbol Error Ratio (SER) can be achieved by using VA, although it cannot guarantee that the SER is minimized, because it is an MLSE algorithm.

#### 2.2.3.3 Maximum-A-Posteriori

The MAP algorithm is capable of guaranteeing that the minimum SER is achieved, but naturally at the cost of an increased complexity. In this section, a reduced-complexity version of the MAP algorithm that operates in the logarithmic domain (log-domain) will be discussed. Figure 2.4 illustrates the operations of the symbol-based MAP algorithm [115]. Each information symbol $u_k$ has $M$ possible values. The *a priori* probabilities of the information symbol $u$ can be obtained from external sources:

$$P_{apri_{k,m}} = p(u_k = m), \tag{2.8}$$

If the *a priori* information $p(u_k)$ is not available, we have $P_{apri_{k,m}} = 1/M$ for all m. The channel's output values can be computed as:

$$\eta_k(j,m) = \exp \frac{-|y_k - S_L(j,m)|^2}{2\sigma^2}, \tag{2.9}$$

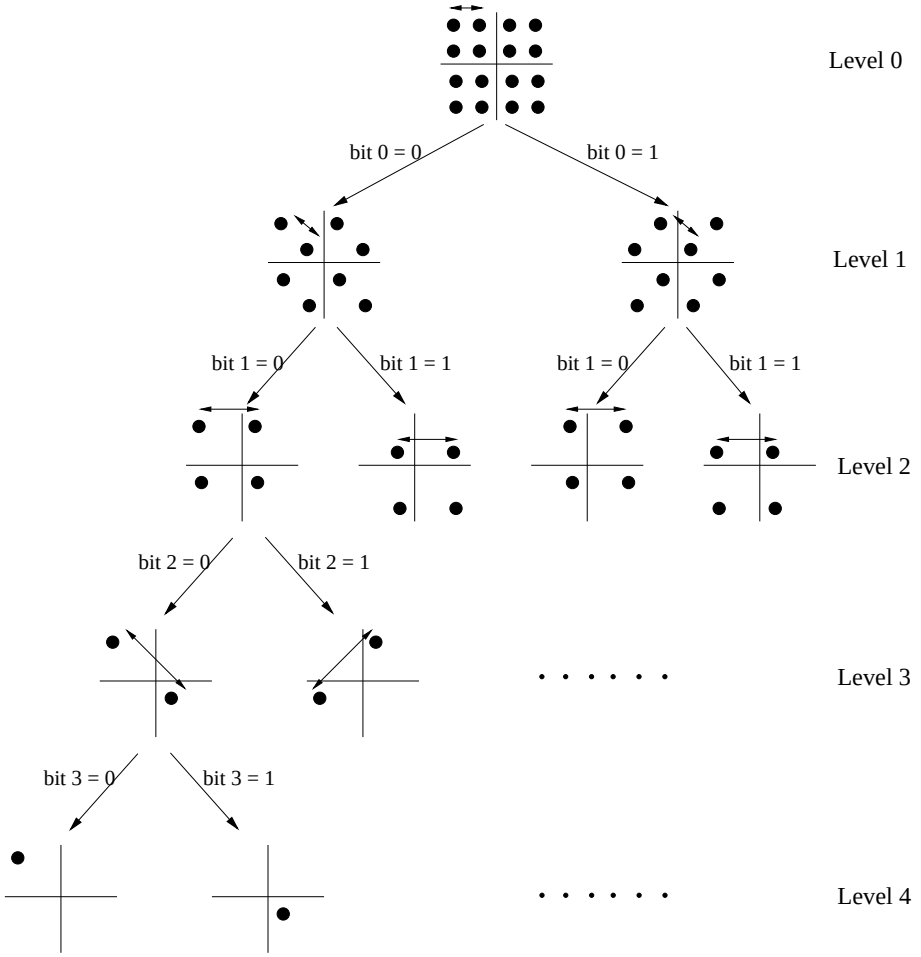


Figure 2.3: Set-Partitioning of a 16QAM signal constellation. The minimum Euclidean distance at a partition level is denoted by the line between the signal points [115] ©IEEE, 1982, Ungerböck.

where the transmitted symbol is $x_k = S_L(j,m)$ and the received signal is $y_k = x_k + n_k$, where $n_k$ is the complex-valued AWGN having a variance of $\sigma^2 = N_0/2$ per-dimension and $N_0$ is the noise's Power Spectral Density (PSD). The transition probabilities are computed according to $\gamma_k(i,m) = P_{apri_{k,m}} \cdot \eta_k(j,m)$. Then these values are used for recursively computing the forward recursion [6]:

$$\alpha_{k-1}(j) = \sum_{m=0}^{M-1} a_{k-1}[S_P(i,m)] \cdot \gamma_k[P(i,m),m], \tag{2.10}$$

where $S_P(i,m)$ is the previous state, while the backward recursion can be computed from [6]:

$$\beta_{k-1}(j) = \sum_{m=0}^{M-1} \beta_k[S_N(j,m)] \cdot \gamma_k(j,m), \tag{2.11}$$

where $S_N(j,m)$ presents the next state. Finally, the APP can be obtained from:

$$\bar{A}_{k,m} = P_{apri_{k,m}} \cdot \sum_{j=0}^{S-1} \beta_k[S_N(j,m)] \cdot \alpha_{k-1}(j) \cdot \eta_k(j,m). \tag{2.12}$$

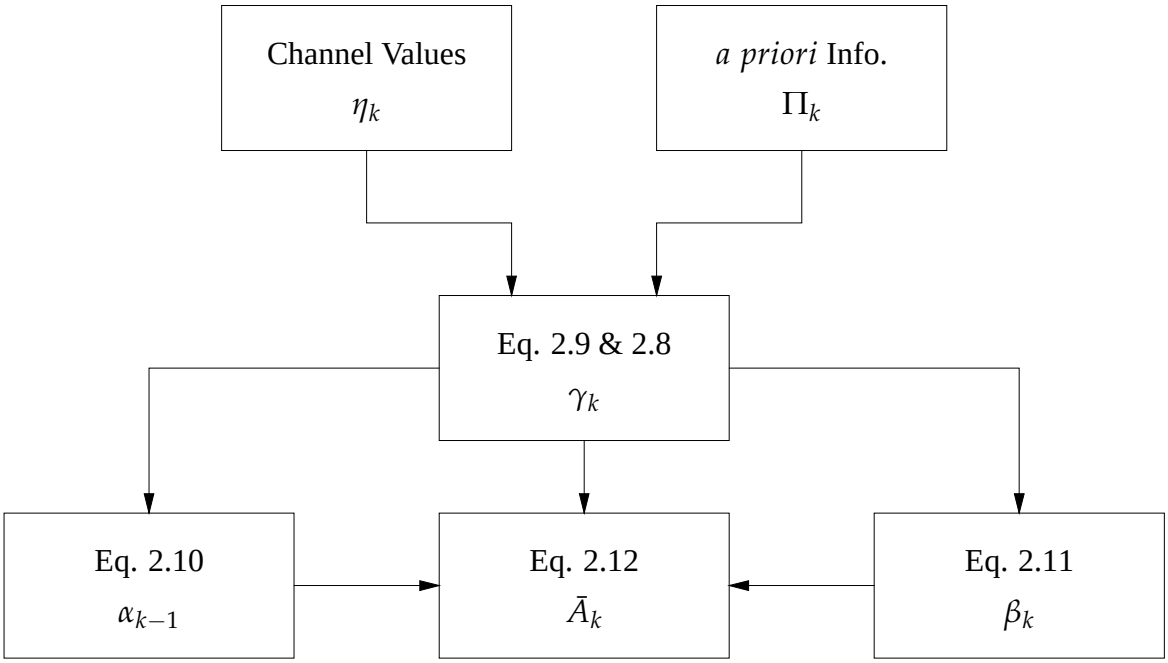


Figure 2.4: Summary of the symbol-based MAP algorithm operations [115].

Moreover, the MAP algorithm exhibits a high complexity. As a remedy, the Log-Map algorithm was proposed by Robertson [52], where the addition of two exponential terms can be computed using the Jacobian logarithm as:

$$\begin{aligned} g(\Phi_1,\Phi_2) &= \ln(e^{\Phi_1}+e^{\Phi_2}) && (2.13)\\ &= \max\{\Phi_1,\Phi_2\}+\ln(1+e^{-|\Phi_1-\Phi_2|}) && (2.14)\\ &= \max\{\Phi_1,\Phi_2\}+f_c(|\Phi_1-\Phi_2|). && (2.15) \end{aligned}$$

The correction term $f_c$, which depends on the magnitude difference of $\Phi_1$ and $\Phi_2$, can be determined with the aid of the following three methods:

1. The Exact-Log-MAP algorithm [52], which is defined by computing the exact value of the correction term $f_c$ using:
$$f_c = \ln(1+e^{-|\Phi_1+\Phi_2|}). \quad (2.16)$$

2. The Approx-Log-MAP algorithm [52] employs an approximation of the correction term $f_c$. A look-up table containing eight values of $f_c$ ranging from 0 to 5, gives practically the same performance as the Exact-Log-MAP algorithm [119].

3. The Max-Log-MAP [30, 120], which simply relies on $\max\{\Phi_1,\Phi_2\}$. Compared to the Approx-Log-MAP algorithm, it has a lower performance, but imposes a reduced complexity.

Based on the above discussions, the Approx-Log-MAP algorithm is the best compromise scheme in terms of its performance and complexity. Hence it was employed for all simulations in this

thesis. It is worth noting that the MAP decoder is more suitable for the decoding of finite-length, short sequences, because the associated memory requirements increase linearly with the sequence-length.

#### 2.2.3.4 TTCM Encoder

We will employ TTCM [52] for avoiding the obvious disadvantage of rate loss that one would encounter, when applying the principle of parallel concatenation to TCM without the aid of puncturing. The TTCM encoder is seen in Figure 2.5, which comprises two identical TCM encoders linked by a symbol interleaver. The first TCM encoder encodes the original input bit sequence, while the second encoder manipulates the interleaved version of the input bit sequence and then the codewords are then mapped to complex symbols by the signal mapper using the SP-based labelling method. Moreover, the complex output symbols of the signal mapper at the output of Trellis Encoder 2 are symbol de-interleaved according to the inverse operation of the symbol interleaver. More specifically, the interleaver and de-interleaver are symbol based [121]. The TTCM codewords of both component encoders have identical information bits before the selector due to the de-interleaver. Therefore, the selector that selects the symbols of the upper and lower component encoders is effectively a puncturer that removes half of the parity bits. The output of the selector is fed to the channel interleaver, which is another symbol interleaver. The channel interleaver disperses the symbol errors experienced during transmission over fading channels. This improves the time-diversity order of the code [122]. Finally, the output symbols are transmitted through the channel. Figure 2.1 shows the generator polynomials of some component TCM codes that

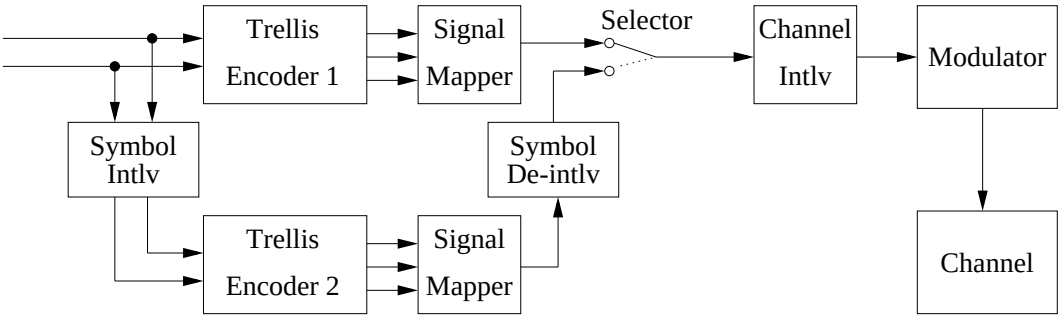


Figure 2.5: Schematic of the TTCM encoder [115] ©IEEE, 1998, Robertson and Wörz.

can be employed in the TTCM schemes. These generator polynomials were obtained by using an exhaustive computer search of all polynomials and then finding the one that maximises the minimal Euclidean distance, taking into account the alternative selection of parity bits for the TTCM scheme.

| Code | State, $\nu$ | $\tilde{m}$ | $H^0(D)$ | $H^1(D)$ | $H^2(D)$ | $H^3(D)$ | $d^2_{free}/\triangle^2_0$ |
|---|---|---|---|---|---|---|---|
| $2\bar{D}$, 8PSK | 4, 2 | 2 | 07 | 02 | 04 | - | |
| $2\bar{D}$, 8PSK | 8, 3 | 2 | 11 | 02 | 04 | - | 3 |
| $4\bar{D}$, 8PSK | 8, 3 | 2 | 11 | 06 | 04 | - | 3 |
| $2\bar{D}$, 8PSK | 16, 4 | 2 | 23 | 02 | 10 | - | 3 |
| $4\bar{D}$, 8PSK | 16, 4 | 2 | 23 | 14 | 06 | - | 3 |
| $2\bar{D}$, 16QAM | 8, 3 | 3 | 11 | 02 | 04 | 10 | 2 |
| $2\bar{D}$, 16QAM | 16, 4 | 3 | 21 | 02 | 04 | 10 | 3 |
| $2\bar{D}$, 64QAM | 8, 3 | 2 | 11 | 04 | 02 | - | 3 |
| $2\bar{D}$, 64QAM | 16, 4 | 2 | 21 | 04 | 10 | - | 4 |

Table 2.1: 'Punctured' TCM codes exhibiting the best minimum distance for 8PSK, 16QAM and 64QAM, where octal format is used for specifying the generator polynomials [121]. The notation $\bar{D}$ denotes the dimensionality of the code, $\nu$ denotes the code memory, $\triangle^2_0$ denotes the squared Euclidean distance of the signal set itself and $d^2_{free}$ denotes the squared FED of the TCM code.

#### 2.2.3.5 TTCM Decoder

The schematic of a component decoder of a binary turbo code and of a non-binary TTCM scheme are shown in Figure 2.6 and Figure 2.7, respectively. Both have a similar structure, albeit there is a difference in the nature of the information passed from one decoder component to the other. Moreover, each decoder alternately processes its corresponding encoder's channel-impaired output symbol, and then the other encoder's channel-impaired output symbol. In a binary turbo coding scheme the component encoder's output can be divided into three additive parts of each information bit $u_k$ at step $k$, which are detailed bellow:

1. the systematic component $(S/s)$, which is the received systematic value for bit $u_k$;

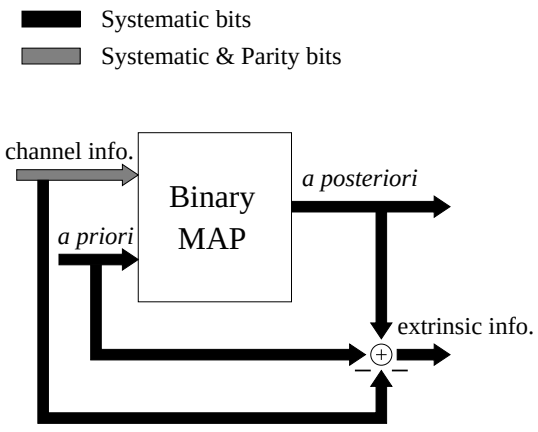


Figure 2.6: Schematic of a binary turbo component decoder [115].

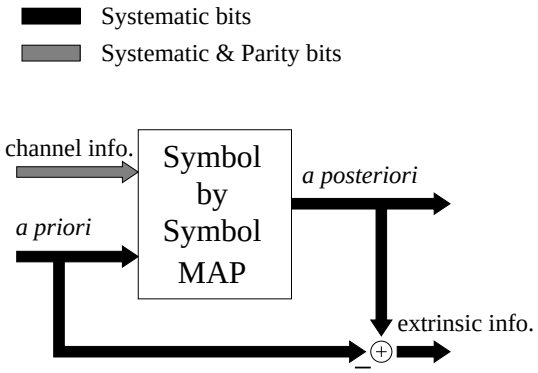


Figure 2.7: Schematic of a non-binary TTCM component decoder [115].

2. the *a priori* component $(A/a)$, which corresponds to the information provided by the other component decoder for bit $u_k$;

3. the extrinsic information component $(\mathrm{E}/\mathrm{e})$, which does not depend on bit $u_k$ itself, but on the surrounding bits.

Compared to the binary turbo decoding scheme, the non-binary TTCM scheme has only two components:

1. the *a priori* component of a non-binary symbol $(A/a)$, which is provided by the other component decoder;

2. the extrinsic as well as systematic component of a non-binary symbol.

### 2.2.4 Bit-Interleaved Coded Modulation with Iterative Decoding

The bit-based (BICM and BICM-ID) CM schemes will be introduced in this section, commencing with the BICM scheme in Section 2.2.4.1. Then the BICM-ID scheme will be investigated in Section 2.1.3.2. Finally, our simulation results will be discussed in Section 2.1.4.

#### 2.2.4.1 Bit-Interleaved Coded Modulation

Figure 2.8 presents the BICM encoder, while Figure 2.9 shows Paaske's non-systematic rate-$2/3$ eight-state code, exhibiting a free bit-based Hamming distance of four. It is worth noting that the number of bit interleavers equals the number of bits assigned to the non-binary codeword. More importantly, the purpose of bit interleaving is to disperse the bursty errors induced by the correlated fading for rendering the bits associated with a given transmitted symbol uncorrelated or independent of each other. This would increase the time diversity order of the code.

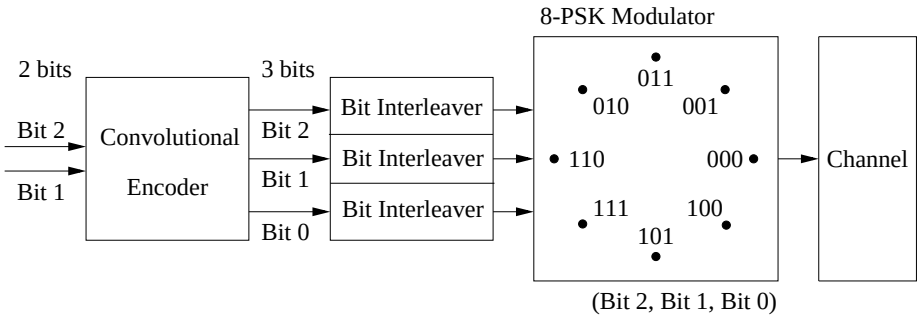


Figure 2.8: BICM encoder schematic employing independent bit interleavers. Note that Gray labelling is employed [42] ©IEEE, 1992, Zehavi.

Here Gray labelling is employed for optimising the performance of the BICM scheme which will be detailed in Section 2.2.4.2. The non-systematic convolutional code exhibiting the highest

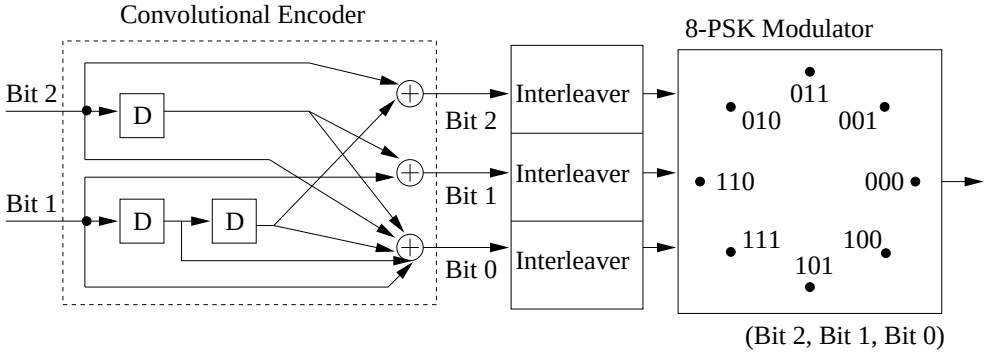


Figure 2.9: Paaske's non-systematic convolutional encoder, bit-based interleavers and modulator forming the BICM encoder [42], where none of the bits are unprotected and Gray labelling is employed.

possible free Hamming distance is used in BICM for obtaining optimum performance for transmission over Rayleigh fading channels. Figure 2.10 shows the BICM decoder, which implements the

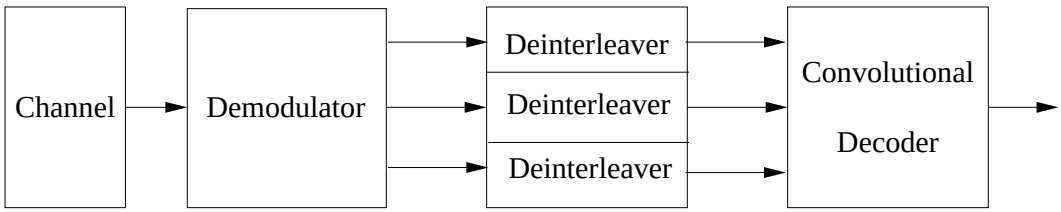


Figure 2.10: BICM decoder [42].

inverse process of the encoder. Table 2.2 presents parameters of Paaske's non-systematic codes utilised in BICM. For a rate-$k/n$ code there are $k$ generator polynomials, each having $n$ coefficients. More explicitly, $\mathbf{g_i} = (g^0, g^1, \ldots, g^n)$, $i \leq k$, is the generator polynomial associated with the $i$th information bit. The generator matrix of the encoder used in Figure 2.9 may be expressed as:

$$\mathbf{G}(\mathbf{D}) = \begin{bmatrix} 1 & D & 1+D \\ D^2 & 1 & 1+D+D^2 \end{bmatrix}, \tag{2.17}$$

| Rate | State, $\nu$ | $g^{(1)}$ | $g^{(2)}$ | $g^{(3)}$ | $g^{(4)}$ | $d_{free}$ |
|---|---|---|---|---|---|---|
| 1/2 | 8, 3 | 15 | 17 | - | - | 5 |
| (4QAM) | 16, 4 | 23 | 35 | - | - | 7 |
| | 64, 6 | 133 | 171 | - | - | 10 |
| 2/3 | 8, 3 | 4 | 2 | 6 | - | 4 |
| (8PSK) | | 1 | 4 | 7 | - | |
| | 16, 4 | 7 | 1 | 4 | - | 5 |
| | | 2 | 5 | 7 | - | |
| | 64, 6 | 64 | 30 | 64 | - | 7 |
| | | 30 | 64 | 74 | - | |
| 3/4 | 8, 3 | 4 | 4 | 4 | 4 | 4 |
| (16QAM) | | 0 | 6 | 2 | 4 | |
| | | 0 | 2 | 5 | 5 | |
| | 32, 5 | 6 | 2 | 2 | 6 | 5 |
| | | 1 | 6 | 0 | 7 | |
| | | 0 | 2 | 5 | 5 | |
| | 64, 6 | 6 | 1 | 0 | 7 | 6 |
| | | 3 | 4 | 1 | 6 | |
| | | 2 | 3 | 7 | 4 | |

Table 2.2: Paaske's non-systematic convolutional codes, page 331 of [123], where $\nu$ denotes the code memory and $d_{free}$ denotes the free Hamming distance. Octal format is used for representing the generator polynomial coefficients [115].

| Rate | State, $\nu$ | $g^{(1)}$ | $g^{(2)}$ | puncturing matrix | $d_{free}$ |
|---|---|---|---|---|---|
| 5/6 | 8, 3 | 15 | 17 | 1 0 0 1 0 | 3 |
| (64QAM) | | | | 0 1 1 1 1 | |
| | 64, 6 | 133 | 171 | 1 1 1 1 1 | 3 |
| | | | | 1 0 0 0 0 | |

Table 2.3: Rate-Compatible Punctured Convolutional (RCPC) codes [124, 125], where $\nu$ denotes the code memory and $d_{free}$ denotes the free Hamming distance. Octal format is used for representing the generator polynomial coefficients [115].

while the equivalent polynomial expressed in octal form is given by:

$$\mathbf{g_1} = \begin{bmatrix} 4 & 2 & 6 \end{bmatrix} \quad \mathbf{g_2} = \begin{bmatrix} 1 & 4 & 7 \end{bmatrix}. \tag{2.18}$$

Table 2.3 summarises the parameters of the Rate-Compatible Punctured Convolutional (RCPC) codes that can be used in the rate=$5/6$ BICM/64QAM schemes.

#### 2.2.4.2 BICM-ID

Although BICM is capable of improving the diversity order of Ungerböck's TCM scheme, it performs poorer in the AWGN channel since TCM has a large minimum Euclidean distance, lending it a edge our BICM. As a further advance, Li and Ritcey [49], [56] proposed BICM-ID win order to improve Zehavi's [42] BICM scheme. Figure 2.11 presents the process of subset partitioning for

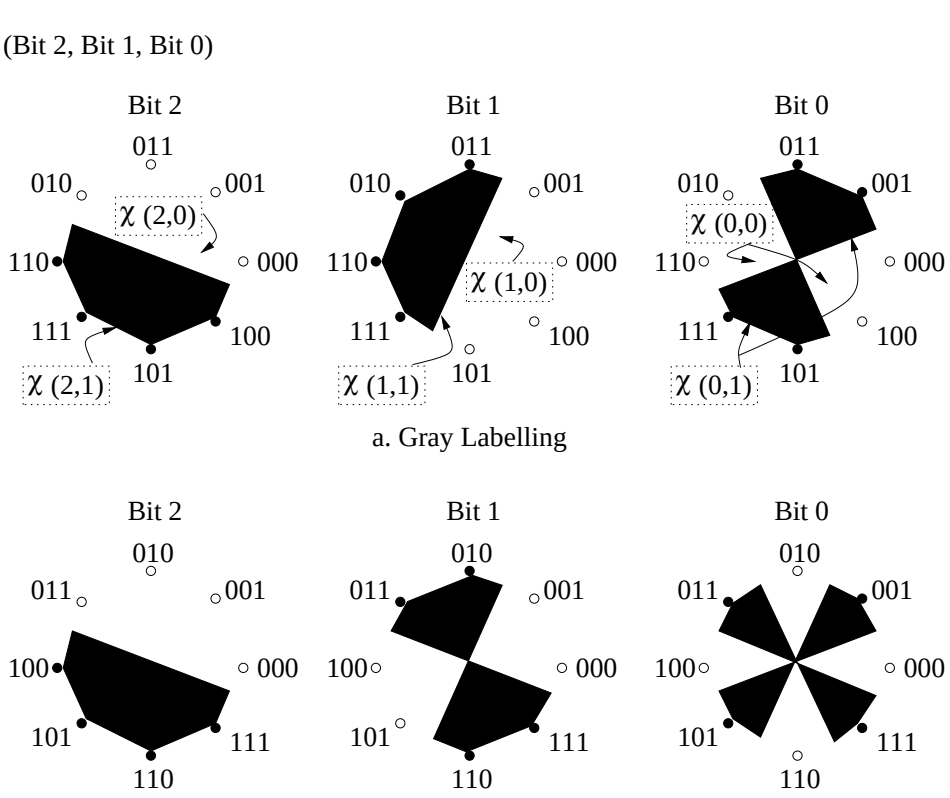


Figure 2.11: SP and Gray labelling methods for 8PSK and the corresponding subset partitioning for each bit [115] ©IEEE, 1999, Li and Ritcey.

each of the three bit positions for both Gray labelling and SP labelling. These subsets are also the decision regions for each bits. Observe in Figure 2.11 that the two labelling methods have the same intersubset distances but the different number of nearest neighbours. We can see from Figure 2.11 that Gray labelling has a lower number of nearest neighbours. The lower the number of nearest neighbours, the lower the chances for a bit to be decoded into the wrong region. Therefore, Gray labelling is a more appropriate mapping non-iterative BICM scheme.

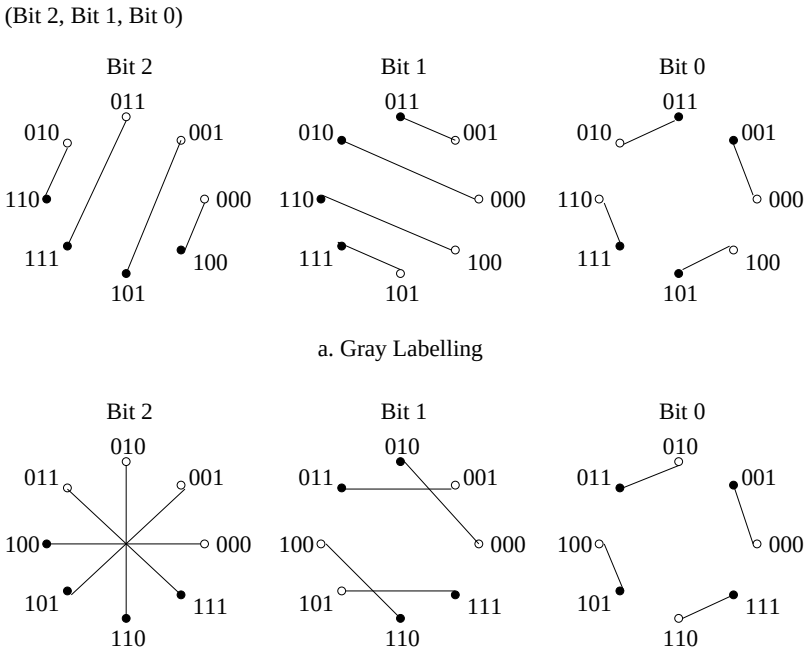


Figure 2.12: Iterative decoding translates the 8PSK scheme into three parallel binary sub-channels, each associated with a BPSK constellation selected from the four possible signal sets [115] ©IEEE, 1999, Li and Ritcey.

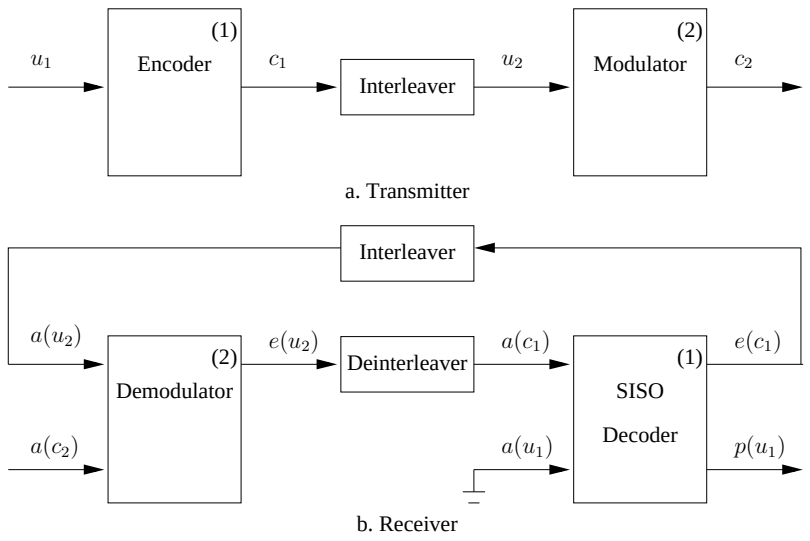


Figure 2.13: The transmitter and receiver modules of the BICM-ID scheme using soft-decision feedback [49] ©IEEE, 1998, Li. Note that *a*, *e* and *p* represent the *a priori*, the *extrinsic* and the *a posteriori* information, respectively.

Figure 2.12 illustrates that SP based labelling has a higher minimum Euclidean distance than that of Gray labelling for both Bit 1 and Bit 2, which is important for optimising the decoding performance of BICM-ID during the second and later iterations because these higher-integrity bits would provide more reliable extrinsic information for the lowest-distance bit. Although the first-pass performance is potentially error-infected, error precipitation owing to erroneous feedback bits, may be efficiently mitigated by the soft feedback of the decoder. Hence, in contrast to Gray-labelled BICM, BICM-ID assisted by soft decision feedback uses SP labelling.

Furthermore, the interleaver design is also important. In our design the $m$ number of interleavers used for the $2^m$-ary modulation scheme are produced randomly and separately, without any interactions between them [115].

Having introduced the labelling and interleaver methods, the transmitter and receiver modules of the BICM-ID scheme are illustrated in Figure 2.13. More specifically, a Soft-Input Soft-Output (SISO) decoder, which is actually a MAP decoder, is employed by the receiver module and the enhanced-reliability output of the decoder is fed back to the input of the demodulator.

### 2.2.5 Simulation Results and Discussions

The BER performance of the fixed modem modes of 4PSK, 8PSK, 16QAM and 64QAM for both TTCM and BICM-ID are studied when communicating over both AWGN and uncorrelated Rayleigh fading channels. The complexity of the coded modulation schemes is compared in terms of the number of decoding states and the number of decoding iterations. For a TCM or BICM scheme with memory $v$, the corresponding complexity is proportional to the number of decoding states, namely to $S = 2^v$. For the TTCM scheme, which includes two component TCM codes, a TTCM code associated with $I_t$ iterations and using an $S$-state component code exhibits a complexity proportional to $2 \cdot t \cdot S$ or $t \cdot 2^{v+1}$. By contrast, for the BICM-ID scheme, which only includes a single decoder, the demodulator is invoked in each decoding iteration. However, the complexity of the demodulator is assumed to be insignificant compared to that of the channel decoder. Therefore, a BICM-ID code associated with $I_t$ iterations using an $S$-state code exhibits a complexity proportional to $t \cdot S$ or $t \cdot 2^v$. The corresponding parameters are shown in Table 2.4.

It is worth to noting that in terms of the decoding complexity of 4PSK TTCM using four iterations and 4PSK BICM-ID using eight iterations can be considered similar according to our above arguments. In our forthcoming discourse we will always endeavour to compare schemes of similar decoding complexity, unless otherwise stated. Furthermore, Figure 2.14 and Figure 2.15 present the BER performance of various TTCM and BICM-ID schemes, when transmitting over the AWGN channel. It can be seen from the figures that the TTCM schemes outperform the BICM-ID schemes, when communicating over the AWGN channel. More explicitly, the $E_b/N_0$ value required for maintaining a BER of $10^{-5}$ is 1.56 dB for the TTCM-4PSK scenario, while it is 3.95 dB for the BICM-ID-4PSK scenario. It is worth noting that all the BER curves seen in Figure 2.14 drop off sharply, except that of the TTCM-16QAM scheme due to the employment of low-memory

| | |
|---|---|
| Coded Modulation | TTCM, BICM-ID |
| Modulation Scheme | 4PSK, 8PSK, 16QAM, 64QAM |
| Mapper type | Set-Partitioned |
| Number of iterations | 4,8 |
| Code Rate | 1/2, 2/3, 3/4, 5/6 |
| Code Memory | 3 |
| Decoder type | Approximate Log-MAP |
| Symbols per frame | 12,000 |
| Number of frames | 10,000 |
| Channel | AWGN, Uncorrelated Rayleigh fading channel |

Table 2.4: Simulation parameters.

component codes. Additionally, the $E_b/N_0$ and SNR thresholds of the TTCM schemes having a target BER of $10^{-5}$ and $10^{-6}$ are obtained from Figure 2.14 and are shown in Table 2.5. Furthermore, the $E_b/N_0$ and SNR thresholds of the BICM-ID schemes having a target BER of $10^{-5}$ and $10^{-6}$ are attained from Figure 2.15 and are shown in Table 2.6.

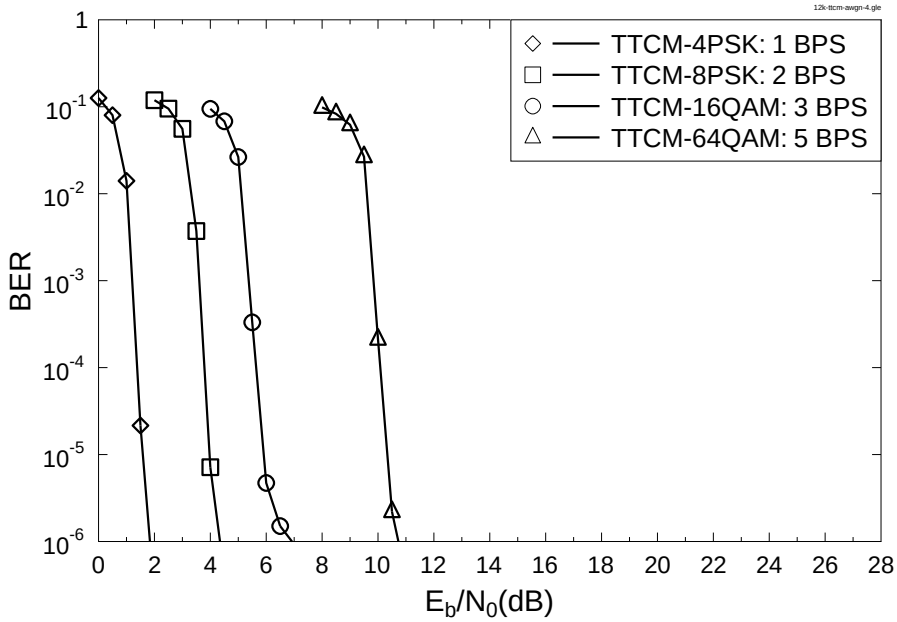


Figure 2.14: BER performance of TTCM aided 4PSK, 8PSK, 16QAM and 64QAM schemes when communicating over the **AWGN channel** using four TTCM iterations. The simulation parameters are shown in Table 2.4.

Figure 2.16 and Figure 2.17 present the BER performance of various TTCM and BICM-ID schemes communicating over uncorrelated Rayleigh fading channels. It can be seen from the figures that the TTCM schemes outperform the BICM-ID schemes, when transmitting over uncorrelated Rayleigh fading channels, except for the case of 64QAM. Note that TTCM-64QAM has a

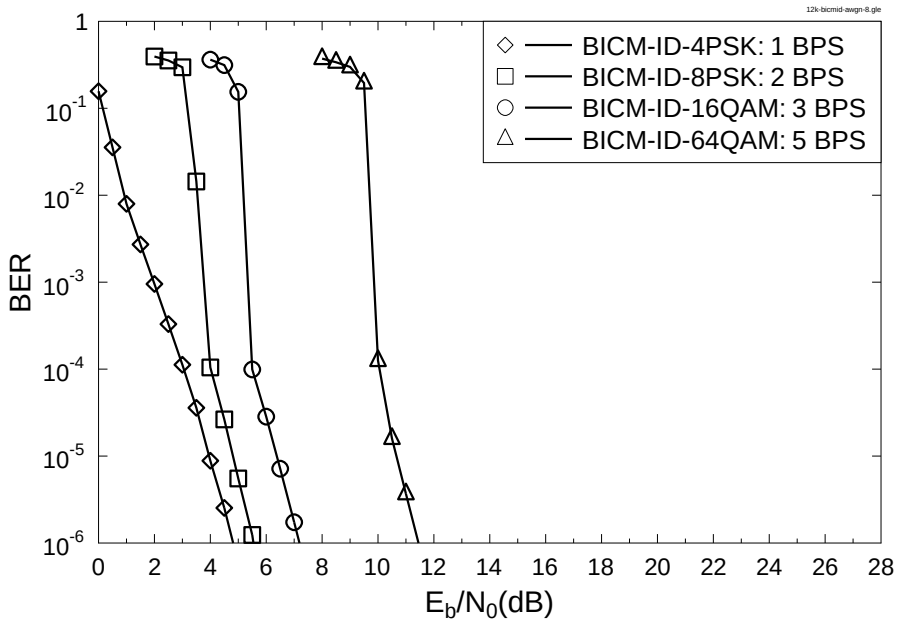


Figure 2.15: BER performance of BICM-ID aided 4PSK, 8PSK, 16QAM and 64QAM schemes when communicating over the **AWGN channel** using **eight** BICM-ID iterations. The simulation parameters are shown in Table 2.4.

| TTCM | $E_b/N_0(dB)$ (BER = $10^{-5}$) | SNR($dB$) (BER = $10^{-5}$) | $E_b/N_0(dB)$ (BER = $10^{-6}$) | SNR($dB$) (BER = $10^{-6}$) |
|---|---|---|---|---|
| 4PSK | 1.56 | 1.56 | 1.83 | 1.83 |
| 8PSK | 3.93 | 6.94 | 4.33 | 7.34 |
| 16QAM | 5.91 | 10.68 | 6.93 | 11.70 |
| 64QAM | 10.29 | 17.28 | 10.73 | 17.72 |

Table 2.5: The $E_b/N_0$ and SNR threshold at BER=$10^{-5}$ and BER=$10^{-6}$ for TTCM schemes when communicating over the **AWGN Channel** using **four TTCM** iterations. The simulation parameters are shown in Table 2.4.

| BICM-ID | $E_b/N_0(dB)$ (BER = $10^{-5}$) | SNR($dB$) (BER = $10^{-5}$) | $E_b/N_0(dB)$ (BER = $10^{-6}$) | SNR($dB$) (BER = $10^{-6}$) |
|---|---|---|---|---|
| 4PSK | 3.95 | 3.95 | 4.80 | 4.80 |
| 8PSK | 4.80 | 7.81 | 5.53 | 8.54 |
| 16QAM | 6.40 | 11.17 | 7.20 | 11.97 |
| 64QAM | 10.67 | 17.66 | 11.47 | 18.46 |

Table 2.6: The $E_b/N_0$ and SNR threshold at BER=$10^{-5}$ and BER=$10^{-6}$ for BICM-ID schemes when communicating over the **AWGN Channel** using **eight BICM-ID** iterations. The simulation parameters are shown in Table 2.4.

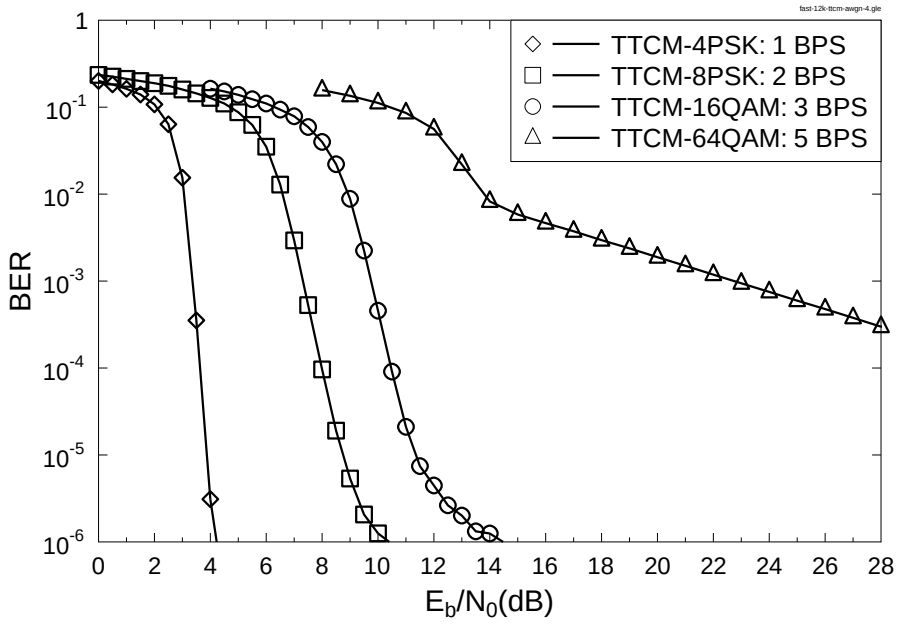


Figure 2.16: BER performance of TTCM aided 4PSK, 8PSK, 16QAM and 64QAM schemes when communicating over the **uncorrelated Rayleigh fading channel** using four TTCM iterations. The simulation parameters are shown in Table 2.4.

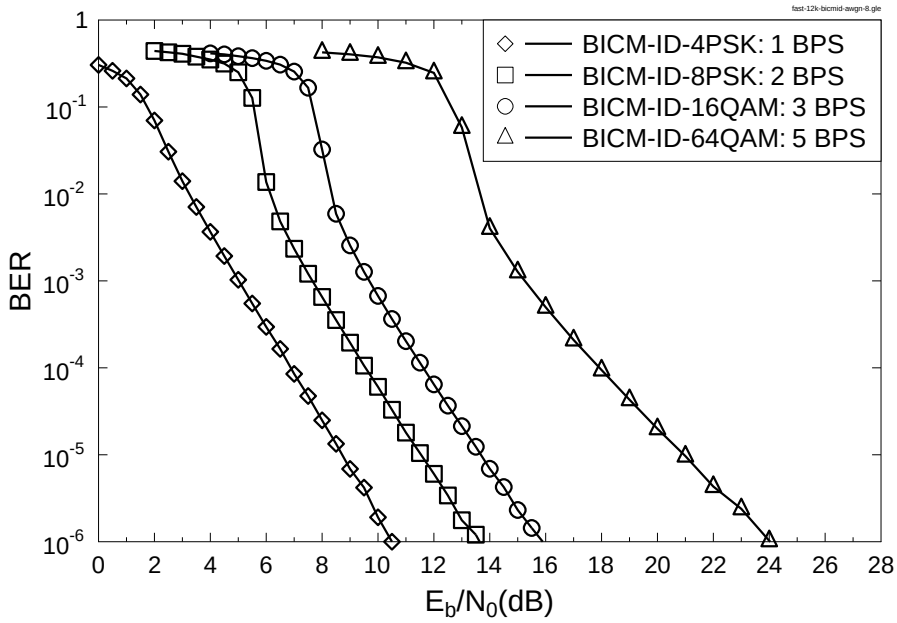


Figure 2.17: BER performance of BICM-ID aided 4PSK, 8PSK, 16QAM and 64QAM schemes when communicating over the **uncorrelated Rayleigh fading channel** using **eight** BICM-ID iterations. The simulation parameters are shown in Table 2.4.

worse BER performance than that of BICM-ID-64QAM over uncorrelated Rayleigh fading channels. This is because the octally represented generator polynomial [6] of $[11\ 02\ 4\ 0\ 0\ 0]$ has three zeros corresponding to no coding for the three systematic bits. This is fine for AWGN channels [52], but it would cause a high error floor when communicating over Rayleigh fading channels [22]. A TTCM-64QAM scheme was proposed for Rayleigh fading channels in [17], which requires a high-complexity trellis having 32 states. By contrast, we only consider 8-state trellises in this chapter. More specially, the $E_b/N_0$ value at a BER of $10^{-5}$ for TTCM-16QAM is about 11.37 dB, while for that of BICM-ID-16QAM it is not far from 13.67 dB. Furthermore, the $E_b/N_0$ and SNR thresholds for the TTCM and BICM-ID schemes having a target BER of $10^{-5}$ are attained from Figure 2.16 and Figure 2.17 that are shown in Table 2.7, which will be employed in Section 2.3.

| Code | $E_b/N_0(dB)$ (BER = $10^{-5}$) | SNR($dB$) (BER = $10^{-5}$) | $E_b/N_0(dB)$ (BER = $10^{-6}$) | SNR($dB$) (BER = $10^{-6}$) |
|---|---|---|---|---|
| 4PSK (TTCM) | 3.87 | 3.87 | 4.21 | 4.21 |
| 8PSK (TTCM) | 7.75 | 10.76 | 10.40 | 13.41 |
| 16QAM (TTCM) | 11.37 | 16.14 | 14.47 | 19.24 |
| 64QAM (BICM-ID) | 20.93 | 26.95 | 24.67 | 31.66 |

Table 2.7: The values of $E_b/N_0(dB)$ and SNR($dB$) for TTCM and BICM-ID over the uncorrelated Rayleigh fading channel. The simulation parameters are shown in Table 2.4.

Based on the EXIT charts which is introduced in Section 1.1.2, we find the minimum SNR ($SNR_{min}$) required by the various fixed CM modes, where the corresponding EXIT charts exhibit an open tunnel and at least one of the Monte-Carlo simulation based decoding trajectory can traverse through the small slit between the inner and outer EXIT curves [126]. Figure 2.18 presents the EXIT charts when communication over AWGN channel using the parameters listed in Table 2.4. Figure 2.19 was obtained by transmitting 10 000 frames, each having the block length 12 000 symbols. The number of iterations was $I_t = 16$ over AWGN channel. It is worth noting that the value of SNR$_{min}$ varies with the number of iterations and block size. Table 2.8 presents SNR and SNR$_{min}$ values for TTCM at a BER of $10^{-5}$, when communicating over AWGN channels. Observe in Figure 2.16 and

| $E_b/N_0(dB)$ $BER = 10^{-5}$ | $SNR_{min}(dB)$ $BER = 10^{-5}$ | Code | $E_b/N_0(dB)$ $BER = 10^{-5}$ | SNR($dB$) $BER = 10^{-5}$ |
|---|---|---|---|---|
| 0.62 | 0.62 | 4PSK | 1.56 | 1.56 |
| 3.06 | 6.07 | 8PSK | 3.93 | 6.94 |
| 5.10 | 9.87 | 16QAM | 5.91 | 10.68 |
| 9.38 | 16.36 | 64QAM | 10.29 | 17.28 |

Table 2.8: The values of SNR and $SNR_{min}$ for TTCM over the AWGN Channel.

Figure 2.17 that TTCM-64QAM has a higher error floor than BICM-ID-64QAM, when communi-

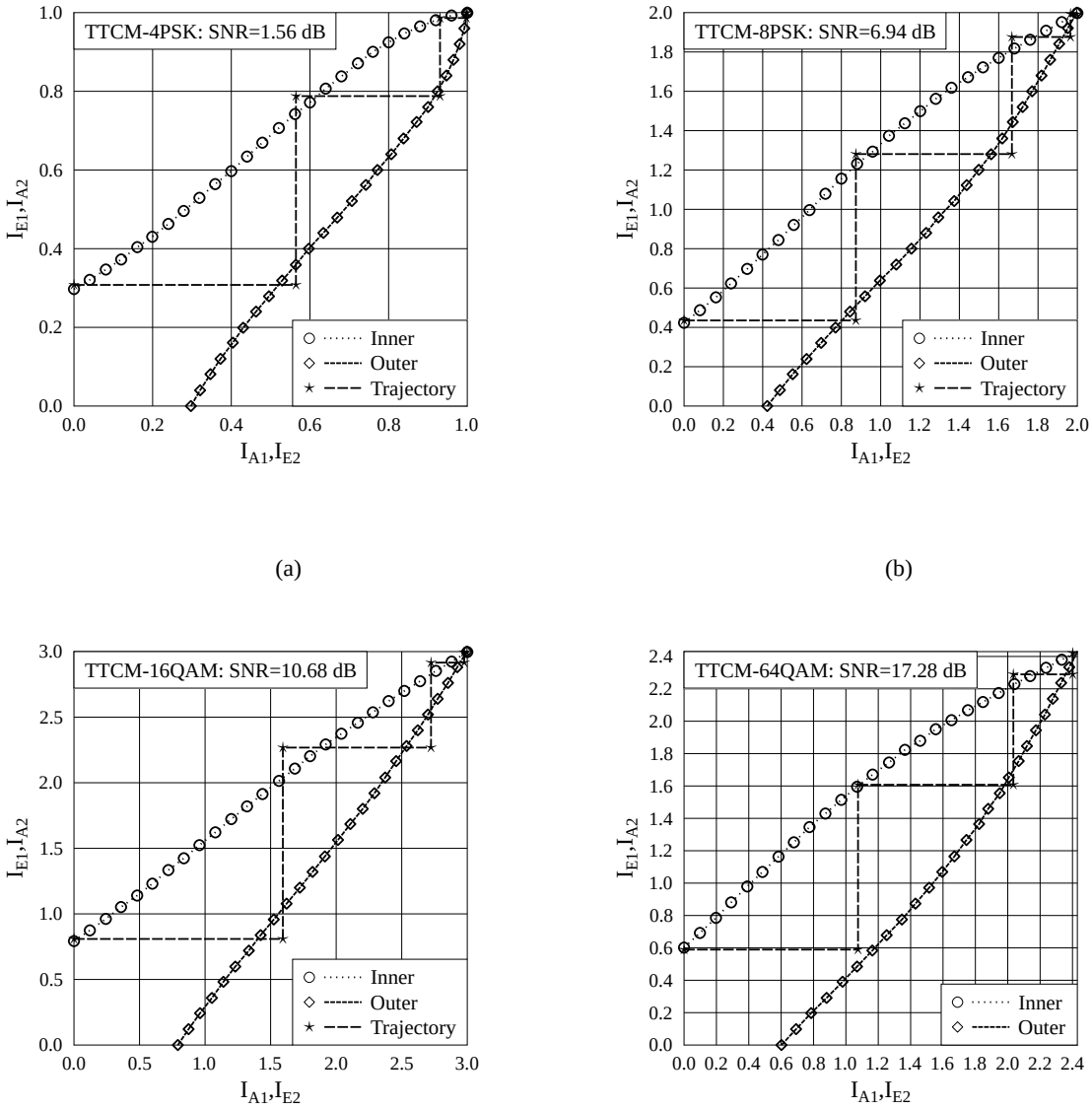


Figure 2.18: EXIT charts of **4PSK, 8PSK, 16QAM and 64QAM** for **TTCM** when communicating over the **AWGN channel** with a SNR value at a BER of $10^{-5}$.

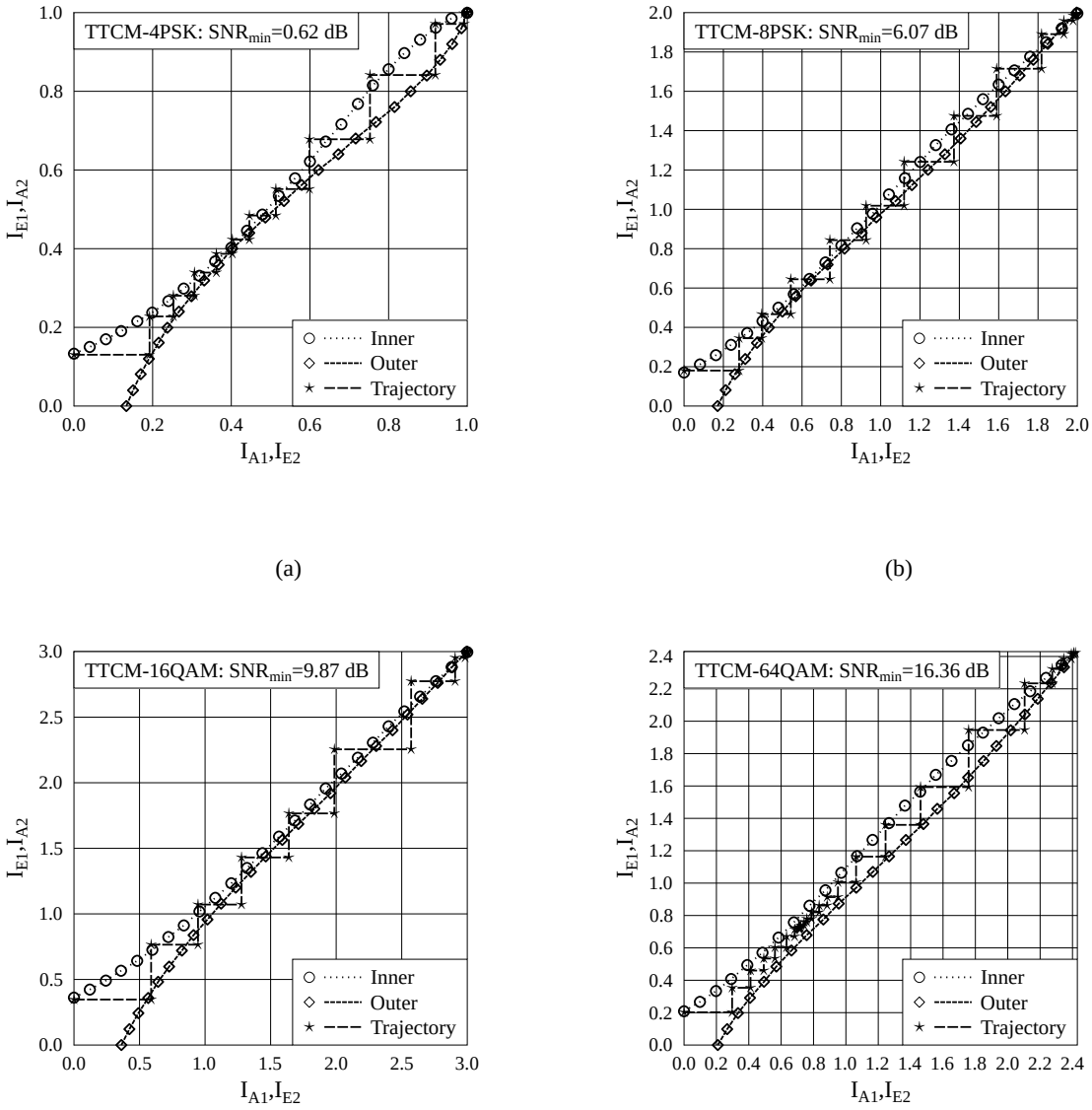


Figure 2.19: EXIT charts of **4PSK, 8PSK, 16QAM and 64QAM** for **TTCM** when communicating over the **AWGN channel** with SNR$_{min}$.

cating over uncorrelated Rayleigh fading channels, since BICM-ID encodes all the five information bits, while TTCM only encodes two of the five information bits. Hence, we favour BICM-ID-64QAM instead of TTCM-64QAM for achieving a throughput of 5 bits-per-symbol (BPS). The related $E_b/N_0$ and SNR values are shown in Table 2.7. Finally, after showing the EXIT charts for transmitting over uncorrelated Rayleigh fading channel with a SNR at a BER of $10^{-5}$ in Figure 2.20, we use EXIT charts to calculate the minimum required SNR. Figure 2.21 was generated for the 12 000 symbol block length and $I_t = 16$ iterations over the uncorrelated Rayleigh fading channel. The related threshold values are presented in Table 2.9. More specifically, for BICM-ID-64QAM an $E_b/N_0 = 21\ dB$ is required for $BER < 10^{-5}$ when communicating over the uncorrelated Rayleigh fading channel. This is due to the limitation imposed by its outer EXIT

| $E_b/N_0(dB)$ | $SNR_{min}(dB)$ | Code | $E_b/N_0(dB)$ | SNR($dB$) |
|---|---|---|---|---|
| 2.30 | 2.30 | 4PSK (TTCM) | 3.87 | 3.87 |
| 6.40 | 9.41 | 8PSK (TTCM) | 8.75 | 11.76 |
| 9.10 | 13.87 | 16QAM (TTCM) | 11.37 | 16.14 |
| 19.93 | 26.92 | 64QAM (BICM-ID) | 20.93 | 27.95 |

Table 2.9: The values of SNR and $SNR_{min}$ for TTCM and BICM-ID over uncorrelated Rayleigh fading channel.

curve.

## 2.3 Adaptive Mode Selection Regime

Having introduced the various fixed-mode based CM schemes in Section 2.2, we will now introduce the family of near-instantaneously Adaptive Coded Modulation (ACM) schemes, which employ the mode selection regime detailed later in this section. The ACM modes are controlled by the near-instantaneous channel quality fluctuations. Specifically, for example, if the channel is good, a rate-3/4 channel encoder and 16QAM can be employed, while if the channel is poor, a rate-1/2 channel encoder and QPSK can be adopted. ACM is capable of maximizing the throughput, when the channel quality improves and vice versa. Having quantified the performance of TTCM and BICM-ID schemes for transmission over both AWGN and independent Rayleigh fading channels in Section 2.2, the ACM mode selection method is proposed in this section. Finally, the performance of this scheme, which is based on that of the individual fixed modulation modes quantified in Section 2.2.5 will be compared in terms of its BER and BPS.

### 2.3.1 ACM System Architecture

The schematic of the near-instantaneous ACM is depicted in Figure 2.22. The transmitter extracts the ACM mode signalled back by the receiver employing the mode selection mechanism in order

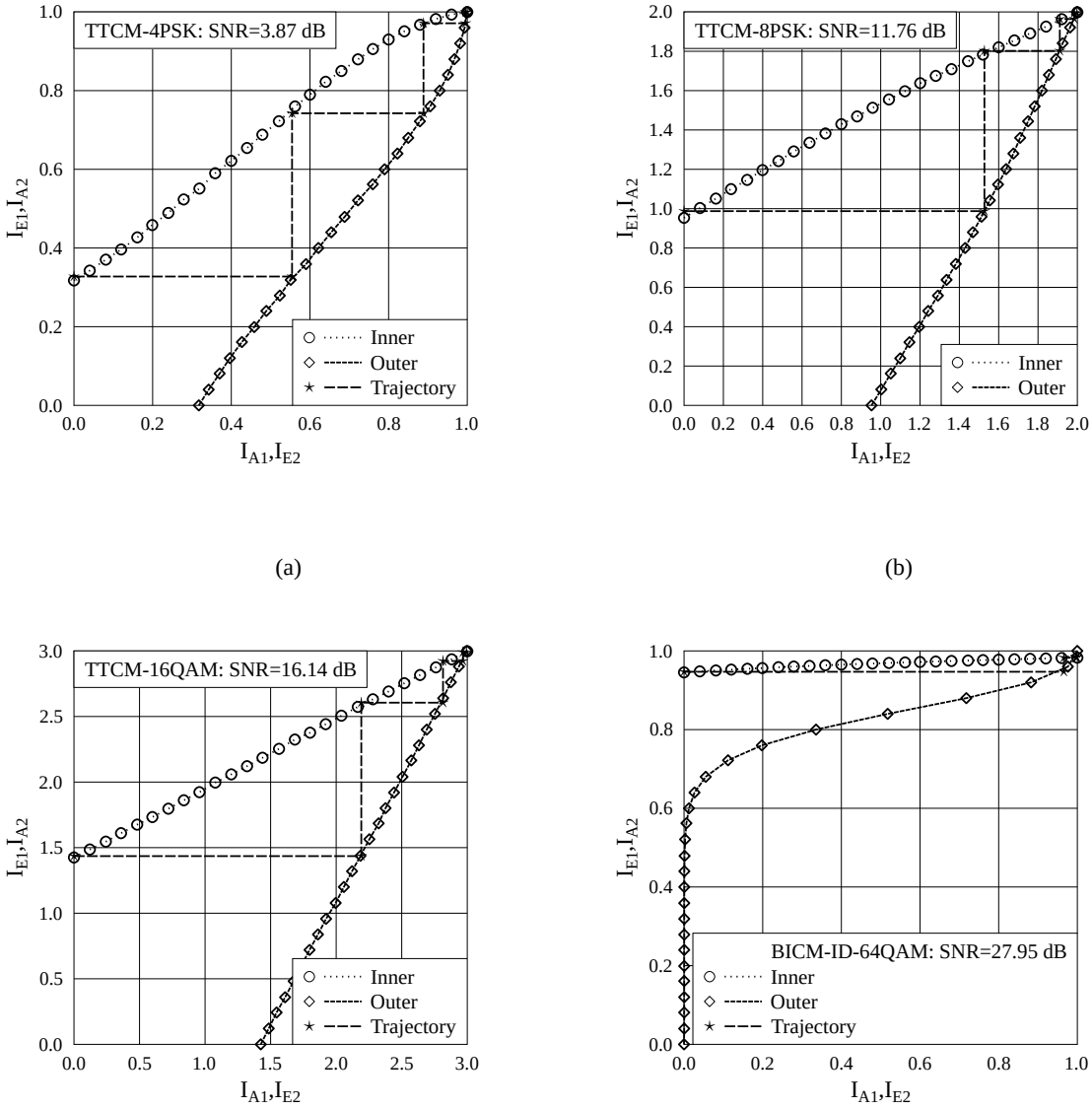


Figure 2.20: EXIT charts of **4PSK, 8PSK, 16QAM and 64QAM** for **TTCM** when communicating over the **uncorrelated Rayleigh fading channel** with a SNR value at a BER of $10^{-5}$.

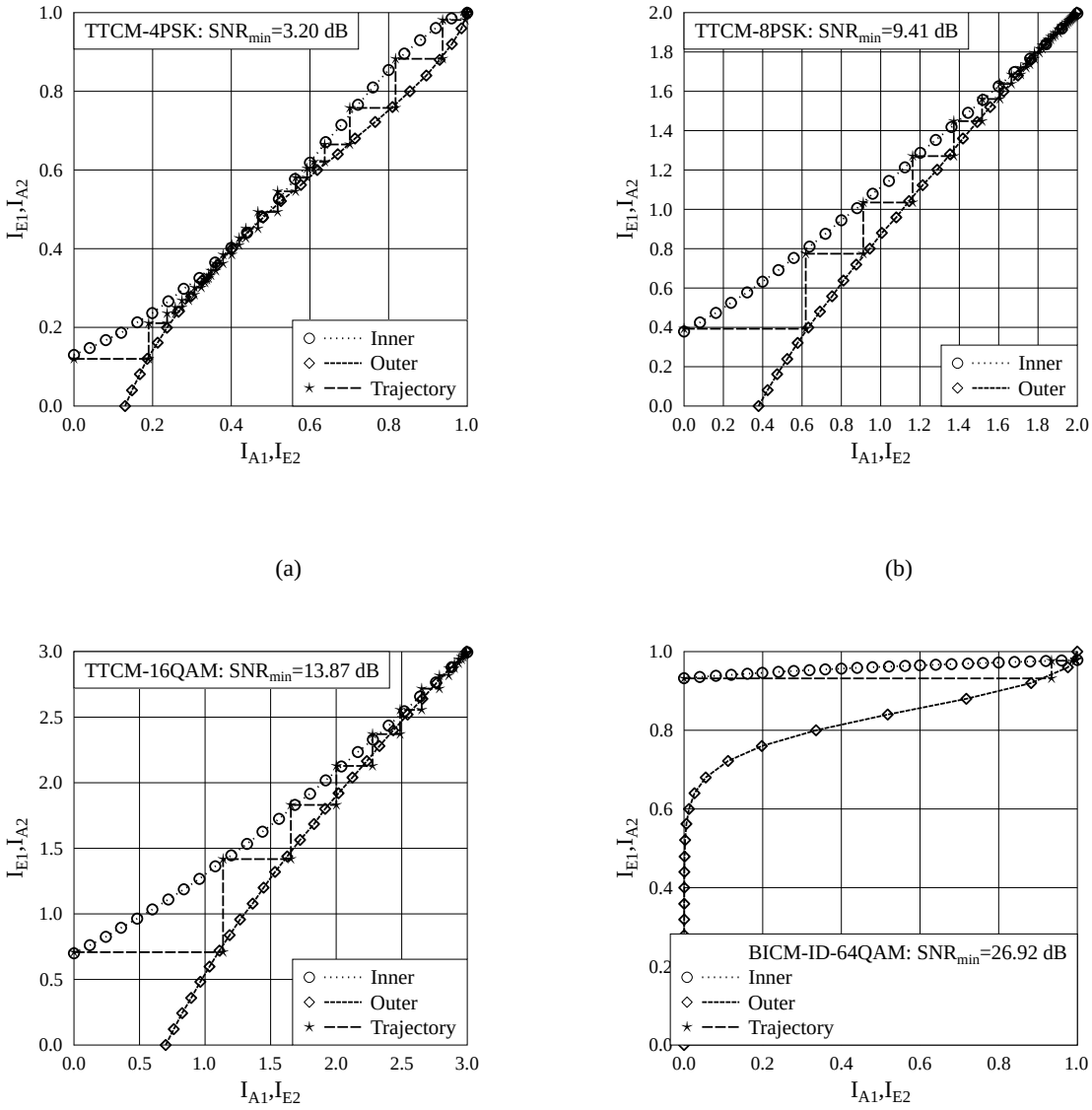


Figure 2.21: EXIT charts of **4PSK, 8PSK, 16QAM and 64QAM** for **TTCM** when communicating over the **uncorrelated Rayleigh fading channel** with $SNR_{min}$.

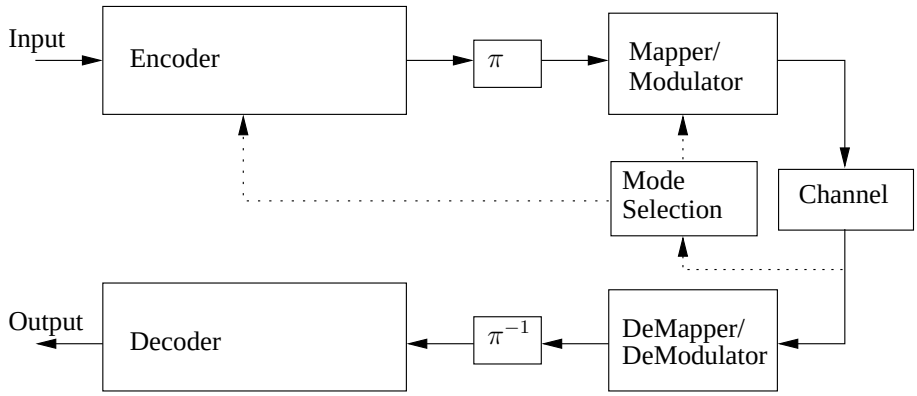


Figure 2.22: Schematic of adaptive coded modulation, where $\pi$ and $\pi^{-1}$ represent the interleaver and deinterleaver, respectively.

to adjust the ACM mode suitable for the prevalent channel. We invoke five ACM encoder modes, namely:

- No transmission (NoTx): 0 BPS;
- TTCM-4PSK: 1 BPS;
- TTCM-8PSK: 2 BPS;
- TTCM-16QAM: 3 BPS;
- TTCM/BICM-ID-64QAM: 5 BPS.

The corresponding coding rates are 1/2 for 4PSK, 2/3 for 8PSK, 3/4 for 16QAM and 5/6 for 64QAM.

#### 2.3.1.1 ACM Mode Selection

The Burst-by-Burst (BbB) ACM mode selecting mechanism is characterized by the set of switching thresholds value of [$\gamma_0$, $\gamma_1$, $\gamma_2$, $\gamma_3$], which are determined based on the required target BER performance. More specifically, our ACM mode selection method can be summarized as follows:

- No transmission (NoTx): 0 BPS, if $\gamma_r \leq \gamma_0$;
- TTCM-4PSK: 1 BPS, if $\gamma_0 < \gamma_r \leq \gamma_1$;
- TTCM-8PSK: 2 BPS, if $\gamma_1 < \gamma_r \leq \gamma_2$;
- TTCM-16QAM: 3 BPS, if $\gamma_2 < \gamma_r \leq \gamma_3$;
- TTCM/BICM-ID-64QAM: 5 BPS, if $\gamma_3 < \gamma_r$,

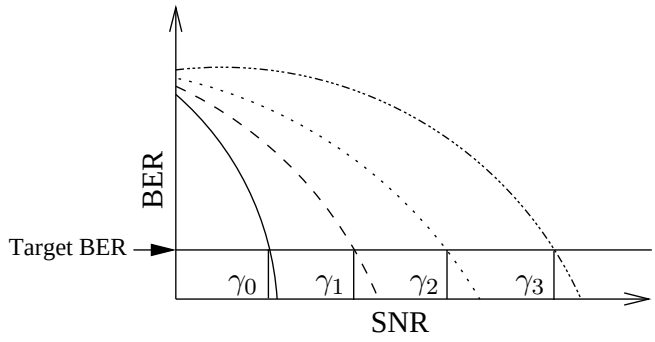


Figure 2.23: Mode selection according to a target BER.

where $\gamma_r$ is the SNR at the receiver. The mode selection operations are illustrated in Figure 2.23. Based on the target BER, the related threshold value can be obtained. Then the instantaneous received SNR $\gamma_r$ is compared to the threshold value and the appropriate CM can be selected.

#### 2.3.1.2 Overall Throughput

It is worth noting that the achievable throughput [73] is an important parameter of the ACM system. The aim of choosing different CM schemes is to maximize the throughput at a given channel condition. For the classic non-adaptive coded modulation schemes, the BER is reduced and the BPS throughput remains constant, when the SNR increases. By contrast, for the ACM system, the BER is kept below the target BER threshold and the throughput improves, as the SNR increases.

The overall throughput may be expressed as:

$$R_o = R_s \cdot R_c \cdot R_m, \tag{2.19}$$

where $R_s = \frac{number\ of\ sources}{time\ slots}$ is the system's overall normalised throughput, while $R_c$ is the coding rate and $R_m$ is the number of bits per modulated symbol.

### 2.3.2 Simulation Results and Discussions

The fixed coded modulation modes were characterized in Section 2.2.5, employing the simulation parameters listed in Table 2.4. In this section, we still use the simulation parameters listed in Table 2.4, but in order to study the near-instantaneous ACM, we employ two different Rayleigh fading channels: quasi-static Rayleigh fading channels, shadow-and-fast Rayleigh fading channels. We will detailed the two different Rayleigh fading channels in Section 2.3.2.1 and then present the related simulation results in Section 2.3.2.2.

### 2.3.2.1 Fading Channel Models

In this treatise, the block-based Rayleigh fading channel is used, where the channel's path gain remains constant over a transmission block and this constant is faded independently between blocks. Explicitly, the complex-valued channel envelope in constituted by the combination of the channel's constant gain and constant phase values. The channel's quality is assumed to be known at the transmitter.

As seen in Figure 2.1, the time-variant channel can be divided into two parts, namely the fast fading and slow fading, where the fast fading is characterized by its Doppler frequency ($f_d$) [112, 127]. Figure 2.24 presents the stylized quality variation of the 'shadow-and-fast' Rayleigh fading channel and the stylized BPS throughput of our ACM system. When the channel gain incorporates

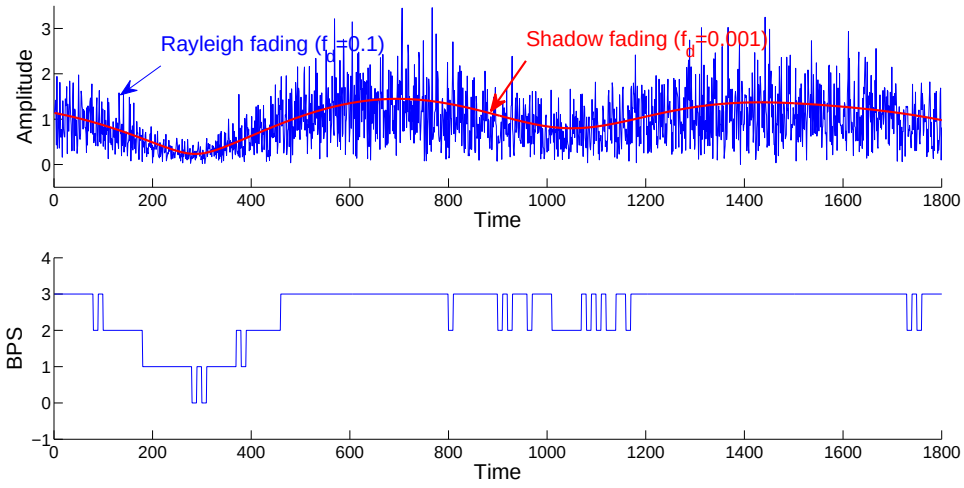


Figure 2.24: The envelope of both the shadow fading and Rayleigh fading.

both the shadow- and fast- fading components, the adaptive transmission may adapt to both if channel gain fluctuates very slowly, but in most practical cases it only counteracts the shadow fading. Figure 2.24 also demonstrates the qualitative effects of the combined shadow-and-fast Rayleigh fading channels on the achievable BPS throughput.

### 2.3.2.2 Simulation Results

Our experimental ACM results are presented in Figures 2.25 – 2.28 based on the simulation parameters listed in Table 2.4, when communicating over quasi-static and shadow-and-fast Rayleigh fading channels.

The mode selection probability of activating the 4PSK, 8PSK, 16QAM and 64QAM ACM modes is shown in Figure 2.25, while the BER vs SNR and BPS vs SNR performance of the near-instantaneous ACM schemes communicating over quasi-static Rayleigh fading channels using the adaptive thresholds of Table 2.5 are shown in Figure 2.26. To elaborate a little further, Figure 2.25

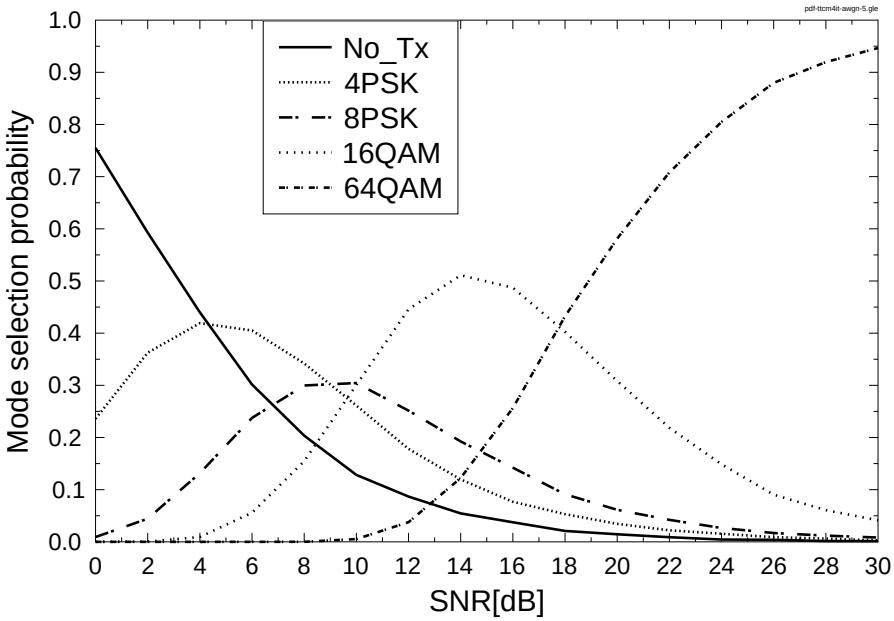


Figure 2.25: The **mode selection probability** of 4PSK, 8PSK, 16QAM, and 64QAM for **TTCM** transmissions over **quasi-static Rayleigh fading channels** using block size of 12 000 symbols, frames of 10 000, and iteration numbers of 4. The related simulation parameters are detailed in Table 2.4.

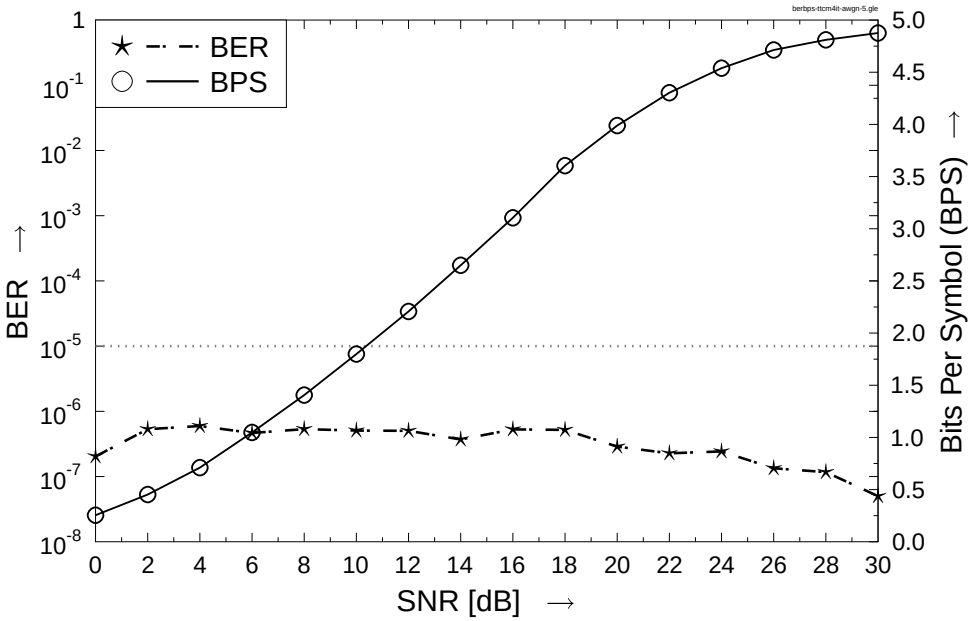


Figure 2.26: The **BER, BPS** of 4PSK, 8PSK, 16QAM, and 64QAM for **TTCM** transmissions over **quasi-static Rayleigh fading channels** using block size of 12 000 symbols, frames of 10 000, iteration numbers of 4. The related simulation parameters are detailed in Table 2.4 and the target BER is $10^{-5}$ as are shown in Table 2.5.

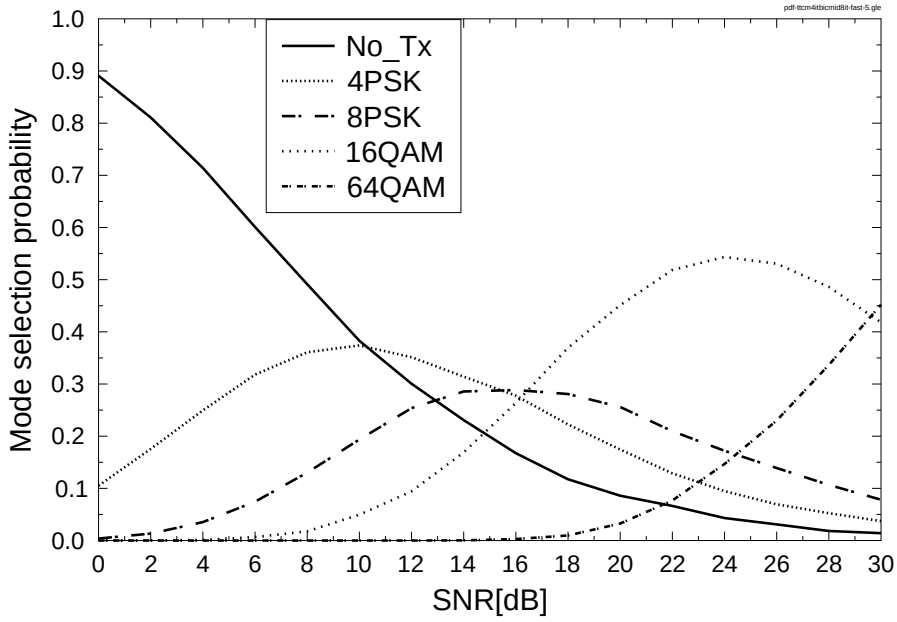


Figure 2.27: The **mode selection probability** of 4PSK, 8PSK, 16QAM for **TTCM**, and 64QAM for **BICM-ID** transmissions over **shadow-and-fast Rayleigh fading channels**. The related simulation parameters are detailed in Table 2.4 the target BER is $10^{-5}$.

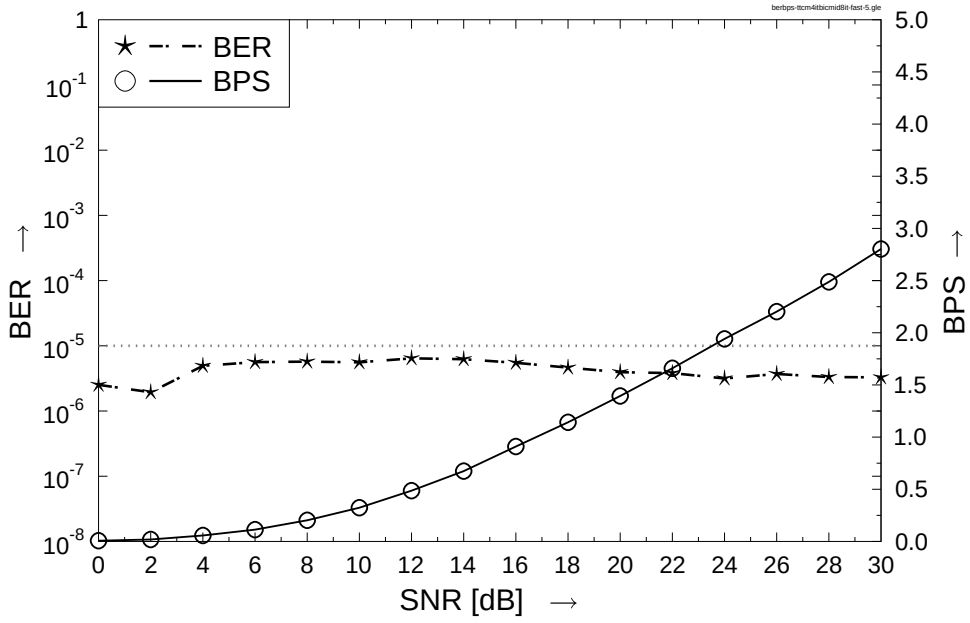


Figure 2.28: The **BER, BPS** of 4PSK, 8PSK, 16QAM for **TTCM**, and 64QAM for **BICM-ID** transmissions over **shadow-and-fast Rayleigh fading channels**. The related simulation parameters are detailed in Table 2.4 the target BER is $10^{-5}$.

presents the long-term CM mode selection probability for a range of SNR values. Observe in Figure 2.25 that when the channel quality is poor, the TTCM-NoTx mode is employed more frequently, while the TTCM-64QAM mode is used more frequently upon increasing the SNR. The BER and BPS vs SNR performance of our adaptive TTCM system using four iterations is shown in Figure 2.26, where we observe that the overall BER was indeed always lower than the target BER of $10^{-5}$.

Furthermore, Figure 2.27 shows the mode selection probability versus SNR of the 4PSK, 8PSK, 16QAM and 64QAM modes of the near-instantaneous ACM schemes, when transmitting over shadow-and-fast Rayleigh fading channels. To provide further insights, Figure 2.28 presents the corresponding BER vs SNR and BPS vs SNR performance of the near-instantaneous ACM schemes communicating over the same shadow-and-fast Rayleigh fading channels. Figure 2.27 shows the long-term CM mode selection probability for a range of SNR values using the ACM mode-switching configured for a BER of $10^{-5}$ in Table 2.7. The comparison of Figure 2.25 and Figure 2.27 reveals that higher-order modulation modes are used more frequently by the quasi-static Rayleigh fading channels. Observe in Table 2.5 and Table 2.6 that as expected, the adaptive thresholds determined for the AWGN channels are lower than those of independently-fading Rayleigh channels, when the BER is $10^{-5}$. Hence higher-order modulation modes were chosen more frequently for transmission over quasi-static Rayleigh fading channels than for shadow-and-fast Rayleigh fading channels. The BER and BPS performance of the ACM scheme transmitting over shadow-and-fast Rayleigh fading channels using the adaptive thresholds configured for a BER of $10^{-5}$ in Table 2.7 are shown in Figure 2.28. As expected, Figure 2.26 has a lower BER and also a higher BPS throughput compared to Figure 2.28.

## 2.4 Chapter Conclusions

In this chapter, the family of coherently detected fixed-mode and ACM schemes was studied. Firstly, the fixed coherently detected TCM, TTCM, BICM, BICM-ID using 4PSK, 8PSK, 16QAM and 64QAM schemes were introduced in Section 2.2. The TCM and the TTCM scheme relying on SP assisted signal labelling employed symbol-based channel interleaving, while the BICM scheme used Gray based signal labelling. Finally, the BICM-ID scheme relying on SP assisted signal labelling invoked bit-based channel interleaving. Recall from Figure 2.14 and Figure 2.15 that the TTCM scheme outperforms the BICM-ID scheme when communicating over AWGN, while imposing a similar complexity. By contrast, when communicating over uncorrelated Rayleigh fading channels, the BER performance of the TTCM-64QAM scheme is worse than that of the BICM-ID scheme, as portrayed in Figure 2.14 and Figure 2.15. More specifically, the SNR threshold values at a target BER of the various CM schemes are tabulated in Table 2.10.

Having studied the fixed CM modes, the required adaptive thresholds were obtained in Section 2.2.5. Then the near-instantaneous ACM scheme employing adaptive mode selection was proposed in Section 2.3. More specifically, the near-instantaneous ACM scheme is depicted in Fig-

| Channel | | AWGN | | Uncorrelated Rayleigh | |
|---|---|---|---|---|---|
| Memory | | 3 | | | |
| Decoder | | Approximate Log-MAP | | | |
| Code | BPS | SNR (dB) at BER | | | |
| | | $10^{-5}$ | $10^{-6}$ | $10^{-5}$ | $10^{-6}$ |
| TTCM-4PSK | 1 | 1.56 | 1.83 | 3.87 | 4.21 |
| TTCM-8PSK | 2 | 6.94 | 7.34 | 10.76 | 13.41 |
| TTCM-16QAM | 3 | 10.68 | 11.70 | 16.14 | 19.24 |
| TTCM-64QAM | 5 | 17.28 | 17.72 | error-floor | error-floor |
| BICM-ID-4PSK | 1 | 3.95 | 4.80 | 8.71 | 10.50 |
| BICM-ID-8PSK | 2 | 7.81 | 8.54 | 14.54 | 16.61 |
| BICM-ID-16QAM | 3 | 11.17 | 11.97 | 18.44 | 20.73 |
| BICM-ID-64QAM | 5 | 17.66 | 18.46 | 26.95 | 31.66 |

Table 2.10: SNR threshold values of various CM schemes when transmitting over AWGN and uncorrelated Rayleigh fading channels. The values are tabulated from Figures 2.14–2.17.

ure 2.22 and the mode selection mechanism is portrayed in Figure 2.23. The corresponding simulation results recorded for transmission over both quasi-static Rayleigh fading channels as well as over shadow-and-fast Rayleigh fading channels are shown in Figure 2.25, Figure 2.26, Figure 2.27 and Figure 2.28.

Having studied the family of coherent CM and its ACM counterpart, the class of non-coherent CM and non-coherent ACM will be introduced in the next chapter. More specifically, the soft-decision aided differentially detected non-coherent QAM will be proposed.

Chapter 3

# Noncoherent Coded Modulation

## 3.1 Introduction

In Section 2.2 we have investigated the performance of coherently detected coded modulation modes for transmission over both AWGN and uncorrelated Rayleigh fading channels. Then, in Section 2.3 the transmission of the adaptive modes over quasi-static Rayleigh fading channels as well as shadow-and-fast Rayleigh fading channels was considered. Naturally, low-complexity modem schemes are desirable in many applications. Hence, in Section 3.2 low-complexity soft-decision aided differentially encoded non-coherently detected constant-throughput systems are proposed, which are then invoked in the near-instantaneously adaptive schemes of Section 3.3.

Differentially encoded non-coherently detected modulation techniques have a low complexity, since they do not require any Channel State Information (CSI). Differential Phase Shift Keying (DPSK) is a classic differentially encoded modulation scheme, which only takes the phase information into account. Upon increasing the number of amplitude-rings, the concept of Differential Amplitude and Phase-Shift Keying (DAPSK) was conceived, which can also be interpreted as an extension of the DPSK scheme [6,128–130]. More specifically, both the amplitude and the phase information are differentially encoded. Owing to its robustness to false phase-locking of the carrier-recovery and due to its better performance than that of the identical-throughput DPSK scheme, there has been growing interest in differentially encoded multilevel modulation schemes conceived for achieving a high data-rate [6, 128–130]. In this thesis, the notation M-DAPSK ($M_a$,$M_p$) associated with $M_a$ amplitudes and $M_p$ different phases is used, which may also be written as $M_a$-DASK/$M_p$-DPSK. The twin-ring based DAPSK scheme is also often referred to as Star-QAM (StQAM) [131].

When channel coding is incorporated into M-DAPSK ($M_a$,$M_p$) as in [131], its performance remains far from the corresponding detection-dependent Discrete-input Continuous-output Memoryless Channel's (DCMC) capacity owing to the employment of hard-decision based demodulation. Hence, a variety of techniques have been proposed in the literature [50, 51, 132, 133] for overcoming the performance loss imposed by employing hard-decision M-DAPSK ($M_a$,$M_p$). More specifi-

cally, a sub-optimal yet high-complexity soft Viterbi decoding metric was proposed in [50,51,133], which requires a high SNR and a slowly fading channel. In order to reduce the high computational complexity of the receiver, the authors of [132] quantized the received signals as part of the demodulation process based on the maximum likelihood sequence estimator derived in [51]. As another approach of reducing the complexity, the idea of decoupling the joint amplitude and phase detection, the Bit Metric of Iterative *a posteriori* probability Decoders (BMIAD), was proposed as an improvement by [133]. More specifically, the BMIAD scheme assumes that the channel SNR is high enough to ensure that the channel noise can be ignored [133][Equation (37)]. However, we are interested in achieving a high integrity at low SNRs, when designing near-capacity coding schemes. An attractive soft-decision aided demodulator capable of reliably operating right across the entire SNR region is proposed for a two-ring based DAPSK scheme in Section 3.2.1. In Section 3.2.2, we extend the soft-decision demodulation algorithm derived for the twin-ring Star-QAM [103] to multiple-ring based DAPSK schemes. Turbo Coding aided BICM (TuCM) [46] is employed in our DAPSK scheme in order to achieve further improvements. The important technical breakthrough of TC was proposed in [43,134], where exchanging extrinsic information between two Recursive Systematic Convolutional (RSC) decoders was shown to achieve a substantial performance improvement. The appealing iterative decoding of concatenated codes has inspired numerous researchers to aim for achieving a near-capacity performance in diverse system contexts [135]. Moreover, the concept of Extrinsic Information Transfer (EXIT) charts was proposed in [15] for analysing the convergence behaviour of turbo detection. The EXIT curve [15] of a TuCM coder was found to have a better match with that of the M-DAPSK ($M_a$,$M_p$) demapper, than the match between the BICM-ID and M-DAPSK ($M_a$,$M_p$) demapper EXIT-curves. Since having a smaller area between these two EXIT curves indicates that the system operates closer to the achievable capacity [135], the TuCM aided M-DAPSK ($M_a$,$M_p$) arrangement approaches the channel capacity more closely than the BICM-ID aided M-DAPSK scheme. Similar to the conventional PSK/QAM scheme, after the transmit filter the modulated signal envelope of our M-DAPSK ($M_a$,$M_p$) scheme will pass through the zero-amplitude point, which requires a higher-linearity class-A power amplifier. Unfortunately, these class-A amplifiers tend to have a low power-efficiency. Hence, in Section 3.2.2.3 we also incorporate the classic offset DPSK technique [136–138] into our scheme in order to prevent the signal envelope from passing through the zero-amplitude point. In Section 3.3, the transmission of the corresponding adaptive modes over the quasi-static Rayleigh fading as well as shadow-and-correlated Rayleigh fading channels is investigated. Finally, our conclusion are provided in Section 3.4.

## 3.2 Fixed Mode Soft-Decision aided M-DAPSK

In this section, we derive the relevant soft-decision demodulation probability formulas for 16-DAPSK (2,8) aided BICM-ID. Then we generalise the soft-decision demodulation probability formulas for M-DAPSK ($M_a$,$M_p$) aided TuCM schemes in Section 3.2.2, which has more than two

concentric PSK constellations. Moreover, we used the existing BMIAD 16-DAPSK (2,8) scheme of [133] as a benchmark of our proposed 16-DAPSK (2,8) TuCM schemes. Thirdly, the angular offset-based M-DAPSK ($M_a$,$M_p$) system is studied and the specific characteristics of the offset M-DAPSK ($M_a$,$M_p$) scheme are exploited. Finally, the corresponding simulation results, our EXIT chart analysis and the achievable capacity will be discussed in Section 3.2.2.4.

### 3.2.1 Soft-Decision DAPSK aided BICM-ID

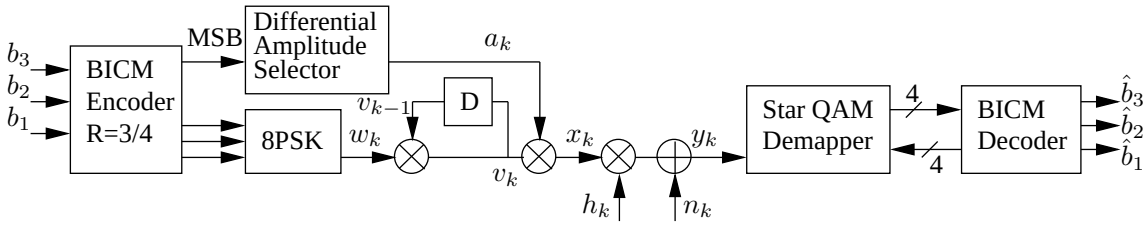


Figure 3.1: The schematic of the 16-DAPSK (2,8) aided BICM-ID scheme, where the parallel bit interleavers between the encoder/decoder and mapper/demapper are not shown for avoiding obfuscating details.

Figure 3.1 shows the simplified schematic of the proposed 16-DAPSK (2,8) aided BICM-ID scheme. A sequence of 3-bit information symbols is encoded by a rate-3/4 BICM encoder for yielding a sequence of 4-bit coded symbols. The Most Significant Bit (MSB) of the 4-bit encoded symbol will be used for selecting the amplitude of the Phase-Shift-Keying (PSK) ring, while the remaining 3 bits will be used for selecting the phase of the complex-valued 16-DAPSK (2,8) symbol $x_k$, where the subscript $k$ denotes the symbol index. The BICM-encoded 16-DAPSK (2,8) symbol is corrupted by both the Rayleigh fading channel $h_k$ and the Additive White Gaussian Noise (AWGN) $n_k$, when it is transmitted to the receiver, as shown in Figure 3.1. Iterative detection is then carried out by exchanging extrinsic information between the 16-DAPSK (2,8) soft demapper and BICM decoder based on the received sequence $\{y_k\}$ without the CSI.

#### 3.2.1.1 DAPSK Mapper

As seen in Figure 3.1, the 16-DAPSK (2,8) mapper consists of three components, namely the differential amplitude selector, the 8PSK mapper and a differential encoder. The 8PSK mapper and the differential encoder jointly form a conventional 8-level DPSK (8DPSK) mapper. The MSB of the BICM-encoded symbol, namely $b_3$, is used for selecting one of the two possible amplitudes. The remaining 3 bits, namely $b_2$ $b_1$ $b_0$, are used by the 8DPSK mapper. Note that similar to any DPSK scheme, we insert a reference symbol at the beginning of each frame before the 16-DAPSK (2,8) mapper.

**3.2.1.1.1 Differential Amplitude Selection** The MSB, $b_3$, is used for selecting the amplitude of the PSK ring, $a_k$. The two possible amplitude values are denoted as $a^{(1)}$ and $a^{(2)}$, respectively.

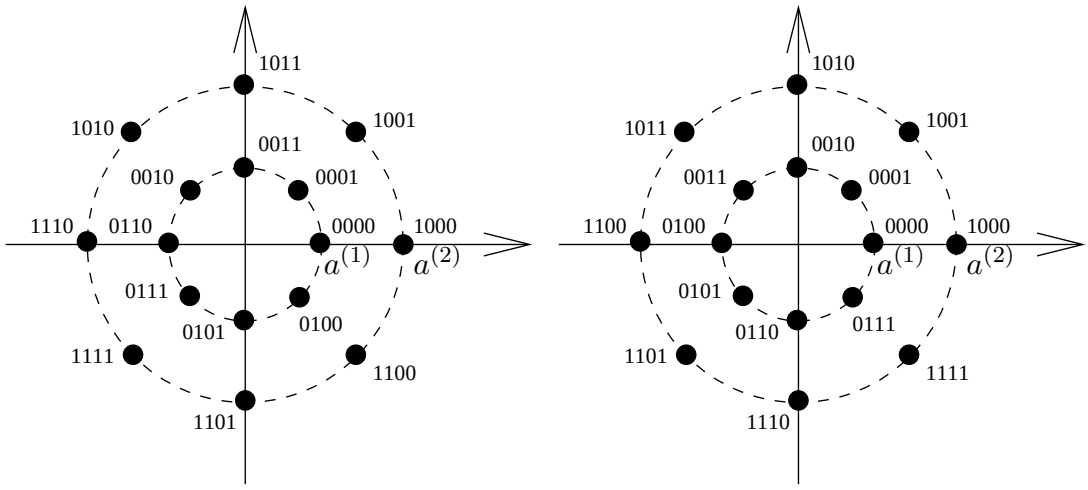


(a) Gray Mapping (b) Set Patitioning Mapping

Figure 3.2: The 16-DAPSK (2,8) ($b_3b_2b_1b_0$) constellation with different mapping methods.

When the MSB of the $k$th BICM-encoded symbol is given by $b_3 = 0$, the amplitude of the PSK ring will remain the same as that of the previous value $a_k = a_{k-1}$. The amplitude of the PSK ring will be switched to another value, if $b_3 = 1$. This amplitude selection mechanism may be referred to as 2-level Differential Amplitude Shift Keying (2DASK). The 16-DAPSK (2,8) constellation using different mapping methods is shown in Figure 3.2. After normalisation for maintaining a symbol energy of unity, we have $a^{(1)} = 1/\sqrt{2.5}$ and $a^{(2)} = 2/\sqrt{2.5}$ for twin-ring DAPSK. The amplitude value of the reference symbol is given by $a_0 = a^{(1)}$. The reason why we choose the ring ratio being 2 will be illustrated in Section 3.2.1.3.

**3.2.1.1.2 Phase Selection** The $k$th differentially encoded symbol $v_k$ can be expressed as:

$$v_k = v_{k-1}w_k, \tag{3.1}$$

where $w_k = \mu(b_2\ b_1\ b_0)$ is the $k$th 8PSK symbol based on the 8PSK mapping function of $\mu(.)$, while $v_{k-1}$ is the $(k-1)$st 8DPSK symbol and $|v_k|^2 = 1$. The reference symbol for the 8DPSK part is given by $v_0 = \mu(0\ 0\ 0)$.

The $k$th 16-DAPSK (2,8) symbol is then given by:

$$x_k = a_k v_k, \tag{3.2}$$

where $a_k \in \{a^{(1)}, a^{(2)}\}$.

#### 3.2.1.2 DAPSK Soft Demapper

The soft-decision based 16-DAPSK (2,8) block is placed in front of the BICM decoder of Figure 3.1. The $k$th received symbol may then be written as:

$$y_k = h_k x_k + n_k = h_k a_k v_k + n_k \,, \tag{3.3}$$

where $h_k$ is the Rayleigh fading channel's coefficient, while $n_k$ represents the AWGN having a variance of $N_0/2$ per dimension. Assuming a slow Rayleigh fading channel, where $h_k \approx h_{k-1}$, we can rewrite Equation (3.3) using Equation (3.1) as:

$$\begin{aligned} y_k &= h_{k-1} a_k v_{k-1} w_k + n_k \,, \\ &= \frac{a_k}{a_{k-1}} \left( y_{k-1} - n_{k-1} \right) w_k + n_k \,, \\ &= p_k y_{k-1} w_k + \tilde{n}_k \,, \end{aligned} \tag{3.4}$$

where $p_k = \frac{a_k}{a_{k-1}}$ is the ratio of the $k$th and $(k-1)$th amplitudes, while $\tilde{n}_k = -\frac{a_k}{a_{k-1}} n_{k-1} w_k + n_k$ is the effective noise.

**3.2.1.2.1 Amplitude Detection** Three amplitude ratios can be derived from the two PSK ring amplitudes of 16-DAPSK (2,8) as follows:

$$p_k = \begin{cases} R_0 = \dfrac{a^{(1)}}{a^{(1)}} \text{ or } \dfrac{a^{(2)}}{a^{(2)}} = 1 \\ R_1 = \dfrac{a^{(1)}}{a^{(2)}} \\ R_2 = \dfrac{a^{(2)}}{a^{(1)}} \,. \end{cases} \tag{3.5}$$

When the noise power is low, the amplitude ratio $p_k$ may be approximated as:

$$\begin{aligned} \frac{|y_k|}{|y_{k-1}|} &= \frac{|h_k a_k v_k + n_k|}{|h_{k-1} a_{k-1} v_{k-1} + n_{k-1}|} \,, \qquad (3.6) \\ &\approx \frac{|a_k|}{|a_{k-1}|} \,, \\ &\approx p_k \,. \qquad (3.7) \end{aligned}$$

Figure 3.3[1] shows the PDF of the received signal amplitude ratios $\frac{|y_k|}{|y_{k-1}|}$. It becomes plausible from Figure 3.3 that the PDF peak, which is characteristic of each amplitude ratio experiences a different noise variance, although all the 16-DAPSK (2,8) symbols experience the same AWGN at the same $E_b/N_0$ value of 25 dB. Figure 3.3 also demonstrates the connection between $b_3$ and the amplitude ring ratio. More specifically, three main amplitude ring ratios are shown in Figure 3.3, which are consistent with Equation (3.5).

[1] It is assumed throughout that all amplitude and phase values are equally likely. More specifically, the probability of each amplitude ratio of the 16-DAPSK (2,8) symbols can be expressed as: $p(R_0) = 2 \cdot p(R_1) = 2 \cdot p(R_2) = 0.5$.

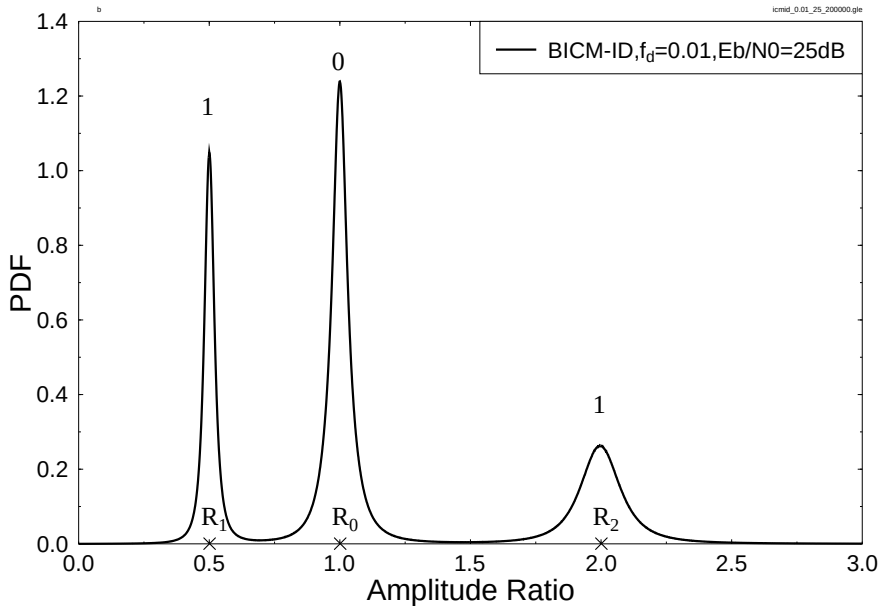


Figure 3.3: The PDF of the received signal amplitude ratios of 16-DAPSK (2,8) $\frac{|y_k|}{|y_{k-1}|}$ based on Equation (3.6), when communicating over correlated Rayleigh fading channels having an $E_b/N_0$ of 25 dB. The related constellation is shown in Figure 3.2.

**3.2.1.2.2 Probability Computation** The effective noise variance of $\tilde{n}_k$ in Equation (3.4) depends on the amplitude ratio used at time instant $k$, which can be computed as:

$$\widetilde{N}_0 \;=\; N_0 + |p_k|^2 |w_k|^2 N_0 = N_0(1+|p_k|^2)\,, \tag{3.8}$$

where $\widetilde{N}_0 = 2N_0 = N_0^{(0)}$ if $b_3 = 0$, while $\widetilde{N}_0 = (1+R_1^2)N_0 = N_0^{(1)}$ or $\widetilde{N}_0 = (1+R_2^2)N_0 = N_0^{(2)}$ for $b_3 = 1$. Based on Equation (3.4) we can express the probability of receiving $y_k$ conditioned on the transmission of $b_0$, $b_1$, $b_2$ and $b_3$ as follows:

$$P(y_k|w^{(m)}, b_3 = 0) \;=\; \frac{1}{\pi N_0^{(0)}} e^{\frac{-\left|y_k - y_{k-1} R_0 w^{(m)}\right|^2}{N_0^{(0)}}}\,, \tag{3.9}$$

$$P(y_k|w^{(m)}, b_3 = 1) \;=\; \frac{1}{\pi N_0^{(1)}} e^{\frac{-\left|y_k - y_{k-1} R_1 w^{(m)}\right|^2}{N_0^{(1)}}} + \frac{1}{\pi N_0^{(2)}} e^{\frac{-\left|y_k - y_{k-1} R_2 w^{(m)}\right|^2}{N_0^{(2)}}}\,, \tag{3.10}$$

where $w^{(m)} = \mu(b_2\ b_1\ b_0)$ and $\mu$ is the conventional 8PSK mapping function. However, when the *a priori* bit probabilities $P^a(b_i)$ become available from the BICM decoder, the extrinsic bit probability that can be gleaned from the 16-DAPSK (2,8) demapper as:

$$P^e(b_i = b) \;=\; \sum_{w^{(m)} \in \chi(i,b)} \Big( P(y_k|w^{(m)}, b_3 = 0) + P(y_k|w^{(m)}, b_3 = 1) \Big) \prod_{\substack{j=0 \\ j \neq i}}^{3} P^a(b_j),$$
$$\text{for } i \in \{0,1,2\},\ \ b \in \{0,1\}\,, \tag{3.11}$$

where $b_i$ denotes the $i$th coded bit of the symbol and $\chi(i,b)$ is the set of constellation points having the $i$th bit set to $b$. The extrinsic bit probability of the MSB may be formulated as:

$$P^e(b_3 = b) \quad = \sum_{w^{(m)}}^{\text{all}} P(y_k|w^{(m)}, b_3 = b) \prod_{j=0}^{2} P^a(b_j), \tag{3.12}$$

where the summation term considers all possible 8PSK constellation points, because the MSB $b_3$ influences only the amplitude selection. The extrinsic bit probabilities can then be employed for generating the Log-Likelihood Ratios (LLRs) [135] of all BICM-coded bits, which are then fed back to the BICM decoder.

#### 3.2.1.3 Simulation Results

| Coded Modulation | BICM | BICM-ID |
|---|---|---|
| Modulation Scheme | 16-DAPSK (2,8), 16PSK 16QAM, 16DPSK | 16-DAPSK (2,8) |
| Mapper type | Gray-labelled | Set-Partitioned |
| Number of iterations | 1 | 1,2,4 |
| Code Rate | 3/4 | |
| Code Memory | 3 | |
| Code Polynomial (octal) | $G = [4\,4\,4\,4\,;\ 0\,6\,2\,4\,;\ 0\,2\,5\,6\,]$ | |
| Decoder type | Approximate Log-MAP | |
| Symbols per frame | 1,200 | |
| Number of frames | 20,000 | |
| Channel | Correlated Rayleigh fading channel | |
| Normalised Doppler Frequency ($f_d$) | 0.01 | |

Table 3.1: Simulation parameters. Note that we declare 'an iteration' being completed when both the demapper and decoder were activated once.

Monte-Carlo simulations have been performed for characterising the proposed soft-decision based 16-DAPSK (2,8) demodulation technique in the context of BICM and BICM-ID coding schemes. The simulation parameters are shown in Table 3.1.

Firstly, we study the BER performance of 16-DAPSK (2,8)-BICM-ID for different ring ratios spanning the range of (1.2–4.0), when communicating over the correlated Rayleigh fading channel associated with $f_d = 0.01$ in Figure 3.4. The results show that the optimum ring ratio (based on the BER performance) of 16-DAPSK (2,8) is within the range of (1.8–2.2). Hence we set the ring ratio to 2 for evaluating the achievable performance. Figure 3.4 illustrated the attainable BER performance of 16-DAPSK (2,8)-BICM-ID for different $f_d$ values, when transmitting over a

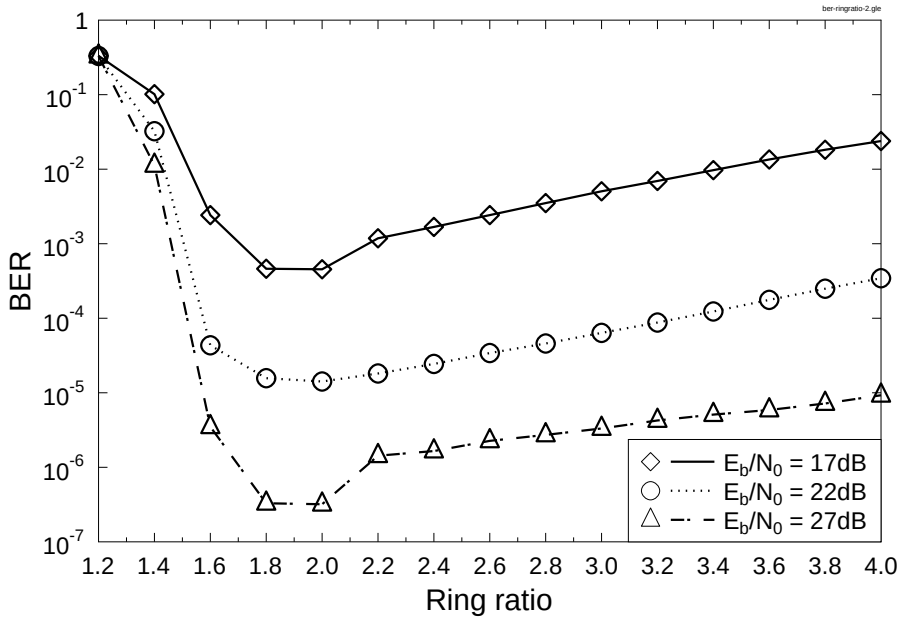


Figure 3.4: BER versus ring ratio performance of the 16-DAPSK (2,8)-BICM-ID schemes for transmission over the correlated Rayleigh fading channel associated with $f_d = 0.01$ and four iterations. The simulation parameters are detailed in Table 3.1.

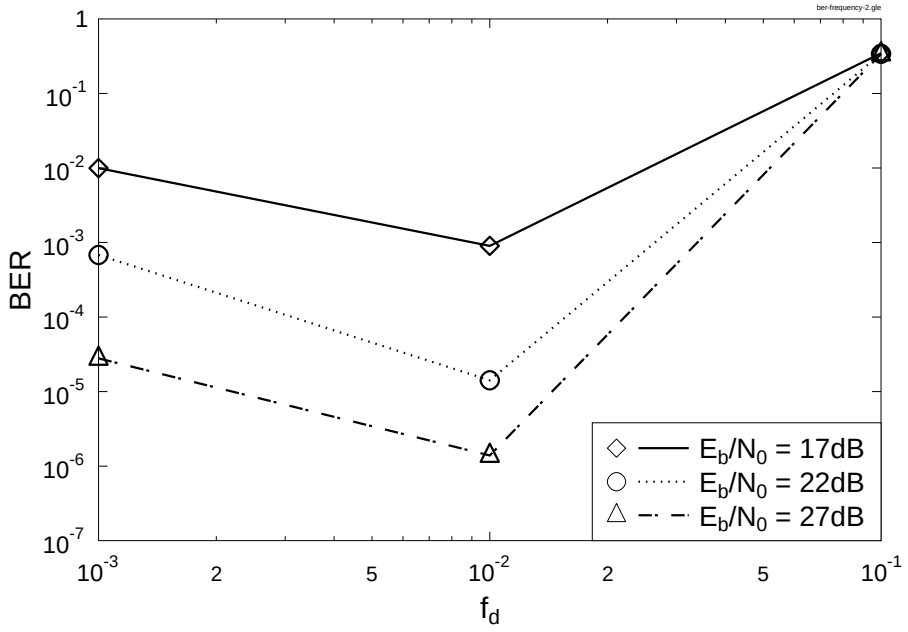


Figure 3.5: BER versus $f_d$ performance of 16-DAPSK (2,8)-BICM-ID schemes for transmission over the correlated Rayleigh fading channel associated with a ring-ratio of two and with four iterations. The simulation parameters are detailed in Table 3.1.

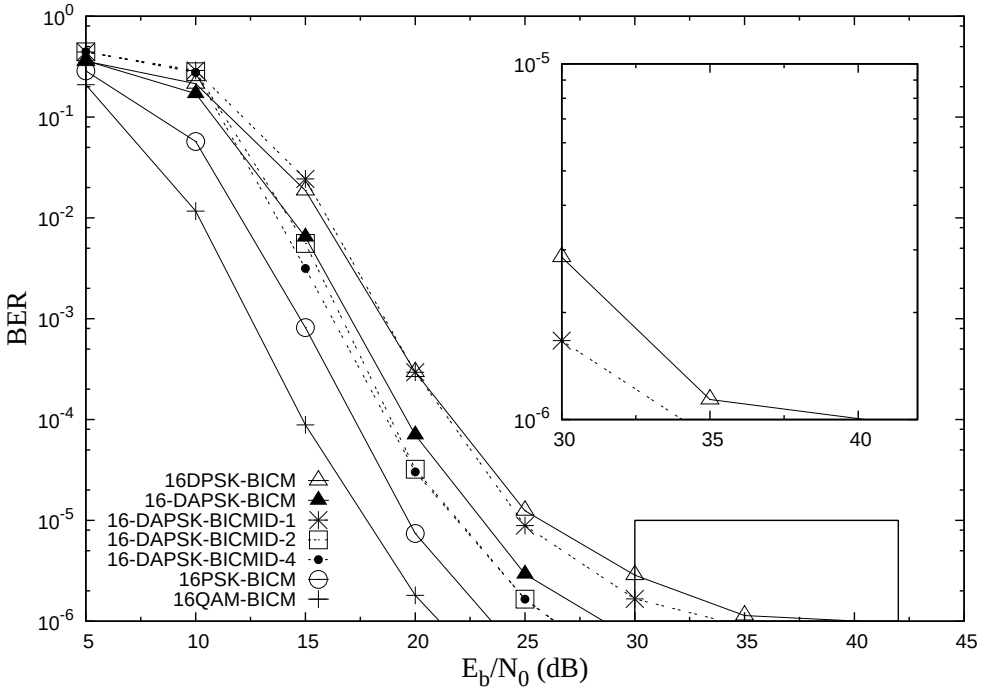


Figure 3.6: BER versus $E_b/N_0$ performance of the 16DPSK-BICM, 16-DAPSK (2,8)-BICM, 16-DAPSK (2,8)-BICM-ID, 16PSK-BICM and 16QAM-BICM schemes. The simulation parameters are shown in Table 3.1.

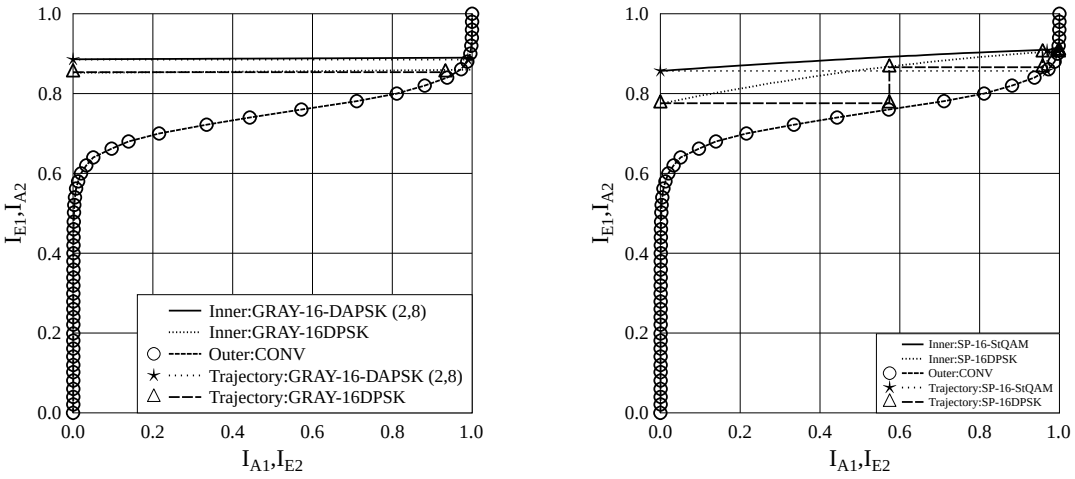


(a) **Gray** labelling (b) **SP** labelling

Figure 3.7: The EXIT Charts performance of 16-DAPSK (2,8) and 16DPSK aided BICM with **Gray** and **SP** labelling over correlated Rayleigh channel with $E_b/N_0$ =16 dB. The detailed simulation parameters are shown in Table 3.1.

correlated Rayleigh fading channel and using four iterations. Based on the BER performance seen in Figure 3.5, we set $f_d$ to 0.01 for the following study.

Figure 3.6 portrays the $E_b/N_0$ performance of the 16DPSK aided BICM, 16-DAPSK (2,8) assisted BICM, 16PSK aided BICM, 16QAM BICM and 16-DAPSK (2,8) based BICM-ID schemes, when communicating over correlated Rayleigh fading channels. Solid lines are used for illustrating the performance of Gray-labelled BICM, while the dotted lines represent the SP based 16-DAPSK (2,8) BICM-ID. As seen from Figure 3.6, the 16DPSK-BICM scheme suffers from a high BER floor, since the minimum Euclidean distance of a 16-point constellation ring is lower than that of the classic square 16QAM or 16-DAPSK (2,8) schemes. The 16-DAPSK (2,8)-BICM scheme outperforms the 16DPSK-BICM scheme by approximately 12 dBs at a BER of $10^{-6}$. The coherently detected 16QAM-BICM and 16PSK-BICM are considered here as our benchmark schemes, while assuming perfect CSI. During the $first\ iteration^2$, the SP-based 16-DAPSK (2,8)-BICM-ID scheme performs worse than the Gray-labelled 16-DAPSK (2,8)-BICM, since the SP-based mapper has a lower minimum Euclidean distance compared to that of the Gray-label-based mapper. Note that both the 16-DAPSK (2,8)-BICM-ID and 16-DAPSK (2,8)-BICM schemes use the bit-probabilities of Equation (5.44) and Equation (5.44) during the first iteration. However, after the *second iteration* the 16-DAPSK (2,8)-BICM-ID outperforms the non-iterative 16-DAPSK (2,8)-BICM by approximately 2 dB with the aid the extrinsic bit-probabilities of Equation (3.11) and Equation (3.12).

Figure 3.7a and Figure 3.7b present the EXIT charts both of 16-DAPSK (2,8) and of 16DPSK aided BICM-ID both for SP and for the Gray mapping method for transmission over correlated Rayleigh channels in the case of $E_b/N_0$ =16 dB, respectively. In Figure 3.7a, the inner code's EXIT curve recorded for our 16-DAPSK (2,8) symbol-to-bit demapper has a higher starting point at $I_{A_1}$=0 than that of the 16DPSK, and it remain higher also at $I_{A_1}$=1. Both inner EXIT curves are represented by a straight line. Note that the area under a specific EXIT curve is related to the achievable channel capacity [15, 18, 139]. The area under the 16-DAPSK (2,8) EXIT curve is larger than that under the 16DPSK inner code's EXIT curve. Hence, the capacity of the 16-DAPSK (2,8) based scheme is higher than that of the 16DPSK based scheme. Furthermore, observe in Figure 3.7b that the BICM-ID-aided SP based 16-DAPSK (2,8) has a higher starting point than that of BICM-ID-aided 16DPSK at $I_{A_1}$=0, but a similar ending point at $I_{A_1}$=1. However, the capacity of 16-DAPSK (2,8) is higher than that of 16DPSK in the same scenario. It is worth noting that the the BICM-ID-aided 16DPSK scheme requires a higher number of decoding iterations in order to achieve decoding convergence to a vanishingly low BER compared to that of the BICM-ID-aided 16-DAPSK (2,8) scheme.

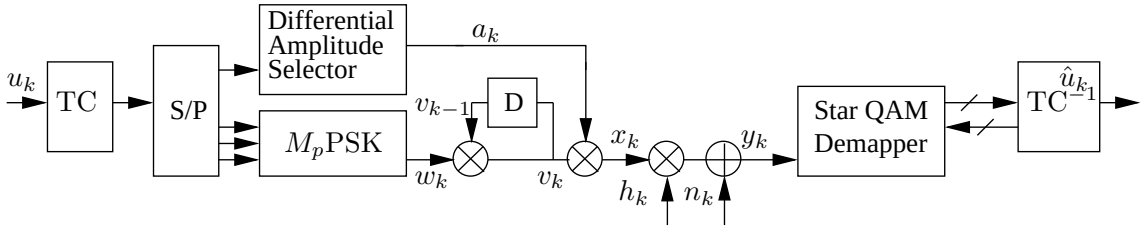


Figure 3.8: The schematic of the M-DAPSK ($M_a$,$M_p$) aided TuCM scheme, where the interleavers and de-interleavers between the encoder/decoder and mapper/de-mapper are not shown for simplicity.

### 3.2.2 Soft-Decision M-DAPSK aided TuCM

Figure 3.8 presents the simplified schematic of our near-capacity TuCM aided M-DAPSK ($M_a$,$M_p$) scheme, where the number of constellation points is M = $M_a \cdot M_p = 2^{\mathrm{m}}$, while the number of amplitudes is $M_a = 2^{m_a}$ and the number of phases per amplitude-circle is $M_p = 2^{m_p}$. A sequence of coded symbols is generated by a sequence of a rate-1/2 TuCM encoded information symbols. Out of the total number of modulated bits per symbol, which is m, $m_a$ bits will be assigned for the selection of the Phase-Shift-Keying (PSK) amplitude ring, while the remaining $(m_p = \mathrm{m} - m_a)$ bits will be used for selecting the phase of the complex-valued M-DAPSK ($M_a$,$M_p$) symbol $x_k$, where the subscript $k$ denotes the symbol index. The near-capacity TuCM aided M-DAPSK ($M_a$,$M_p$) system will be illustrated in Section 3.2.2.1 and Section 3.2.2.2.

As shown in Figure 3.8, the TuCM-encoded M-DAPSK ($M_a$,$M_p$) symbol is corrupted by both the Rayleigh fading channel and the Additive White Gaussian Noise (AWGN), when it is transmitted to the receiver. Then, based on the received sequence $\{y_k\}$ but without exploiting any CSI, we exchange extrinsic information between the M-DAPSK soft demapper and the TuCM decoder to accomplish iterative detection.

#### 3.2.2.1 M-DAPSK Mapper

The M-DAPSK ($M_a$,$M_p$) mapper shown in Figure 3.8 consists of two components, namely the amplitude selector and a conventional $M_p$-level DPSK ($M_p$-DPSK) mapper. Note that $M_p$-DPSK is formed by the $M_p$-PSK mapper and the differential encoder. It is worth noting that similar to any classic DPSK scheme, we insert a reference symbol at the beginning of each differentially encoded transmission frame before the M-DAPSK ($M_a$,$M_p$) mapper. Additionally, the 16-DAPSK (2,8) scheme and the 64-DAPSK (4,16) scheme were used as examples for illustrating the philosophy of our proposed soft-decision based demapper.

**3.2.2.1.1 Amplitude Selection** $m_a$ bits are used for selecting the amplitude of the PSK ring, $a_k = \varrho(b_k)$, where $\varrho(b_k)$ represents the function mapping the $m_a$-bit symbol $b_k$ to the amplitude

[2]Note that we declare 'an iteration' being completed when both the demapper and decoder were activated once.

$a_k$ under the combined constraint of $0 \leq b_k \leq (M_a - 1)$ and $b_k = (b_{k-1} + f_k) \mod M_a$, with $f_k = \sum_{i=m_p}^{m-1} 2^{(i-m_p)} c_{mk+i}$, where $c_{mk+i}, 0 \leq mk + i \leq (N_c - 1)$, is the binary coded sequence of length $N_c$.

For the 16-DAPSK (2,8) scheme, we have $b_k = (b_{k-1} + c_{4k+3}) \mod 2$ for 16-DAPSK (2,8), while for the 64-DAPSK (4,16) scheme, we have $b_k = (b_{k-1} + 2c_{6k+5} + c_{6k+4}) \mod 4$.

Note that the classic Gray Mapping [135] method is employed by the bit-to-symbol mapper.

This amplitude selection mechanism may be referred to as $M_a$-level Differential Amplitude Shift Keying ($M_a$-DASK). After normalisation to a symbol energy of unity, we have $\varrho(b_k) = \alpha^{b_k}/\sqrt{\beta}$, here $\sum_{i=1-m_a}^{m_a-1} |\alpha^{b_k}|^2 = \beta$. We use the optimum amplitude ratio of $\alpha$ = 1.4, $\beta$ = 3.58 for M-DAPSK (4, $M_p$) and $\alpha$ = 2.0, $\beta$ = 2.5 for M-DAPSK (2, $M_p$) [140]. The amplitude of the reference symbol is given by $a_{-1} = \varrho(0)$.

**3.2.2.1.2 Phase Selection** When we consider $m_p$, the $k$th differentially encoded symbol $v_k$ can be expressed as:

$$v_k = v_{k-1} w_k, \tag{3.13}$$

where $w_k = \mu(d_k) = \exp(j\pi d_k / M_p)$ is the $M_p$-PSK symbol obeying $d_k = \sum_{i=0}^{m_p-1} 2^i c_{mk+i}$. More specifically, $d_k = 4c_{4k+2} + 2c_{4k+1} + c_{4k}$ for the 16-DAPSK (2,8) scheme, while $d_k = 8c_{6k+3} + 4c_{6k+2} + 2c_{6k+1} + c_{6k}$ for the 64-DAPSK (4,16) scheme and $\mu(.)$ is the $M_p$-PSK mapping function. Furthermore, $v_{k-1}$ is the $(k-1)$st $M_p$-DPSK symbol and $|v_k|^2 = 1$. The reference symbol of the $M_p$-DPSK part of the constellation is given by $v_{-1} = \mu(0) = 1$.

When relying on the above-mentioned amplitude and phase selection methods, the $k$th M-DAPSK ($M_a$,$M_p$) symbol may be written as:

$$x_k = a_k v_k. \tag{3.14}$$

### 3.2.2.2 Differential Detection

In this sub-section, we firstly study the BMIAD, which is as our benchmark scheme. Then detail the proposed M-DAPSK ($M_a$,$M_p$) Soft Demapper.

**3.2.2.2.1 BMIAD** The BMIAD is based on the 16-DAPSK (2,8) scheme. The $k$th received symbol may be formulated as:

$$y_k = h_k x_k + n_k = \rho_k e^{j\phi_k} x_k + n_k \,, \tag{3.15}$$

where $h_k = \rho_k e^{j\phi_k}$ represents the non-dispersive Rayleigh fading coefficients, while $n_k$ represents the AWGN having a variance of $N_0/2$ per dimension. Furthermore, $\rho_k$ and $\phi_k$ represent the amplitude and the phase of the fading channel, respectively.

For the *A Posteriori* Probability (APP) decoder, the amplitude bit metric can be obtained from the exact *a posteriori* probability of $\Upsilon_{y,k}$, $\Delta\theta_k$, given $a_k$, $a_{k-1}$, $\psi_k$ and $\rho_k$ as [133]:

$$P_A(\Upsilon_{y,k}, \Delta\theta_k | a_k, a_{k-1}, \psi_k, \rho_k) \approx e^{-\frac{[|y_{k-1}|^2(\Upsilon_{y,k}-\alpha^{q_k})^2]}{N_0(1+\Upsilon_{y,k}^2)}}. \tag{3.16}$$

where $a_k$ and $\psi_k$ denote the amplitude and phase of $x_k$. Moreover, $\Upsilon_{y,k} = \frac{|y_k|}{|y_{k-1}|}$ and $\Delta\theta_k = \theta_k - \theta_{k-1}$ represent the envelope and the phase difference, where $\theta_k = \angle y_k$ and $\Delta\theta_k \in [-\pi, \pi)$. Finally, $\alpha^{q_k} = \frac{a_k}{a_{k-1}}$, where we have $q_k \in [1 - M_a, M_a - 1]$.

The approximate form of the phase bit metric can be expressed with the aid of the exact *a posteriori* probability of $\Upsilon_{y,k}$ and $\Delta\theta_k$ given $a_k$, $a_{k-1}$, $\psi_k$ and $\rho_k$, which is formulated as [133]:

$$P_P(\Upsilon_{y,k}, \Delta\theta_k | a_k, a_{k-1}, \psi_k, \rho_k) \approx e^{-\frac{[|y_k|^2+|y_{k-1}|^2\Upsilon_{y,k}^2-2|y_k||y_{k-1}|\Upsilon_{y,k}\cos(\Delta\theta_k-\psi_k)]}{N_0(1+\Upsilon_{y,k}^2)}}. \tag{3.17}$$

**3.2.2.2.2 Proposed M-DAPSK ($M_a$,$M_p$) Soft Demapper** The soft-decision based M-DAPSK ($M_a$,$M_p$) block is placed in front of the TuCM decoder, as portrayed in Figure 3.8. The $k$th received symbol may then be formulated as:

$$y_k = h_k x_k + n_k = h_k a_k v_k + n_k\,, \tag{3.18}$$

where $h_k$ represents the non-dispersive Rayleigh fading coefficients, while $n_k$ represents the AWGN having a variance of $N_0/2$ per dimension. For the sake of ensuring that two consecutive symbols experience a similar complex-valued fading envelop, which is a prerequisite for avoiding an error-floor in differential detection, we assume a slowly Rayleigh fading channel, where we have $h_k \approx h_{k-1}$, based on Equation (3.13), Equation (3.18) can be rewritten as:

$$\begin{aligned} y_k &\approx h_{k-1}a_k v_{k-1} w_k + n_k\,, \\ &= \frac{a_k}{a_{k-1}}\left(y_{k-1} - n_{k-1}\right) w_k + n_k\,, \\ &= \frac{a_k}{a_{k-1}} y_{k-1} w_k + \tilde{n}_k\,, \end{aligned} \tag{3.19}$$

where $\frac{a_k}{a_{k-1}}$ is the ratio of the $k$th and $(k-1)$st amplitudes, while

$$\tilde{n}_k = -\frac{a_k}{a_{k-1}} n_{k-1} w_k + n_k \tag{3.20}$$

is the effective noise [3].

**3.2.2.2.2.1 Amplitude Detection** $(2M_a - 1)$ amplitude ratios can be derived from the $M_a$-PSK ring radii of the M-DAPSK ($M_a$,$M_p$) scheme, which may be expressed as:

$$\frac{a_k}{a_{k-1}} = \alpha^{b_k - b_{k-1}} = \alpha^{q_k}, \tag{3.21}$$

where $q_k$ obeys $(1 - M_a) \leq q_k \leq (M_a - 1)$.

[3] Since $-\frac{a_k}{a_{k-1}} w_k$ is a constant during a symbol period, the multiplication of the Gaussian noise $n_{k-1}$ by $-\frac{a_k}{a_{k-1}} w_k$ in Equation (3.20) only affects the effective noise variance and the term $-\frac{a_k}{a_{k-1}} w_k n_{k-1}$ remains a Gaussian noise process. The sum of two Gaussian noise processes in Equation (3.20) is also another Gaussian noise process, albeit associated with a different noise variance.

**3.2.2.2.2.2 Probability Computation** The effective noise variance of $\tilde{n}_k$ in Equation (3.19) depends on the amplitude ratio used at time instant $k$, which may be formulated as:

$$\widetilde{N}_0 \quad = \quad N_0 + \alpha^{2q_k} {w_k}^2 N_0 = N_0(1+\alpha^{2q_k}) \,, \tag{3.22}$$

where we have $\widetilde{N}_0 = (1+\alpha^{2q_k})N_0 = N_0^{(q_k)}$. Based on Equation (3.19) we have computed the probability of receiving $y_k$ conditioned on the transmission of $d_k$ and $f_k$ in Equation (3.23) and Equation (3.24), which are for the M-DAPSK (2, $M_p$) scheme and for the M-DAPSK (4, $M_p$) scheme, respectively. The bit-probabilities may then be converted to the Log-Likelihood Ratio (LLR) [135] based representations of $c_{\mathrm{m}k+i}, 0 \leq i \leq (\mathrm{m}-1)$:

$$\begin{aligned} P(y_k|d_k, f_k = 0) &\approx e^{\frac{-\left|y_k - y_{k-1}\alpha^0 \mu(d_k)\right|^2}{N_0^{(0)}}}, \\ P(y_k|d_k, f_k = 1) &\approx e^{\frac{-\left|y_k - y_{k-1}\alpha^{-1} \mu(d_k)\right|^2}{N_0^{(-1)}}} + e^{\frac{-\left|y_k - y_{k-1}\alpha^{1} \mu(d_k)\right|^2}{N_0^{(1)}}}. \end{aligned} \tag{3.23}$$

$$\begin{aligned} P(y_k|d_k, f_k = 0) &\approx e^{\frac{-\left|y_k - y_{k-1}\alpha^0 \mu(d_k)\right|^2}{N_0^{(0)}}}, \\ P(y_k|d_k, f_k = 1) &\approx e^{\frac{-\left|y_k - y_{k-1}\alpha^{-3} \mu(d_k)\right|^2}{N_0^{(-3)}}} + e^{\frac{-\left|y_k - y_{k-1}\alpha^{1} \mu(d_k)\right|^2}{N_0^{(1)}}}, \\ P(y_k|d_k, f_k = 2) &\approx e^{\frac{-\left|y_k - y_{k-1}\alpha^{-2} \mu(d_k)\right|^2}{N_0^{(-2)}}} + e^{\frac{-\left|y_k - y_{k-1}\alpha^{2} \mu(d_k)\right|^2}{N_0^{(2)}}}, \\ P(y_k|d_k, f_k = 3) &\approx e^{\frac{-\left|y_k - y_{k-1}\alpha^{-1} \mu(d_k)\right|^2}{N_0^{(-1)}}} + e^{\frac{-\left|y_k - y_{k-1}\alpha^{3} \mu(d_k)\right|^2}{N_0^{(3)}}}. \end{aligned} \tag{3.24}$$

### 3.2.2.3 Offset M-DAPSK ($M_a$, $M_p$)

When the M-DAPSK ($M_a$, $M_p$) signals are pulse shaped, they lose their constant-envelope property. Any hard-limiting or non-linear amplification results in the regrowth of the previously removed side-lobes. To prevent the regeneration of side-lobes and the resultant spectral widening, it is imperative that the analogue M-DAPSK ($M_a$, $M_p$) signals should be amplified after pulse shaping using a linear amplifier. However, it is a costly and challenging task to construct a strictly linear power amplifier. The offset M-DAPSK ($M_a$, $M_p$) scheme [6] is less susceptible to these deleterious effects and supports more power-efficient amplification, because the constellation is rotated for each successive symbol by a certain phase offset, thereby avoiding the envelope's passage through the zero amplitude point [141]. The discrete signal $x_k$ is typically shaped by a raised-cosine pulse shaping filter before it is modulated onto the carrier, in order to reduce the resultant bandwidth occupancy [136–138]. The relationship between $x_k$ and the timing of the transmitted analogue stream $x(t)$ may be expressed as:

$$x(t) = \sum_{k=-1}^{N-1} x_k g(t - kT_s) e^{j\psi_k}, \tag{3.25}$$

where $(N+1)$ is the number of symbols and $\psi_k = (k \mod 2)\pi/M_p$. More specifically, the conventional DAPSK constellation is used when $k$ is even, while a $\pi/M$-rotated DAPSK constellation

is employed when $k$ is odd[4]. Furthermore, $g(t)$ corresponds to the raised-cosine pulse shaping filter given by [137]:

$$g(t) = \frac{\sin(\frac{\pi t}{T_s})}{\pi t} \cdot \frac{\cos\left(\frac{\pi \alpha_{rc} t}{T_s}\right)}{1 - \left(\frac{4\alpha_{rc} t}{2T_s}\right)^2}, \tag{3.26}$$

where $T_s$ is the symbol period and $\alpha_{rc}$ is the Nyquist roll-off factor. Then $x(t)$ is split into an in-phase stream, $x_I(t) = \text{Re}\{\text{x(t)}\}$, and a quadrature stream, $x_Q(t) = \text{Im}\{\text{x(t)}\}$, as seen in Figure 3.8. The offset-modulated signal may be expressed as:

$$x_{HF}(t) = x_I(t)\cos(w_c t) + x_Q(t)\sin(w_c t), \tag{3.27}$$

where $w_c$ is the carrier frequency. In this section, 16-DAPSK (2,8) and $\psi_k = (k \mod 2)\pi/8$ are employed for the sake of illustration. The signal will be appropriately de-rotated in the receiver.

The constellation diagrams of our proposed systems after the raised-cosine pulse shaping filter are shown in Figure 3.11. More specifically, Figure 3.11a and Figure 3.11c illustrate the constellation of the offset 16-DAPSK (2,8) system using $\alpha_{rc} = 0.9$ and $\alpha_{rc} = 0.5$, respectively, while Figure 3.11b and Figure 3.11d depict that of the 16-DAPSK (2,8) system associated with $\alpha_{rc} = 0.9$ and $\alpha_{rc} = 0.5$, respectively. As seen in Figure 3.11a and Figure 3.11c, the analogue envelope of the offset 16-DAPSK (2,8) scheme does not pass through the origin, while that of 16-DAPSK (2,8) passes directly through the origin, as shown in Figure 3.11b and Figure 3.11d. Figure 3.12 presents the BER versus SNR performance comparison of the offset and non-offset 16-DAPSK (2,8) systems, when communicating over a correlated Rayleigh fading channel using a TuCM block length of 1200 symbols. When perfect time synchronization is assumed, both schemes exhibit the same performance, as seen in Figure 3.12. Hence, we only consider the non-offset DAPSK scheme in our simulation study in Section 3.2.2.4.

#### 3.2.2.4 Simulation Results

In this section, we characterize the performance of the proposed TuCM-aided soft-decision based M-DAPSK (4,$M_p$) schemes. The classic square-constellation based 64-QAM and 64-DPSK schemes are used as benchmark schemes. The simulation parameters are shown in Table 3.2.

Firstly, we study the BER performance of 64-DAPSK (4,16)-TuCM in conjunction with different ring ratios of (0.8–3.0), when communicating over the correlated Rayleigh fading channel associated with $f_d = 0.01$ in Figure 3.9. The results show that the optimum ring ratios (minimizing the BER) for 64-DAPSK (4,16) are within the range of (0.8–3.0). We set the ring ratio to 1.4 for further investigating the performance.

[4]We found that this method gives the same result as that of the conventional offset scheme where the constellation is always rotated by $\pi/M$ for each symbol.

| | |
|---|---|
| Modulation | 64-DAPSK (4,16), 32-DAPSK (4,8), 16-DAPSK (4,4) 8-DAPSK (4,2), 64-QAM, 64-DPSK |
| Mapping | Set Partitioning (SP) |
| Coding | TuCM |
| Constituent Code | Half-rate Recursive Systematic Convolutional (RSC) code Code Polynomial G=[15 17] |
| Code Memory | 3 |
| Outer iterations | 2 |
| Inner TuCM iterations | 4 |
| Decoder | Approximate Log-MAP |
| Symbols per 64-DAPSK block | 400 |
| Number of 64-DAPSK blocks per TuCM block | 1, 10, 100 |
| Number of TuCM blocks | 5000 |
| Channel | Correlated Rayleigh fading channel having a normalised Doppler frequency of 0.01 |

Table 3.2: System parameters.

Figure 3.10[5] presents the PDF of the received signal amplitude ratios $\frac{|y_k|}{|y_{k-1}|}$ of TuCM aided 64-DAPSK (4,16), when communicating over correlated Rayleigh fading channels at an $E_b/N_0$ of 30 dB. The connection between $b_5$, $b_4$ and the amplitude ring ratio are shown in Figure 3.10. More specifically, seven main amplitude ring ratios are shown in Figure 3.10, in accordance with Equation (3.24).

The EXIT charts of the 64-QAM, 64-DAPSK (4,16) and 64-DPSK aided TuCM schemes recorded, when communicating over a correlated Rayleigh channel at SNR=17.5 dB are shown in Figure 5. The SNR-independent EXIT curve of the outer TuCM decoder is also shown. More specifically, the dashed and un-marked curves are the EXIT curves of the inner decoder[6], namely those of the 64-QAM, 64-DAPSK (4,16) and 64-DPSK schemes, respectively. Moreover, the solid curve stands for the EXIT curve of the outer TuCM decoder, while the circled-dashed line is that of the outer convolutional decoder (CC). According to [15, 18, 139], the area under the EXIT curve of the inner decoder is approximately equal to the channel capacity. It is clear that the area under the square-constellation 64-QAM scheme's EXIT curve is the largest, while that of the 64-DPSK is the smallest. It can be seen in Figure 3.13 that the area under the square-constellation 64-QAM scheme's EXIT curve is larger than that under the 64-DAPSK (4,16) scheme's curve, which is in turn higher than that of the 64-DPSK arrangement. In both cases an open is observed tunnel between the inner curves and the outer curves indicating, that convergence is possible at this SNR. Note that only the EXIT function of the inner decoder depends on the SNR and an open EXIT chart tunnel implies having an infinitesimally low BER [139, 142]. Hence we may argue based on Figure 3.13 that a vanishingly low BER may be achieved by the TuCM aided 64-DAPSK (4,16)

[5]It is assumed throughout that all amplitude and phase values are equally likely. More specifically, the probability of each amplitude ratio of the 64-DAPSK (4,16) symbols can be expressed as: $p(\alpha^0) = 2 \cdot p(\alpha^{-3}) = 2 \cdot p(\alpha^1) = 2 \cdot p(\alpha^{-2}) = 2 \cdot p(\alpha^2) = 2 \cdot p(\alpha^{-1}) = 2 \cdot p(\alpha^1) = 0.25$.

[6]In serially concatenated and turbo-detected schemes the soft-output demodulator is often referred to as the inner decoder for the sake of a unified terminology.

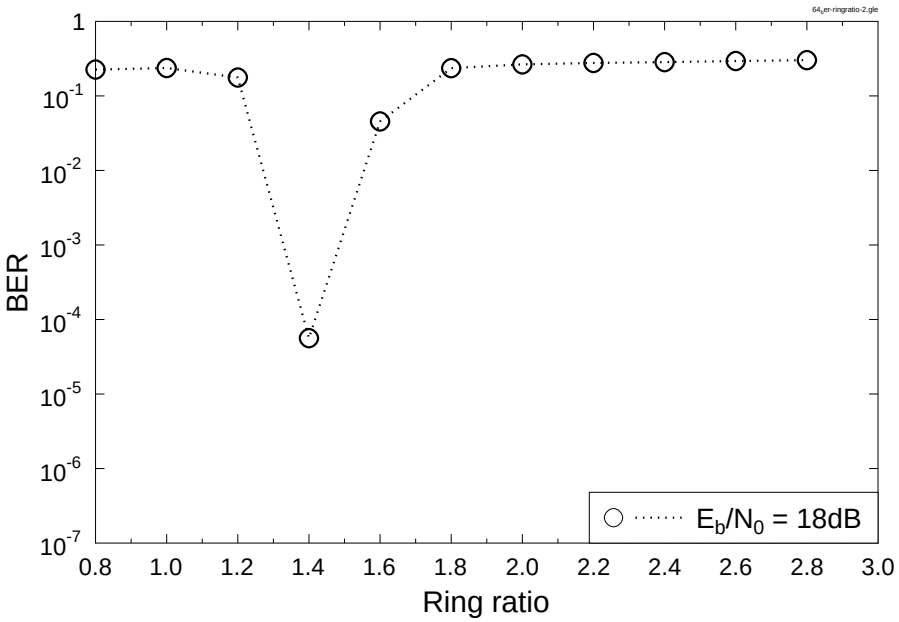


Figure 3.9: BER versus ring ratio performance of the 64-DAPSK (4,16)-TuCM schemes for transmission over the correlated Rayleigh fading channel associated with $f_d = 0.01$ and four iterations. The simulation parameters are detailed in Table 3.2.

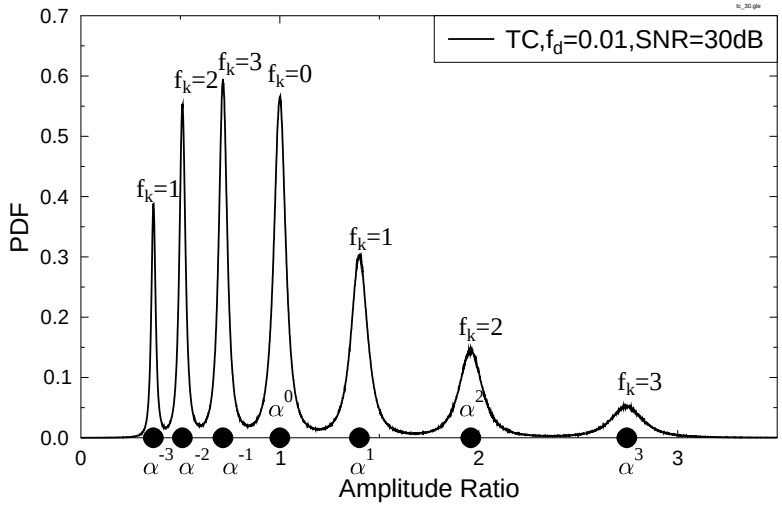


Figure 3.10: The PDF of the received signal amplitude ratios of TuCM aided 64-DAPSK (4,16) $\frac{|y_k|}{|y_{k-1}|}$ based on Equation (3.6), when communicating over correlated Rayleigh fading channels at an $E_b/N_0$ of 30 dB. The constellation diagram of the 64-DAPSK (4,16) scheme is shown in Figure A.4.

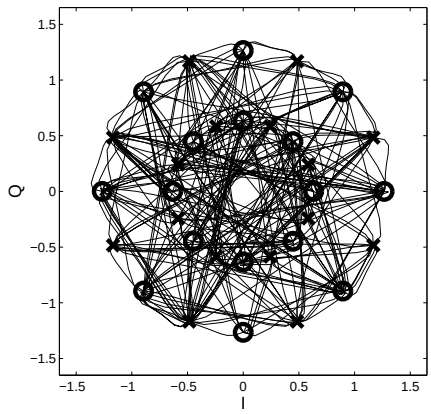


(a) Offset 16-DAPSK (2,8), $\alpha_{rc} = 0.9$

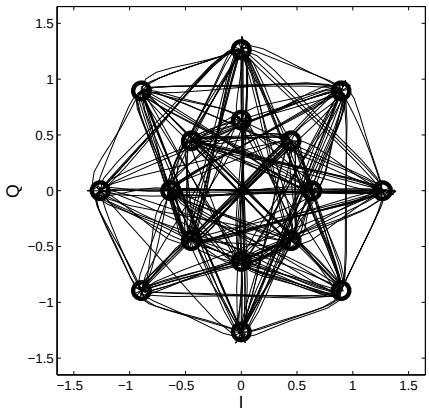


(b) 16-DAPSK (2,8), $\alpha_{rc} = 0.9$

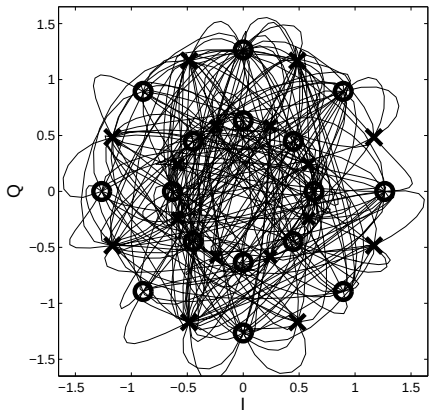


(c) Offset 16-DAPSK (2,8), $\alpha_{rc} = 0.5$

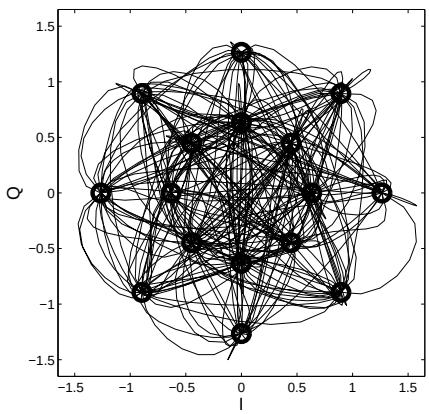


(d) 16-DAPSK (2,8), $\alpha_{rc} = 0.5$

Figure 3.11: The corresponding constellation diagrams after the raised-cosine pulse shaping for both the offset 16-DAPSK (2,8) and the non-offset 16-DAPSK (2,8) system.

scheme for SNR values in excess of 17.5 dB. By contrast, no open EXIT chart tunnel is maintained for the same SNR value in the case of the 64-DPSK benchmark scheme. Note that the EXIT curve of the CC does not match that of the 64-DAPSK (4,16) demapper, while that of the TuCM does.

Figure 3.14 shows the corresponding BER versus SNR performance, which compares the performance of the TuCM-aided 64-QAM, 64-DAPSK (4,16) and 64-DPSK aided TuCM schemes, when communicating over correlated Rayleigh fading channels using different transmission block lengths[7] and turbo-interleaved block lengths (Table 3.2). When the number of 64-DAPSK (4,16) modulated transmission blocks per TuCM block is one, which corresponds to the curve marked by circles in Figure 3.14, the SNR difference between the classic coherently detected square-constellation 64-QAM and our low-complexity 64-DAPSK (4,16) dispensing with channel-estimation is 5 dB. As a substantial further benefit, our scheme outperforms 64-DPSK by about 4.2 dB. More-

[7] In this chapter, the TuCM block length is given by the number of modulated symbols per 64-DAPSK (4,16) transmission block times the number of transmission blocks per TuCM block.

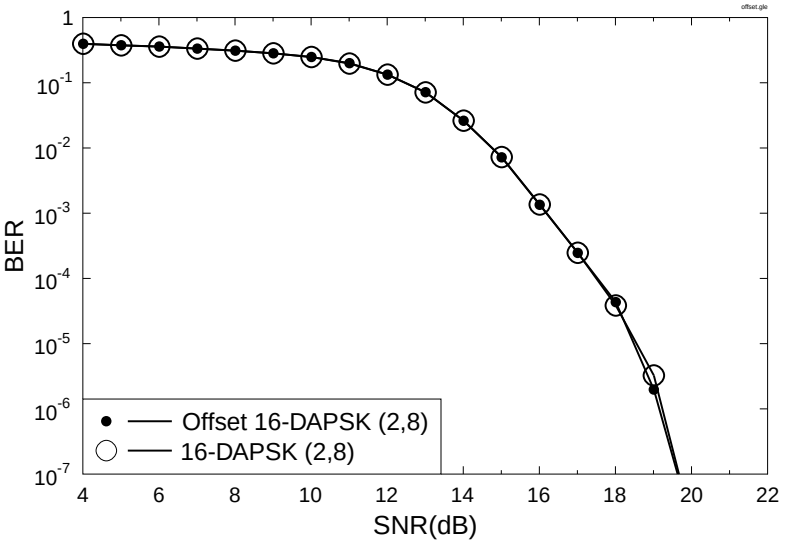


Figure 3.12: BER versus SNR (dB) performance comparison of the 16-DAPSK (2,8) and offset 16-DAPSK (2,8) schemes for transmission over correlated Rayleigh fading channels. The corresponding system parameters are summarized in Table 3.2.

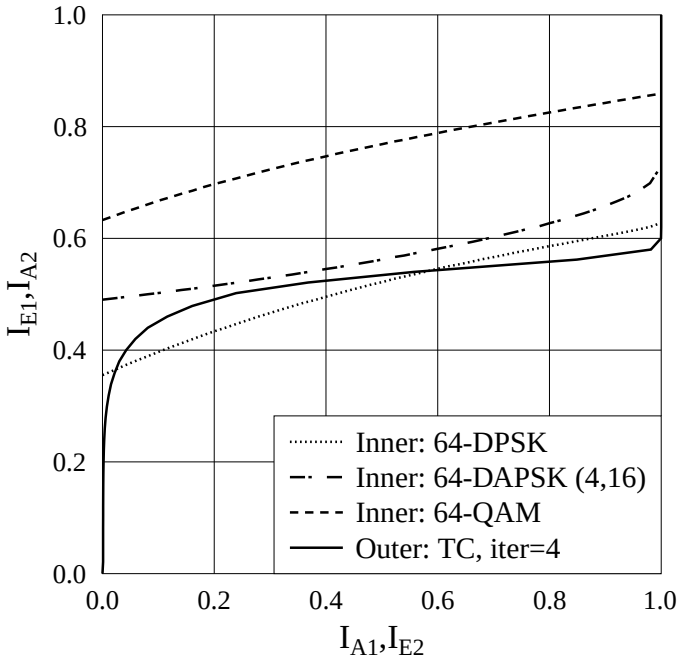


Figure 3.13: EXIT Charts of the 64-QAM, 64-DAPSK (4,16) and 64-DPSK aided TuCM schemes when communicating over a correlated Rayleigh channel at SNR=17.5 dB. The SNR-independent EXIT curve of the outer TuCM decoder is also shown. The corresponding simulation parameters are presented in Table 3.2.

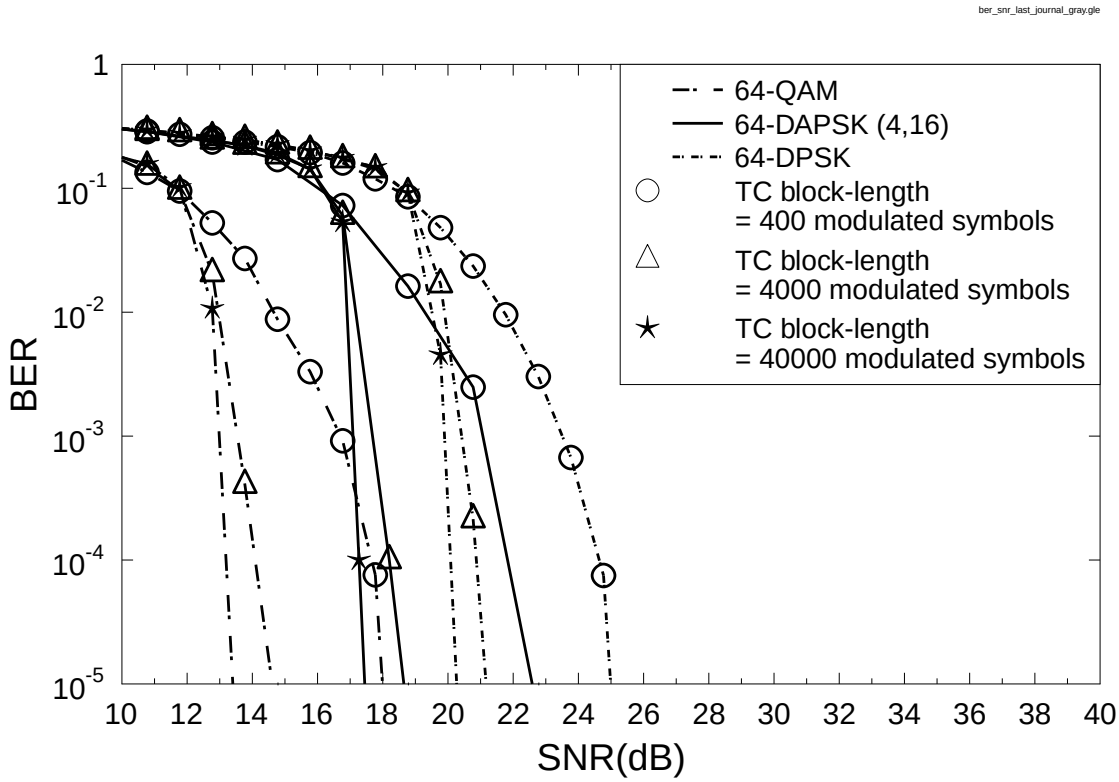


Figure 3.14: BER versus SNR (dB) performance comparison of the 64-QAM, 64-DAPSK (4,16) and 64-QAM schemes for transmission over correlated Rayleigh fading channels. The corresponding system parameters are summarized in Table 3.2. A TC block-length of 400 modulated symbols corresponds to one 64-DAPSK block-length, while a 4000-modulated-symbol TC block corresponds to ten 64-DAPSK block-length.

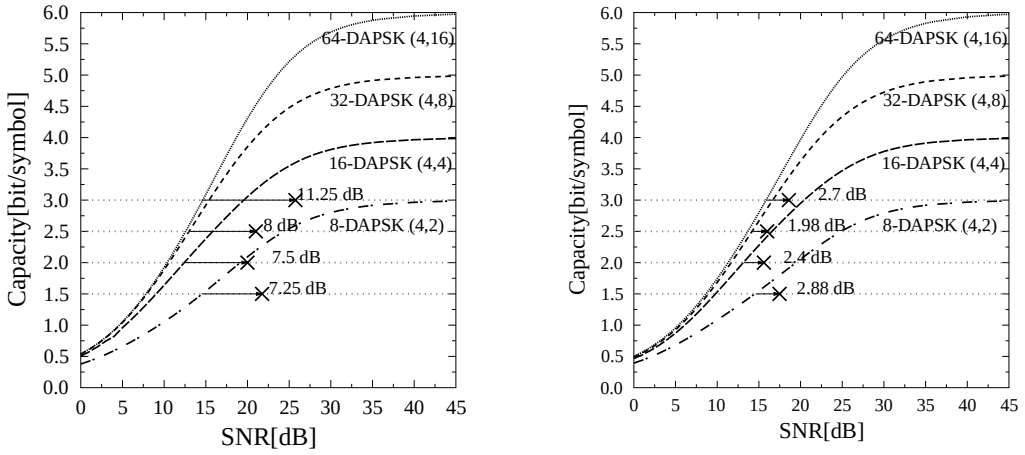


(a) TuCM block length of 400 modulated symbols.

(b) TuCM block length of 40,000 modulated symbols.

Figure 3.15: Achievable throughput versus SNR (dB) for transmission over correlated Rayleigh fading channels, while using different TuCM block length.

over, when the number of 64-DAPSK (4,16) blocks per TuCM block is increased to one hundred (the curve marked by star), all the BER performances are improved. Compared to the scenario, when the number of 64-DAPSK (4,16) blocks per TuCM block is one, the SNR gain of the arrangement having 100 blocks per TuCM block is improved by 8.6 dB. In general, the longer the TuCM block-length, the closer the BER performance curve to the channel capacity.

Figure 3.15 quantifies the maximum achievable throughput of various M-DAPSK (4, $M_p$) schemes, where the curves were generated by evaluating the area under the corresponding EXIT curves, as mentioned above and detailed in [135, 142]. The horizontal dotted lines represent the throughput values of the different turbo-coded modulation schemes considered. More explicitly, 1.5, 2.0, 2.5 and 3.0 bits/symbol are the throughputs that of TuCM aided 8-DAPSK (4,2), 16-DAPSK (4,4), 32-DAPSK (4,8) and 64-DAPSK (4,16), respectively. Each large cross is located at the SNR required for the corresponding TuCM-aided modulation scheme to achieve an identical throughput to each other at a target BER of $10^{-5}$. The SNR values shown next to the large crosses indicate the distances to the corresponding channel capacity. Figure 3.15a presents the achievable throughput versus SNR (dB) at a TuCM block length of 400 modulated symbols for the various TuCM-aided 64 DAPSK(4, $m_p$) schemes are capable of operating within 11.5 dB from their corresponding capacity curves. When using a longer TuCM block length of 40 000 modulated symbols, the various TuCM-aided M DAPSK(4, $m_p$) schemes are capable of operating within 3 dB from their corresponding capacity curves, as shown in Figure 3.15b. Hence, as expected, the larger the TuCM block size employed, the closer the system operates to capacity. The large crosses represent the SNR required for the corresponding modulation schemes to achieve an identical throughput to each other at a target BER of $10^{-5}$.

## 3.3 Adaptive Mode

In Section 3.2 we have quantified the performance of the soft-decision aided fixed mode DAPSK schemes. As the next logical development, in this section we will investigate soft-decision aided differentially encoded and non-coherently detected modulation scheme in the adaptive regime.

The adaptive system will be presented in Section 3.3.1, while the corresponding simulation results will be provided in Section 3.3.2.

### 3.3.1 System Architecture and Performance Study

The schematic of the near-instantaneous ACM is depicted in Figure 3.16, where the transmitter extracts the coded modulation mode required by the receiver for achieving its target integrity from the reverse-link transmission burst in order to accommodate the channel-quality fluctuations. We invoke five encoders, which are activated based on their BER versus SNR performance seen in Figure 3.17. These five modes are listed as follows:

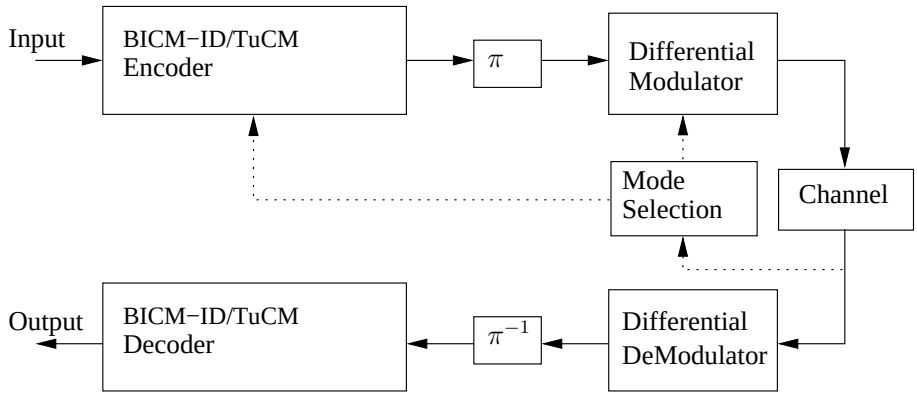


Figure 3.16: Schematic of adaptive coded modulation. Note that $\pi$ and $\pi^{-1}$ represents the interleaver and deinterleaver, respectively.

- No transmission (NoTx): $R_o$=0;
- TuCM-4DPSK: $R_o$=1;
- BICM-ID-8PSK: $R_o$=2;
- TuCM-64-DAPSK (4,16): $R_o$=3;
- BICM-ID-64-DAPSK (4,16): $R_o$=5.

The mode selection mechanism were detailed in Section 2.3.1.1.

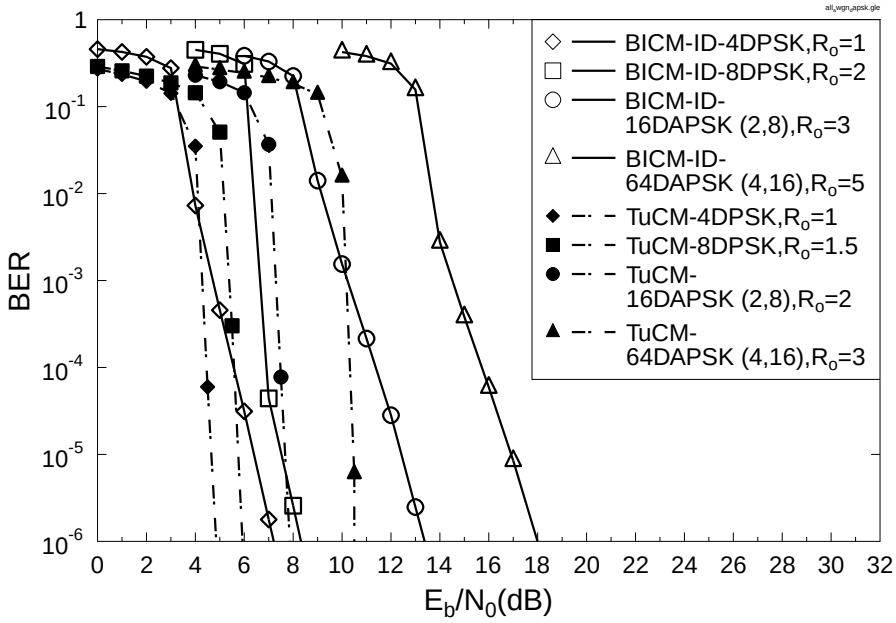


Figure 3.17: BER performance of BICM-ID and of the TuCM-aided 4DPSK, 8DPSK, 16-DAPSK (2,8) and 64-DAPSK (4,16) schemes, when communicating over the **AWGN channel**. The simulation parameters are shown in Table 3.7.

Figure 3.17 characterizes the BER performance of the BICM-ID aided 4DPSK, 8DPSK, 16-DAPSK (2,8) and 64-DAPSK (4,16) schemes when communicating over the AWGN channel using the parameters listed in Table 3.7. In this figure the BER performance of the TuCM is also shown for comparison. The results reflect that the BER performance of TuCM assisted schemes does not exhibit an error floor, while those of BICM-ID do. The throughput should be the same for the fair comparison. For example, the rate-1/2 64-DAPSK (4,16)-TuCM scheme achieves an approximately 2 dB $E_b/N_0$ gain at a BER of $10^{-5}$, compared to the rate-3/4 16-DAPSK (2,8)-BICM-ID scheme. Based on Figure 3.17, the $E_b/N_0$ and SNR thresholds configures for maintaining a BER of $10^{-5}$ are obtained and listed in Table 3.3 and Table 3.4.

| BICM-ID | Throughput | $E_b/N_0(dB)$ (BER = $10^{-5}$) | SNR($dB$) (BER = $10^{-5}$) |
|---|---|---|---|
| 4DPSK | 1.0 | 6.40 | 6.40 |
| 8DPSK | 1.5 | 7.53 | 10.54 |
| 16DAPSK (2,8) | 2.0 | 12.43 | 17.20 |
| 64DAPSK (4,16) | 3.0 | 16.90 | 23.89 |

Table 3.3: The values of $E_b/N_0(dB)$ and SNR($dB$) for TuCM over AWGN channels. The simulation parameters are shown in Table 3.7.

| TuCM | Throughput | $E_b/N_0(dB)$ (BER = $10^{-5}$) | SNR($dB$) (BER = $10^{-5}$) |
|---|---|---|---|
| 4DPSK | 1.0 | 4.67 | 4.67 |
| 8DPSK | 2.0 | 5.75 | 7.51 |
| 16DAPSK (2,8) | 3.0 | 7.67 | 10.68 |
| 64DAPSK (4,16) | 5.0 | 10.47 | 15.24 |

Table 3.4: The $E_b/N_0(dB)$ and SNR($dB$) values determined for BICM-ID over AWGN channels. The simulation parameters are shown in Table 3.7.

Figure 3.18 shows the BER performance of BICM-ID and of the TuCM aided 4DPSK, 8DPSK, 16-DAPSK (2,8) and 64-DAPSK (4,16) schemes when communicating over the correlated Rayleigh fading channel associated with $f_d = 0.01$ using the parameters listed in Table 3.7. As seen in Figure 3.18, the BER performance of TuCM does not exhibit an error floor, while that of BICM-ID does. Furthermore, the error floor of the BICM-ID aided 64-DAPSK (4,16) scheme exists, because the channel's fluctuation is too rapid. When $f_d = 0.001$, the BER generally drops seen in Figure A.3 of Appendix A.2. Hence, in the near-instantaneous by adaptive system, considered the BICM-ID aided 64-DAPSK (4,16) scheme will not be employed. Based on Figure 3.18, the $E_b/N_0$ and SNR thresholds configured for maintaining a BER of $10^{-5}$ are listed in Table 3.5 and

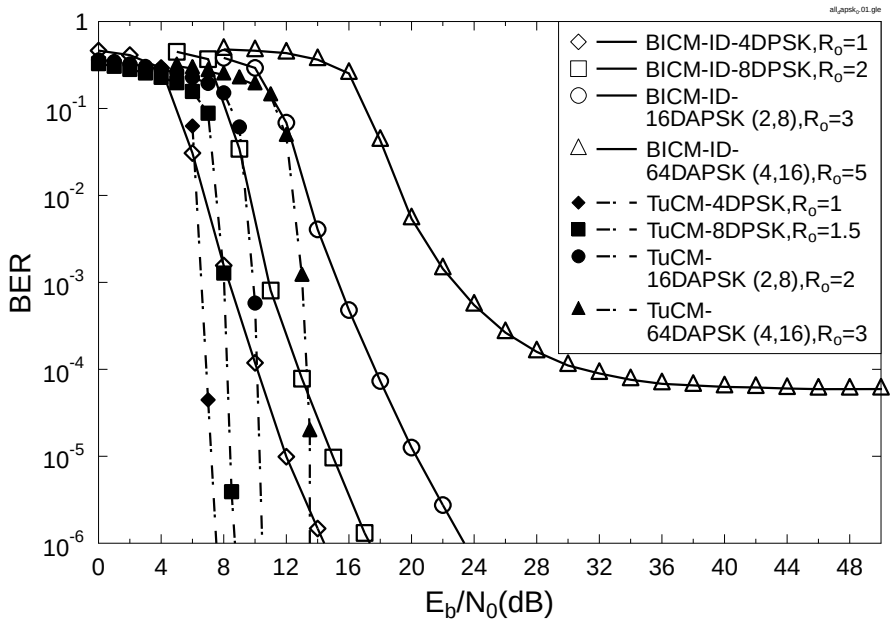


Figure 3.18: BER performance of BICM-ID and TuCM aided 4DPSK, 8DPSK, 16-DAPSK (2,8) and 64-DAPSK (4,16) schemes when communicating over the **correlated Rayleigh fading channel** with $f_d = 0.01$. The simulation parameters are shown in Table 3.7.

| BICM-ID | Throughput | $E_b/N_0(dB)$ (BER = $10^{-5}$) | SNR($dB$) (BER = $10^{-5}$) |
|---|---|---|---|
| 4DPSK | 1.0 | 12 | 12 |
| 8DPSK | 2.0 | 14.96 | 17.97 |
| 16DAPSK (2,8) | 3.0 | 20.30 | 25.07 |

Table 3.5: The $E_b/N_0(dB)$ and SNR($dB$) values determined for BICM-ID over correlated Rayleigh fading channels having $f_d = 0.01$. The simulation parameters are shown in Table 3.7.

Table 3.6.

| TuCM | Throughput | $E_b/N_0(dB)$ (BER = $10^{-5}$) | SNR($dB$) (BER = $10^{-5}$) |
|---|---|---|---|
| 4DPSK | 1.0 | 7.22 | 7.22 |
| 8DPSK | 1.5 | 8.43 | 10.19 |
| 16DAPSK (2,8) | 2.0 | 10.30 | 13.31 |
| 64DAPSK (4,16) | 3.0 | 13.52 | 18.29 |

Table 3.6: The $E_b/N_0(dB)$ and SNR($dB$) values determined for TuCM for transmission over correlated Rayleigh fading channels associated with $f_d = 0.01$. The simulation parameters are shown in Table 3.7.

### 3.3.2 Simulation Results

In this section, we will investigate the performance of adaptive soft-decision aided differentially encoded non-coherently detected modulation schemes communicating over quasi-static Rayleigh fading channels. The system parameters are given in Table 3.7.

| Coded Modulation | BICM-ID | TuCM |
|---|---|---|
| Modulation Scheme | 4DPSK, 8DPSK, 16-DAPSK (2,8), 64-DAPSK (4,16) | |
| Mapper type | Set-Partitioned | Gray Mapping |
| Number of iterations | 8 | Inner iterations 4, Outer iterations 2 |
| Code Rate | 1/2, 2/3, 3/4, 5/6 | 1/2 |
| Code Memory | 3 | |
| Decoder type | Approximate Log-MAP | |
| Symbols per frame | 12,000 | |
| Number of frames | 10,000 | |
| Channel | AWGN, Quasi-static Rayleigh fading channel Correlated Rayleigh fading channel with $f_d = 0.01$ | |

Table 3.7: Simulation parameters. Note that we declare 'an iteration' being completed, when both the demapper and decoder were activated once.

The mode selection probability for the occurrence of the 4PSK, 8PSK, 16QAM and 64QAM modes when transmitting over quasi-static Rayleigh fading channels using the $E_b/N_0$ and SNR threshold seen in Table 3.3 and Table 3.4 are shown in Figure 3.19. Observe in Figure 3.19 that when the channel quality is poor, the NoTx mode is employed most frequently, while the BICM-ID-64DAPSK (4,16) mode is used more frequently when the SNR increases. The BER and BPS

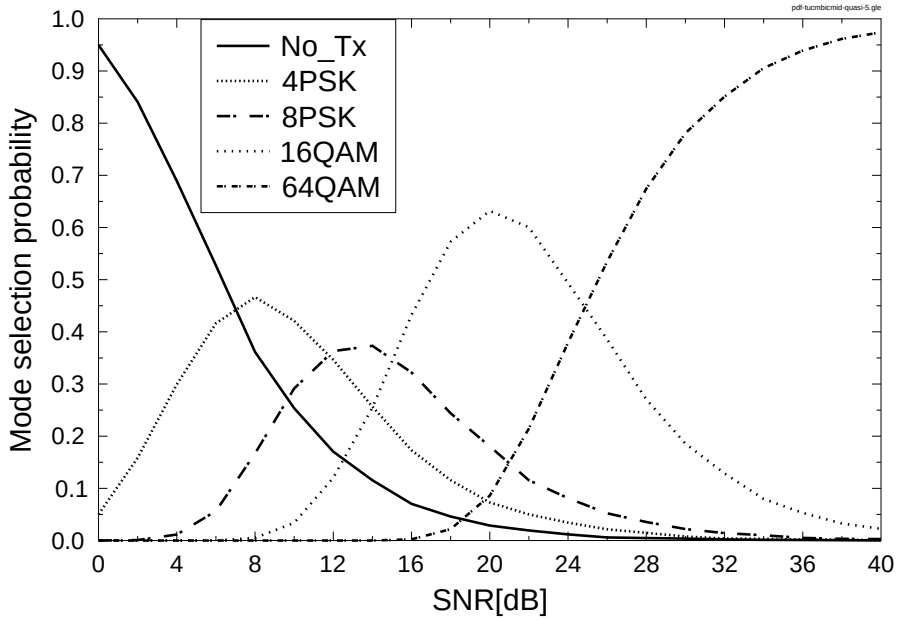


Figure 3.19: The **mode selection probability** of the 4PSK, 8PSK, 16QAM, and 64QAM modes for **TuCM** transmissions over **quasi-static Rayleigh fading channels**. The related simulation parameters are detailed in Table 3.7.

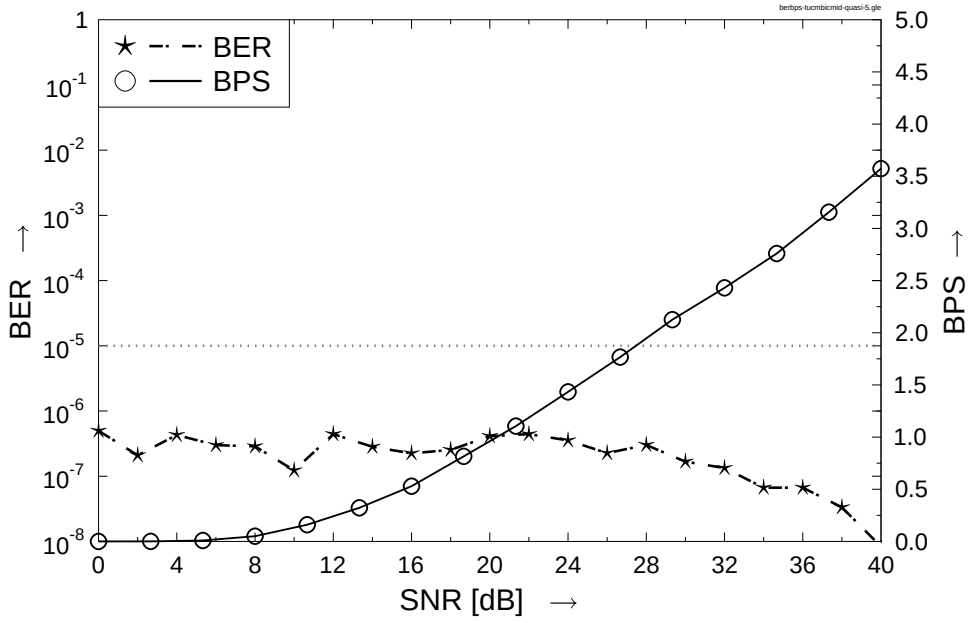


Figure 3.20: The **BER and BPS** of 4PSK, 8PSK, 16QAM, and 64QAM for **TuCM** transmissions over **quasi-static Rayleigh fading channels**. The related simulation parameters are detailed in Table 3.7.

performance curves of adaptive system are shown in Figure 3.20, where we observed that the overall BER was lower than the target BER of $10^{-5}$, while the BPS curve improves as the SNR increases.

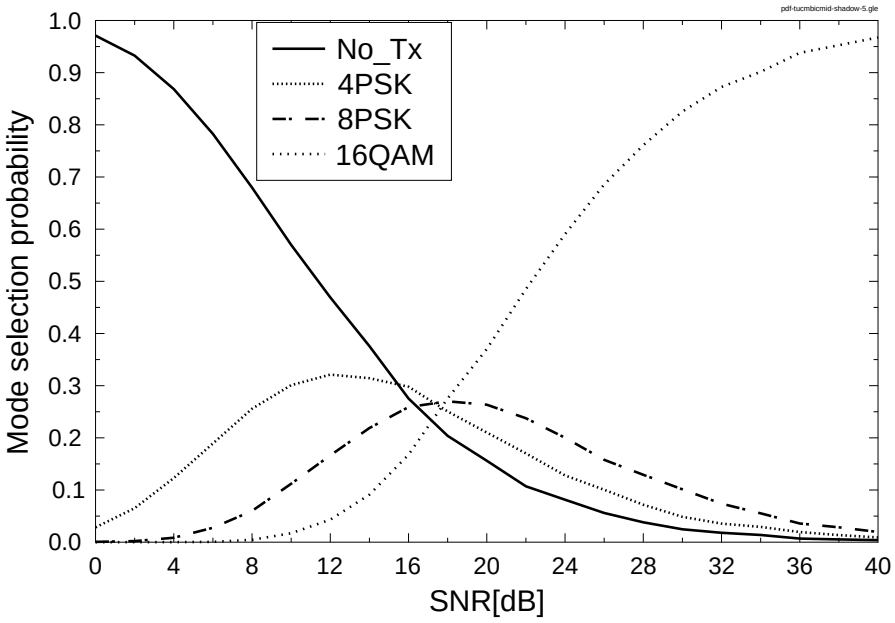


Figure 3.21: The **mode selection probability** of the 4PSK, 8PSK, 16QAM modes for **TuCM** transmissions over **shadow-and-correlated Rayleigh fading channels**. The related simulation parameters are detailed in Table 3.7.

Figure 3.21 shows the mode selection probability of the various CM modes, when the thresholds of Table 3.5 and Table 3.6 are employed. The BER and BPS performance curves of the ACM scheme communicating over shadow-and-fast Rayleigh fading channels using the adaptive thresholds of Table 3.5 and Table 3.6 are shown in Figure 3.22.

## 3.4 Conclusions

In this chapter, we have derived the symbol-to-bit soft-demapper probability formulas of 16-DAPSK (2,8) aided BICM-ID and extended it to the TuCM aided M-DAPSK ($M_a$,$M_p$) scheme. We also compared our proposed soft-decision demapper aided 16-DAPSK (2,8) scheme to the BMIAD scheme. Then the offset-M-DAPSK ($M_a$,$M_p$) system, which requires a less stringent linear power amplifier specification was investigated. More specifically, when time-synchronization is perfect, the offset M-DAPSK ($M_a$,$M_p$) has the same BER performance as its zero-offset
M-DAPSK ($M_a$,$M_p$) counterpart. EXIT charts were used for quantifying the achievable DCMC capacity of the various TuCM-aided M-DAPSK ($M_a$,$M_p$) modulation schemes. The 64-DAPSK-TuCM scheme outperforms the identical-throughput 64-DPSK-TuCM scheme by about 4 dB at a BER of $10^{-5}$, when communicating over correlated Rayleigh fading channels having a normalised Doppler frequency of 0.01 and a TuCM block length of 40 000 modulated symbols. The SNR distance of the performance curve of 64-DAPSK-TuCM from the capacity is 2.7 dB. Finally, the

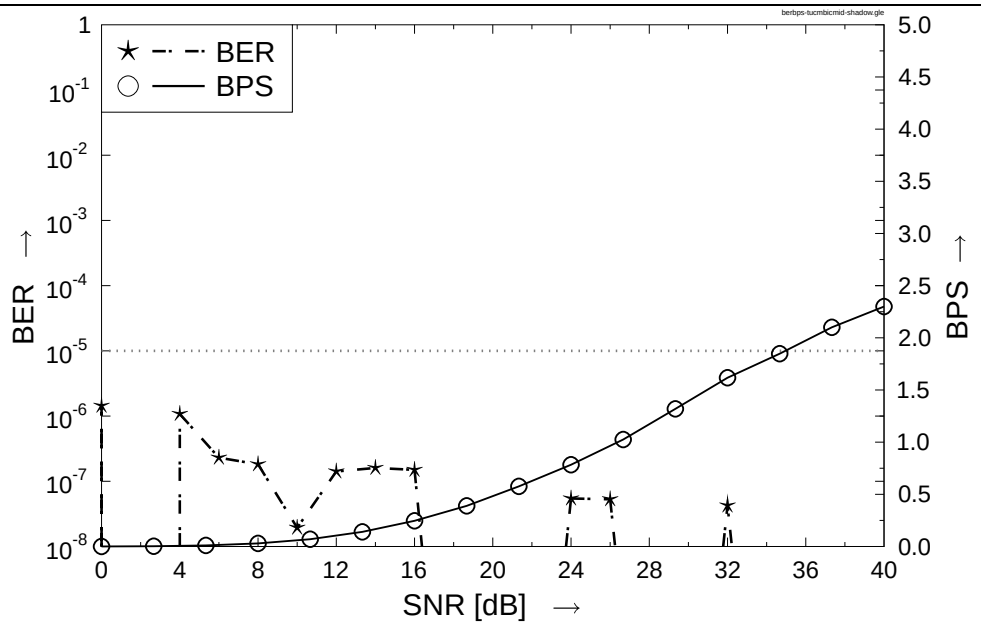


Figure 3.22: The **BER and BPS** of 4PSK, 8PSK, 16QAM aided **TuCM** transmissions over **shadow-and-correlated Rayleigh fading channels**. The related simulation parameters are detailed in Table 3.7.

adaptive soft-decision aided M-DAPSK scheme communicating over quasi-static as well as our shadow-and-correlated Rayleigh fading channels was investigated in Section 3.3. It worth noting that our the SNR threshold values at a target BER of the various soft-decision aided non-coherently detected CM schemes are summarized in Table 3.8.

In the next chapter, we will explore the application of both the coherent and non-coherent coded modulation schemes in the context of cooperative communications.

| Channel | | AWGN | | Correlated Rayleigh ($f_d = 0.01$) | |
|---|---|---|---|---|---|
| Memory | | 3 | | | |
| Decoder | | Approximate Log-MAP | | | |
| Code | BPS | SNR (dB) at BER | | | |
| | | $10^{-5}$ | $10^{-6}$ | $10^{-5}$ | $10^{-6}$ |
| BICM-ID-4DPSK | 1 | 6.40 | 7.10 | 12.00 | 14.30 |
| BICM-ID-8DPSK | 2 | 10.54 | 11.31 | 17.97 | 20.11 |
| BICM-ID-16DAPSK (2,8) | 3 | 17.20 | 17.07 | 25.07 | 28.07 |
| BICM-ID-64DAPSK (4,16) | 5 | 23.89 | 24.99 | error-floor | error-floor |
| TuCM-4DPSK | 1 | 4.67 | 4.90 | 7.22 | 7.50 |
| TuCM-8DPSK | 1.5 | 7.51 | 7.71 | 10.19 | 10.36 |
| TuCM-16DAPSK (2,8) | 2 | 10.68 | 10.91 | 13.31 | 13.31 |
| TuCM-64DAPSK (4,16) | 3 | 15.24 | 15.27 | 18.29 | 18.17 |

Table 3.8: SNR threshold values of various soft-decision non-coherently detected CM schemes when transmitting over AWGN and Correlated Rayleigh fading channels. The values are tabulated from Figures 3.17– 3.18.

Chapter 4

# Coherent Coded Modulation for Cooperative Communications

## 4.1 Introduction

In Chapter 2 and Chapter 3, we have designed and investigated a range of coherent and non-coherent coded modulation schemes designed for over conventional point-to-point links. The traditional direct point-to-point transmission has its shortcomings, because when the Source Node (SN) roams at the edge of the coverage region of a traffic cell bordering onto another cell might not be able to initiate a handoff due to the unavailability of unused channels or owing to the lack of a sufficiently high received signal level at the adjacent cell. The call in process may be dropped in this scenario [143]. As a remedy, in this chapter, as well as in Chapter 5, we will apply both the coherent and non-coherent CM schemes studied in Chapter 2 and Chapter 3 in the context of relay aided cooperative communications scenarios.

Cooperative communications [139, 143] is capable of supporting the users either at an improved integrity or at an increased throughput in wireless networks with the advent of user cooperation. The simplest cooperative two-hop communications scheme consists of three terminals, namely a SN, a Relay Node (RN) and a Destination Node (DN) [144]. In a simple cooperative regime the SN transmits its information to both the RN and the DN during the first cooperative transmission period. Then the RN retransmits the information during the second cooperative transmission period. In a slightly more sophisticated cooperative diversity regime, two users may cooperate by exchanging their roles as SN and RN [145]. The source-to-relay (SR) link and source-to-destination (SD) link typically fade independently and the destination beneficially combines the two links' signals for achieving diversity gain. A key aspect of the cooperative communication process is the specific choice of how to process the signal transmitted from the SN at the RN. Cooperative communications protocols can be generally categorized into *fixed relaying* schemes and *adaptive relaying* schemes. In fixed relaying schemes, the communications resources are divided between the SN and

the RN in a fixed manner. The fixed relaying techniques can be further divided into four categories, namely: *Amplify-and-Forward (AF)* [146], *Decode-and-forward (DF)* [147, 148], *Compress-and-Forward* [144] and *Coded Cooperation* [149]. Although fixed relaying schemes tend to have a lower complexity, they have a lower bandwidth efficiency, because half of the communications resources are allocated to the relay for transmission, which reduces the overall throughput. The Adaptive Relaying Protocol (ARP) of [150] might be capable of overcoming this problem owing to the ARP scheme selecting the forwarding protocol of relays where a protocol selection criterion depends on the success of decoding at each relay. The basic idea of cooperative communication can be traced back to the work of Meulen [151] on the concept of the relay channel model, while the main milestones in the development of cooperative communications schemes are summarized in Tables 4.1 – 4.3.

Networking Coding (NC) [189] is a multi-cast technology. The core idea of NC is that an intermediate node no longer performs simple store-and-forward function, but instead, efficiently encodes and forwards the specifically processed information of both sources of a duplex link to both destinations, thus improving the capacity and robustness of the whole network. The network coding concept was originally conceived for wired networks [189]. Nonetheless, the broadcast nature of radio channels is also amenable to the employment of NC. As a result, the combination of NC and cooperative communications is capable of effectively improving the performance of wireless communication systems. Motived by these observations, in this chapter, we consider a 'butterfly' topology based NC scheme, where two SNs and two DNs are assisted by a single RN.

In Section 4.2, the relay-induced error propagation is reduced in the context of DF relaying. Then based on our study provided in Chapter 2, ACM is invoked for cooperative communications in Section 4.3. Finally, adaptive TTCM aided distributed STTCs are proposed for cooperative communications in Section 4.4.

## 4.2 Relay-Induced Error Propagation Reduction for Decode-and-Forward Cooperation

Cooperative communications [139] is capable of supporting users in the quest for achieving either an improved integrity or a higher throughput in wireless networks with the advent of user cooperation. However, in practice decoding errors may be imposed by the RN's erroneous decisions, which would be propagated to the DN, potentially inflicting avalanche-like error propagation.

The potential error propagation limits the attainable end-to-end performance. Hence, various methods have been proposed for mitigating the effects of error propagation imposed by the RN [190, 191]. In this section, two methods are studied.

1. The *first method* considered was proposed in [175, 192], where the decoding error probability encountered at the RN was taken into account during the decoding process at the

| Year | Author(s) | Contribution |
|---|---|---|
| 1971 | Meulen [151] | The concept of relay channel model was introduced |
| 1979 | Cover and Gamal [144] | The capacity of relay channel was quantified |
| 1998 | Sendonaris *et al.* [152] | A new form of spatial diversity was achieved by the cooperation of mobile users |
| 2001 | Laneman *et al.* [146] | A hybrid DF method was conceived for attaining a cooperative diversity gain in wireless networks |
| 2002 | Hunter and Nosiratinia [149] | Coded cooperation was proposed |
| | Dohler *et al.* [153] | Extended the applicability of space-time block codes (STBC) to virtual antenna arrays |
| 2003 | Sendonaris *et al.* [147] | The concept of user cooperation was invoked for a CDMA system |
| | Sendonaris *et al.* [148] | The implementation aspects and performance of cooperative systems were considered |
| | Laneman *et al.* [154] | Distributed space-time-coded protocols were conceived |
| | Zhao and Valenti [155] | Distributed turbo codes were proposed for cooperative communications |
| 2004 | Laneman *et al.* [145] | Cooperative connectivity models were introduced for wireless relay networks |
| | Nabar *et al.* [156] | Performance limits and space-time signal designs were provided for fading relay channels |
| | Ribeiro *et al.* [157] | Symbol error probabilities were derived for general cooperative links |
| | Janani *et al.* [158] | Space-time transmission and iterative decoding was proposed for coded cooperation |
| | Stefanov *et al.* [159] | Cooperative coding was introduced |

Table 4.1: Milestone of Cooperative Communications (1971-2004).

| | | |
|---|---|---|
| 2005 | Azarian *et al.* [160] | The achievable diversity-multiplexing tradeoffs were quantified in half-duplex cooperative channels |
| | Sneessens *et al.* [161] | Soft DF was conceived |
| | Host-Madsen and Zhang [162] | Upper and lower bounds were derived for the attainable capacity of wireless relay channels |
| | Kramer *et al.* [163] | Efficient DF and CF relaying protocols and capacity theorems were provided for relay networks |
| | Larsson and Vojcic [164] | Cooperative transmit diversity was proposed based on superposition modulation |
| 2006 | Li *et al.* [165] | Distributed turbo coding relaying on SD was designed for multihop relay networks |
| | Xiao *et al.* [166] | Cooperative diversity based on code superposition was proposed |
| | Host-Madsen [167] | Capacity bounds were derived for cooperative diversity |
| | Chen and Laneman [168] | Efficient modulation and demodulation techniques were conceived for achieving a cooperative diversity gain |
| 2007 | Bao and Li [169] | Decode-Amplify-Forward (DAF) and Hybrid DAF was amalgamated with Coded-Cooperation |
| | Xiao [170] | Radical network coding approaches were proposed |
| | Zhao *et al.* [171] | Optimal power allocation versus relay selection strategies were investigated in AF cooperative communications |
| 2008 | Bao [172] | Adaptive network coded cooperation was proposed |
| | Yue [173] | Superposition coding schemes were designed for user cooperation |
| | Li and Vucetic [150] | A simple adaptive relaying protocol were devised |
| 2009 | Letaief and Zhang [174] | Cooperative techniques were combined with cognitive radio networks |
| | Lee and Hanzo [175] | MIMO-assisted hard versus soft DF was conceived for network coding aided relaying systems |
| | Chatzinotas *et al.* [176] | Capacity limits in cooperative cellular systems |
| 2010 | Kong *et al.* [177] | Near-capacity cooperative space-time coding employing irregular code design and successive relaying was proposed |
| | Dong *et al.* [178] | Improved wireless physical layer security was conceived for cooperating relays |
| | Xu *et al.* [179] | Joint channel- and networking- coding was devised for two sources sharing a single relay |

Table 4.2: Milestone of Cooperative Communications (2005-2010).

| Year | Author(s) | Contribution |
|---|---|---|
| 2011 | Peters and Heath [180] | Cooperative algorithms were conceived for MIMO-aided Interference-limited scenarios |
| | Talwar *et al.* [181] | Joint relay selection and power allocation was conceived for two-way relay networks |
| | Sugiura *et al.* [182] | Coherent versus non-coherent DF relaying aided cooperative space-time shift keying was proposed |
| 2012 | Clarke [183] | Transmit diversity and relay selection algorithms were designed for multirelay cooperative MIMO systems |
| | Rebelatto *et al.* [184] | Multiuser cooperative diversity relying on network coding and classic coding theory was proposed |
| | M. F. U. Butt *et al.* [185] | Self-concatenated code design and its application was conceived |
| | Qi *et al.* [186] | Hybrid automatic repeat re-quest strategies are proposed for relaying schemes |
| 2013 | Nasri *et al.* [187] | Optimization of Network-coded cooperative diversity systems |
| | Zhang *et al.* [188] | An overview of advances in cooperative communications |

Table 4.3: Milestone of Cooperative Communications (2011-2013).

destination. Hence we refer to it as 'Correcting the Relay's Decoding Errors at the Destination (CRDED)'. However, both the location of RNs and the corresponding transmit power was fixed in [175, 192].

2. The *second method* considered is based on the scheme advocated in [65, 101, 193], where joint signal design and coding was invoked both at the SN and the RN. We term this method as the joint SN-RN-DN design. The system selected the most appropriate relay based on the transmit power level required for guaranteeing reliable relaying. Although the joint SN-RN-DN design technique of [65,101,193] efficiently mitigated the RN-induced error propagation, when the power received at the RN was too low, the effect of error propagation still remained a persistent problem.

The apparent trade-off between the above-mentioned CRDED method of [175, 192] and the joint SN-RN-DN design of [65, 101, 193] has motivated our research to beneficially amalgamate these meritorious mechanisms for the sake of mitigating the error propagation imposed by the RN. We considered transmission over quasi-static Rayleigh fading channels, where the channel's envelope remains approximately constant during a transmission frame, but fades between the different frames. In this section, we will employ the BICM-ID [56, 194] scheme of Chapter 2 for assisting our DF based system. Set-Partitioning (SP) based signal labelling [3] is employed by the BICM-ID scheme for increasing the Euclidean distance of the constellation points and for exploiting the full advantage of bit interleaving with the aid of soft-decision feedback-based iterative decoding. Furthermore, the DF protocol is employed in the proposed scheme. Although using a strong channel

code is capable of mitigating the error propagation for transmission over idealized uncorrelated Rayleigh fading channels in a DF scheme, the error propagation is hard to mitigate for transmission over slowly-fading quasi-static Rayleigh fading channels owing to the lack of time diversity during a transmission frame.

Again, we amalgamate the CRDED technique of [175, 192] and the joint SN-RN-DN design of [65, 101, 193]. In the context of the latter technique we either select a RN near the desired location, or allocate the most appropriate transmit power to the RN in order to attain the desired received SNR at the DN, as in [65, 101, 193]. Hence this enhanced technique is referred to here as 'RN Selection or Power Allocation (RNSPA)'. Naturally, a beneficial amalgam of these techniques is expected to have a better end-to-end performance than the above-mentioned two methods in isolation.

### 4.2.1 System Model and Analysis

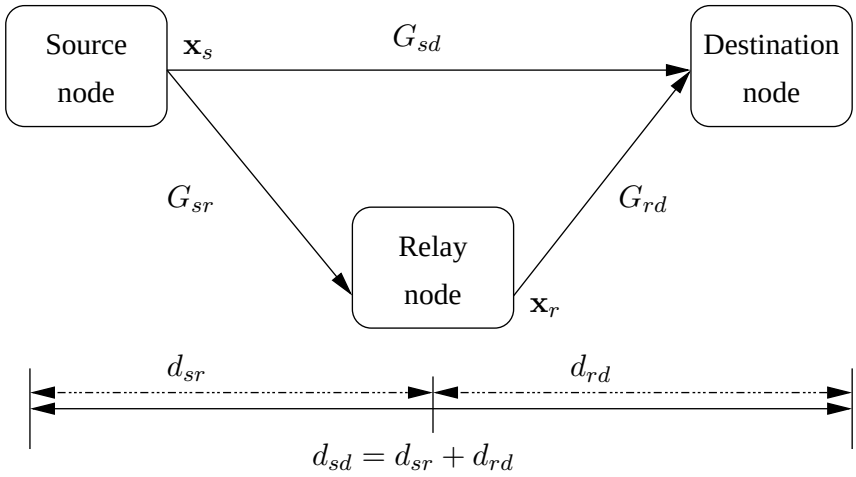


Figure 4.1: The schematic of a two-hop relay-aided system.

Figure 4.1 shows the basic schematic of a two-hop relay-aided system, which is used in our design. During the first cooperative transmission period the SN transmits a frame of coded symbols $\mathbf{x}_s$ to both the RN and DN. Then the RN decodes the information and transmits a frame of coded symbols $\mathbf{x}_r$ to the DN during the second cooperative transmission period. More specifically, during the first transmission period, the $k$th symbol received at DN may be written as:

$$y_{sd,k} = \sqrt{G_{sd}} h_{sd,k} x_{s,k} + n_{sd,k}, \tag{4.1}$$

where $k \in \{1, ...,\mathrm{N}\}$ and $N$ is the number of symbols transmitted from the SN, while $h_{sd,k}$ denotes the quasi-static Rayleigh fading coefficient between the SN and the DN. Moreover, $n_{sd,k}$ represents the AWGN having a variance of $N_0/2$ per dimension. Similarly, the $k$th symbol received at the RN may be expressed as:

$$y_{sr,k} = \sqrt{G_{sr}} h_{sr,k} x_{s,k} + n_{sr,k}, \tag{4.2}$$

where $h_{sr,k}$ denotes the quasi-static Rayleigh fading coefficient of the link between the SN and the RN, while $n_{sr,k}$ represents the AWGN having a variance of $N_0/2$ per dimension. It is assumed that the number of symbols transmitted from the SN is the same as that from the RN. The $k$th symbol received during the second transmission period may, therefore, be formulated as:

$$y_{rd,k} = \sqrt{G_{rd}} h_{rd,k} x_{r,k} + n_{rd,k}, \tag{4.3}$$

where $h_{rd,k}$ represents the quasi-static Rayleigh fading coefficient of the RN to DN link, while, $n_{rd,k}$ represents the AWGN having a variance of $N_0/2$ per dimension. The reduced-distance-related pathloss reduction (RDRPLR) of the SR link related to the SD link can be expressed as [195], [65]:

$$G_{sr} = \left(\frac{d_{sd}}{d_{sr}}\right)^{\aleph}. \tag{4.4}$$

Here, the pathloss exponent equals to $\aleph = 2$, because a free-space pathloss model is assumed. Similarly, the RDRPLR of the relay-to-destination (RD) link related to the SD link may be formulated as:

$$G_{rd} = \left(\frac{d_{sd}}{d_{rd}}\right)^{2}. \tag{4.5}$$

Naturally, the RDRPLR of the SD link related to itself is unity, yielding, $G_{sd} = 1$, where $d_{sr}$ represents the distance between the SN and RN, while $d_{rd}$ is that of the RD link and $d_{sd}$ is that of the SD link. Moreover, for the sake of simplicity we assumed without loss of generality that the SN, the RN and the DN are positioned along a straight line. Therefore, we have:

$$d_{sd} = d_{sr} + d_{rd}. \tag{4.6}$$

Again, below we beneficially combine the CRDED [175, 192] and the RNSPA [65, 101, 193] techniques. The proposed algorithm and its analysis will be presented in the following subsections.

#### 4.2.1.1 Correcting the Relay's Decoding Errors at the Destination

Practically, the RN may have decoding errors and if so, then the erroneous packets are transmitted from the RN to DN, which inevitably degrades the achievable end-to-end performance [192]. We denote the BER of the BICM coded bits at the RN as RN-BER. More specifically, the RN-BER is given by the BER of the BICM decoded bits at the RN, which can be estimated form the soft-metrics of the BICM decoder. Figure 4.2 shows the schematic of the entire system[1], where the interleaver and de-interleaver are represented by $\pi$ and $\pi^{-1}$, respectively. The estimated RN-BER has to be signalled to the DN, where it is employed for mitigating the effects of error propagation. In this model, the RN's location is fixed. Let $q_k^i$ denote the RN-BER of the $i$th bit of the $k$th symbol, where we have $i \in \{1, ..., m\}$ and $m$ represents the number of coded bits per BICM

[1] In this context, we note that the achievable performance of this scheme might be further improved by exchanging extrinsic information between the SD and RD receiver. This may also be viewed as a diversity combiner, which exploits the independent fading of the SD and RD links.

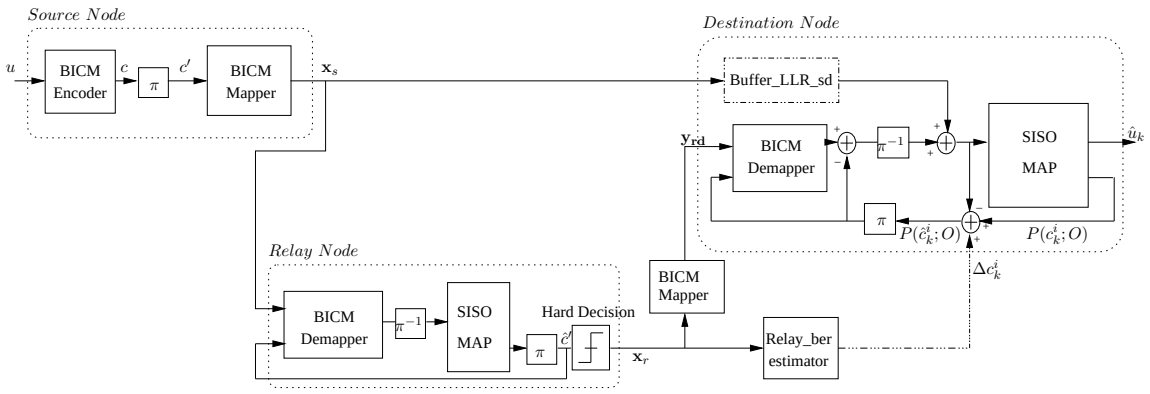


Figure 4.2: The block diagram of the RN-BER-aided system.

symbol. For simplicity, we assume that the RN-BER is perfectly known at the DN, which may be accurately estimated based on the decoder's soft output. It was shown in [192] that only a modest performance degradation is imposed, when a realistically estimated BER value is relied upon. Here, we introduced the sequence $\Delta c_k^i$, which hosts a logical one to indicate the position of the decoding errors, where the probability of the decoding errors $\Delta c_k^i$ can be expressed as:

$$P(\Delta c_k^i) = \begin{cases} 1 - q_k^i & \text{, if } \Delta c_k^i = 0 \\ q_k^i & \text{, if } \Delta c_k^i = 1. \end{cases} \tag{4.7}$$

During the BICM-ID decoding iterations at the DN the *extrinsic a pOsteriori* probability $P(c_k^i; O)$ of the original coded bits ($c_k^i$) and the error-indicator sequence $\Delta c_k^i$ [135] are interleaved independently, and then they are fed back to the input of the demapper as the probability of the *a priori* information, where again $O$ refers to the *extrinsic a pOsteriori* information. Considering the RN-BER and the *a posteriori* probability $P(c_k^i; O)$ of the BICM decoder's output bits [135], the joint probability $P(\hat{c}_k^i; O)$ may be calculated as:

$$P(\hat{c}_k^i; O) = \begin{cases} (1 - q_k^i) P(c_k^i = 0; O) + q_k^i P(c_k^i = 1; O) \\ \qquad\qquad \text{, if } \hat{c}_k^i = 0 \\ (1 - q_k^i) P(c_k^i = 1; O) + q_k^i P(c_k^i = 0; O) \\ \qquad\qquad \text{, if } \hat{c}_k^i = 1, \end{cases} \tag{4.8}$$

which may be used to generate the Log-Likelihood Ratio (LLR) [135] of $c_k^i$. Considering $P(c_k^i = 1; O)$ as an example, we have [135, 192]:

$$\begin{aligned} P(c_k^i = 1; O) \quad &= P(c_k^i = 1) \cdot \Big\{ (1 - q_k^i) \textstyle\sum_{\mathbf{x}_r \in \chi(i,1)} \exp\left( \frac{-|\mathbf{y_{rd}} - \sqrt{G_{rd}} \mathbf{h_{rd}} \mathbf{x}_r|^2}{N_0} \right) \prod_{j \neq i}^{m} P(\hat{c}_k^i = 1; O) \\ &+ \; q_k^i \textstyle\sum_{\mathbf{x}_r \in \chi(i,0)} \exp\left( \frac{-|\mathbf{y_{rd}} - \sqrt{G_{rd}} \mathbf{h_{rd}} \mathbf{x}_r|^2}{N_0} \right) \prod_{j \neq i}^{m} P(\hat{c}_k^i = 0; O) \Big\}, \end{aligned} \tag{4.9}$$

where $\chi(i, 0)$ is the set of constellation points having the $i$th bit set to 0 and $\chi(i, 1)$ is the set of constellation points having the $i$th bit set to 1. It is worth mentioning that the conventional BICM-ID decoder may be employed for the SD link without any modification, since this link is free from

any RN-induced decoding errors, where the corresponding probability can be simplified to:

$$P(c_k^i = b; O) = P(c_k^i = b) \cdot \left\{ \sum_{\mathbf{x}_r \in \chi(i,b)} \exp\left( \frac{-|\mathbf{y_{rd}} - \sqrt{G_{rd}}\mathbf{h_{rd}}\mathbf{x}_r|^2}{N_0} \right) \prod_{j \neq i}^{m} P(\hat{c}_k^i = b; O) \right\}, \tag{4.10}$$

where b $\in$ (0,1). Although error propagation may be encountered at the DN, it is mitigated with the aid of the RN-BER estimator shown in Figure 4.2, which can help the DN to correct the decoding errors induced at the RN.

Having considered the CRDED method, let us now focus our attention on the RNSPA technique.

#### 4.2.1.2 RN Selection or Power Allocation

When transmitting over quasi-static Rayleigh fading channels, the constant fading coefficient and the power of the AWGN determines the received SNR for each transmission frame. The estimated SNR can be used for choosing the optimum RN location. According to [101], the average SNR at the RN may be expressed as:

$$SNR_{r,sr} = \frac{E\{G_{sr}\}E\{|h_{sr}|^2\}E\{|x_{s,k}|^2\}}{N_0}, \tag{4.11}$$

where $x_{s,k}$ is the $k$th symbol transmitted from the SN. For the sake of simplifying our analysis, we define the 'equivalent SNR'[2] characterizing the ratio of the power transmitted from SN to the noise power encountered at the RN as:

$$SNR_{t,sr} = \frac{E\{|x_{s,k}|^2\}}{N_0}, \tag{4.12}$$

where we have $E\{|x_{s,k}|^2\} = 1$. Hence, we arrive at:

$$SNR_{r,sr} = SNR_{t,sr} G_{sr} |h_{sr}|^2 \tag{4.13}$$

$$\gamma_{r,sr} = \gamma_{t,sr} + 10\log_{10}(G_{sr}|h_{sr}|^2) \ \text{[dB]}, \tag{4.14}$$

where we have $\gamma_{r,sr} = 10\log_{10}(SNR_{r,sr})$ and $\gamma_{t,sr} = 10\log_{10}(SNR_{t,sr})$. Furthermore, we assume having the same transmit power at the SN and at the RN, which corresponds to equal-power-sharing between them. Hence, we have:

$$\gamma_{r,rd} - 10\log_{10}(G_{rd}|h_{rd}|^2) = \gamma_{r,sr} - 10\log_{10}(G_{sr}|h_{sr}|^2) \tag{4.15}$$

$$\frac{G_{rd}|h_{rd}|^2}{G_{sr}|h_{sr}|^2} = 10^{\frac{\gamma_{r,rd} - \gamma_{r,sr}}{10}}. \tag{4.16}$$

[2]We note that this definition does not represent a physically tangible or measurable quantity, since it relates the transmit power of the SN to the AWGN power encountered at the RN. Nonetheless, this convenient definition simplifies our discussions, which was proposed in [155].

Based on Equations (5.2), (5.3) and (5.4), the relationship between $G_{sr}$ and $G_{rd}$ may be expressed as:

$$G_{rd} = \left(\frac{1}{1 - 1/\sqrt{G_{sr}}}\right)^2. \tag{4.17}$$

If $\gamma_{r,sr}$ is fixed to $\gamma_{r,sr\,\min}$, the following relationship may be derived from Equations (4.16) and (4.17):

$$G_{sr} = |h_{sr}|^{-2} 10^{\frac{(\gamma_{r,sr\,\min} - \gamma_{t,sr})}{10}}. \tag{4.18}$$

Then, based on Equation (4.17), $G_{rd}$ can be obtained.

#### 4.2.1.3 Analysis of Both Methods for Perfect Relaying

In this sub-section, the performance of the CRDED and RNSPA methods is presented for the idealized perfect relaying scenario, where we have RN-BER = 0. Figure 4.3 shows the BER performance of the perfect relaying scenario. The dotted lines represent the performance of the CRDED method in the following three scenarios: 1) the RN is half-way between the SN and DN, 2) the RN is closer to the SN and 3) the RN is closer to the DN. As seen in Figure 4.3, if the RN is located close to the SN, $G_{rd}$ is relatively low, hence the DN receives the data at a relatively low SNR, thus we have a poorer performance. By contrast, if the RN is closer to the DN, the situation is reversed. At a BER of $10^{-4}$, there is an almost 5 dB SNR difference between these two scenarios. As seen in Figure 4.3, the performance curves of the RNSPA method are represented by the solid lines. Note that the BER curves of the RNSPA method decay faster than those of the CRDED method. The corresponding Frame Error Ratio (FER) performance is presented in Figure 4.4.

### 4.2.2 Simulation Results

The performance of the proposed systems is characterized in this section using the simulation parameters of Table 4.4. Firstly, the performance of the CRDED method recorded for RN-BER aided BICM-ID is characterized in Figure 4.6, which illustrates the BER performance of the CRDED system for a fixed RN location. When the RN is half-way between the SN and the DN, there is an almost 7 dB difference between the BER performance curve of the CRDED scheme exploiting the estimate of RN-BER and that operating without exploiting the knowledge of the RN-BER. Furthermore, encountering different RN locations results in a different performance. More specifically, the longer the SR link, the more substantially the BER performance of the CRDED technique improves, since the effects of the avalanche-like RN-induced error propagation become more catastrophic in the absence of the RN-BER knowledge, i.e. in the absence of the CRDED technique. For instance, the performance of the RN-BER aided scenario was improved by approximately 19 dB in the case of $G_{sr} = G_{rd}/3$. By contrast, we have a modest 2 dB improvement with the aid of the CRDED scheme for $G_{sr} = 3G_{rd}$. Therefore, the employment of the CRDED technique becomes more crucial, when the RN is closer to the DN. The corresponding FER performance shown in Figure 4.7 exhibits similar trends. Observe from Figure 4.3 and Figure 4.4 that when the SNR

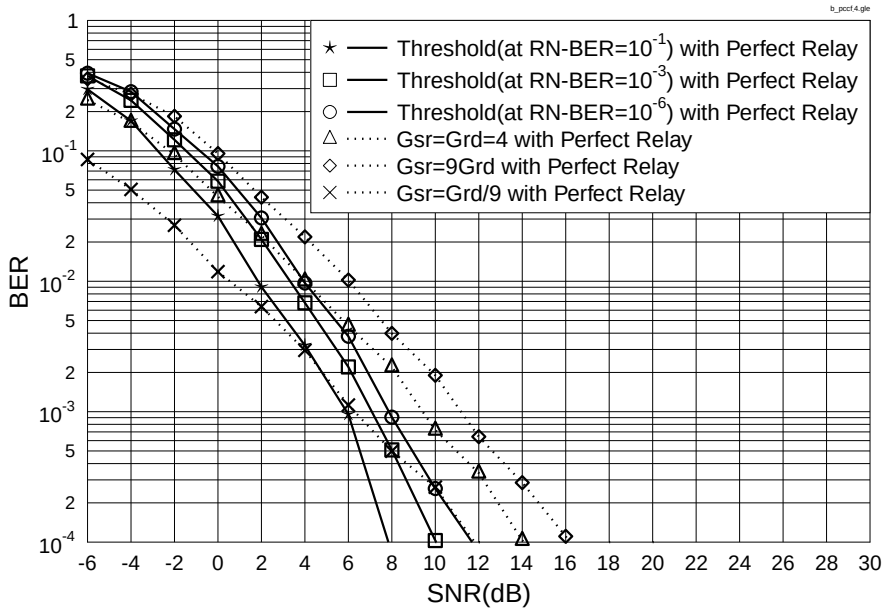


Figure 4.3: BER versus SNR performance for perfect relay aided BICM-ID for transmission over quasi-static Rayleigh fading channels both for the CRDED and for the RNSPA method. The system's schematic is portrayed in Figure 4.2 and the simulation parameters are summarised in Table 4.4.

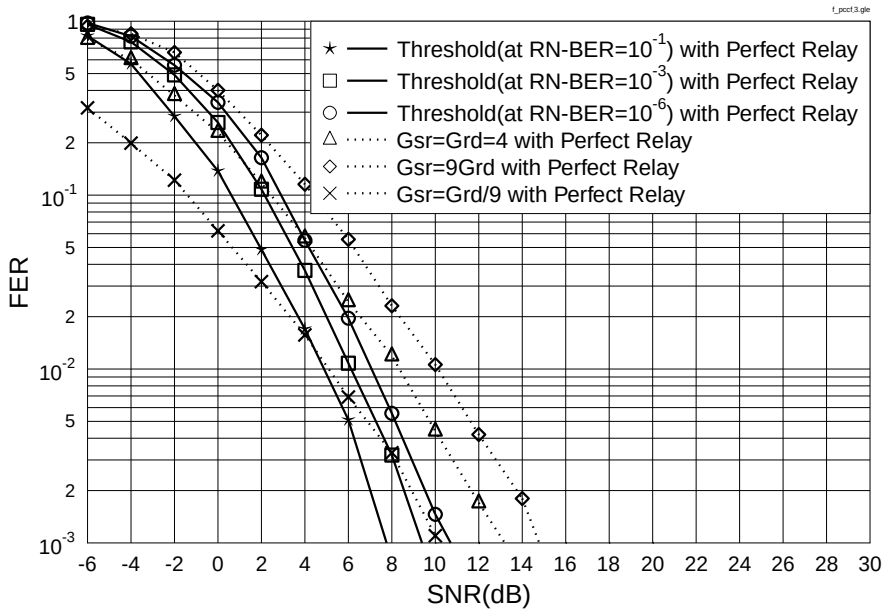


Figure 4.4: FER versus SNR performance for perfect relay aided BICM-ID for transmission over quasi-static Rayleigh fading channels both for the CRDED and for the RNSPA method. The system's schematic is portrayed in Figure 4.2 and the simulation parameters are summarised in Table 4.4.

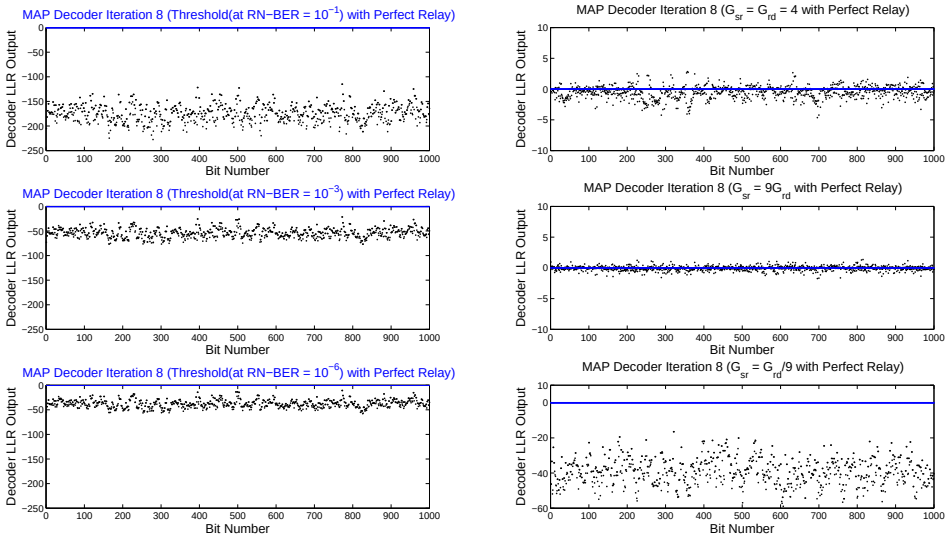


Figure 4.5: Soft outputs from the MAP decoder for a transmitted stream of all -1 in the **Perfect Relay** scenario both for the **CRDED** and for the **RNSPA** method.

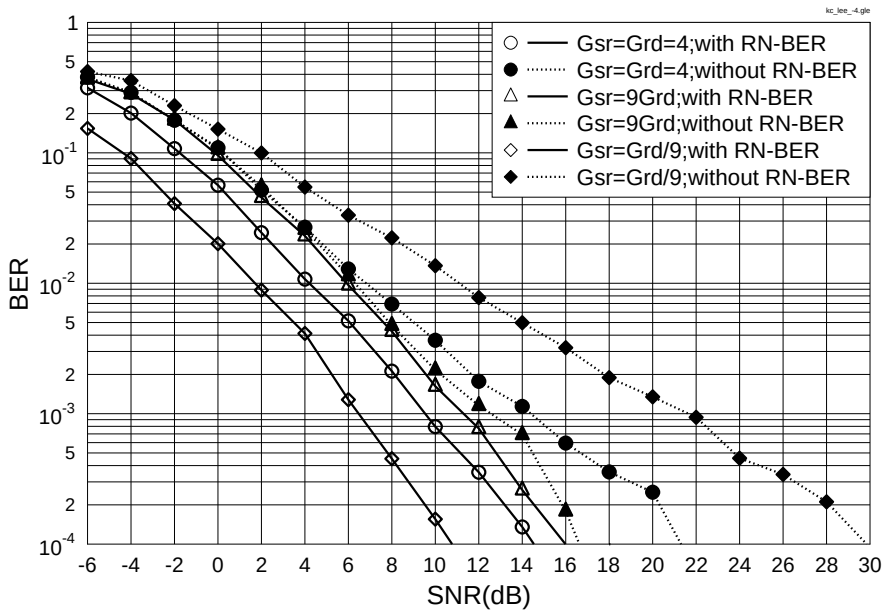


Figure 4.6: BER versus SNR performance for RN-BER aided BICM-ID for transmission over quasi-static Rayleigh channels for the CRDED method. It is worth noting that the differences in comparison to Figure 4.3 are 1) the RN-BER is used instead of employing perfect relaying, 2) only the CRDED method is used.

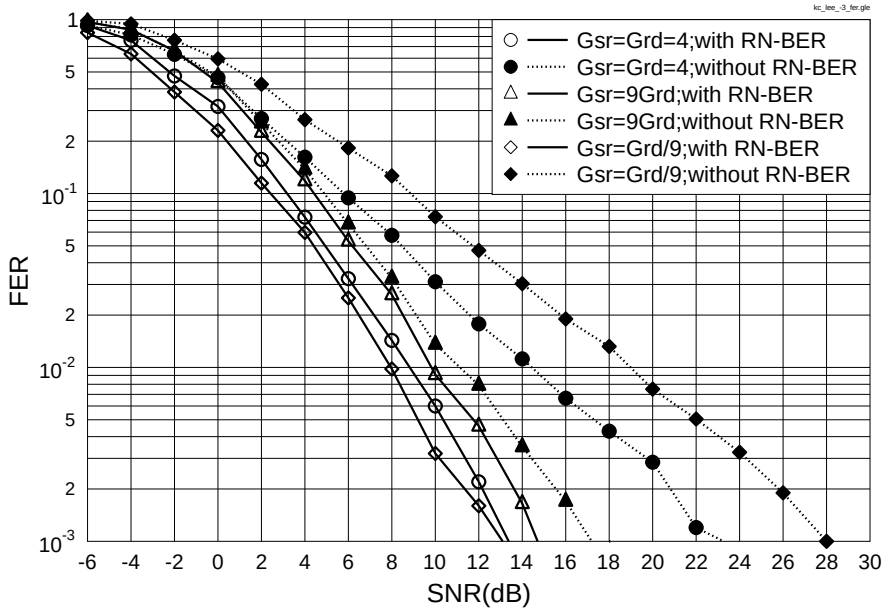


Figure 4.7: FER versus SNR performance for RN-BER aided BICM-ID for transmission over quasi-static Rayleigh fading channels for the CRDED method. It is worth noting that the differences in comparison to Figure 4.4 are 1) the RN-BER is used instead of employing perfect relaying, 2) only the CRDED method is used.

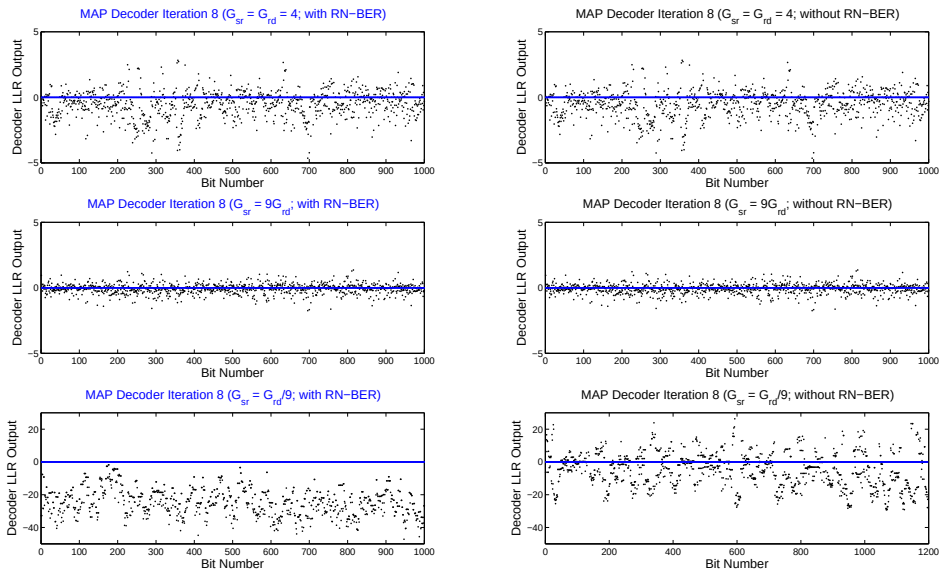


Figure 4.8: Soft outputs from the MAP decoder for a transmitted stream of all -1 for the **CRDED** method.

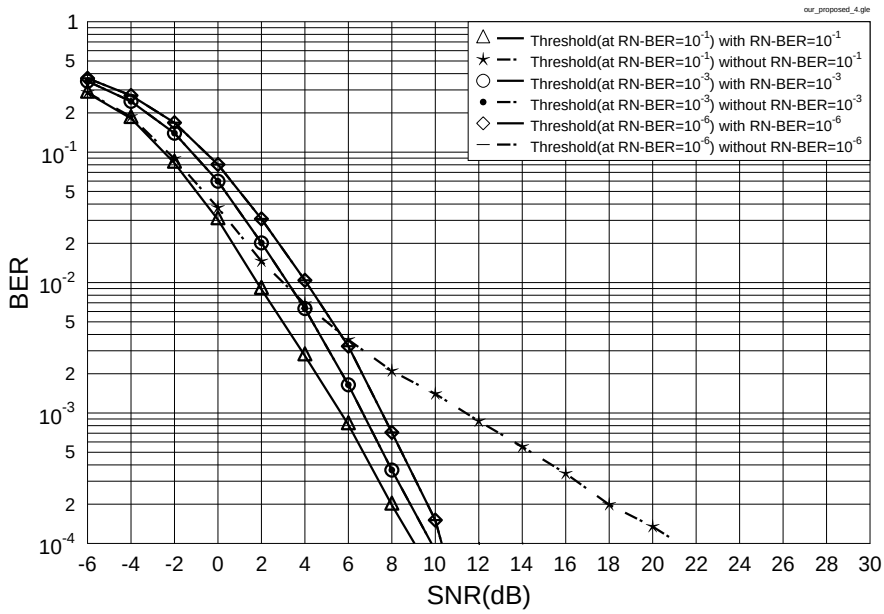


Figure 4.9: BER versus SNR performance for RN-BER aided BICM-ID for transmission over quasi-static Rayleigh fading channels both for the RNSPA method and for the proposed hybrid method. The system's schematic is portrayed in Figure 4.2 and the simulation parameters are summarised in Table 4.4. The RN-BER values of $10^{-1}$, $10^{-3}$ and $10^{-6}$ were exploited, respectively.

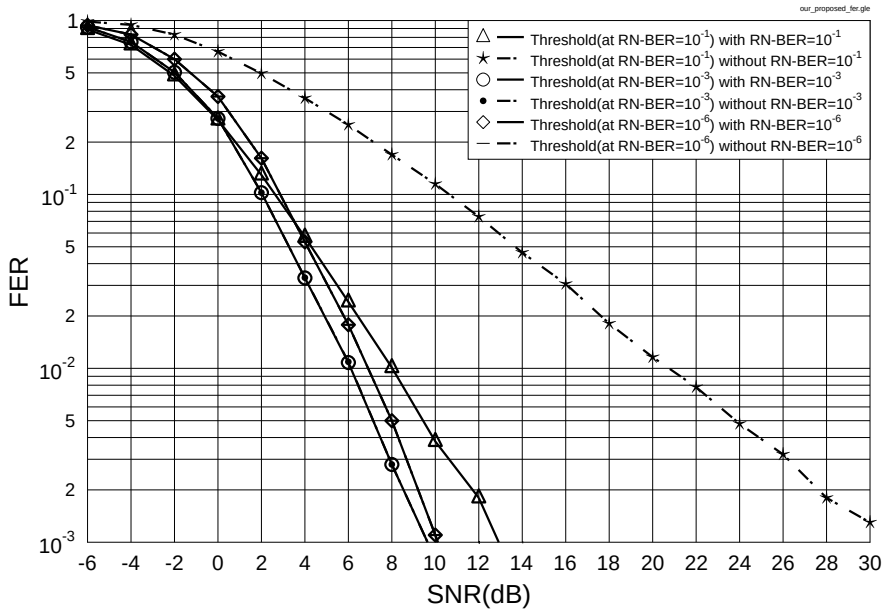


Figure 4.10: FER versus SNR performance for RN-BER aided BICM-ID for when communicating over quasi-static Rayleigh fading channels both for the RNSPA method and for the proposed hybrid method. The system's schematic is portrayed in Figure 4.2 and the simulation parameters are summarised in Table 4.4. The RN-BER values of $10^{-1}$, $10^{-3}$ and $10^{-6}$ were exploited, respectively.

| | | | | | | |
|---|---|---|---|---|---|---|
| Coded Modulation | BICM-ID | | | | | |
| Modulation | QPSK | | | | | |
| Code | R=$\frac{1}{2}$ Convolutional | | | | | |
| Code Memory length | 3 | | | | | |
| Number of iterations | 8 | | | | | |
| Decoder | Approximate Log-MAP [19] | | | | | |
| Symbols per frame | 1,200 | | | | | |
| Number of frames | 10,000 | | | | | |
| Channel | Quasi-static Rayleigh channel | | | | | |
| Pathloss | $G_{sr} = G_{rd}$ | | $G_{sr} = G_{rd}/9$ | | $G_{sr} = 9G_{rd}$ | |
| | $G_{sr} = 4$ (6.02dB) | $G_{rd} = 4$ (6.02dB) | $G_{sr} = 1.78$ (2.50dB) | $G_{rd} = 16$ (12.04dB) | $G_{sr} = 16$ (12.04dB) | $G_{rd} = 1.78$ (2.50dB) |
| Threshold | 0.89 dB | | 5.35 dB | | 8.09 dB | |
| Corresponding AWGN BER | RN-BER = $10^{-1}$ | | RN-BER = $10^{-3}$ | | RN-BER = $10^{-6}$ | |

Table 4.4: System parameters.

increases in the idealized perfect relaying scenario, the RNSPA method has a better performance than the CRDED since the latter is expected to have no benefits in the absence of errors. Hence the philosophy of our hybrid method is that we activate the RNSPA and CRDED modes of operation, depending on whether the SR channel's SNR exceeds a threshold value, above which the RNSPA technique is activated. This is because in the presence of a sufficiently high $SNR_{r,sr}$ the RN-BER becomes low and hence we no longer have to exploit this RN-BER knowledge. Table 4.4 shows the threshold value $\gamma_{r,sr\,\min}$ expressed in $dB$, which is used for selecting a RN at a desired location or using the appropriate transmit power at the RN. This threshold directly corresponds to a specific RN-BER under the assumption of a quasi-static Rayleigh fading channel, which corresponds to an AWGN channel having a fading-dependent SNR. More specifically, the optimum relay location or the transmit power required at the RN can be chosen based on the optimum $G$ (Section 4.2.1.2), which can be generated from the knowledge of the transmit power at the SN and that of the received power at the RN. The simulation results provided below will justify, why our proposed system is superior to both the CRDED and the RNSPA method. Let us now consider the performance of our proposed method in comparison to the RNSPA technique. Figure 4.9 shows the BER performance of employing our proposed method and the RNSPA method respectively. When using the threshold of RBER being $10^{-3}$ and $10^{-6}$, the performance does not change between our proposed method

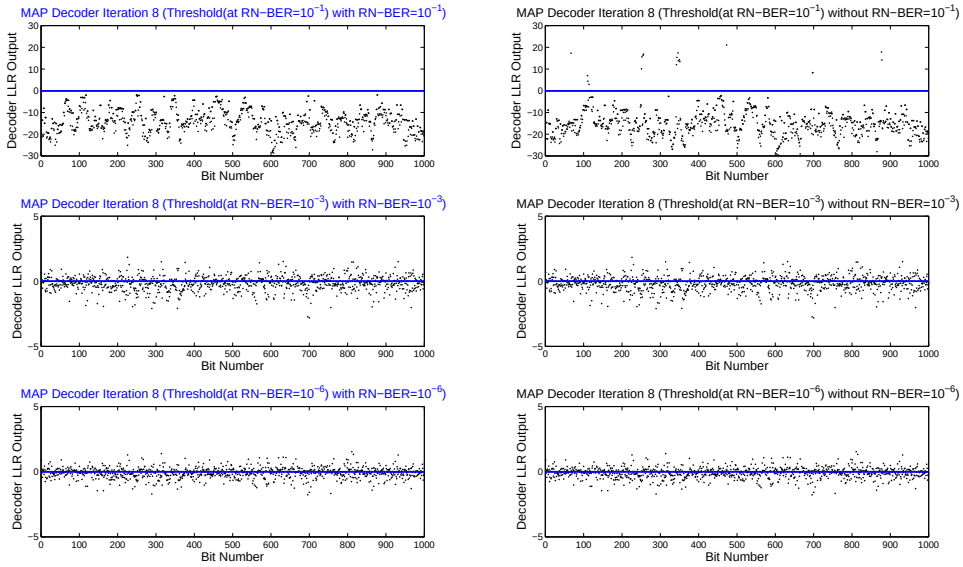


Figure 4.11: Soft outputs from the MAP decoder for a transmitted stream of all -1 for **our proposed** method.

and RNSPA method. While when the threshold of RBER being $10^{-1}$, there are 12 dB improvement with our proposed system. Figure 4.9 and Figure 4.10 illustrate the BER and FER performance of the proposed hybrid system, respectively. The comparison are shown by the simulation results. Observe in Figure 4.9 that regardless, whether the RN-BER-knowledge is exploited or not, the achievable performance remains similar when RN-BER $\leq 10^{-3}$. However, when the decoding error probability is high at the RN, the exploitation of the RN-BER becomes more crucial for the sake of limiting the RN-induced error propagation. For instance, as seen in Figure 4.9, our proposed method achieves an approximately 12 dB power reduction over the RNSPA method, when using a RN-BER threshold of $10^{-1}$ for activating the CRDED technique. More specifically, an SNR of almost 21 dB is required for achieving a target BER of $10^{-4}$ by the RNSPA, which becomes about 9 dB for our proposed technique, as indicated by the dotted-starred and by the continuous-triangle lines, respectively.

It is worth noting that the FER seen in Figure 4.10 is poor, when the RN-BER threshold used for activating the CRDED technique is set to $10^{-1}$. In contrast to Figure 4.4 and Figure 4.7, the FER performance of the CRDED scheme approaches that of the perfect relaying situation, while the FER performance remains inferior in comparison to that of our proposed scheme. Since the CRDED method implicitly relies on having a fixed RN location, which is associated with a time-invariant RN-BER, its performance is expected to degrade in the presence of high RN velocity or low RN-BER signalling rates. It can also be observed in Figure 4.10 that if the RN-BER is in excess of $10^{-1}$, then the FER also becomes too high to be effectively reduced by the proposed system.

## 4.3 Adaptive Coded Modulation in Cooperative Communications

The wireless communication systems of future generations are required to provide reliable transmissions at high data rates in order to offer a variety of multimedia services to both commercial and private customers. Cooperative diversity schemes were proposed for satisfying the requirements. Although diverse relaying protocols may be used between the source, relay and destination nodes, this section will employ Decode-and-Forward (DF) relaying. The DF system can adopt a strong channel code for mitigating the potential error propagation, when communicating over uncorrelated Rayleigh fading channels. However, it performers poorly for transmission over quasi-static fading channels owing to the lack of temporal diversity during a transmission frame. In order to counteract the time-varying nature of the mobile radio channels, near-instantaneous adaptive coded modulation (ACM) schemes have been proposed, where both a higher-rate code and/or a higher-order modulation mode may be employed, when the instantaneous estimated channel quality is high in order to increase the number of Bits Per Symbol (BPS) transmitted. Conversely, a more robust lower-rate code and/or a lower-order modulation mode are employed, when the instantaneous channel quality is low, in order to improve the mean BER performance.

### 4.3.1 System Design and Analysis

Based on our study of ACM designed for traditional point-to-point transmission in Chapter 2, ACM will be introduced in this section in the context of cooperative communications. The aim of the section is to find the optimum ACM scheme for cooperative communications over quasi-static Rayleigh fading channels. This section will detail both the design and performance analysis of ACM in the context of three cooperative communications schemes: single relay node (RN) aided ACM, twin RN aided ACM and single RN aided ACM additionally combined with the source-to-destination (SD) link at the DN.

#### 4.3.1.1 First-In-First-Out Buffer

In an ACM system, the attainable throughput of the SR and the RD links depends on the channel quality in the scenario of considering a SN-RN-DN based system. For instance, if the channel quality between the SN to the RN is high, a rate 3/4 CM-16QAM scheme may be adopted, whose block size is 400 symbols, when there are 1200 information bits in a frame. However, if the channel quality between the RN node and the DN is low, a rate 1/2 CM-4PSK scheme may be adopted, whose block size is 1200 symbols. In order to solve this problem, we introduce a first-in-first-out buffer at the RN. More explicitly, the decoded bits at the RN are written into the buffer and the RN will only re-encode and re-transmit a CM frame, when there is sufficient information bits in the buffer to form a CM frame according to the RD channel quality encountered.

#### 4.3.1.2 Single-Relay aided ACM in Cooperative Communications

Similarly to the non-cooperative regime of Section 2.3, we consider BbB ACM, where the channel fading is constant across a transmission frame, but varies from frame to frame by obeying an uncorrelated Rayleigh distribution. Accordingly, in a quasi-static fading channel, each transmission frame effectively experiences an AWGN channel having an SNR given by Equation (4.22) or Equation (4.24). By contrast, in the shadow plus fast Rayleigh fading channel, each transmission frame experiences an uncorrelated Rayleigh fading channel having an SNR given by Equation (4.29) or Equation (4.30).

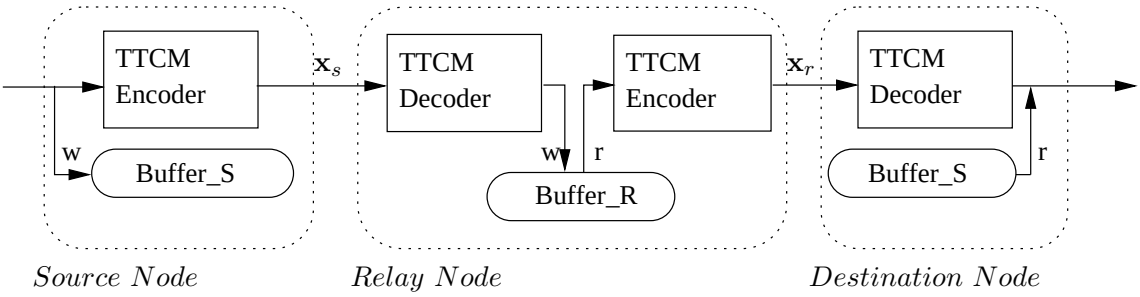


Figure 4.12: Schematic of each node with buffers in a two-hop relay-aided ACM system assuming the absence of the SD link, where w stands for writing into the buffer, while r represents reading the information from the buffer.

The schematic of the ACM system designed for cooperative communication and operating without relying on the low-quality SD link is presented in Figure 4.12. In order to minimise the potential error propagation and energy efficient, the adaptive mode-switching threshold of BER = $10^{-6}$ is employed by the SR link, while we aim for a target BER of $10^{-5}$ in the RD link.

When transmitting over quasi-static Rayleigh fading channels, the block-fading coefficient and the power of the AWGN jointly determine the received SNR for each transmission frame. From Equation (4.2), the average received SNR at the RN may be expressed as:

$$SNR_{r,sr} = \frac{E\{G_{sr}\}E\{|h_{sr}|^2\}E\{|x_{s,k}|^2\}}{N_0} = \frac{G_{sr}|h_{sr}|^2}{N_0}, \tag{4.19}$$

where $x_{s,k}$ is the $k$th symbol transmitted from the SN. For the sake of simplifying our analysis in line with [155], we define the 'equivalent SNR'[3] characterizing the SN to RN link as:

$$SNR_{t,sr} = \frac{E\{|x_{s,k}|^2\}}{N_0} = \frac{1}{N_0}, \tag{4.20}$$

where we have $E\{|x_{s,k}|^2\} = 1$. Hence, we arrive at:

$$SNR_{r,sr} = SNR_{t,sr}G_{sr}|h_{sr}|^2 \tag{4.21}$$

$$\gamma_{r,sr} = \gamma_{t,sr} + 10\log_{10}(G_{sr}|h_{sr}|^2) \ \text{[dB]}, \tag{4.22}$$

[3]We note that this definition does not represent a physically tangible or measurable quantity, since it relates the transmit power of the SN to the AWGN power encountered at the RN. Nonetheless, this convenient definition simplifies our discussions, which was proposed in [155].

where we have $\gamma_{r,sr} = 10\log_{10}(SNR_{r,sr})$ and $\gamma_{t,sr} = 10\log_{10}(SNR_{t,sr})$. Then, the performance of the CM scheme communicating over the AWGN channels is compared to $\gamma_{r,sr}$, in order to select the right CM mode, as detailed in Section 2.3.1.1. Similarly, we may arrive at:

$$SNR_{r,rd} = SNR_{t,rd} G_{rd} |h_{rd}|^2 \tag{4.23}$$

$$\gamma_{r,rd} = \gamma_{t,rd} + 10\log_{10}(G_{rd}|h_{rd}|^2) \ \text{[dB]}, \tag{4.24}$$

which is used for selecting the CM mode to be used between the RN and DN. Furthermore, the relationship between the $E_b/N_0$ value and the SNR may be expressed as:

$$E_b/N_0 = SNR - 10\log(R_o). \tag{4.25}$$

For the shadow-and-fast Rayleigh fading channel of Section 2.3.2.1, the buffers shown in Fig-


Figure 4.13: Brief schematic of transmission.

ure 4.12 are still employed. The schematic of a node to node transmission link is shown in Figure 4.13. More specifically, during the first transmission period, the $k$th received symbol $\mathbf{y}_{sr,k}$ may be expressed for transmission over the shadow-and-fast Rayleigh fading channel of Section 2.3.2.1 as:

$$\mathbf{y}_{sr,k} = \sqrt{G_{sr}} h_{sr} h_{f,sr,k} \mathbf{x}_{s,k} + n_{sr,k}, \tag{4.26}$$

where $h_{sr}$ and $h_{f,sr,k}$ represent the shadow-and-fast Rayleigh fading coefficients of the link between the SN and the RN, while $n_{sr,k}$ represents the AWGN having a variance of $N_0/2$ per dimension. It is assumed that the number of modulated symbols transmitted from the SN is the same as that from the RN. The $k$th symbol received during the second transmission period may, therefore, be formulated as:

$$\mathbf{y}_{rd,k} = \sqrt{G_{rd}} h_{rd} h_{f,rd,k} \mathbf{x}_{r,k} + n_{rd,k}, \tag{4.27}$$

where $n_{rd,k}$ is the noise, while $h_{rd}$ and $h_{f,rd,k}$ are the coefficients between the two nodes. Note that we have $E\{|h_{f,rd,k}|^2\} = 1$, because it is the fast Rayleigh fading channel coefficient. Hence, we have:

$$SNR_{r,sr} = \frac{E\{G_{sr}\}E\{|h_{sr}|^2\}E\{|h_{f,sr,k}|^2\}E\{|x_{s,k}|^2\}}{N_0} = \frac{G_{sr}|h_{sr}|^2}{N_0}. \tag{4.28}$$

Finally, we arrive at:

$$\gamma_{r,sr} = \gamma_{t,sr} + 10\log_{10}(G_{sr}|h_{sr}|^2) \ \text{[dB]}. \tag{4.29}$$

Similarly, $\gamma_{r,rd}$ may be expressed as:

$$\gamma_{r,rd} = \gamma_{t,rd} + 10\log_{10}(G_{rd}|h_{rd}|^2) \ \text{[dB]}. \tag{4.30}$$

Then, both $\gamma_{r,sr}$ and $\gamma_{r,rd}$ are used for selecting the appropriate CM schemes.

#### 4.3.1.3 Twin-Relays aided ACM in Cooperative Communications

Having studied the single RN aided ACM in communications system, the characteristics of a twin-RN aided ACM system will be investigated in this section. Figure 4.14 shows the structure of the twin-RN aided ACM. The SN transmits a frame of coded symbols $\mathbf{x}_s$ to the first RN ($RN_1$) during the first transmission period. Then $RN_1$ decodes the information and encoded it again. During the second transmission period, a frame of coded symbols $\mathbf{x}_{r_1}$ is transmitted from $RN_1$ to the second RN ($RN_2$), similarly to the operation of $RN_1$, $RN_2$ decodes the information and encode it again. Finally, during the third transmission period, a frame of coded symbols $\mathbf{x}_{r_2}$ transmitted from $RN_2$ to

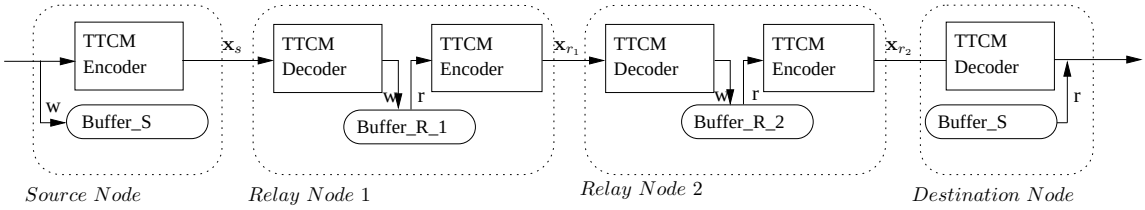


Figure 4.14: Schematic of each node relying on buffers. Here, w represents writing information into the butter meanwhile reading information from the buffer.

the DN is received. More specifically, during the first transmission period, the $k$th symbol received at the RN may be written as:

$$y_{sr_1,k} = \sqrt{G_{sr_1}} h_{sr_1,k} x_{s,k} + n_{sr_1,k}, \tag{4.31}$$

where $h_{sr_1,k}$ denotes the quasi-static Rayleigh fading coefficient of the link between the SN and the RN, while $n_{sr_1,k}$ represents the AWGN having a variance of $N_0/2$ per dimension. It is assumed that the number of symbols transmitted from the SN is the same as that from the RN. The $k$th symbol received during the second transmission period may, therefore, be formulated as:

$$y_{r_1r_2,k} = \sqrt{G_{r_1r_2}} h_{r_1r_2,k} x_{r_1r_2,k} + n_{r_1r_2,k}, \tag{4.32}$$

where $h_{r_1r_2,k}$ represents the quasi-static Rayleigh fading coefficient of the RN to DN link, while, $n_{r_1r_2,k}$ represents the AWGN having a variance of $N_0/2$ per dimension. The symbol received during the third period becomes:

$$y_{r_2d,k} = \sqrt{G_{r_2d}} h_{r_2d,k} x_{r,k} + n_{r_2d,k}, \tag{4.33}$$

where $h_{r_2d,k}$ represents the quasi-static Rayleigh fading coefficient of the RN to DN link, while, $n_{r_2d,k}$ represents the AWGN having a variance of $N_0/2$ per dimension. The RDRPLR of the source-to-relay-1 ($SR_1$) link related to the SD link can be expressed as [195], [65]:

$$G_{sr_1} = \left( \frac{d_{sd}}{d_{sr_1}} \right)^{\aleph}. \tag{4.34}$$

Here, the pathloss exponent equals to $\aleph = 2$, because a LOS pathloss model is assumed. Similarly, the RDRPLR of the relay-1-to-relay-2 ($R_1R_2$) link related to the SD link may be formulated as:

$$G_{r_1r_2} = \left(\frac{d_{sd}}{d_{r_1r_2}}\right)^2, \tag{4.35}$$

while the RDRPLR of the relay-2-to-destination ($R_2D$) link related to the SD link may be expressed as:

$$G_{r_2d} = \left(\frac{d_{sd}}{d_{r_2d}}\right)^2, \tag{4.36}$$

Naturally, the RDRPLR of the SD link related to itself is unity, yielding, $G_{sd} = 1$, where $d_{sr}$ represents the distance between the SN and RN, while $d_{rd}$ is that of the RD link and $d_{sd}$ is that of the SD link. Moreover, for the sake of simplicity we assumed without loss of generality that the SN, the RN and the DN are positioned along a straight line. Therefore, we have:

$$d_{sd} = d_{sr_1} + d_{r_1r_2} + d_{r_2d}. \tag{4.37}$$

For example, when the RNs' location are $d_{sr_1} = d_{r_1r_2} = d_{r_2d} = \frac{1}{3}d_{sd}$, based on Equations (4.34)−(4.36), we obtain a power-reduction factor of: $G_{sr_1} = G_{r_1r_2} = G_{r_2d} = 9$, which is achieved at the cost of a throughput reduction of $\frac{1}{3}$, as augmented earlier in Section 2.3.1.2.

#### 4.3.1.4 Single-Relay aided ACM Additionally Exploiting the SD Link in Cooperative Communications

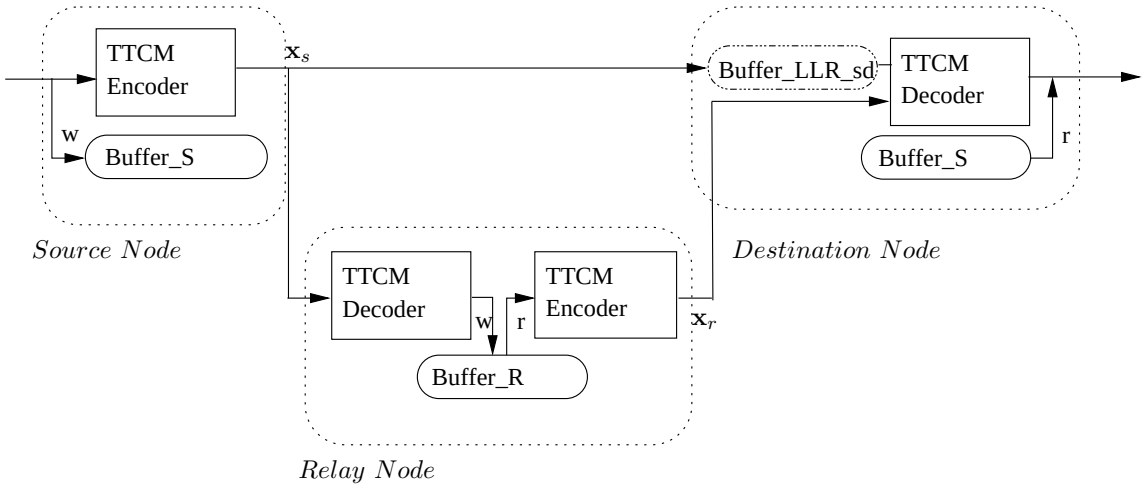


Figure 4.15: The schematic of the ACM aided SD link.

In this section, we additionally exploit the presence of the SD link in our single-RN aided ACM system. Figure 4.15 shows the schematic of our ACM aided system relying on the SD link. The difference between the scenarios operating with and without the SD link manifests itself during the first transmission period, when $\mathbf{x_r}$ transmits to both the RN and the DN. More specifically, the

information received at the DN is written into the LLR buffer first. Once the DN obtained the information from the RN, the DN decodes the information of the RN and SN jointly. It is worth noting that the throughput of the single-RN aided cooperative system recorded both with the aid of the SD link and without the SD link is $\frac{1}{2}$, as argued in Section 2.3.1.2.

### 4.3.2 Simulation Results

Having introduced our ACM-aided cooperative communications scheme, our numerical performance results will be presented in this section, which may be viewed as an extended version of the ACM performance results of Section 2.3.2. Firstly, the performance of our ACM aided cooperative system using a single RN and operating without the SD link will be characterized for transmission over both quasi-static Rayleigh fading channels and over shadow-and-fast Rayleigh fading channels. Then the performance of the ACM scheme employing two RNs and communicating over quasi-static Rayleigh fading channels will be illustrated. Finally, the ACM system invoking a single relay combined with the SD link will be characterized, when communicating over quasi-static Rayleigh fading channels. The corresponding simulation parameters are listed in Table 4.5.

| | | | | | | |
|---|---|---|---|---|---|---|
| Coded Modulation | TTCM, BICM-ID | | | | | |
| Modulation Scheme | 4PSK, 8PSK, 16QAM, 64QAM | | | | | |
| Mapper type | Gray Mapping, Set-Partitioned | | | | | |
| Number of iterations | 4,8 | | | | | |
| Code Rate | 1/2, 2/3, 3/4, 5/6 | | | | | |
| Code Memory | 3 | | | | | |
| Decoder type | Approximate Log-MAP | | | | | |
| Symbols per frame | 12,000 | | | | | |
| Number of frames | 10,000 | | | | | |
| Channel | Quasi-static Rayleigh fading channel, shadow-and-fast Rayleigh fading channel | | | | | |
| RDRP | $G_{sr} = G_{rd}$ | | $G_{sr} = G_{rd}/9$ | | $G_{sr} = 9G_{rd}$ | |
| | $G_{sr} = 4.00$ (6.02dB) | $G_{rd} = 4.00$ (6.02dB) | $G_{sr} = 1.78$ (2.50dB) | $G_{rd} = 16.00$ (12.04dB) | $G_{sr} = 16.00$ (12.04dB) | $G_{rd} = 1.78$ (2.50dB) |

Table 4.5: Simulation parameters.

Figure 4.16 illustrates the performance of ACM invoked for cooperative communications with the aid of a single RN employing the ACM mode-switching SNR thresholds of Table 2.5. More specifically, the mode selection probability of encountering the 4PSK, 8PSK, 16QAM and 64QAM modes when transmitting over quasi-static Rayleigh fading channels is presented in Figure 4.16a. It can been seen that when the SNR is low, the TTCM-NoTx mode is employed most frequently, while the TTCM-64QAM is selected more frequently, when the SNR increases. The related BER and BPS vs SNR performance is shown in Figure 4.16b. All the BERs are lower than the target BER of $10^{-5}$.

When using the switching thresholds of Table 2.7, the ACM performance recorded for a single RN operating without the SD link in our cooperative communications scenario, when transmitting

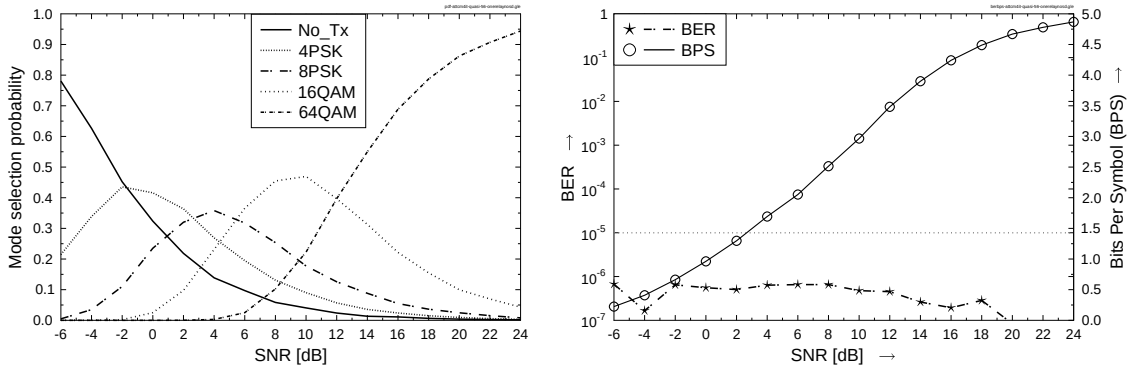


(a) Mode selection probability

(b) BER and BPS versus SNR

Figure 4.16: ACM performance relying on the 4PSK, 8PSK, 16QAM and 64QAM **TTCM** modes, when transmitting over **quasi-static Rayleigh fading channels** using a block size of 12 000 symbols, and $I_t = 4$ iterations. The simulation parameters are listed in Table 4.5 and the system's structure is presented in **Figure 4.12**. The switching levels were optimized and set according to Table 2.5. The RN is half-way between the SN and the DN.

over shadow-and-fast Rayleigh fading channels are presented in Figure 4.17. Figure 4.17a shows the modulation mode probability results, when the system of Figure 4.12 is communicating over shadow-and-fast Rayleigh fading channels.

Figure 4.18 shows the performance of ACM, when employing two serial RNs in our cooperative communications system communicating over quasi-static Rayleigh fading channels. We can observe in Figure 4.18a that when the SNR increases, the next higher order modulation mode becomes the dominant modulation scheme and eventually the highest order of 64-QAM mode of the five-mode ACM scheme prevails. The related BER and BPS versus SNR performance is presented in Figure 4.18b, when communicating over a quasi-static Rayleigh fading channel. The BPS throughput asymptotically trends to a constant value upon increasing the SNR owing to the limitation imposed by the highest-order constituent QAM mode.

Figure 4.19 characterizes the performance of the ACM for a single RN additionally relying on the SD link aided cooperative system, as shown in Figure 4.15. More specifically, Figure 4.19a illustrates the mode selection probability. As usual, the high-order modulation modes are selected more often upon increasing the SNR. Figure 4.19b depicts the associated BER and BPS versus SNR performance, when communicating over quasi-static Rayleigh fading channels. Compared to Figure 4.16b, the BER performance seen in Figure 4.19a is better, which is a benefit of the diversity gain attained due to the additional employment of the SD link.

Furthermore, Figure 4.20, Figure 4.22, Figure 4.21 and Figure 4.23 compare the performance of our RN aided ACM system operating both with and without the SD link, when the RN locating is not in the middle of the link, while communicating over quasi-static Rayleigh fading channels. More specifically, Figure 4.20 illustrates the ACM performance for the cooperative system operat-

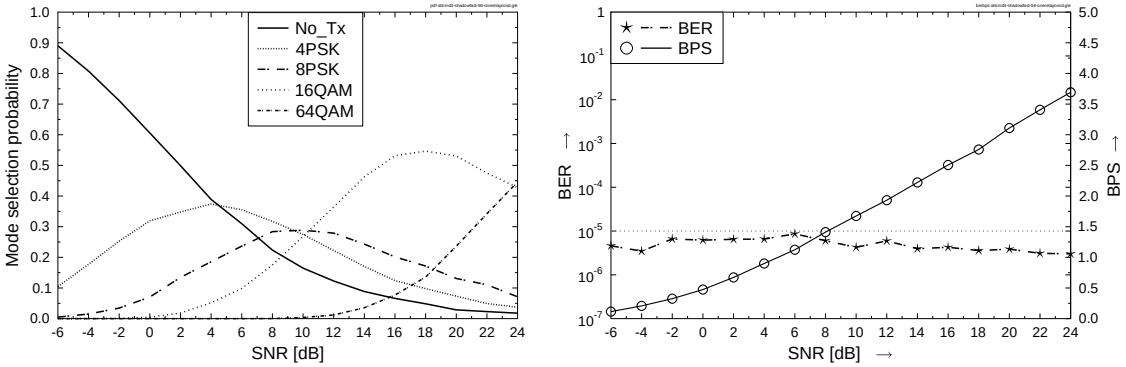


(a) Mode selection probability (b) BER and BPS versus SNR

Figure 4.17: ACM performance of the TTCM-4PSK, TTCM-8PSK, TTCM-16QAM and BICM-ID-64QAM modes, when transmitting over **shadow-and-fast Rayleigh fading channels** using a block size of 12 000 symbols, and $I_t = 4$ iterations. The simulation parameters are listed in Table 4.5 and the system's structure is presented in **Figure 4.12**. The switching levels were optimized and set according to Table 2.7. The RN is half-way between the SN and the DN.

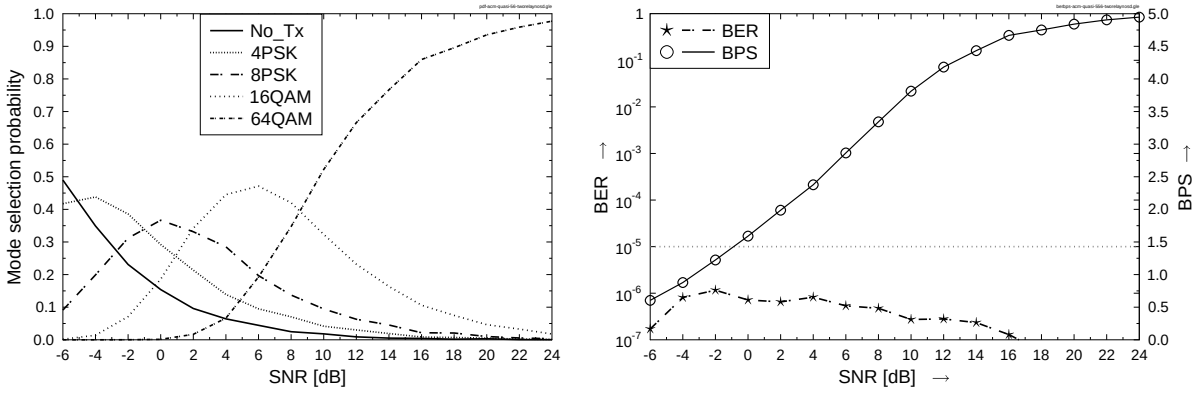


(a) Mode selection probability (b) BER and BPS versus SNR

Figure 4.18: ACM performance relying on the 4PSK, 8PSK, 16QAM and 64QAM **TTCM** modes, when transmitting over **quasi-static Rayleigh fading channels** using a block size of 12 000 symbols, and $I_t = 4$ iterations. The simulation parameters are listed in Table 4.5 and the system structure is presented in **Figure 4.14**. The switching levels were optimized and set according to Table 2.5. The RNs' location is fixed as: $d_{sr_1} = d_{r_1r_2} = d_{r_2d} = \frac{1}{3}d_{sd}$.

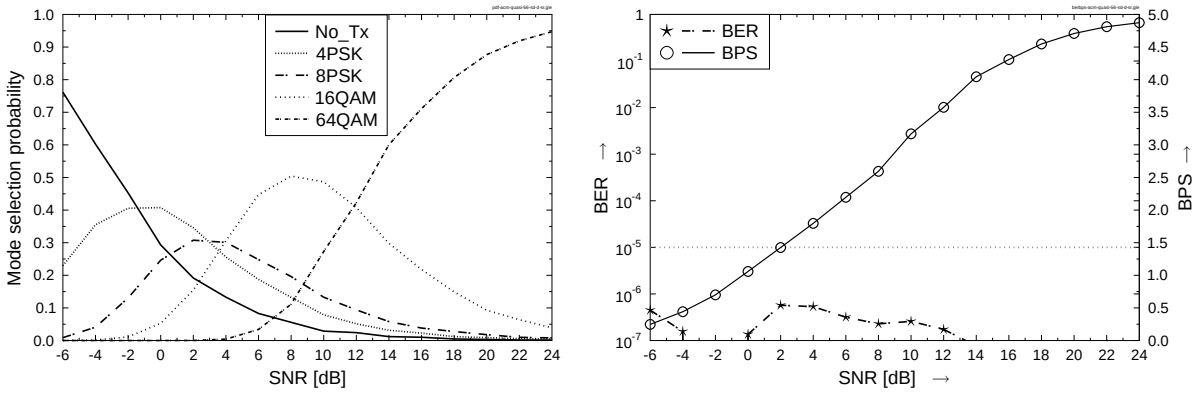


(a) Mode selection probability

(b) BER and BPS versus SNR

Figure 4.19: ACM performance relying on the 4PSK, 8PSK, 16QAM and 64QAM **TTCM** modes, when transmitting over **quasi-static Rayleigh fading channels** using a block size of 12 000 symbols, and $I_t = 4$ iterations. The simulation parameters are listed in Table 4.5 and the system structure is presented in **Figure 4.15**. The switching levels were optimized and set according to Table 2.5. The RN is half-way between the SN and the DN.

ing without the assistance of the SD link, when communicating over quasi-static Rayleigh fading channels, where the RN is near the SN. By contrast, Figure 4.21 presents the related performance for the cooperative system operating with the aid of the SD link. We could observe that the mode selection probability of the BPS throughput seen in Figure 4.20 and Figure 4.21 does not explicitly reflect an improved throughput, but nonetheless, the BER performance of the system operating with the aid of the SD link is better than that of the system operating without the SD link. The BER performance seen in Figure 4.22 is also worse than that seen in Figure 4.23.

## 4.4 Adaptive TTCM Aided Distributed STTC for Cooperative Communications

The wireless communication systems of future generations are required to provide reliable transmissions at high data rates in order to offer a variety of multimedia services. Space time coding schemes such as Space-Time Trellis Coding (STTC) [196] employ multiple transmitters and receivers. They are among the most efficient techniques designed for providing a high diversity gain, especially for slowly-fading quasi-static Rayleigh fading channels, where the channel's envelope remains near-constant within a transmission frame albeit varies from frame to frame. Hence, all symbols of a transmission frame tend to fade together. However, when using multiple antennas at the mobile unit it is difficult to eliminate the correlation of the signals due to its limited size. In order to circumvent this problem, cooperative diversity schemes were proposed in [145, 147, 197, 198]. More specifically, each mobile unit collaborates with a few partners for the sake of reliably transmitting its own information and that of its partners jointly, which emulates a virtual Multiple-Input

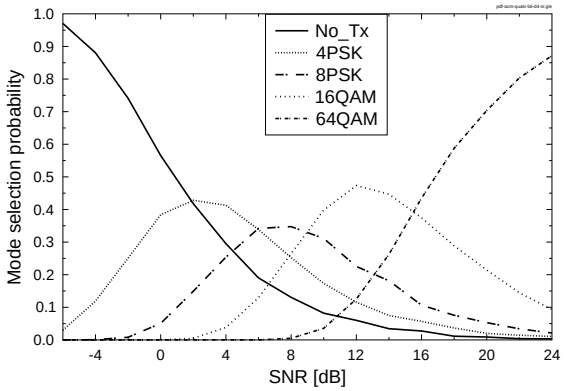


(a) Mode selection probability

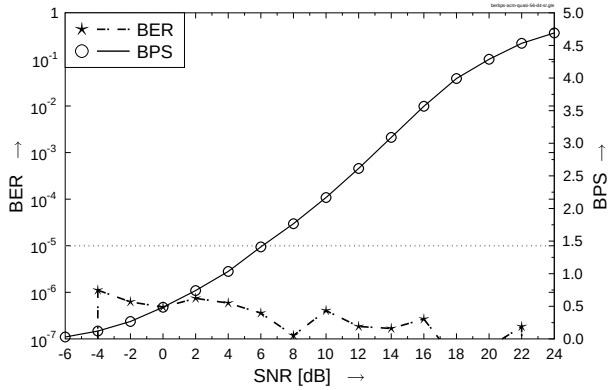


(b) BER and BPS versus SNR

Figure 4.20: ACM performance relying on the 4PSK, 8PSK, 16QAM and 64QAM **TTCM** modes, when transmitting over **quasi-static Rayleigh fading channels** using a block size of 12 000 symbols, and $I_t = 4$ iterations. The simulation parameters are listed in Table 4.5 and the system's structure is presented in **Figure 4.12**. The switching levels were optimized and set according to Table 2.5. $G_{sr} = G_{rd}/9$.

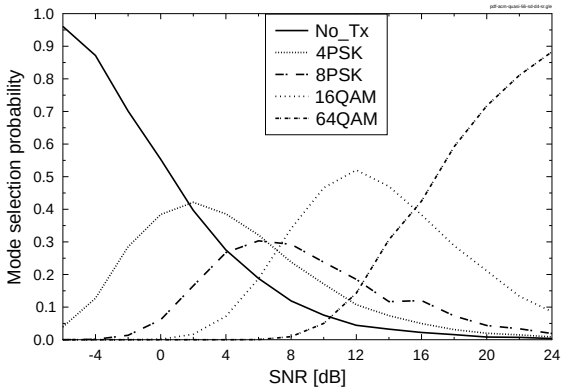


(a) Mode selection probability

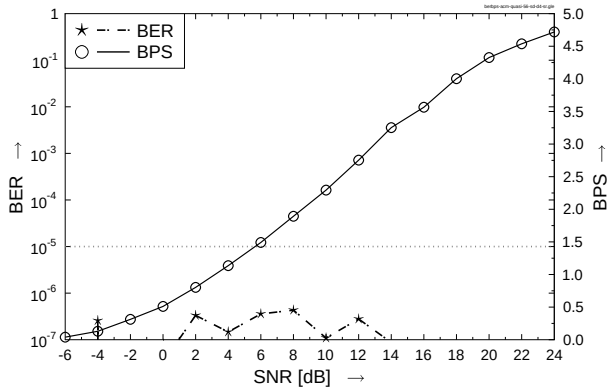


(b) BER and BPS versus SNR

Figure 4.21: ACM performance based on the 4PSK, 8PSK, 16QAM and 64QAM **TTCM** modes, when transmitting over **quasi-static Rayleigh fading channels** using a block size of 12 000 symbols, and $I_t = 4$ iterations. The simulation parameters are listed in Table 4.5 and the system's structure is presented in **Figure 4.15**. The switching levels were optimized and set according to Table 2.5. $G_{sr} = G_{rd}/9$.

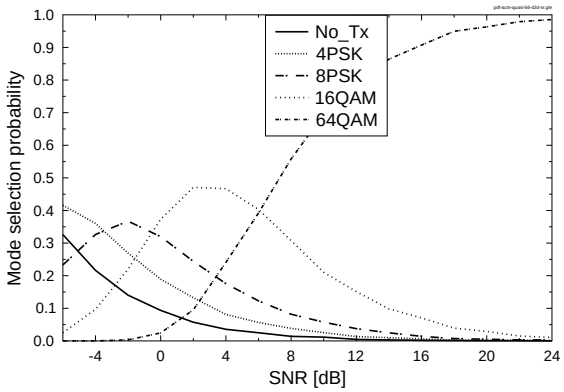


(a) Mode selection probability

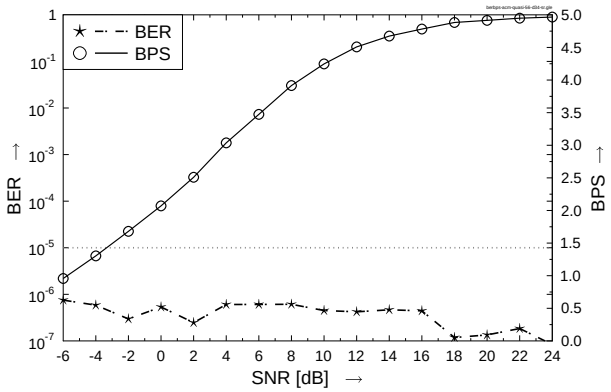


(b) BER and BPS versus SNR

Figure 4.22: ACM performance relying on the 4PSK, 8PSK, 16QAM and 64QAM **TTCM** modes, when transmitting over **quasi-static Rayleigh fading channels** using a block size of 12 000 symbols, and $I_t = 4$ iterations. The simulation parameters are listed in Table 4.5 and the system's structure is presented in **Figure 4.12**. The switching levels were optimized and set according to Table 2.5. $G_{sr} = 9G_{rd}$.

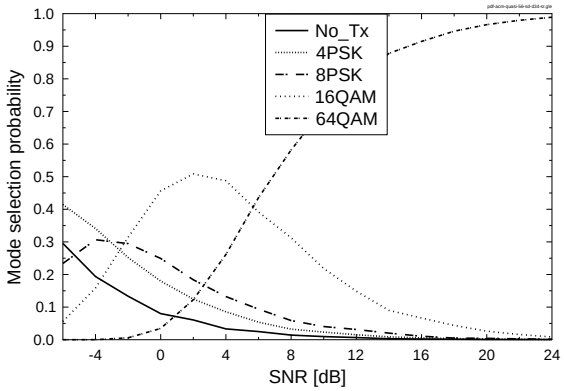


(a) Mode selection probability

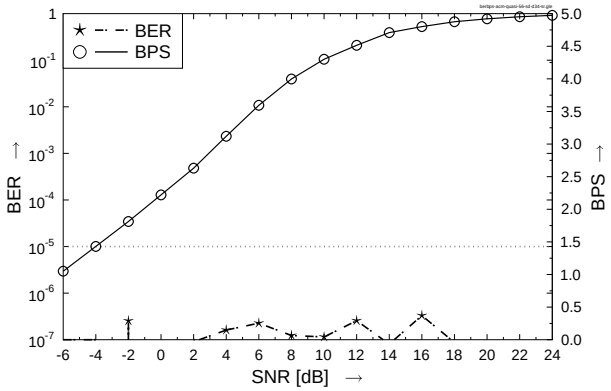


(b) BER and BPS versus SNR

Figure 4.23: ACM performance relying on the 4PSK, 8PSK, 16QAM and 64QAM **TTCM** modes, when transmitting over **quasi-static Rayleigh fading channels** using a block size of 12 000 symbols, and $I_t = 4$ iterations. The simulation parameters are listed in Table 4.5 and the system's structure is presented in **Figure 4.15**. The switching levels were optimized and set according to Table 2.5. $G_{sr} = 9G_{rd}$.

Multiple-Output (MIMO) scheme. The two most popular collaborative protocols used between the source, relay and destination nodes are the Decode-And-Forward (DF) as well as the Amplify-And-Forward (AF) schemes.

Although a strong channel code can be used for mitigating the potential error propagation in the DF scheme when communicating over uncorrelated Rayleigh fading channels, its performance becomes limited when communicating over quasi-static Rayleigh fading channels, due to the lack of temporal diversity within a transmission frame. In order to counteract the time-varying nature of the mobile radio channels, near-instantaneous adaptive coded modulation schemes [199–201] have been proposed, where a higher-rate code and/or a higher-order modulation mode are employed, when the instantaneous estimated channel quality is high in order to increase the number of Bits Per Symbol (BPS) transmitted. Conversely, a more robust lower-rate code and/or a lower-order modulation mode are employed, when the instantaneous channel quality is low, in order to improve the mean Bit Error Ratio (BER) performance.

When communicating over quasi-static Rayleigh fading channels, each transmission frame effectively experiences an Additive White Gaussian Noise (AWGN) channel with a received SNR determined by the constant fading coefficient and the noise power. Turbo Trellis Coded Modulation (TTCM) [52], which employs two identical parallel-concatenated Trellis Coded Modulation (TCM) [10] schemes as component codes, is one of the most powerful channel coding scheme designed for communicating over AWGN channels. In this contribution, we will employ Adaptive TTCM (ATTCM) for protecting the source-to-relay links, where the effective throughput range is given by $\eta = \{0, 1, 2, 3, 5\}$ BPS. A virtual MIMO system in the form of a Distributed STTC (DSTTC) scheme will be created by the cooperating relay nodes in order to circumvent the quasi-static nature of Rayleigh fading channels between the relay nodes and the destination node. In our study, both the source node and the relay nodes are equipped with a single transmit antenna, while the destination node, which could be a base-station, is equipped with two received antennas.

This section proposed an effective solution for mitigating the lack of temporal diversity, when communicating over quasi-static Rayleigh fading channels. On one hand, the ATTCM scheme effectively realised the full-potential of various TTCM schemes, when communicating over the source-to-relay links, where error propagation imposed by the DF-aided relay nodes is minimised. On the other hand, the DSTTC scheme offers spatial diversity to the relay-to-destination links for assisting the STTC-TTCM decoder at the destination node to minimise the probability of decoding errors.

The section is organised as follows. Our system model is described in Section 4.4.1, while our system design is outlined in Section 4.4.2. Our results are discussed in Section 4.4.3.

### 4.4.1 System Model

The schematic of a two-hop relay-aided system is shown in Figure 4.24, where the source node ($s$) transmits a frame of coded symbols $\mathbf{x}_s$ to $N$ number of relay nodes ($r$) during the first transmission

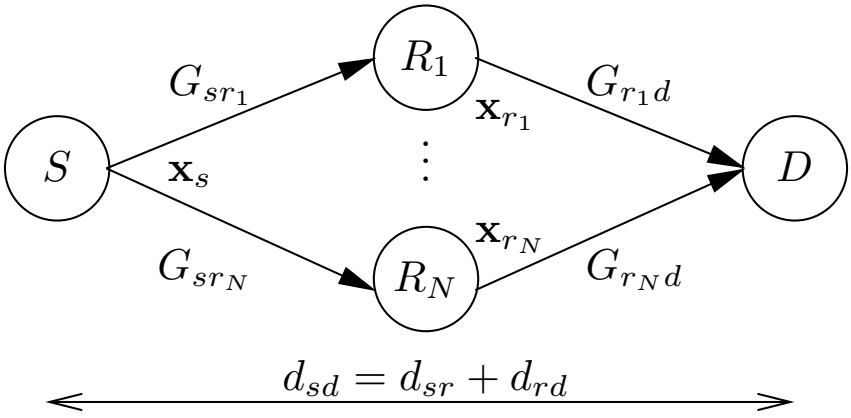


Figure 4.24: Schematic of a two-hop relay-aided system, where $d_{ab}$ is the geographical distance between node $a$ and node $b$.

period. Each relay node first decodes and re-encodes the information. Then all the $N$ cooperating relay nodes will collectively form a virtual MIMO frame of coded symbols $\mathbf{X}_r = [\mathbf{x}_1, \mathbf{x}_2, \ldots, \mathbf{x}_N]^T$ for transmission to the destination node during the second transmission period. The communication links seen in Figure 4.24 are subject to both free-space propagation path loss as well as to quasi-static Rayleigh fading. We consider $N = 2$ relay nodes in this paper. Each source and relay node is equipped with a single antenna, while the destination node is considered to be a base-station assisted by $M = 2$ receive antennas.

Let $d_{ab}$ denote the geometrical distance between nodes $a$ and $b$. The path loss between these nodes can be modelled by [195]:

$$P(ab) = K/d_{ab}^{\alpha}\,, \tag{4.38}$$

where $K$ is a constant that depends on the environment and $\alpha$ is the path-loss exponent. For a free-space path loss model we have $\alpha = 2$. The relationship between the energy $E_{sr_i}$ received at the $i$th relay node and that of the destination node $E_{sd}$ can be expressed as:

$$E_{sr_i} = \frac{P(sr_i)}{P(sd)} E_{sd} = G_{sr_i} E_{sd}\,, \tag{4.39}$$

where $G_{sr_i}$ is the geometrical-gain [195] experienced by the link between the source node and the $i$th relay node with respect to the source-to-destination link as a benefit of its reduced distance and path loss, which can be computed as:

$$G_{sr_i} = \left(\frac{d_{sd}}{d_{sr_i}}\right)^2 . \tag{4.40}$$

Similarly, the geometrical-gain of the $i$th relay-to-destination link with respect to the source-to-destination link can be formulated as:

$$G_{r_i d} = \left(\frac{d_{sd}}{d_{r_i d}}\right)^2 . \tag{4.41}$$

Naturally, the geometrical-gain of the source-to-destination link with respect to itself is unity, i.e. we have $G_{sd} = 1$.

The $k$th received signal at the $i$th relay node during the first transmission period, where $N_s$ symbols are transmitted from the source node, can be written as:

$$y_{sr_i,k} = \sqrt{G_{sr_i}}\, h_{sr_i}\, x_{s,k} + n_{r_i,k}\,, \tag{4.42}$$

where $k \in \{1,\ldots,N_s\}$, $i \in \{1,\ldots,N\}$ and $h_{sr_i}$ is the quasi-static Rayleigh fading coefficient between the source node and the $i$th relay node, while $n_{r_i,k}$ is the AWGN having a variance of $N_0/2$ per dimension. The $j$th symbol received at the destination node during the second transmission period, where $N_r$ symbols are transmitted from each relay node, is given by:

$$y_{rd,j} = \sum_{i=1}^{N} \sqrt{G_{r_id}}\, h_{r_id}\, x_{r_i,j} + n_{d,j}\,, \tag{4.43}$$

where $j \in \{1,\ldots,N_r\}$ and $h_{r_id}$ denotes the quasi-static Rayleigh fading coefficient between the $i$th relay node and the destination node, while $n_{d,j}$ is the AWGN having a variance of $N_0/2$ per dimension. Note that the power transmitted by each relay node is normalised to ensure that $\sum_{i=1}^{N} |x_{r_i,j}|^2 = 1$.

If $x_{a,j}$ is the $j$th symbol transmitted from node $a$ equipped with a single transmit antenna, the average received Signal to Noise power Ratio (SNR) experienced at each receive antenna at node $b$ is given by:

$$\mathrm{SNR}_r = \frac{\mathrm{E}\{G_{ab}\}\mathrm{E}\{|h_{ab}|^2\}\mathrm{E}\{|x_{a,j}|^2\}}{N_0} = \frac{G_{ab}}{N_0}\,, \tag{4.44}$$

where $\mathrm{E}\{|h_{ab}|^2\} = 1$ and $\mathrm{E}\{|x_{a,j}|^2\} = 1$. For the ease of analysis, we define the ratio of the power transmitted from node $a$ to the noise power encountered at the receiver of node $b$ as:

$$\mathrm{SNR}_t = \frac{\mathrm{E}\{|x_{a,j}|^2\}}{N_0} = \frac{1}{N_0}\,. \tag{4.45}$$

Hence, we have:

$$\begin{aligned} \mathrm{SNR}_r &= \mathrm{SNR}_t\, G_{ab}\,, \\ \gamma_r &= \gamma_t + 10\log_{10}(G_{ab})\ [\mathrm{dB}]\,, \end{aligned} \tag{4.46}$$

where $\gamma_r = 10\log_{10}(\mathrm{SNR}_r)$ and $\gamma_t = 10\log_{10}(\mathrm{SNR}_t)$. Therefore, we can achieve the desired $\mathrm{SNR}_r$ either by changing the transmit power or by selecting a relay node at a different geographical location.

### 4.4.2 System Design

If each relay node is equipped with a single antenna, a non-adaptive scheme would require a high transmit power in order to maintain a low number of decoding errors at the relay node, even when a powerful channel encoder is utilised for communicating over quasi-static Rayleigh fading channels. This is due to the lack of temporal diversity within a transmission frame. Hence, if the destination node is equipped with two antennas, a non-cooperative coded scheme may potentially outperform

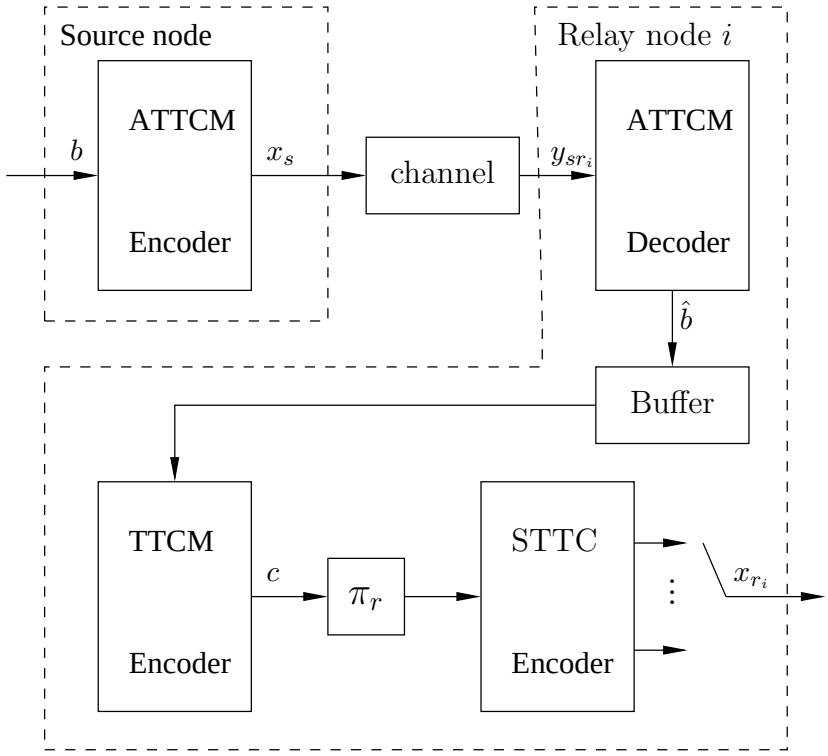


Figure 4.25: The schematic of the proposed ATTCM-DSTTC system.

the DF-aided cooperative coded schemes assisted by single-antenna relay nodes due to the high error inflicted by each relay node, when communicating over quasi-static Rayleigh fading channels. Furthermore, unless a separate power-control loop is provided for the source-to-relay links, the associated BER would be high. Finally, the co-channel interference also exhibits a substantial fluctuation. Due to these reasons, we proposed a near-instantaneous adaptive coded modulation scheme for protecting the source-to-relay links.

In our ATTCM-DSTTC scheme, we consider the following five TTCM modes:

1. No transmission (NoTx): 0 BPS,
2. TTCM-4PSK: 1 BPS,
3. TTCM-8PSK: 2 BPS,
4. TTCM-16QAM: 3 BPS,
5. TTCM-64QAM: 5 BPS,

where all TTCM schemes employ memory-three TCM component codes [116]. We consider $N = 2$ relay nodes in the system. The signal received at each relay node is decoded according to the TTCM mode used and the decoded bits are stored in a buffer, as shown in Figure 4.25. Then, a fixed-mode TTCM scheme, namely TTCM-4PSK, is used at each relay node in order to re-encode the decoded bits stored in the buffer. The re-encoded TTCM symbols are then symbol-interleaved

using $\pi_r$ and passed to an STTC encoder. Since each relay node has a single antenna, the first relay node will act as the first antenna of a two-antenna STTC scheme, while the second relay node will act as the the corresponding second antenna. Our destination node is a base-station equipped with $M = 2$ receive antennas. Hence, a virtual $(2 \times 2)$-element MIMO system is created between the relay and destination nodes. Finally, iterative decoding between the STTC and TTCM

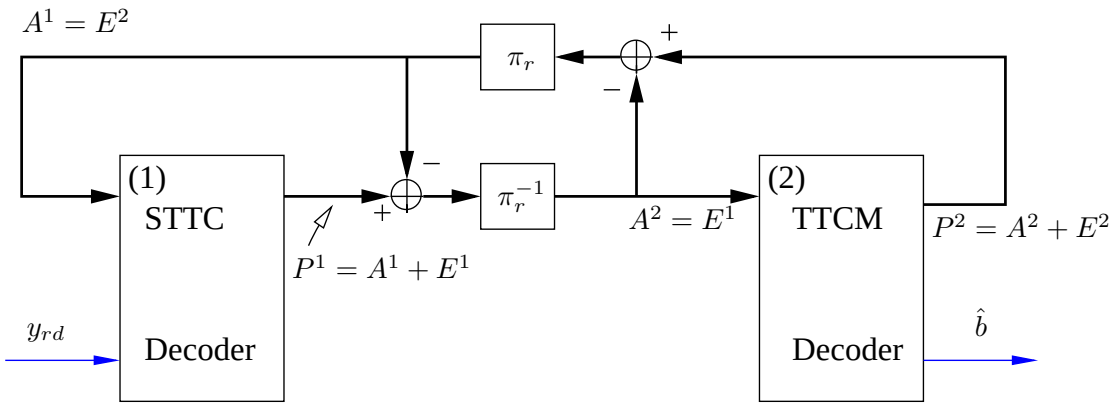


Figure 4.26: The schematic of the STTC-TTCM decoder.

decoders is carried out at the destination node. The schematic of the STTC-TTCM decoder is shown in Figure 4.26, where *extrinsic* information is passed between the two decoders in the form of probability vectors. More specifically, each of the two constituent decoders is labelled with a round-bracketed index. The notations $P$, $E$ and $A$ denote the *a posteriori*, *extrinsic* and *a priori* symbol probabilities, respectively. The probabilities associated with one of the two constituent decoders are differentiated by the superscripts of 1 and 2. The notations $\pi_r$ and $\pi_r^{-1}$ denote the symbol-based interleaver and deinterleaver, respectively.

The ATTCM switching thresholds $\Gamma = [\gamma_0, \gamma_1, \gamma_2, \gamma_3]$ are determined based on the performance of each of the four TTCM modes in the AWGN channel shown in Figure 4.27, where we have $\text{SNR}_r = \text{SNR}_t$ when $G_{sr_i} = 1$. Specifically, the ATTCM mode switching operation is based on the following algorithm:

$$\text{Mode} = \begin{cases} \text{NoTx}, & \text{if } \gamma_r \leq \gamma_0 \\ \text{TTCM-4PSK}, & \text{if } \gamma_0 < \gamma_r \leq \gamma_1 \\ \text{TTCM-8PSK}, & \text{if } \gamma_1 < \gamma_r \leq \gamma_2 \\ \text{TTCM-16QAM}, & \text{if } \gamma_2 < \gamma_r \leq \gamma_3 \\ \text{TTCM-64QAM}, & \text{if } \gamma_3 < \gamma_r \,, \end{cases} \tag{4.47}$$

where $\gamma_r = \sqrt{G_{sr_i}}\,|h_{sr_i}|^2 \;/\; N_0$ is the instantaneous received SNR at a given relay node. In order to minimise the potential error propagation imposed by the relay nodes, we chose the switching thresholds to ensure that the BER at the relay node is lower than $10^{-6}$, which is given by $\Gamma = [1.5, 8.0, 12.0, 18.5]$ dB. Since we have $N = 2$ source-to-relay links, the ATTCM mode switching is based on the link having the lowest instantaneous received SNR.

The selection probability of each TTCM mode chosen for a given $\text{SNR}_r$ is shown in Figure 4.28

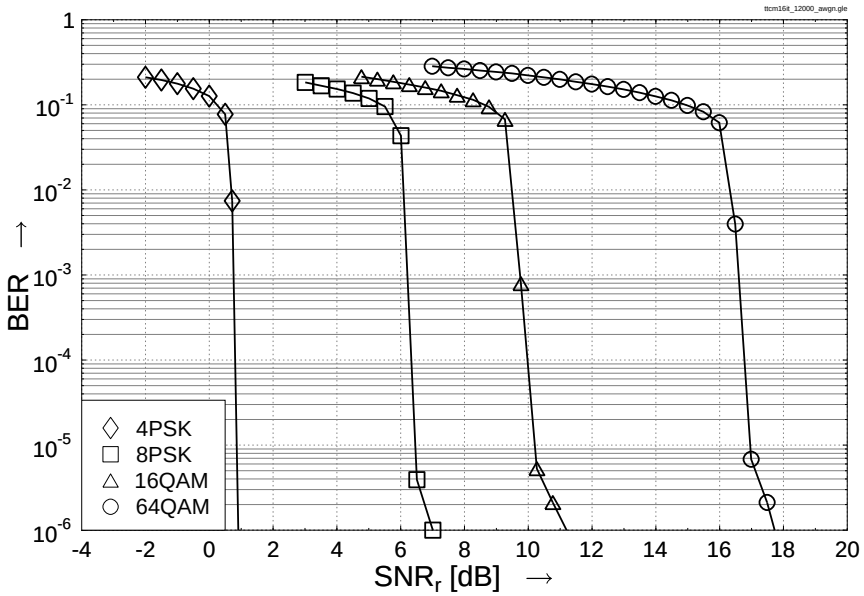


Figure 4.27: BER versus SNR$_r$ performance of the various TTCM modes using a frame length of $N_s = 12\,000$ symbols when communicating over AWGN channels. 16 turbo iterations is invoked in each TTCM decoder.

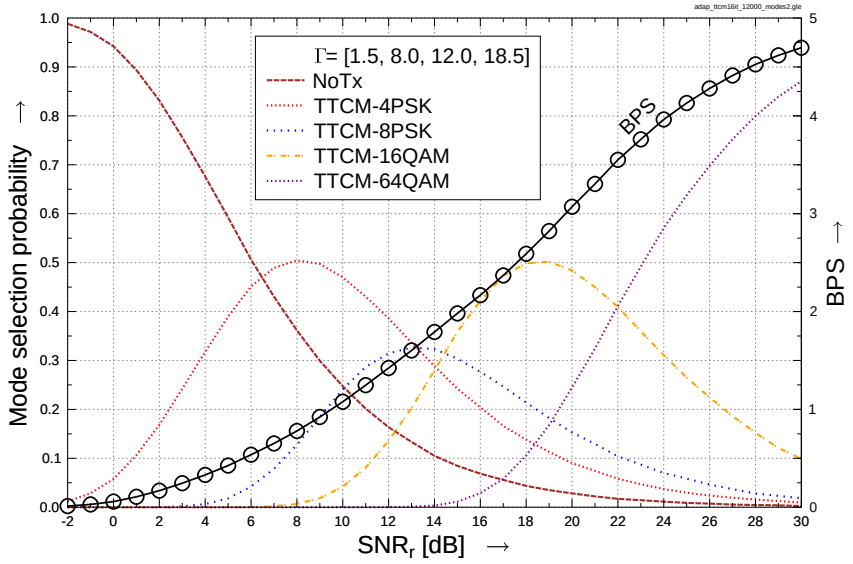


Figure 4.28: The mode selection probability of each TTCM mode chosen for a given SNR$_r$ as well as the corresponding BPS values, when communicating over quasi-static Rayleigh fading channels and maintaining a BER below $10^{-6}$.

together with the corresponding BPS curve. Note from Figure 4.28 that as $SNR_r$ increases, the higher-order TTCM modes are chosen more frequently compared to the lower-order counterparts. As a result, the BPS throughput increases smoothly, as $SNR_r$ increases.

### 4.4.3 Results and Discussions

In order to benchmark our ATTCM-DSTTC scheme, we have also studied the following five non-cooperative schemes: uncoded BPSK-1x2, BPSK-STTC-2x2, TTCM-4PSK-1x1, TTCM-4PSK-1x2 and TTCM-4PSK-STTC-2x2, where the notation $N \times M$ denotes a system employing $N$ transmitters[4] and $M$ receivers. All destination nodes in the benchmark schemes employ two receivers. The Frame Error Ratio (FER) performance of these four non-cooperative schemes is plotted together with that of the proposed ATTCM-DSTTC-2x2 scheme in Figure 4.29.

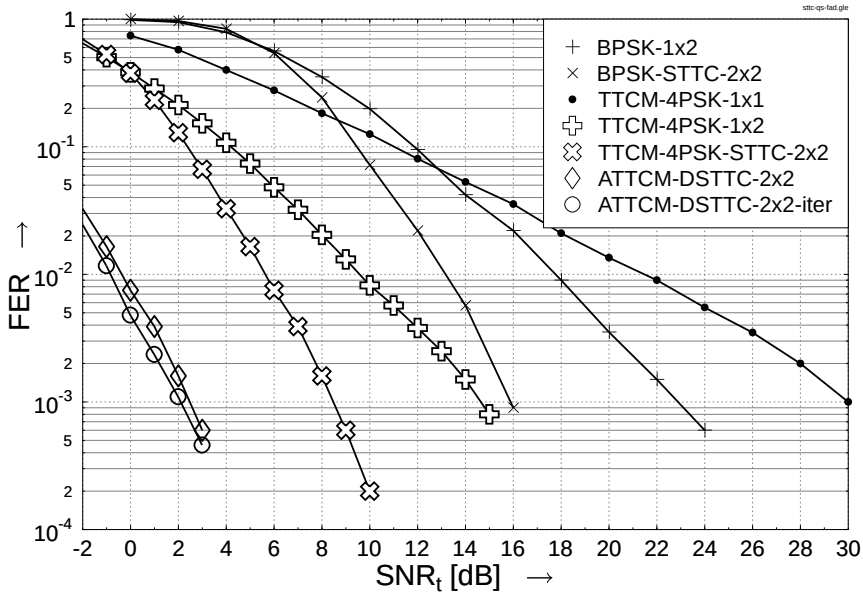


Figure 4.29: FER versus $SNR_t$ performance of the BPSK, BPSK-STTC, TTCM-4PSK, TTCM-4PSK-STTC and ATTCM-DSTTC schemes when communicating over quasi-static Rayleigh fading channels. The notation $N \times M$ denotes a system employing $N$ transmitters and $M$ receivers. A BER below $10^{-6}$ is maintained at the relay nodes of the ATTCM-DSTTC scheme.

The $N = 2$ relay nodes are located at the mid-point between the source and destination nodes, hence we have $G_{sr_i} = G_{r_i d} = 4$, which corresponds to 6 dBs geometrical-gain for both the source-to-relay and relay-to-destination links. As seen from Figure 4.29, the uncoded BPSK-1x2 scheme requires $SNR_t = 23$ dBs in order to achieve an FER of $10^{-3}$. With the aid of two transmit antennas, the BPSK-STTC-2x2 scheme requires 7 dBs less transmit power to achieve the same FER of $10^{-3}$, as compared to the single transmit antenna aided BPSK-1x2 scheme. When the TTCM-4PSK scheme is introduced to replace the BPSK scheme, more than 6 dBs gain can be achieved for both

[4]Or $N$ number of relay nodes as in the case of our proposed ATTCM-DSTTC scheme.

the single-antenna and twin-antenna aided systems. As a benefit of the space-diversity offered by the STTC component and the temporal diversity offered by the TTCM component, the TTCM-4PSK-STTC-2x2 scheme outperforms the BPSK-1x2 scheme by more than 14 dBs at FER $= 10^{-3}$. Further 6 dBs of geometrical-gain was achieved by the proposed ATTCM-DSTTC-2x2 scheme. Observe in Figure 4.29 that the cooperative ATTCM-DSTTC-2x2 scheme outperforms the non-cooperative TTCM-4PSK-1x2 with the aid of two relay nodes, by approximately 12 dBs, when aiming for a FER of $10^{-3}$. The above-mentioned BPSK-STTC-2x2, TTCM-4PSK-STTC-2x2, ATTCM-DSTTC-2x2 schemes do not perform decoding iterations between the inner STTC decoder and the corresponding outer decoder. A further coding gain of 0.5 dB is attained by the ATTCM-DSTTC-2x2-iter scheme with respect to the ATTCM-DSTTC-2x2 scheme, when a single iteration is invoked between the STTC and TTCM decoders.

Notice from Figure 4.29 that the TTCM-4PSK-1x1 scheme requires $\text{SNR}_t = 30$ dBs in order to achieve an FER of $10^{-3}$. Hence, if a non-adaptive TTCM-4PSK scheme is employed at the single-antenna aided source node and all the single-antenna assisted relay nodes are located at the mid-point between the source and destination nodes, then $\text{SNR}_t = 30 - 6 = 24$ dBs is required between each of the source-to-relay links. On the other hand, the non-cooperative TTCM-4PSK-1x2 scheme requires only $\text{SNR}_t \approx 14.5$ dBs to achieve the same FER, when the destination node is equipped with two receive antennas. Hence, when the destination node is assisted by two receive antennas, a DF-aided cooperative scheme employing a fix-mode coded scheme at the source node would not be able to outperform the non-cooperative coded scheme due to the high error inflicted by each single-antenna assisted relay node for transmission over quasi-static Rayleigh fading channels. This observation further justifies the rationale of employing adaptive coded modulation at the source node.

It is also worth mentioning that at $\text{SNR}_t = 3$ dB as shown in Figure 4.29, the corresponding average received SNR at each relay node is given by $\text{SNR}_r = 3 + 10\log_{10}(4) = 9$ dBs, when the relay nodes are located at the mid-point between the source and destination nodes. This $\text{SNR}_r$ value corresponds to BPS$\approx$ 1.0 according to the ATTCM scheme in Figure 4.28. Hence, the ATTCM scheme requires approximately $24 - 3 = 21$ dBs lower transmission power compared to a fixed mode TTCM-4PSK scheme, for transmitting 1 BPS from the source node to the relay nodes.

## 4.5 Conclusions

In this chapter, we have examined the performance of coherent coded modulation invoked for co-operative communications. Firstly, in Section 4.2 a hybrid technique of mitigating the effects of RN-induced error propagation was proposed, which takes into consideration both the RN location and the RN-BER for mitigating the error propagation. The results of Figure 4.3$-$4.11 have demonstrated that this technique is particularly beneficial, when the BER at the RN is high, since a transmit power reduction of up to 19 dB was attained at a BER of $10^{-4}$. More specifically, the SNR threshold values at a target FER of $10^{-2}$, when employing our proposed RNSPA scheme are tabu-

| Coded modulation | BICM-ID | | | | | |
|---|---|---|---|---|---|---|
| Modulation scheme | QPSK | | | | | |
| Code memory | 3 | | | | | |
| Decoder type | Approximate Log-MAP | | | | | |
| Channel | Quasi-static Rayleigh fading channel | | | | | |
| Pathloss | $G_{sr} = G_{rd}$<br>$G_{sr} = 4G_{sd}$ | | $G_{sr} = G_{rd}/9$<br>$G_{sr} = 16G_{sd}/9$ | | $G_{sr} = 9G_{rd}$<br>$G_{sr} = 16G_{sr}$ | |
| Threshold | 0.89 dB | | 5.35 dB | | 8.09 dB | |
| Corresponding AWGN BER | RN-BER = $10^{-1}$ | | RN-BER = $10^{-3}$ | | RN-BER = $10^{-6}$ | |
| Mode | With RN-BER | Without RN-BER | With RN-BER | Without RN-BER | With RN-BER | Without RN-BER |
| SNR (dB) at FER=$10^{-2}$ | 8.00 | 20.80 | 6.20 | 6.20 | 7.00 | 7.00 |

Table 4.6: SNR threshold values of our designed RNSPA scheme when transmitting over quasi-static Rayleigh fading channels. The values are tabulated from Figure 4.10.

lated in Table 4.6. In our future work, cooperative spatial multiplexing schemes will be considered, but we note that the proposed techniques are applicable to a broad class of DF-aided cooperative schemes.

Then in Section 4.3, we have studied the performance of ACM schemes in the context of cooperative communications. More specifically, three ACM schemes were considered, namely single-RN aided ACM, twin-RNs aided ACM operating with the aid of the SD link, when transmitting over a cooperative network.

Finally, in Section 4.4 an attractive cooperative scheme was proposed based on adaptive coded modulation and distributed space-time coding for communicating over quasi-static Rayleigh fading channels. The adaptive coded modulation scheme was utilised for protecting the source-to-relay links, while a distributed space-time code was employed for enhancing the reliability of the relay-to-destination links. It was shown in Figure 4.15 that mobile units equipped with a single antenna are capable establishing an energy-efficient wireless cooperative network. More specifically, as seen in Figure 4.29 the proposed cooperative ATTCM-DSTTC-2x2 scheme outperforms the uncoded non-cooperative BPSK-1x2 scheme by more than 20 dBs at a FER of $10^{-3}$, when communicating over quasi-static Rayleigh fading channels. Explicitly, SNR threshold values at FER = $10^{-2}$ and $10^{-3}$, when employing our proposed ATTCM-DSTTC schemes for transmitting over quasi-static Rayleigh fading channels are tabulated in Table 4.7.

| Decoder type | | | Approximate Log-MAP |
|---|---|---|---|
| Channel | | | Quasi-static Rayleigh fading channel |
| Adaptive Switching Threshold (dB) | | | 1.5, 8.0, 12.0, 18.5 |
| SNR (dB) at FER | TTCM-4PSK-STTC-2×2 | ATTCM-DSTTC-2×2 | ATTCM-DSTTC-2×2-iter |
| $10^{-2}$ | 5.58 | -0.54 | -0.98 |
| $10^{-3}$ | 8.46 | 2.38 | 2.00 |

Table 4.7: SNR threshold values of our proposed ATTCM-DSTTC schemes when transmitting over quasi-static Rayleigh fading channels. The values are tabulated from Figure 4.29.

Chapter 5

# Non-coherent CM scheme for Cooperative Communications

## 5.1 Introduction

Having studied coherent CM assisted cooperative communications schemes in Chapter 4, we will now embark on investigating the employment of DAPSK schemes of Chapter 3 in the context of cooperative communications systems. As mentioned in Chapter 4, there has been increasing interest in applying network coding for cooperative communications [166, 170, 179, 202]. This is well justified, because non-coherent detection allows us to dispense with channel estimation, which would be somewhat unrealistic to use in cooperative system relaying on mobile relays. Star-QAM aided TC and network coding dispensing with channel estimation will be proposed in Section 5.2. Then soft-decision aided DAPSK will be invoked for AF cooperative communications in Section 5.3. Furthermore, cooperative wireless and optical-fiber communications will be amalgamated in Section 5.4. Our conclusions concerning the various schemes are presented in Section 5.5.

## 5.2 Star-QAM Aided Turbo Coded Network Coding Dispensing with Channel Estimation

Coherent detection aided Quadrature Amplitude Modulation (QAM) requires accurate Channel State Information (CSI) in order to avoid false-phase locking, especially when communicating over Rayleigh fading channels [6, 128, 129]. As a remedy, differentially detected non-coherent Star-QAM (StQAM) was proposed in [131] in order to dispense with high-complexity CSI estimation. Operating without CSI is of particular importance in the context of relay-aided NC assisted systems, where the relay nodes (RN) cannot be realistically expected to estimate all the channels invoked. More specifically, 16-level Star-QAM (16-StQAM) is based on two concentric 8-level Phase-Shift Keying (8PSK) constellations having two different amplitudes. StQAM schemes hav-

ing more than two PSK constellations are also referred to as Differential Amplitude and Phase-Shift Keying (DAPSK) schemes [203, 204]. The authors of [203, 204] have further improved the performance of DAPSK/StQAM schemes [203, 204]. However, despite its attractive performance versus complexity characteristics, soft-decision based demodulation has not been conceived for these StQAM and DAPSK schemes. This also implies that without soft-decision based demodulation, the potential power of sophisticated channel coding or coded modulation schemes cannot be fully exploited. Hence, when channel coding was incorporated into StQAM as in [131], its performance was far from the channel capacity due to the employment of hard-decision rather than soft-decision based demodulation. Soft-decision assisted StQAM was designed for Iteratively Detected Bit-Interleaved Coded Modulation (BICM-ID) in [103]. As a further improvement, Turbo Coding (TC) [43] is adopted in this contribution because its EXIT curve was found to have a better match with that of the 16-StQAM demapper. Furthermore, this improved physical layer design is combined with network coding (NC) in this section. Both NC [189] and cooperative communications [147, 148] have recently been widely researched. In a cooperative communication scheme, RNs are used to forward signals received from other users to the destination nodes (DN). By contrast, a NC scheme allows RNs to combine the information received from different information source nodes (SN) before broadcasting them to various DNs. In this contribution, we consider a 'butterfly' topology based NC scheme [205], where two SNs and two DNs are assisted by a single RN. Our novel contributions are : *we employ the 16-StQAM aided TC based physical layer scheme for assisting a butterfly topology based NC system. A power sharing mechanism is also proposed for further reducing the overall transmit power requirement of the network.* The outline of this section is as follows. Our system model is described in Section 5.2.1, while our results and discussions are detailed in Section 5.2.2.

## 5.2.1 System Model and Analysis

Since we rely on soft-decision aided DAPSK principles, familiarity with the basic concepts of Chapter 3 is assumed. Soft-decision aided DAPSK combined with NC is proposed in Section 5.2.1.1, followed by our power sharing solutions. Then the capacity of our NC scheme is presented in Section 5.2.1.2 and Section 5.2.1.3, respectively.

### 5.2.1.1 Network Coding Model

Figure 5.1 shows the NC topology used in our study. The system consists of two SNs: $SN_1$ and $SN_2$, a RN and two DNs: $DN_1$ and $DN_2$. During the first cooperative transmission period, the binary sequence $\mathbf{b}_1$ emanating from $SN_1$ is turbo-encoded and (16-StQAM or DPSK) modulated to generate the sequence $\mathbf{x}_{s_1}$, before it is transmitted to both RN and $DN_2$. The estimated sequence $\hat{\mathbf{b}}_1$ is available at both RN and $DN_2$ after demodulation and decoding. Similarly, during the second cooperative transmission period, the binary sequence $\mathbf{b}_2$ emerging from $SN_2$ is turbo-encoded and (16-StQAM or DPSK) modulated to generate $\mathbf{x}_{s_2}$, before it is transmitted to both RN and $DN_1$.

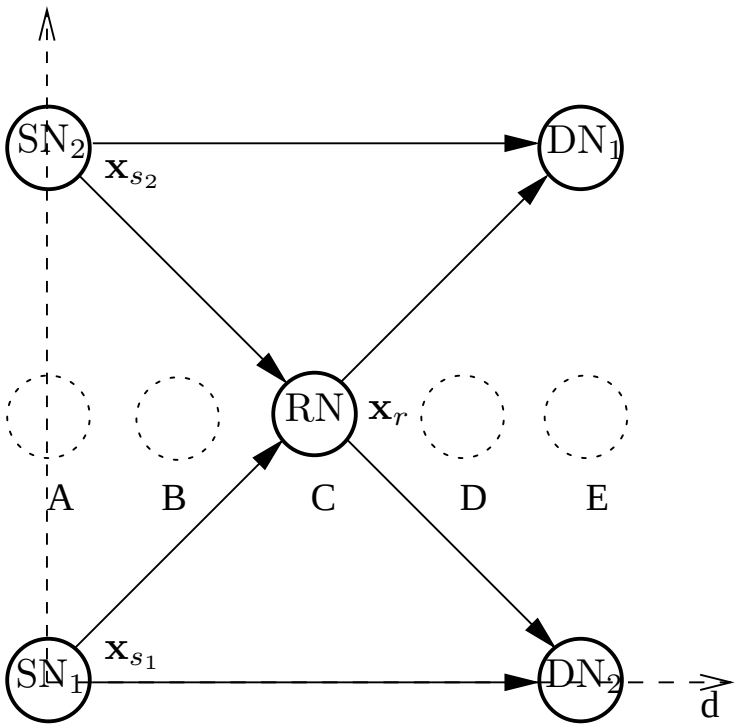


Figure 5.1: The schematic of our squared butterfly network topology. A, B, C, D and E represent different RN locations which are in the centre line of $SN_1$ and $SN_2$.

The estimated sequence $\hat{\mathbf{b}}_2$ is available at both RN and $DN_1$ after demodulation and decoding. Then, RN combines both decoded information sequences with the aid of binary modulo addition as $\mathbf{b}_3 = \hat{\mathbf{b}}_1 \oplus \hat{\mathbf{b}}_2$, before it is turbo-encoded and modulated, yielding $\mathbf{x}_r$. In the last cooperative transmission period, $\mathbf{x}_r$ is broadcast to both $DN_1$ and $DN_2$. After demodulation and decoding the estimated sequence $\hat{\mathbf{b}}_3$ becomes available at both $DN_1$ and $DN_2$. Finally, the estimate of $\mathbf{b}_1$ can be obtained at $DN_1$ with the aid of $\hat{\mathbf{b}}_1 = \hat{\mathbf{b}}_3 \oplus \hat{\mathbf{b}}_2$. Similarly, we have $\hat{\mathbf{b}}_2 = \hat{\mathbf{b}}_3 \oplus \hat{\mathbf{b}}_1$ at $DN_2$ . Let us now consider the overall throughput and the path-loss reduction factor in the following two subsections:

**5.2.1.1.1 Overall Throughput of Our System** In our NC aided system, the overall throughput can be formulated as:

$$R_o = R_s \times R_c \times R_m, \tag{5.1}$$

where $R_s = \frac{number\ of\ sources}{time\ slots}$ is the overall system's normalised throughput, i.e. rate, while $R_c$ is the coding rate and $R_m$ is the number of bits per modulated symbol. Hence, in our proposed system we have $R_o = 2/3 \times 1/2 \times 4 = 4/3$. The throughput of a non-cooperative scheme is given by $R_o = 1/1 \times 1/2 \times 4 = 2$.

**5.2.1.1.2 Reduced-Distance-Related Pathloss Reduction** The Reduced-Distance-Related Pathloss Reduction (RDRPLR) of the $S_1R$ link with respect to the $S_1D_1$ link can be expressed as [65, 195]:

$$G_{S_1R} = \left(\frac{d_{S_1D_1}}{d_{S_1R}}\right)^{\aleph}, \tag{5.2}$$

where the pathloss exponent equals to $\aleph = 2$, when a free-space pathloss model is assumed. Similarly, the RDRPLR of the $RD_1$ link in relation to the $S_1D_1$ link may be formulated as:

$$G_{RD_1} = \left(\frac{d_{S_1D_1}}{d_{RD_1}}\right)^{2}. \tag{5.3}$$

Naturally, the RDRPLR of the $S_1D_1$ link related to itself is unity, yielding, $G_{S_1D_1} = 1$, where $d_{S_1R}$ represents the distance between $SN_1$ and RN, while $d_{RD_1}$ is that of the $RD_1$ link and $d_{S_1D_1}$ is that of the $S_1D_1$ link.

From the network topology of Figure 5.1, $d_{S_1D_2}$ may be calculated as:

$$d_{S_1D_2} = \frac{d_{S_1D_1}}{\sqrt{2}}. \tag{5.4}$$

Furthermore, the above algorithm can be used for the $S_2D_2$ link. When RN is located at the centre denoted as 'C' in Figure 5.1, we have $G_{S_1R} = G_{RD_1} = G_{S_2r} = G_{RD_2} = 4$ (6 dB) and $G_{S_1D_2} = G_{S_2D_1} = 2$ (3 dB).

### 5.2.1.2 Power Sharing Methodology

When the RDRPLR factor between node $a$ and node $b$, namely $G_{ab}$, as well as the transmit power of node $a$, namely $P_{t,a}$, are considered in the communication link from node $a$ to node $b$,

the received signal becomes:

$$y_k = \sqrt{P_{t,a}}\sqrt{G_{ab}}h_k x_k + n_k\,. \tag{5.5}$$

The average received Signal to Noise power Ratio (SNR) at node $b$ is given by:

$$SNR_r = \frac{P_{t,a}\mathrm{E}\{|G_{ab}|\}\mathrm{E}\{|h_k|^2\}\mathrm{E}\{|x_k|^2\}}{N_0} = \frac{P_{t,a}\,G_{ab}}{N_0}\,, \tag{5.6}$$

where $\mathrm{E}\{|h_k|^2\} = 1$, $\mathrm{E}\{|x_k|^2\} = 1$ and the received power at node $b$ is given by $P_{t,a}\mathrm{E}\{|G_{ab}|\}\mathrm{E}\{|h_k|^2\}\mathrm{E}\{|x_k|^2\}$. For ease of analysis, we define the ratio of the power transmitted from node $a$ to the noise power encountered at the receiver of node $b$ as the *transmit SNR*[1] [195] given by:

$$SNR_t = \frac{P_{t,a}\,\mathrm{E}\{|x_k|^2\}}{N_0} = \frac{P_{t,a}}{N_0}\,. \tag{5.7}$$

[1]We note that this definition is based on measuring the signal power and noise power at different physical locations, but this unusual definition simplifies our discourse.

Hence, we have:

$$\begin{aligned} SNR_r &= SNR_t\, G_{ab}\,, \\ \gamma_r &= \gamma_t + 10\log_{10}(G_{ab})\ [\text{dB}]\,, \end{aligned} \tag{5.8}$$

where $\gamma_r = 10\log_{10}(SNR_r)$ and $\gamma_t = 10\log_{10}(SNR_t)$. Note that the effective receive power (or $\gamma_r$) at the RN and that at the DNs will be different when the corresponding communication links experience different RDRPLR. Therefore, it is not power-efficient, if the SN and RN use the same transmit power (or transmit SNR, $\gamma_t$), because not all communication links in Figure 5.1 experience the same RDRPLR. In order to minimise the overall transmission power in the network, we also investigate an appropriately designed power sharing approach, where the SN and RN can use different transmit power levels, as long as the sum of them equals to the targeted average transmit power. Even when the SR and RD distance is identical, because the RN is at the half way position, their propagation channels, physical-layer solutions and BER-requirements may be different. These differences underline the importance accurate power-sharing and control.

Let us denote the transmit SNR at $SN_1$, $SN_2$, RN, $DN_1$ and $DN_2$ as $\gamma_{t,S_1} = 10\log_{10}(SNR_{t,S_1})$, $\gamma_{t,S_2} = 10\log_{10}(SNR_{t,S_2})$, $\gamma_{t,R} = 10\log_{10}(SNR_{t,R})$, $\gamma_{t,D_1} = 10\log_{10}(SNR_{t,D_1})$ and $\gamma_{t,D_2} = 10\log_{10}(SNR_{t,D_2})$, respectively. We also define the transmit SNR difference between $SN_1$ and RN, as well as that between $SN_2$ and RN as:

$$\begin{aligned} \Delta_{S_1R} &= \gamma_{t,S_1} - \gamma_{t,R} \\ 10\log_{10}(\delta_{S_1R}) &= 10\log_{10}(SNR_{t,S_1}/SNR_{t,R})\,, \end{aligned} \tag{5.9}$$

and

$$\begin{aligned} \Delta_{S_2R} &= \gamma_{t,S_2} - \gamma_{t,R} \\ 10\log_{10}(\delta_{S_2R}) &= 10\log_{10}(SNR_{t,S_2}/SNR_{t,R})\,, \end{aligned} \tag{5.10}$$

respectively. From Eqs. (5.9) and (5.10), we can compute the average transmit SNR as:

$$\begin{aligned} \overline{SNR_t} &= \frac{SNR_{t,S_1} + SNR_{t,S_2} + SNR_{t,R}}{3} \\ &= \frac{SNR_{t,R}\,(\delta_{S_1R} + \delta_{S_2R} + 1)}{3}\,. \end{aligned} \tag{5.11}$$

Hence, once we know the target average transmit SNR as well as $\delta_{S_1R}$ and $\delta_{S_2R}$, we can compute the transmit SNR at the RN from:

$$SNR_{t,R} = \frac{3\,\overline{SNR_t}}{\delta_{S_1R} + \delta_{S_2R} + 1}\,. \tag{5.12}$$

Similarly, we can determine the transmit SNR values at $SN_1$ and $SN_2$ from:

$$SNR_{t,S_1} = \frac{3\,\overline{SNR_t}\,\delta_{S_1R}}{\delta_{S_1R} + \delta_{S_2R} + 1} \tag{5.13}$$

$$SNR_{t,S_2} = \frac{3\,\overline{SNR_t}\,\delta_{S_2R}}{\delta_{S_1R} + \delta_{S_2R} + 1}\,. \tag{5.14}$$

Note that when no power sharing is employed, all nodes use the same transmit SNR, yielding $SNR_{t,S_1} = SNR_{t,S_2} = SNR_{t,R} = \overline{SNR}_t$.

The quantities $\Delta_{S_1R}$ and $\Delta_{S_2R}$ are determined based on the RN location and hence they are dependent on the corresponding RDRPLR factors. More specifically, $\Delta_{S_1R}$ is the difference of the RDRPLR factors between the $RD_2$ and $S_1D_2$ links:

$$\Delta_{S_1R} = 10\log_{10}(G_{RD_2}) - 10\log_{10}(G_{S_1D_2}) . \tag{5.15}$$

Similarly, $\Delta_{S_2R}$ is the difference of the RDRPLR factors between the $RD_1$ and $S_2D_1$ links:

$$\Delta_{S_2R} = 10\log_{10}(G_{RD_1}) - 10\log_{10}(G_{S_2D_1}) . \tag{5.16}$$

Note that we have $G_{S_1D_2} = G_{S_2D_1} = 2$ in the network topology shown in Figure 5.1. Hence, when the RN is situated at location 'C' in Figure 5.1, we have $\Delta_{S_1R} = \Delta_{S_2R} = 10\log_{10}(4) - 10\log_{10}(2) = 3$ dB. The $\Delta_{S_1R}$ and $\Delta_{S_2R}$ values corresponding to different locations are given in Table 5.1.

Our aim is to make sure that the received SNR for the $RD_1$ ($RD_2$) link and that for the $S_2D_1$ ($S_1D_2$) link are always identical for any combinations of the RDRPLR values $G_{RD_1}$ and $G_{S_2D_1}$ ($G_{RD_2}$ and $G_{S_1D_2}$). The difference between the RDRPLR values is compensated by the assignment of different transmit power levels.

#### 5.2.1.3 Network Coding Capacity

The capacity of network coding aided scheme for transmission over correlated Rayleigh channels is still an open problem [2, 162, 206]. In this section, the relay channel capacity achievable rate of our system will be investigated.

Cut-set Theorem: Consider a general network with $m$ nodes, where node $i$ has a transmitted signal $x^{(i)}$ and a received signal $y^{(i)}$. We divide the nodes into two sets, $S$ and its complement set $S^c$. The rate of information flow from the nodes in $S$ to nodes in $S^c$ is bounded by:

$$\sum_{i\in S, j\in S^c} R^{(ij)} \leq I(x^{(S)}; y^{(S^c)}|x^{(S^c)}), \tag{5.17}$$

where $S, S^c \subset 1, 2, ..., m$. For the case of a two-user multiple-access channel, the bounds of the cut-set Theorem may reduce to [162, 206]:

$$R^1 \leq I(x^1; y|x^2) , \quad R^2 \leq I(x^2; y|x^1) , \quad R^1 + R^2 \leq I(x^1, x^2; y). \tag{5.18}$$

Based on the above theorem, we may deduce the following proposition for characterizing the upper bound of both the $SN_1$-to-RN link and of the $SN_2$-to-RN link:

Proposition: The capacity region of the network coding regime is upper bounded by:

$$C_{total} = m \cdot \min\{\lambda \cdot \min\{C^{SN_1-to-RN}, C^{SN_2-to-RN}\}, (1-\lambda) \cdot \min\{C^{RN-to-DN_1}, C^{SN_2-to-DN_1}\}\}, \tag{5.19}$$

where $\lambda = \frac{N_s}{N_s+N_r}$. Proof: According to the cut-set theorem [2], we may obtain:

$$C^1 = \min\{C^{SN_1-to-RN}, C^{SN_2-to-RN}\}. \tag{5.20}$$

Similarly, the upper bound of the RN-to-$DN_1$ link and the $SN_2$-to-$DN_1$ link may be written as:

$$C^2 = \min\{C^{RN-to-DN_1}, C^{SN_2-to-DN_1}\}. \tag{5.21}$$

Given the above structure, we first define the two-hop single-relay-aided network's capacity as the maximum achievable rate attained during the transmission of the sources $SN_1$ and $SN_2$ in the broadcast phase, which consists of $N_s$ symbol periods, and an independent transmission by the RN during the relaying phase, when $N_r$ symbols are transmitted. Initially a perfect $SN_2$-to-RN link and a perfect $SN_2$-to-$DN_2$ link are assumed in order to reduce the influence of $SN_2$. Hence, the capacity of the $SN_1$-to-$DN_1$ scheme aided by an error-free $SN_2$ may be formulated as:

$$C = \min\{\lambda C^1, (1-\lambda)C^2\}. \tag{5.22}$$

Furthermore, the total capacity of the NC system may be formulated as:

$$C_{total} = m \cdot C. \tag{5.23}$$

### 5.2.2 Simulation Results

The performance of the 16-StQAM-TC and 16DPSK-TC schemes combined with the related NC schemes is investigated based on the simulation parameters of Table 5.1.

Figure 5.2 shows the Bit Error Ratio (BER) performance of the 16-StQAM-TC aided NC system, when employing RNs at different locations shown in Figure 5.1, at a given SNR per bit of $E_b/N_0 = 13$ dB. When R is located at 'E', which is in the middle of $DN_1$ and $DN_2$, the BER of the NC scheme without power sharing is the highest compared to other locations. As seen in Figure 5.2, when the RN is located at 'C', which is in the centre of the butterfly-topology of Figure 5.1, the best BER performance is obtained for the scheme operating without power sharing. The dotted line illustrates the BER performance of the system invoking power sharing. It is worth noting that a RN situated at location 'D' would attain the best performance amongst the five locations considered in the presence of power sharing. This is because at location 'D' we have $d_{S_1R} \approx d_{S_1D_2}$, which means that the received SNR at the RN is almost identical to that at the $DN_2$, when $SN_1$ broadcasts its signals to RN and $DN_2$.

Figure 5.3 shows the BER versus $E_b/N_0$ performance of the proposed hybrid system, when communicating over correlated Rayleigh fading channels. As seen in Figure 5.3, the 16-StQAM-TC scheme outperforms the 16DPSK-TC arrangement by about 1.5 dB at a BER of $10^{-5}$. This is mainly because the 16DPSK scheme has a lower minimum Euclidean distance between its adjacent constellation points than that of the 16-StQAM scheme. The 16-StQAM-TC assisted NC aided scheme operating without the power sharing mechanism outperforms the 16-StQAM-TC scheme

| | | | | | | |
|---|---|---|---|---|---|---|
| Modulation | 16-StQAM, 16DPSK | | | | | |
| Mapping | Set Partitioning (SP) | | | | | |
| Coding | TC | | | | | |
| Constituent Code | Half-rate Recursive Systematic Convolutional (RSC) code | | | | | |
| Code Memory | 2 | | | | | |
| Outer iterations | 2 | | | | | |
| Inner TC iterations | 4 | | | | | |
| Decoder | Approximate Log-MAP | | | | | |
| Symbols per frame | 1,200 | | | | | |
| Number of frames | 10,000 | | | | | |
| Channel | Correlated Rayleigh fading channel having a normalised Doppler Frequency of 0.01 | | | | | |
| RN Position: | $G_{S_1R}$ (dB) | $G_{S_2R}$ (dB) | $G_{RD_1}$ (dB) | $G_{RD_2}$ (dB) | $\Delta_{S_1R}$ (dB) | $\Delta_{S_2R}$ (dB) |
| A | 9.03 | 9.03 | 2.04 | 2.04 | -0.96 | -0.96 |
| B | 8.06 | 8.06 | 3.91 | 3.91 | 0.91 | 0.91 |
| C | 6 | 6 | 6 | 6 | 3 | 3 |
| D | 3.91 | 3.91 | 8.06 | 8.06 | 5.06 | 5.06 |
| E | 2.04 | 2.04 | 9.03 | 9.03 | 6.03 | 6.03 |

Table 5.1: System parameters.

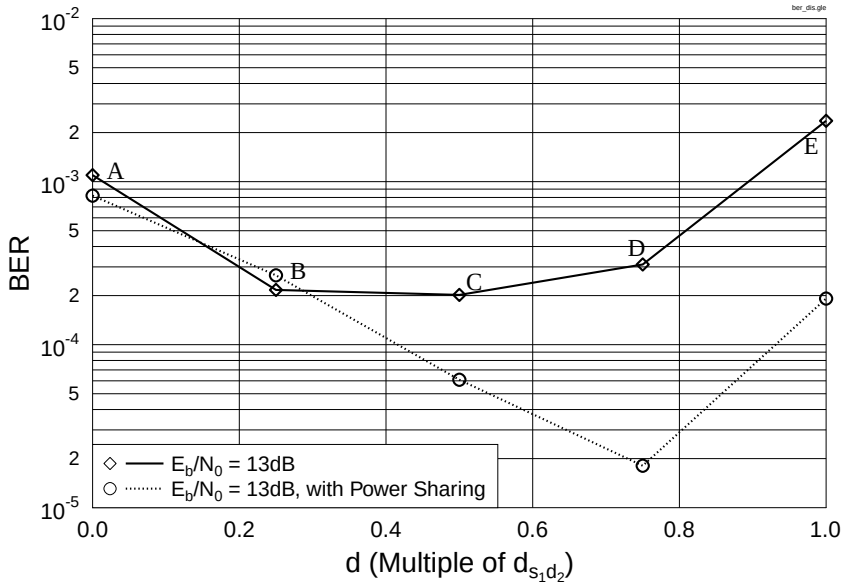


Figure 5.2: BER performance in the case of $E_b/N_0 = 13$ dB for different RN positions for transmission over correlated Rayleigh channels using the system of Figure 5.1 and the simulation parameters of Table 5.1.

by approximately 1.2 dB. When power sharing is used, the optimum RN location is closer to the DNs, so that $d_{S_1R} = d_{S_1D_2}$ and $d_{S_2R} = d_{S_2D_1}$, where the corresponding RDRPLR values are $G_{S_1R} = G_{S2R} = 3$ dB and $G_{RD_1} = G_{RD_2} = 8.73$ dB. Another 1 dB of gain is attained by

the power sharing based NC scheme. Similar trends can also be observed from the Frame Error Ratio (FER) versus $E_b/N_0$ performance curves seen in Figure 5.4. Figure 5.5 characterises the

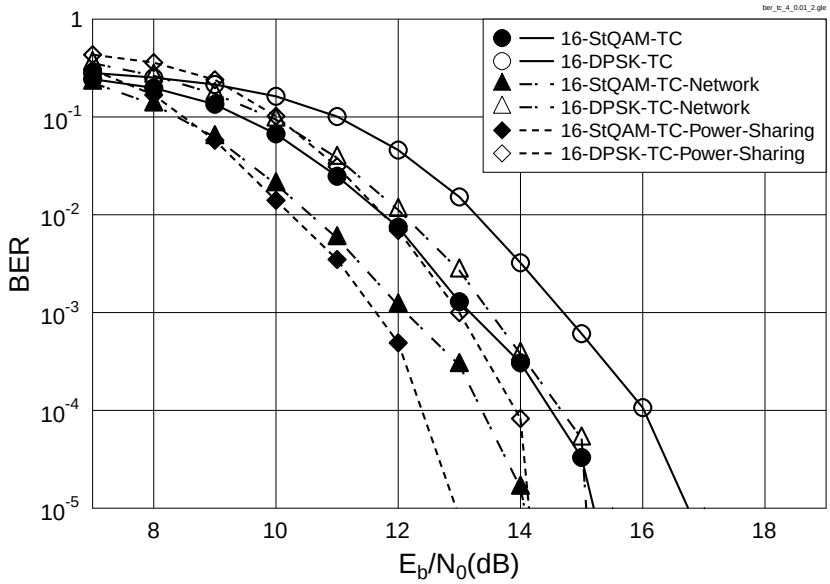


Figure 5.3: BER versus $E_b/N_0$ performance for 16-StQAM and 16DPSK aided TC for transmission over correlated Rayleigh channel using the system of Figure 3.8 and Figure 5.1, as well as the simulation parameters of Table 5.1.

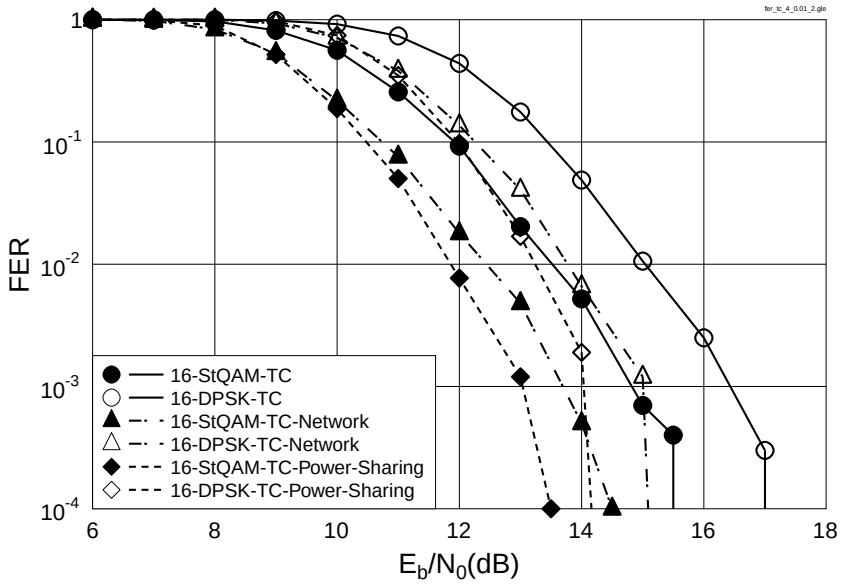


Figure 5.4: FER versus $E_b/N_0$ performance for 16-StQAM and 16DPSK aided TC for transmission over a correlated Rayleigh channel using the system of Figure 3.8 and Figure 5.1, as well as the simulation parameters of Table 5.1.

achievable capacity of the 16-StQAM-TC and 16-StQAM-TC-NC schemes, respectively. It is clear from Figure 5.5 that the achievable capacity of the NC scenario is improved compared to the single-link scenario.

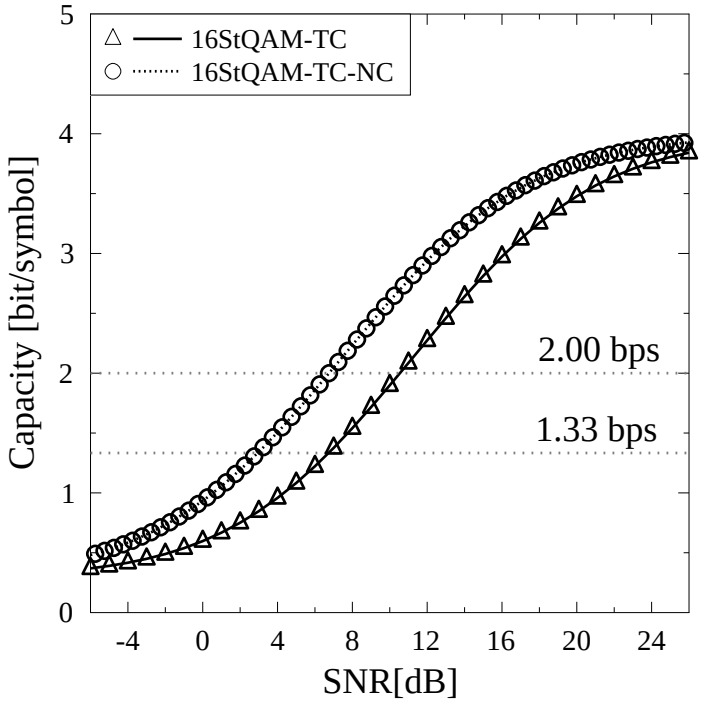


Figure 5.5: Achievable capacity versus SNR for the 16-StQAM-TC scenario, when communicating over correlated Rayleigh fading channels using the system of Figure 5.1 and Figure 3.8, as well as the simulation parameters of Table 5.1.

## 5.3 Soft-Decision Aided DAPSK for AF Cooperative Communications

Cooperative communications [145, 147] is capable of supporting the users either at an improved integrity or throughput in wireless networks. In contrast to the DF protocol, neither demodulation nor decoding is required at the relay by the non-regenerative AF protocol. Hence, AF relaying is considered as a beneficial cooperative techniques in low-complexity scenarios. Most of the previous contributions on relay aided systems assume that the destination is capable of acquiring perfect CSI for all transmission links in order to carry out coherent detection [145]. However, in rapidly fading environments, the CSI cannot be accurately estimated at the destination. DAPSK constitutes an ideal candidate for mobile relaying aided wireless communications, since it is unrealistic to expect that the relay altruistically estimates the source-relay channel for both complexity and information security reasons [135]. Despite a wealth of past studies on the employment of DPSK in AF based relaying schemes [207, 208], the single-ring based DPSK scheme yields poorer performance than DAPSK, when the modulation alphabet size is large. As an improvement, the DAPSK [209] was proposed for an AF relaying system communicating over independent Rician fading channels. As a novel application example, in this contribution, we have amalgameted the soft-decision DAPSK aided channel coding scheme with an AF based relaying system transmitting over correlated Rayleigh fading channels. The system design and analysis is detailed in Section 5.3.1, while the relative corresponding simulation results and discussion is presented in Section 5.3.2.

### 5.3.1 System Model and Analysis

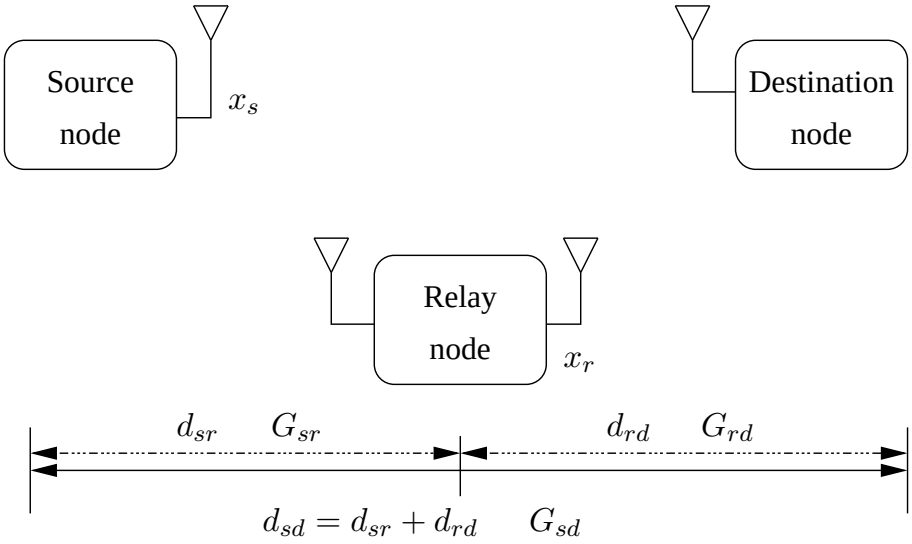


Figure 5.6: The schematic of a two-hop relay-aided wireless system with S-D link.

Figure 5.6 presents the schematic of a two-hop relay-aided wireless system. According to the AF relaying protocol, the Relay Node (RN) amplifies the signal received from the Source Node (SN) and forwards it to the Destination Node (DN) with the objective of achieving a more reliable transmission at a lower SNR when compared to the scheme dispensing with a RN. During the first time slot, the SN broadcasts $x_s$ to both the DN and RN. The $kth$ symbol received at the DN may be expressed as:

$$y_{sd,k} = \sqrt{G_{sd}} h_{sd,k} x_{s,k} + n_{sd,k}, \tag{5.24}$$

while the $kth$ symbol received at the RN could be formulated as:

$$y_{sr,k} = \sqrt{G_{sr}} h_{sr,k} x_{s,k} + n_{sr,k}, \tag{5.25}$$

where $n_{sd,k}$ and $n_{sr,k}$ represents the AWGN having a variance of $N_0/2$ per dimension, respectively. Furthermore, $h_{sd,k}$ and $h_{sr,k}$ represents the uncorrelated Rayleigh fading coefficient of the SD and SR links, respectively. Here, $G_{sr} = \left(\frac{d_{sd}}{d_{sr}}\right)^2$ is the reduced-distance-related pathloss reduction (RDRPLR) of the SR link with respect to the SD link [195], where $d_{ab}$ stands for the distance between node a and node b[2]. Similarly, we have $G_{sd} = 1$.

The RN amplifies the signal received from the SN and forwards it to the DN by simply scaling the received signal by a factor that is inversely proportional to the received power, which can be formulated as:

$$\tilde{\beta}_f = \frac{1}{\sqrt{G_{sr}|h_{sr}|^2 + N_0}}. \tag{5.26}$$

[2]For the sake of simplicity we assumed without loss of generality that the SN, the RN and the DN are positioned along a straight line in this section, so we have $d_{sd} = d_{sr} + d_{rd}$ and $d_{sr} = d_{rd} = d_{sd}/2$.

Since the average SNR at the RN's receiver may be expressed as:

$$\gamma_{sr,k} = \mathrm{E}\left(\frac{G_{sr}|h_{sr,k}|^2}{N_0}\right), \tag{5.27}$$

where E(.) is the expectation of (.), the average value of $\tilde{\beta}_f$ in Equation (5.26) may be written as:

$$\beta_f = \frac{1}{\sqrt{N_0}\sqrt{\gamma_{sr,k}+1}}. \tag{5.28}$$

Hence, the RN does not have to estimate the exact channel coefficient $h_{sr,k}$, when computing the amplification factor at the RN. Specifically, only the corresponding average received SNR $\gamma_{sr,k}$ is required, which is relatively easier to estimate. During the second transmission period, the RN amplifies the received signal as $\beta_f y_{sr}$ and forwards it to the DN. The $kth$ symbol received at the DN may, therefore, be formulated as:

$$\begin{aligned} y_{rd,k} &= \sqrt{G_{rd}}h_{rd,k}x_{r,k} + n_{rd,k}, \\ &= \sqrt{G_{rd}}h_{rd,k}\beta_f y_{sr,k} + n_{rd,k}, \\ &= \underbrace{\sqrt{G_{rd}}h_{rd,k}\beta_f\sqrt{G_{sr}}h_{sr,k}}_{h_{srd,k}}x_{s,k} \\ &+ \underbrace{\sqrt{G_{rd}}h_{rd,k}\beta_f n_{sr,k} + n_{rd,k}}_{n_{srd,k}}, \end{aligned} \tag{5.29}$$

where $n_{rd,k}$ represents the AWGN having a variance of $N_0/2$ per dimension, while $n_{srd,k}$ is another Gaussian noise process with a different noise variance and $G_{rd} = \left(\frac{d_{sd}}{d_{rd}}\right)^2$.

According to Equation (3.14), Equation (5.29) may be rewritten as:

$$y_{rd,k} = h_{srd,k}a_{s,k}v_{s,k} + n_{srd,k}, \tag{5.30}$$

and assuming a slow Rayleigh fading channel, where we have $h_k \approx h_{k-1}$, we arrive at:

$$y_{rd,k} = h_{srd,k-1}a_{s,k}v_{s,k-1}w_k + n_{srd,k} \tag{5.31}$$

$$= \alpha^{q_k}y_{rd,k-1}w_k - \underbrace{\alpha^{q_k}n_{srd,k-1}w_k + n_{srd,k}}_{\tilde{n}_{srd,k}}, \tag{5.32}$$

while based on Equation (5.29), $\tilde{n}_{srd,k}$ may be expressed as:

$$\begin{aligned} \tilde{n}_{srd,k} &= \sqrt{G_{rd}}h_{rd,k}\beta_f n_{sr,k} + n_{rd,k} \\ &- \alpha^{q_k}w_k(\sqrt{G_{rd}}h_{rd,k}\beta_f n_{sr,k} + n_{rd,k}). \end{aligned} \tag{5.33}$$

The effective variance of the noise $\tilde{n}_{srd,k}$ depends on the amplitude ratio $\alpha^{q_k}$, $G_{rd}$, $h_{rd}$, $k$, $\beta_f$ and $w_k$ which are constant during a symbol period. The effective noise variance is given by:

$$N_0^{(i)} = N_0 + N_0 + |\alpha^{q_k}|^2 N_0 + |\alpha^{q_k}|^2 N_0, \tag{5.34}$$

where the variance for each of the four noise terms in Equation (5.33) is given in order by the right hand side of Equation (5.34), respectively. Then, Equation (5.34) may be substituted into Equation (3.24) for the soft-decision M-DAPSK based on the AF relaying protocol.

### 5.3.2 Simulation Results and Discussion

In Section 3.2.2 we have discussed the soft-decision aided DAPSK-TuCM. In this section we present simulation results for soft-decision aided DAPSK-TuCM in the AF relaying environment when communicating over correlated Rayleigh fading channels with a normalized doppler frequency of $f_d = 0.01$. All parameters used in our simulations are shown in Table 5.2. Note that the traditional point-to-point non-cooperative system is regarded as a benchmark scheme here.

| Modulation | 64-DAPSK (4,16) |
|---|---|
| Mapping | Gray labeling |
| Coding | TC |
| Code Memory | 3 |
| Outer iterations | 2 |
| Inner TC iterations | 4 |
| Decoder | Approximate Log-MAP |
| Symbols per 64-DAPSK block ($L_{sf}$) | 400 |
| Number of 64-DAPSK blocks per TC block | 10, 100 |
| Number of TC blocks | 5000 |
| Channel | Correlated Rayleigh fading channel $f_d$=0.01 |

Table 5.2: System parameters.

Figure 5.7 presents the BER versus SNR performance of the soft-decision 64-DAPSK (4,16) benchmark scheme and the cooperative scheme that invokes the AF protocol, where the RN is located in the middle of the SN-DN link. As indicated in Figure 5.7, the BER performance recorded for the AF based scheme is significantly better than that of the 64-DAPSK benchmark scheme. For example, when using a TC block length of 40 000 modulated symbols, the SNR gain of the TC-aided 64-DAPSK (4,16) under the AF relaying protocol is improved by 4.5 dB at BER=$10^{-5}$, when compared to the non-cooperative scenario.

## 5.4 Cooperative Wireless and Optical-fiber Communications

The demand for high data rate wireless services has rapidly increased throughout the development of the mobile communications. The services facilitated by wired networks are now migrating to the wireless domain and are generally characterized by high Quality of Service (QoS) requirements. However, the cost of upgrading the infrastructure is massive. In the wired domain, optical fibers play a vital role in delivering high-rate data services. The family of hybrid techniques, which rely on a sophisticated combination of wireless mobile systems and optical fiber links have received substantial attention [210]. For example, Digital Fiber Optic (DFO) links [211] and Radio-over-Fiber (ROF) techniques [212] have been developed for supporting multicell systems.

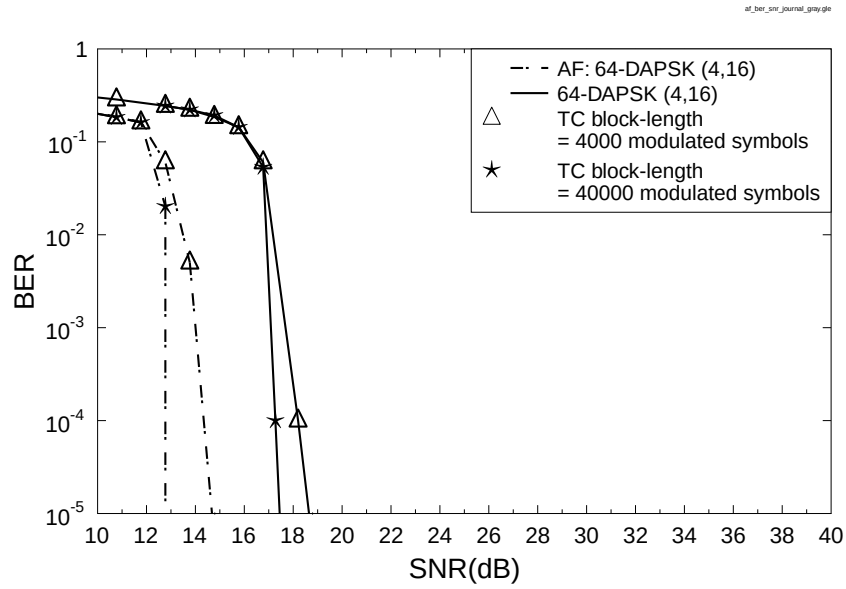


Figure 5.7: BER versus SNR performance comparison of the 64-DAPSK (4,16) schemes when transmitting over correlated Rayleigh fading channels. Both a non-cooperative scheme and at AF-based cooperative scheme are considered. The corresponding system parameters are summarized in Table 5.2. A TC block-length of 4000 modulated symbols corresponds to ten 64-DAPSK transmission block lengths, while a 40 000 modulated-symbol TC block corresponds to one hundred 64-DAPSK transmission block lengths.

The radical Unity Frequency Reuse (UFR) technique has been proposed for improving the attainable area spectral efficiency of multicell systems. However, UFR based schemes exhibit a lower cell-edge throughput due to their increased co-channel interference. Recently, the Fractional Frequency Reuse (FFR) technique has been adopted in the Third Generation Partnership Project's (3GPP) Long-Term Evolution (LTE) standard [213, 214] as well as in the Wordwide interoperability for Microwave Access (WiMAX) system [215], since it is capable of improving the cell-edge throughput. The downlink performance of the FFR based cooperative wireless and DFO aided communication has been investigated in [211], where a good cell-edge performance was reported.

Diversity provides an effective mechanism of combating the effects of channel fading in wireless communication systems [139]. Single-Input Multiple-Output (SIMO) aided techniques are capable of increasing the achievable performance gain, when communicating over wireless fading channels, provided that the Channel State Information (CSI) is known at the receivers [143, 144, 147, 148]. Most previous work on SIMO systems was based on the assumption of perfectly knowing the CSI and hence the corresponding data recovery typically relied on coherent detection. However, in practice it is hard to acquire accurate CSI, especially in rapidly fading mobile environments. Hence, it is of prime significance to design new non-coherent detection techniques, which dispense with channel estimation. More specifically, the soft-decision based low-complexity Star-QAM (StQAM) technique has been proposed in [103], which outperformed its hard-decision based StQAM counterpart [6], when powerful channel coding schemes [216] are invoked. However, a non-adaptive fixed-throughput scheme would require a high transmit power in order to maintain a

low Bit Error Ratio (BER) at the base station, even when a powerful channel encoder is utilised for communicating over slowly fading quasi-static Rayleigh channels. This is due to the lack of temporal diversity within a transmission frame. Our novel contributions in this section may be summarised as follows:

1. We investigated the uplink performance of FFR based multicell multiuser schemes, as a complement of the corresponding downlink investigation in [211].
2. We further extended the Single-Input Single-Output (SISO) based non-coherent 16StQAM scheme of [103] to a SIMO system.
3. We investigated both the Turbo-Coded [216] 16StQAM and 16QAM [6] schemes in the multicell multiuser uplink system considered, when imperfect DFO links are considered.
4. Furthermore, the novel Adaptive Turbo-coded Soft-decision aided Differential Detection (ATSDD) system was designed for wireless-optical communications over the imperfect AROF links.

The outline of the section is as follows. Our system model is described in Section 5.4.1, while our results and discussions are detailed in Section 5.4.2. Our conclusions are presented in Section 5.5.

### 5.4.1 System Model and Analysis

The topology of the FFR based multicell multiuser scheme is shown in Figure 5.8, where we have two tiers of 19 hexagonal cells, surrounding the central Base-Station (BS) $B_0$ located at the origin. The frequency-partitioning strategy of the total available bandwidth $F$ is characterized by $F_c \bigcap F_e = \oslash$, where $F_c$ and $F_e$ represent the cell center's frequency band and the cell edge's frequency band, respectively. Furthermore, $F_e$ is divided into three orthogonal frequency bands $F_i$, for $i \in \{1,2,3\}$. In Figure 5.8, $D$ denotes the distance between two adjacent BSs, while $R_{cell} = D/\sqrt{3}$ is the radius of each hexagonal cell. We employ $D = 3$ km for the Urban-Macro propagation scenario of [211].

#### 5.4.1.1 Digital Fiber Optic and Analogue Radio Over Fiber Model

The ROF and DFO-link-based transmission technique may be used for the optical link in the uplink of wireless-optical fiber scenario, which is more reliable than a wireless back haul and a feasible solution to cope with the increasing demand of high-bandwidth wireless services, albeit also being more costly.

We assume that the links spanning from the RAs to the BS $B_0$ are constituted by realistic rather than perfect optical fiber links as shown in Figure 5.9.

Compared to the family of ROF [217, 218], the DFO link is immune to the sideband cancellation phenomenon, which occurs in the ROF system [211]. Furthermore, it is capable of avoiding both the intermodulation distortion of the optical fiber and the nonlinearity imposed by the optical

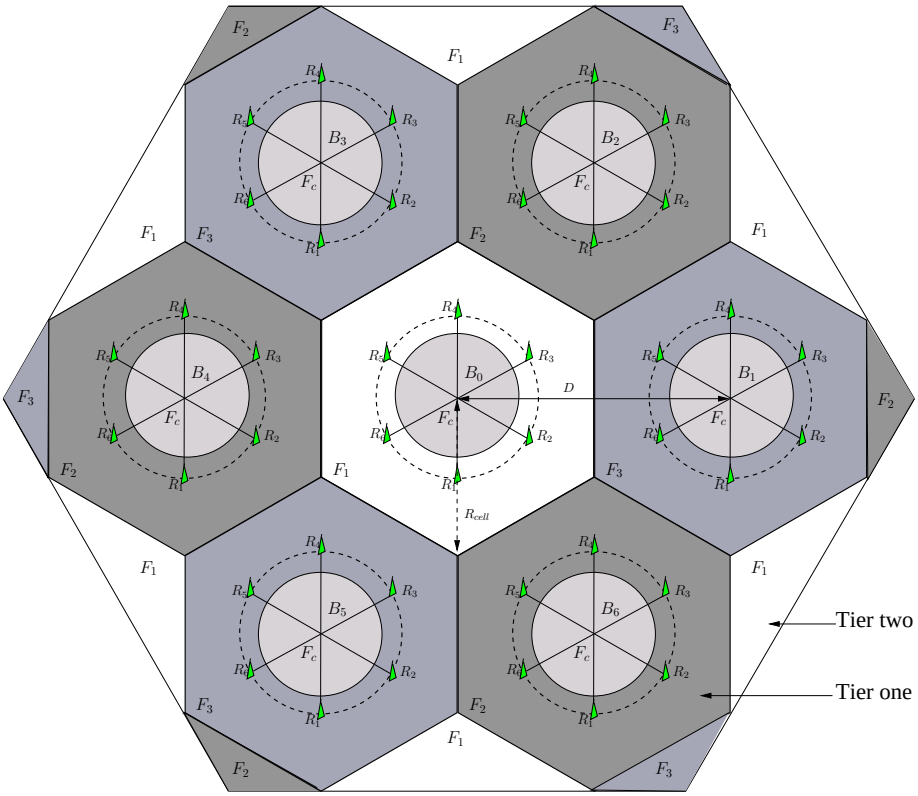


Figure 5.8: Topology of the 19-cell two-tier FFR based arrangement, where $N = 6$ RAs are employed in each cell. .

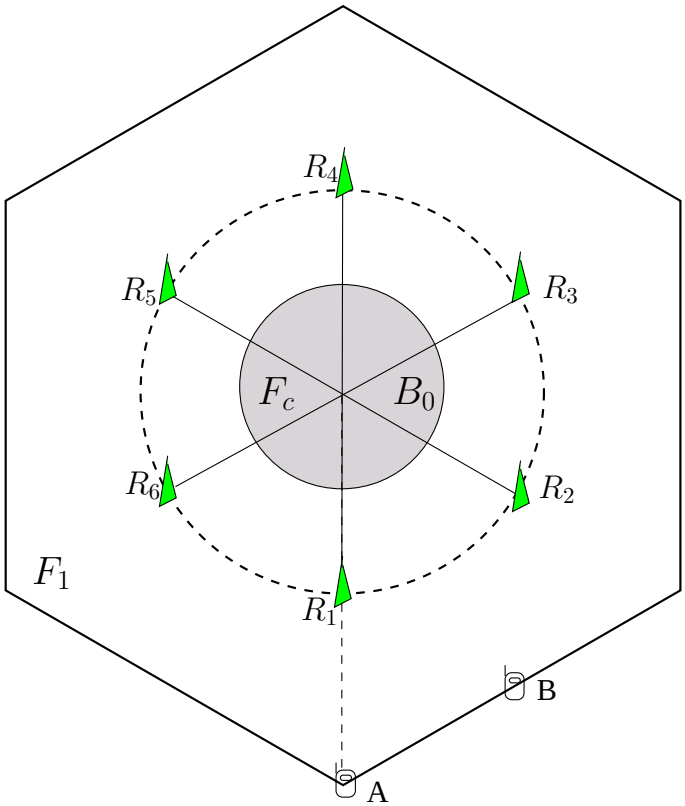


Figure 5.9: The structure of the central cell and the MS considered locations A and B.

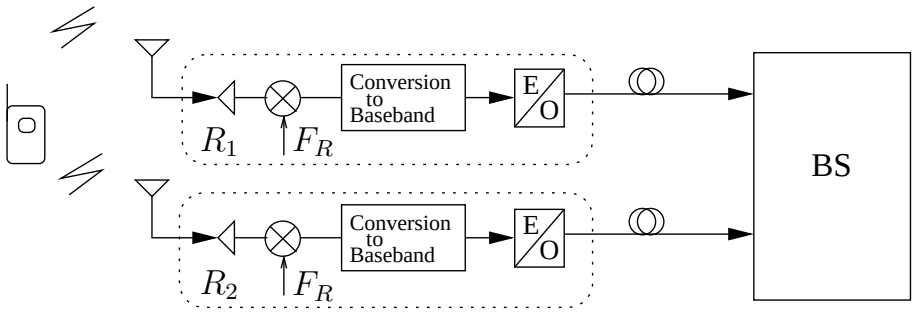


Figure 5.10: The simplified system block diagram of our proposed uplink wireless-optical SIMO system with DFO link, where $F_R$ is the radio frequency carrier and $R_i$ denotes the $i$th RA.

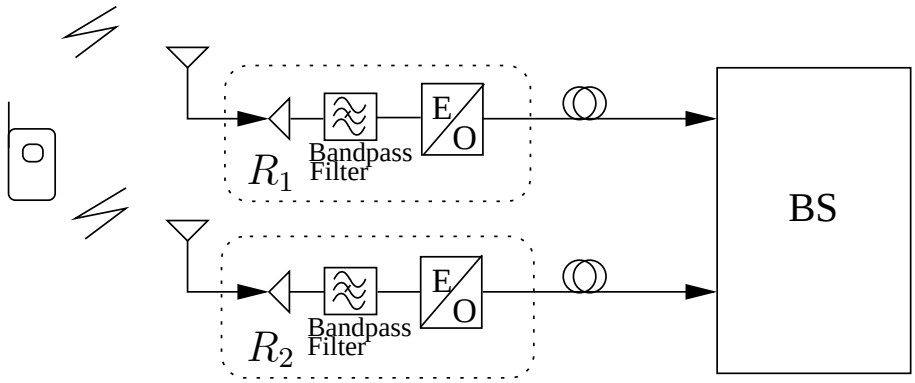


Figure 5.11: The simplified system block diagram of our proposed uplink wireless-optical SIMO system relying on an AROF link, where $F_R$ is the radio frequency carrier and $R_i$ denotes the $i$th RA.

components at the price of complexity and cost [210]. The block digram of a DFO link is shown in Figure 5.10. Furthermore, the advantage of this Analogue ROF (AROF) [219–224] architecture is the low complexity and cost. However, the employment of an analogue optical link results in the AROF system performance being degraded by various impairments [217], such as: modulator, photodetector and the optical fiber ect. Because of the trade-off of the complexity, cost and quality, both kinds of the DFO and AROF technology attenuations in optical link are studied in this section.

For DFO link, the SIMO wireless system is presented in Figure 5.10. We assume that the links spanning from the RAs to the BS $B_0$, as shown in Figure 5.9 and Figure 5.8, are constituted by realistic rather than perfect optical fiber links.

#### 5.4.1.2 Imperfect Optical Fiber Model

Nonlinear Schrödinger (NLS) equation can be formulated as [211, 225, 226]:

$$\frac{\partial A(z,t)}{\partial z} = \left( \underbrace{-i\frac{\beta_2}{2}\frac{\partial^2}{\partial t^2}}_{\widehat{D}} + \underbrace{i\xi|A|^2}_{\widehat{N}} \right) A(z,t), \tag{5.35}$$

where the terms $\widehat{D}$ and $\widehat{N}$ are the simplified forms of the dispersion and the nonlinear effects, respectively. Additionally, $A(z,t)$ is a slowly varying envelope function associated with the optical pulse in the optical-fiber, where $z$ is the propagation distance and $t = t' - z/v_g$[3] is the time, while $\beta_2$ is the second-order propagation constant and the coefficient $\xi$ characterizes the nonlinear effects. However, the NLS equation in Equation (5.35) cannot be readily solved analytically, when both linear dispersion and various optical transmission-induced nonlinear effects are present. The *split-step Fourier method* (SSFM) [225, 226] is one of the popular numerical algorithms used for solving the NLS equations, owing to its accuracy and relatively modest computational cost. In the so-called symmetric split-step scheme, the solution of Equation (5.35) may be approximated as:

$$A(z+l,T) \approx F_T^{-1}\{e^{[l\widehat{D}(-jw)]}F_T[e^{(l\widehat{N})}A(z,T)]\}, \tag{5.36}$$

where $F_T$ and $F_T^{-1}$ represents the Fourier-transform and inverse Fourier-transform operation, respectively. Furthermore, the accuracy of the SSFM can be improved by employing a different procedure[4] to propagate the optical pulse over a fiber-segment spanning from $z$ to $z+l$. Then Equation (5.36) may be expressed as [226]:

$$A(z+l,T) \approx e^{\left(\frac{l}{2}\widehat{D}\right)} \cdot e^{\left[\frac{l}{2}(\widehat{N}(z)+\widehat{N}(z+l))\right]} \cdot e^{\left(\frac{h}{2}\widehat{D}\right)} A(z,T). \tag{5.37}$$

Since the linear dispersion and the nonlinear operators do not commute in general, the solution given in Equation (5.37) constitutes an approximation of the exact solution. The entire fiber length of $L = ml$ may be decomposed into $m$ consecutive $l$-length elements. The total optical fiber attenuation computed based on Equation (5.37) is denoted by $A_L$ for simplicity.

Additionally, we have also investigated the phase-rotation imposed by an imperfect optical fiber. Specifically, the phase of the $k$th optical pulse may be modelled by:

$$\theta_k = \theta_{k-1} + \tilde{\delta}\,, \tag{5.38}$$

where $\tilde{\delta} \in [-\delta, \delta]$ is the phase difference between the $k$th and the $(k-1)$st optical pulse, while $\delta$ is the maximum phase difference considered.

#### 5.4.1.3 Fixed Mode

During the first step of the transmission scenario of Figure 4.24, the MS transmits its information to both the RAs $R_1$ and $R_2$. The $k$th symbol received at the $i$th RA $R_i$ may be expressed as:

$$y_{sr_i,k} = \sqrt{\mathcal{L}_{sr_i}} h_{sr_i,k} x_{s,k} + n_{sr_i,k}, \tag{5.39}$$

where $k \in \{1, ..., K\}$ and $K$ is the number of symbols transmitted from the MS, while $h_{sr_i,k}$ denotes the Rayleigh fading coefficient between the MS and $R_i$. Furthermore, $n_{sr_i,k}$ represents the Additive

[3] Note that $t'$ is the physical time, while $v_g$ is the group velocity at the center wavelength.

[4] The main difference is that the nonlinearity is included in the middle of the segment instead of at the segment boundary.

While Gaussian Noise (AWGN) having a variance of $N_0/2$ per dimension. Note that $\mathcal{L}_{sr_i} = 10^{-L_{sr_i}/10}$ denotes the path-loss factor between the source (MS) and the $i$th RA $R_i$, where $L_{sr_i} = 10\aleph \log_{10}[\frac{d_{sr_i}}{d_0}]$ [127] is the pathloss attenuation in decibel, while $\aleph$ is the pathloss exponent, $d_{sr_i}$ is the distance between the MS, while $R_i$ and $d_0$ is the reference distance for the antenna far-field. We have considered $\aleph = 2$ and $d_0 = 1$ km in this study.

Then, the signals received from $R_i$ are communicated to the BS on a symbol-by-symbol basis, without demodulation or decoding. More specifically, the signal received at the BS from $R_i$ could be expressed as:

$$y_{i,k} = A_L e^{j\theta_k} y_{sr_i,k} + n_f, \tag{5.40}$$

$$= A_L e^{j\theta_k} \sqrt{\mathcal{L}_{sr_i}} x_{s,k} h_{sr_i,k} + A_L e^{j\theta_k} n_{sr_i,k} + n_f, \tag{5.41}$$

where again $A_L$ is the optical fiber's amplitude attenuation, $\theta_k$ is the phase-rotation introduced by the imperfect optical fiber, $n_{sr_i,k}$ is the noise at $R_i$ and $n_f$ is Gaussian-distributed noise with a zero mean for the optical link between $R_i$ and the BS. We considered $N_r = 2$ RAs in our SIMO scheme. By denoting the $(1 \times N_r)$-element received signal vector by $\mathbf{Y}_k$, the $(1 \times N_r)$-element Rayleigh fading channel vector by $\mathbf{H}_k$ and the total $(1 \times N_r)$-element AWGN vector by $\mathbf{N}_k$, the signal received by the BS may be expressed as:

$$\mathbf{Y}_k = A_L e^{j\theta_k} x_{s,k} \mathbf{H}_k + \mathbf{N}_k, \tag{5.42}$$

where $N_r = 2$.

At the BS, our soft-decision aided 16StQAM modem [103] is used, which dispenses with channel estimation for the sake of low-complexity detection. The corresponding probability density function (pdf) of receiving $y_{i,k}$, when an 8PSK symbol $w_k$ and the amplitude-selection bit $b_a$ were transmitted may be written as:

$$P(y_{i,k}|w_k, b_a = 0) = \frac{1}{\pi N_0^{(0)}} e^{\frac{-\left|y_{i,k} - y_{i,k-1}\alpha^{(0)} w_k\right|^2}{N_0^{(0)}}}, \tag{5.43}$$

$$P(y_{i,k}|w_k, b_a = 1) = \frac{1}{\pi N_0^{(1)}} e^{\frac{-\left|y_{i,k} - y_{i,k-1}\alpha^{(1)} w_k\right|^2}{N_0^{(1)}}} + \frac{1}{\pi N_0^{(2)}} e^{\frac{-\left|y_{i,k} - y_{i,k-1}\alpha^{(2)} w_k\right|^2}{N_0^{(2)}}}, \tag{5.44}$$

where $b_a$ is the bit used for the selection of the two possible amplitudes, namely $a^{(1)}$ and $a^{(2)}$, while the amplitude ratio $\alpha^{(i)}$ may be expressed as:

$$\alpha^{(i)} = \begin{cases} \frac{a^{(1)}}{a^{(1)}} \text{ or } \frac{a^{(2)}}{a^{(2)}} = 1 \; ; & i = 0 \\ \frac{a^{(1)}}{a^{(2)}} \; ; & i = 1 \\ \frac{a^{(2)}}{a^{(1)}} \; ; & i = 2. \end{cases} \tag{5.45}$$

The effective noise variance related to the noise at $R_i$ and BS, $n_{i,k}$, depends on the amplitude ratio $\alpha_i$ used at the $k$th time instant, which may be estimated as:

$$N_0^{(i)} = N_f + |\alpha^{(i)}|^2 |A_L|^2 |w_k|^2 N_0 \,, \tag{5.46}$$

$$= N_f + |\alpha^{(i)}|^2 |A_L|^2 N_0 \,, \tag{5.47}$$

where the amplitude of an 8PSK symbol is unity, $|w_k| = 1$, while the noise at the BS $n_f$ represents the AWGN having a variance of $N_f/2$ per dimension. Finally, the pdf of receiving $y_{1,k}$ and $y_{2,k}$ conditioned on the transmission of $\{b_0, b_1, b_2\}$(the three bits mapped to an 8PSK symbol) and $b_a$ can be computed as:

$$P(y_{1,k}, y_{2,k}|b_0, b_1, b_2, b_a) = P(y_{1,k}|w_k, b_a) \times P(y_{2,k}|w_k, b_a) \ , \tag{5.48}$$

which is then fed to the turbo decoder [216] for generating the original information bit sequence transmitted by the mobile user.

#### 5.4.1.4 Adaptive Mode

Based on the fixed mode modulation based SIMO performance of each of the four half-rate Turbo Coding (TC) aided transmission modes recorded for transmission over the combined AWGN and AROF channel, the ATSDD switching thresholds of $\Gamma = [\gamma_0, \gamma_1, \gamma_2, \gamma_3]$ may be obtained, for the adaptive modes using the following:

$$\text{Mode} = \begin{cases} \text{NoTx: 0 BPS,} & \text{if } \gamma_r \leq \gamma_0 \\ \text{TC-4-DPSK: 1 BPS,} & \text{if } \gamma_0 < \gamma_r \leq \gamma_1 \\ \text{TC-8-DPSK: 1.5 BPS,} & \text{if } \gamma_1 < \gamma_r \leq \gamma_2 \\ \text{TC-16-DAPSK (2,8): 2 BPS,} & \text{if } \gamma_2 < \gamma_r \leq \gamma_3 \\ \text{TC-64-DAPSK (4,16): 3 BPS,} & \text{if } \gamma_3 < \gamma_r \ , \end{cases} \tag{5.49}$$

where $\gamma_r$ is the SNR at the BS's receiver relying on the twin-RN-aided SIMO principle and NoTx denotes the no transmission mode.

### 5.4.2 Simulation Results

In this section, we investigated the performance of the proposed fixed and adaptive systems based on the cell structure of Figure 5.9, where the simulation parameters of the wireless and of the optical links are summarized in Table 5.3 and Table 5.4, respectively. More specifically, the fixed modes' performance are presented in Section 5.4.2.1, while the related adaptive mode performance are shown in Section 5.4.2.2.

#### 5.4.2.1 Simulation Results for Fixed Modes

In this section, the fixed modes' performance of both the DFO and AROF scenario is investigated. More specifically, we consider communicating over correlated Rayleigh fading wireless channels, where the RAs are connected by imperfect optical channels. Furthermore, the Turbo-Coded 16 square QAM (TC-16QAM) scheme is discussed in this section as our benchmark scheme.

Figure 5.12a denotes the BER versus SNR performance of both the TC-16QAM and TC-16StQAM aided schemes employing the DFO link of Section 5.4.1.1, when transmitting over cor-

| | |
|---|---|
| Modulation | 16StQAM, 16QAM |
| Mapping | Set Partitioning (SP) [6] |
| Coding | TC |
| Constituent Code | Half-rate Recursive Systematic Convolutional (RSC) code Code Polynomial G=[15 17] |
| Code Memory | 3 |
| Outer iterations | 1 |
| Inner TC iterations | 4 |
| Decoder | Approximate Log-MAP |
| Symbols per block | 1 200 |
| Number of frames | 5 000 |
| Channel | Correlated Rayleigh fading channel having a normalised Doppler frequency of 0.01, Optical channel |

Table 5.3: Simulation parameters for wireless link.

| Optical link | DFO | AROF |
|---|---|---|
| Chirp | -2 | – |
| Centre Frequency | Baseband | 1.95 GHz |
| Transmit Power | 10 dBm (Peak Power) | -6.55 dBm (Average Power[5]) |
| Fiber Length | 4.33 km | |
| Fiber Attenuation coefficient | 0.2 dB/km | |
| Fiber Non-linearity | 2w/km | |

Table 5.4: Simulation parameters for fiber optical link.

related Rayleigh fading wireless channels, where the RAs are connected by imperfect optical channels. As seen in Figure 5.12a, the performance recorded at locations A and B of Figure 5.9 is identical for the SISO scenario, because they have an identical transmission distance of $d_{sr_i} = \sqrt{3}/2$ km from the nearest RA. The TC-16QAM-SISO scheme outperforms the TC-16StQAM-SISO scheme by approximately 4 dB at a BER of $10^{-6}$, when perfect CSI is available at the BS. When the SIMO scheme is considered, the performance at location B of Figure 5.9 improves more significantly than that at location A. This is because location B has the same distance from $R_1$ and $R_2$ according to Figure 5.9, while location A is further away from $R_2$. More specifically, the TC-16QAM-SIMO scheme performs approximately 6 dB better than the TC-16QAM-SISO scheme at a BER of $10^{-6}$. The BER performance curves of the DFO scenario marked by the black legend and of the AROF scenario indicated by the red legend are shown in Figure 5.12b. As expected, the BER performance is almost the same for both the DFO and the AROF scenario, because the optical attenuation is low.

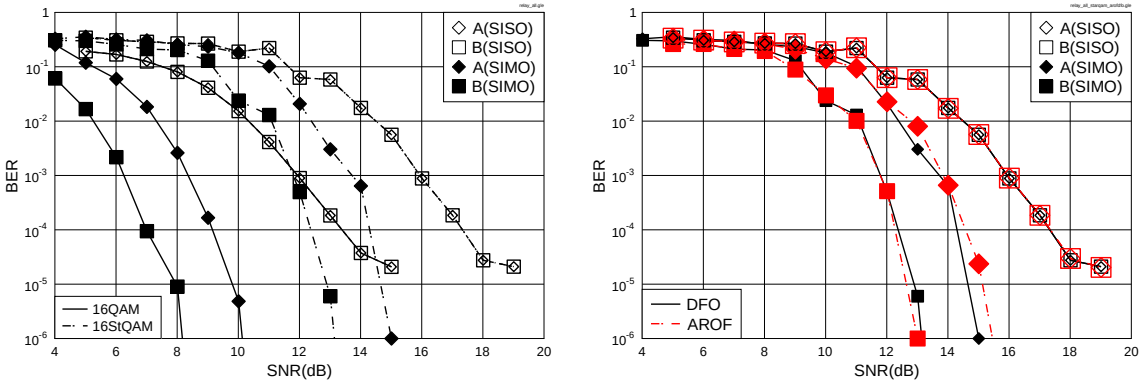


(a) TC-16QAM vs TC-16StQAM for DFO link

(b) DFO vs AROF

Figure 5.12: BER versus SNR performance of the TC-16QAM and TC-16StQAM schemes, when transmitting over correlated Rayleigh fading wireless and imperfect optical channels. The simulation parameters are summarised in Table 5.3 and Table 5.4, while the corresponding cell is shown in Figure 5.9.

We will characterize the performance of the DFO scenario first and then the performance of the AROF scenario will be presented.

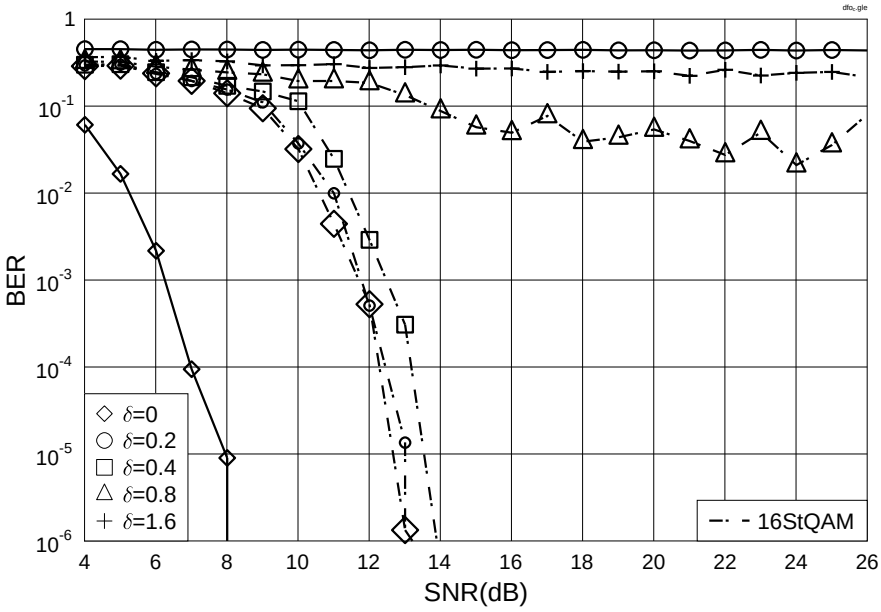


Figure 5.13: BER versus SNR performance of the TC-16QAM-SIMO and 16StQAM-TC-SIMO schemes of Figure 5.9 and Figure 4.24 for transmission over correlated Rayleigh fading and imperfect optical channels. The corresponding simulation parameters are summarised in Table 5.3. Phase rotations of upto $\delta = \{0, 0.2, 0.4, 0.8, 1.6\}$ radian are considered in the optical link.

However, the 16QAM-based scheme does not perform well, when phase-rotations are imposed by the imperfect optical-fiber. More specifically, Figure 5.13 shows the performance of both the TC-16QAM-SIMO and TC-16StQAM-SIMO schemes, when phase rotations of upto

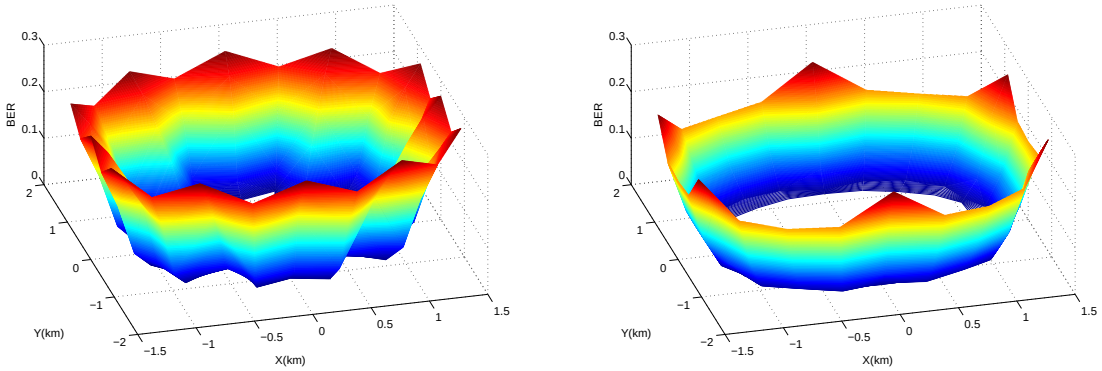


(a) The TC-16StQAM-**SISO** scheme

(b) The TC-16StQAM-**SIMO** scheme

Figure 5.14: The 3D BER versus user location performance of both the TC-16StQAM-SISO scheme and the TC-16StQAM-SIMO scheme of Figure 5.9 for transmission over correlated Rayleigh fading wireless and imperfect optical channels for the whole cell in conjunction with SNR = 5 dB. A phase rotation of upto $\delta = 0.1$ radian is considered in the optical link. The other simulation parameters are summarised in Table 5.3.

$\delta = \{0, 0.2, 0.4, 0.8, 1.6\}$ radian are considered in the optical link. We assume that the CSI of the wireless link is available at the BS for the TC-16QAM-SIMO, but the phase-rotation inflicted by the optical-fiber link is unknown. As seen from Figure 5.13, the TC-16QAM-SIMO scheme breaks down at $\delta = 0.2$ radian, while the proposed TC-16StQAM-SIMO can still perform adequately even for $\delta = 0.4$ radian.

Let us investigate the BER performance at the cell-edge scenario of Figure 5.9 in our FFR-based cellular system. The 3D BER versus user location performance of the TC-16StQAM-SISO scheme is shown in Figure 5.14a for SNR = 5 dB. There are 12 BER peaks in Figure 5.14a, which correspond to all the 12 A and B locations (each $60^o$ sector has one location A and one location B) in the hexagonal cell.

When two RAs are used for detecting the mobile user's signals, the 3D BER performance of the TC-16StQAM-SIMO scheme is depicted in Figure 5.14b for SNR $= 5$ dB. The six BER peaks corresponding to the six locations of B have disappeared, as a benefit of the SIMO scheme. The six BER peaks corresponding to the six A locations have been reduced, although not completely removed. The BER surface seen in Figure 5.14b exhibits a more wide-spread low-BER area compared to that seen in Figure 5.14a. This indicates that a better uplink transmission quality can be achieved, when our SIMO scheme is invoked.

Figure 5.15 presents the performance of both the TC-16QAM-SIMO and TC-16StQAM-SIMO schemes, when phase rotations of upto $\delta = \{0, 0.2, 0.4, 0.8, 1.6\}$ radian are considered in the AROF link. We also assume that the CSI of the wireless link is available at the BS for the TC-16QAM-SIMO, but the phase-rotation inflicted by the optical-fiber link is unknown. As seen from Figure 5.15, the TC-16QAM-SIMO scheme breaks down at $\delta = 0.2$ radian, while the proposed

TC-16StQAM-SIMO can still perform adequately even for $\delta = 0.4$ radian. As expected, the BER performance seen in Figure 5.15 exhibits the same trend as seen in Figure 5.13, albeit it is somewhat inferior in comparison to Figure 5.13. For example, at a BER of $10^{-5}$, SNR = 13.6 dB is required for the DFO system at $\delta = 0.2$ radian, while 13.9 dB is necessitated for the AROF system.

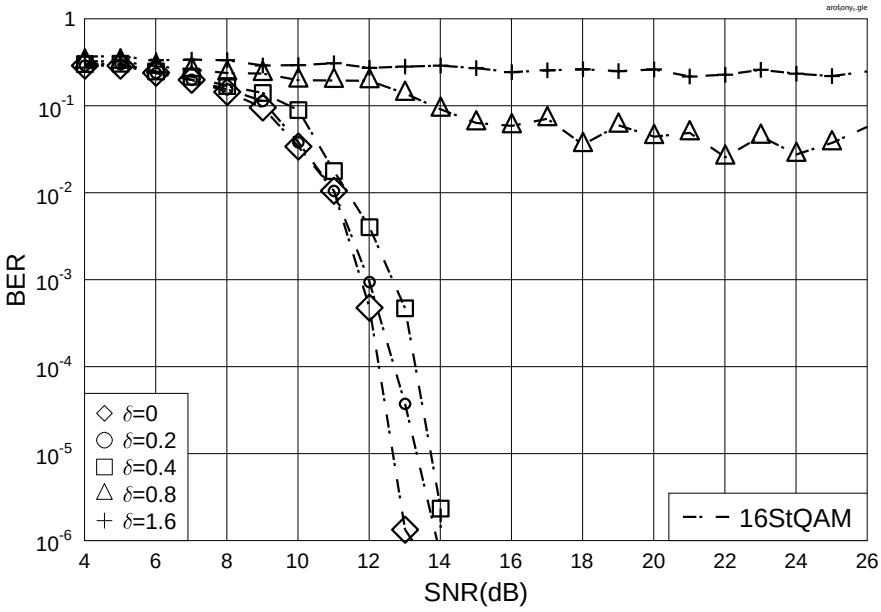


Figure 5.15: BER versus SNR performance of the TC-16QAM-SIMO and 16StQAM-TC-SIMO schemes of Figure 5.9 and Figure 4.24 for transmission over correlated Rayleigh fading and imperfect optical channels. The corresponding simulation parameters are summarised in Table 5.3. Phase rotations of upto $\delta = \{0, 0.2, 0.4, 0.8, 1.6\}$ radian are considered in the optical link.

Figure 5.16a shows the 3D BER performance of the TC-16StQAM-SISO scheme at SNR $= 5$ dB, when communicating over correlated Rayleigh fading wireless and imperfect optical channels, while the corresponding SIMO scenario is characterized in Figure 5.16b. They both exhibit similar performance trends to those of the DFO system characterized in Figure 5.14a and Figure 5.14b. and Figure 5.16b.

#### 5.4.2.2 Simulation Results for Adaptive Modes

In this section, we investigate the performance of the ATSDD scheme in the AROF scenario. We consider communicating over correlated Rayleigh fading wireless channels, where the RAs are connected by imperfect optical channels to the BS.

Firstly, the BER versus SNR performance of the fixed mode based soft-decision aided differential detection is considered in Figure 5.17, when phase-rotations denoted by $\delta$ are imposed by the imperfect ROF link, while assuming that the CSI of the wireless link and the phase-rotations inflicted by the optical-fiber link are both unknown. Observe in Figure 5.17, that $\delta$ imposes different effects on different modes. More specifically, the TC-4DAPK scheme breaks down at a phase-

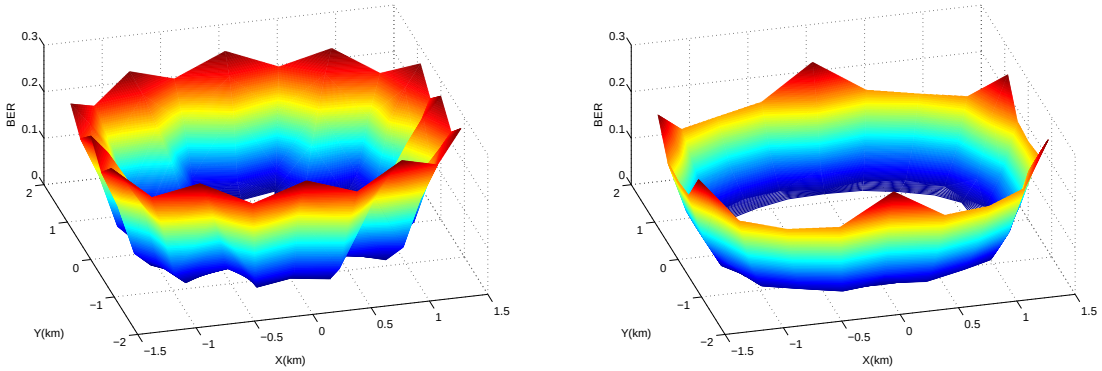


(a) The TC-16StQAM-**SISO** scheme

(b) The TC-16StQAM-**SIMO** scheme

Figure 5.16: The 3D BER versus user location performance of the TC-16StQAM-SISO scheme and the TC-16StQAM-SIMO scheme of Figure 5.9 for transmission over correlated Rayleigh fading wireless and imperfect optical channels for the whole cell with SNR = 5 dB. A phase rotation of upto $\delta = 0.1$ radian is considered in the optical link. The other simulation parameters are summarised in Table 5.3.

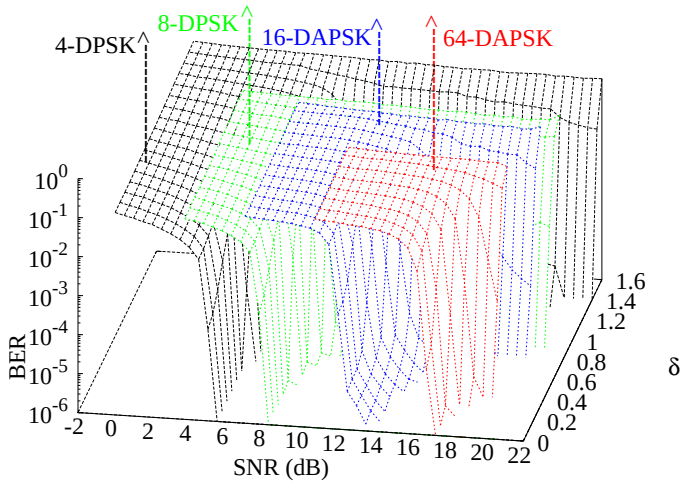


Figure 5.17: BER versus SNR versus $\delta$ performance of the ATSDD schemes of Figure 5.9 and Figure 5.11 for transmission over AWGN and imperfect optical channels. The corresponding simulation parameters are summarised in Table 5.3 and Table 5.4.

rotation of $\delta = 1.4$ radian, while the TC-64DAPK becomes disfunctional at $\delta = 0.6$ radian. Based on the performance seen in Figure 5.17, a phase rotation of upto $\delta = 0.4$ radian will be imposed in the following simulations on our proposed ATSDD scheme. The corresponding modem-mode switching levels are $\Gamma = [5.37, 8.35, 12.75, 18.88]\ dB$ when aiming for a BER of $10^{-5}$.

The PDF of each transmission mode recorded when communicating over quasi-static Rayleigh fading and our ROF channel is presented in Figure 5.18. Observe in Figure 5.18 that when the

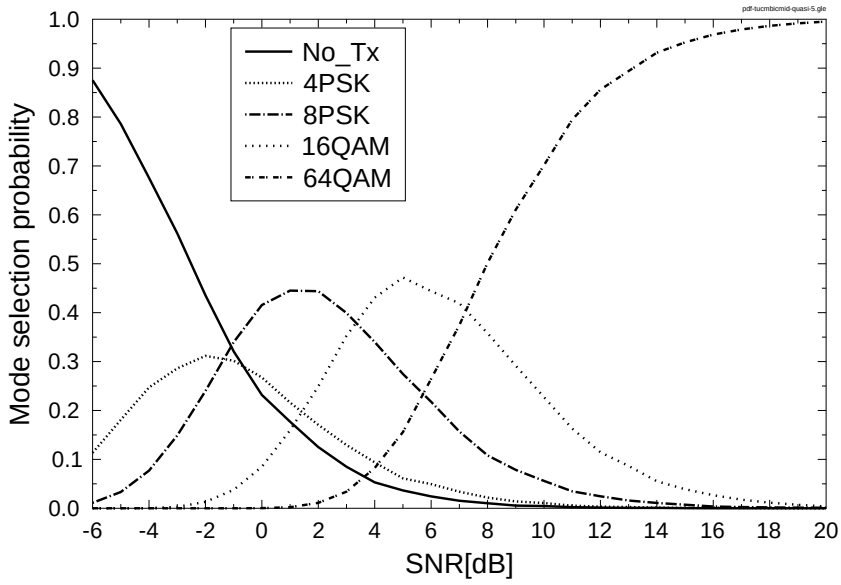


Figure 5.18: The mode selection probability of each differential modes chosen when transmitting over quasi-static Rayleigh fading and AROF optical channels when the MS locates 'B' (in Figure 5.9). A phase rotation of upto $\delta = 0.4$ radian is considered in the optical link.

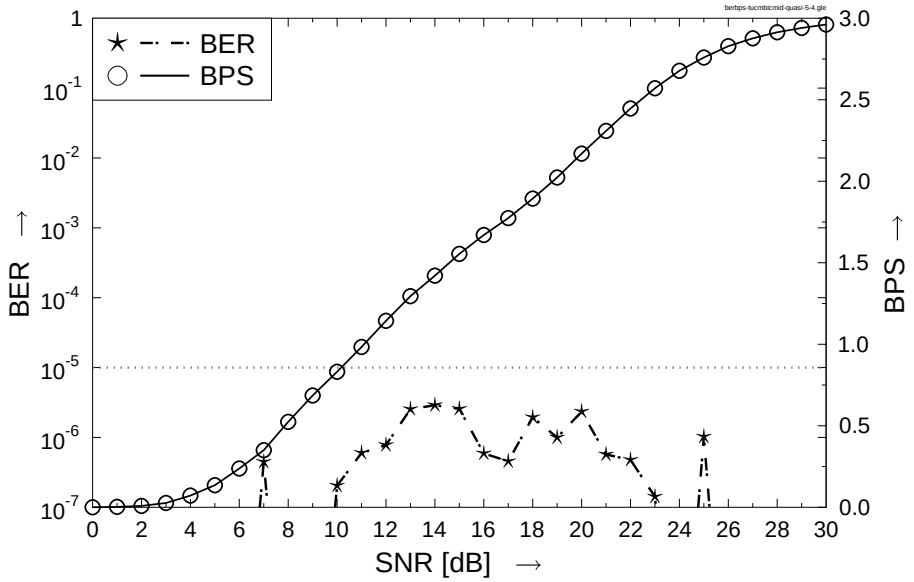


Figure 5.19: The **BER, BPS** of 4-DPSK, 8-DPSK, 16-DAPSK and 64-DAPSK for **TC** transmissions over quasi-static Rayleigh fading and imperfect optical channels when the MS locates 'B' (in Figure 5.9). A phase rotation of upto $\delta = 0.4$ radian is considered in the optical link. The relative simulation parameters are detailed in Table 5.3 and Table 5.4.

channel quality is poor, the NoTx mode is employed more frequently, while the 64-DAPSK (4,16) mode is used more often, when the SNR increases. The BER and BPS performance curves of our adaptive system are shown in Figure 5.19, where we observe that the overall BER was indeed lower than the target BER of $10^{-5}$, while the BPS curve improves, as the SNR increases.

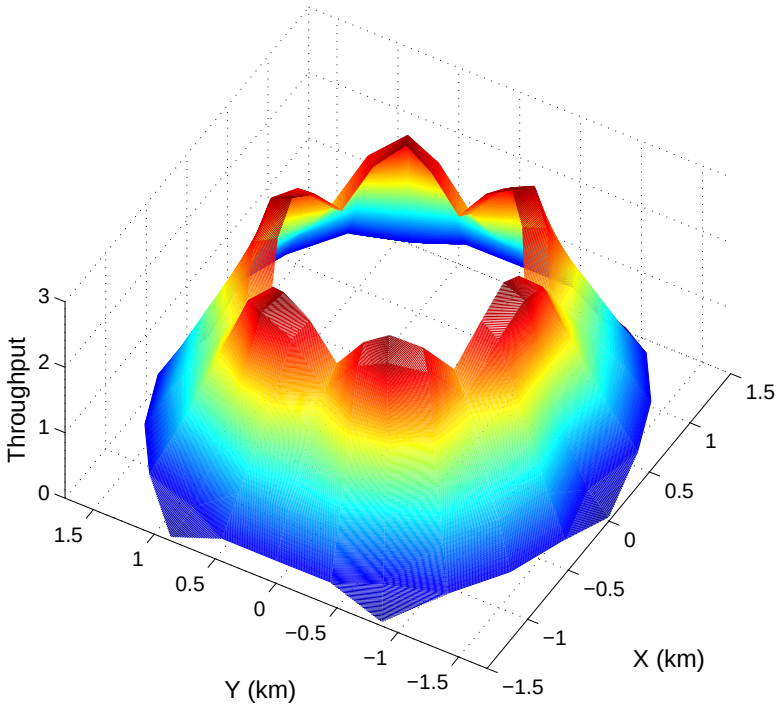


Figure 5.20: The 3D throughput for the ATSDD scheme of Figure 5.9 for transmission over quasi-static Rayleigh fading wireless and imperfect optical channels for the whole cell with SNR = 7 dB. A phase rotation of upto $\delta = 0.4$ radian is considered in the optical link. The other simulation parameters are summarised in Table 5.3 and Table 5.4.

Finally, Figure 5.20 depicts the 3D throughput performance of the ATSDD scheme for the entire area of the cell Figure 5.9 at SNR $= 7$ dB. The six distinctive throughput peaks correspond to the six locations of RAs and indicate that a higher throughput may be obtained, when the MS is closer to the RAs.

## 5.5 Conclusions

In this chapter we have investigated a 16-StQAM-TC assisted NC scheme relying on the butterfly network topology of Figure 5.1. It was found in Figure 5.2 that as expected, the achievable BER performance is affected by the location of the RN. More specifically, when the transmit power at the SNs and RN are identical, the RN located at the centre of the butterfly network topology achieves the best performance as demonstrated in Figure 5.2. However, when the power sharing approach is invoked, the optimum RN location is closer to the DNs, where another dB of power gain can be attained. The SNR threshold values of the NC scheme when transmitting over Correlated Rayleigh fading channels are summarized in Table 5.5. Furthermore, the channel capacity of the butterfly network topology is also studied.

| Channel | | Correlated Rayleigh $f_d = 0.01$ | |
|---|---|---|---|
| Memory | | 2 | |
| Decoder | | Approximate Log-MAP | |
| Code | $R_o$ | SNR Threshold (dB) | |
| | | FER=$10^{-2}$ | FER=$10^{-3}$ |
| 16-DAPSK (2,8)-TC-NC | 4/3 | 12.50 | 13.72 |
| 16-DPSK-TC-NC | 4/3 | 13.75 | 15.00 |
| 16-DAPSK (2,8)-TC-Power-Sharing | 4/3 | 11.92 | 12.90 |
| 16-DPSK (2,8)-TC-Power-Sharing | 4/3 | 13.18 | 14.50 |

Table 5.5: SNR threshold values of the NC scheme when transmitting over Correlated Rayleigh fading channels. The values are tabulated from Figure 5.4.

Then, in Section 5.3 we have proposed a soft-decision M-DAPSK aided AF based relaying scheme, which is capable of attaining a further 4.5 dB SNR gain, as seen in Figure 5.7.

Finally, in Section 5.4.1 we have investigated the uplink performance of FFR based multicell and multiuser schemes, where cooperative wireless and optical-fiber (DFO or AROF) communications were combined. In Section 5.4.1.3, we have derived the SIMO-based soft-demodulation expressions for StQAM and shown in Figure 5.13 that the proposed TC-StQAM scheme is robust to both wireless and optical-fiber induced channel impairments. More explicitly, as seen in Figures 5.14–5.16 the proposed TC-StQAM-SIMO scheme is capable of removing 6 out of 12 BER peaks at the cell-edge, despite dispensing with CSI for both the wireless and optical-fiber links. The proposed TC-StQAM-SIMO scheme constitutes an attractive low-complexity detection candidate for FFR based multicell, multiuser LTE and WiMAX systems. Furthermore, we have proposed an ATSDD scheme for AROF aided and RA-assisted uplink transmission in a FFR based multicell, multiuser system. A combination of the wireless and optical-fiber channels was considered, which imposed different imperfections. The SNR threshold values when employing our TC- soft-decision aided non-coherently detected schemes for transmission over AWGN and optical fiber channels were summarized in Table 5.6. We have demonstrated that our proposed ATSDD scheme is a practical, low complexity and energy efficient design.

| Channel | | AWGN and Optical-Fiber Channel | |
|---|---|---|---|
| Memory | | | 3 |
| Decoder | | | Approximate Log-MAP |
| Code | $\delta$ | SNR Threshold (dB) | |
| | | BER=$10^{-5}$ | BER=$10^{-6}$ |
| 4-DPSK | 0.0 | 5.20 | 5.50 |
| 8-DPSK | 0.0 | 7.80 | 8.26 |
| 16-DAPSK (2,8) | 0.0 | 12.48 | 13.52 |
| 64-DAPSK (4,16) | 0.0 | 16.90 | 17.27 |
| 4-DPSK | 0.2 | 5.20 | 5.50 |
| 8-DPSK | 0.2 | 7.81 | 8.26 |
| 16-DAPSK (2,8) | 0.2 | 12.49 | 13.53 |
| 64-DAPSK (4,16) | 0.2 | 17.11 | 17.35 |
| 4-DPSK | 0.4 | 5.37 | 5.50 |
| 8-DPSK | 0.4 | 8.35 | 8.76 |
| 16-DAPSK (2,8) | 0.4 | 12.75 | 14.51 |
| 64-DAPSK (4,16) | 0.4 | 18.88 | 18.37 |
| 4-DPSK | 0.6 | 5.75 | 6.00 |
| 8-DPSK | 0.6 | 8.40 | 8.78 |
| 16-DAPSK (2,8) | 0.6 | 13.31 | 15.51 |
| 64-DAPSK (4,16) | 0.6 | error-floor | error-floor |

Table 5.6: SNR threshold values of TC- soft-decision aided non-coherently detection schemes when transmitting over AWGN and optical fiber channels. The values are tabulated from Figure 5.17.

Chapter 6

# Conclusions and Future Work

In this concluding chapter, a summary of the thesis and the main findings of our investigations will be presented in Section 6.1, followed by a range of ideas for future research in Section 6.3.

## 6.1 Summary and Conclusions

**Chapter 1** constitutes the background of our research throughout this thesis. More specifically, a rudimentary overview of both the channel capacity and of EXIT charts based on the concept of mutual information was provided in Section 1.1. Then, the history of coded modulation and adaptive coded modulation was outlined in Section 1.2. This provided the foundations for our further investigations of the proposed solutions. Furthermore, the outline of the thesis was presented in Section 1.3. Finally, the motivation and novel contributions of the thesis were detailed in Section 1.4.

In **Chapter 2**, we investigated coherent coded modulation schemes in the context of both *fixed* and *adaptive modes*. The fixed mode based schemes were investigated in Section 2.2. More specifically, we commenced our discussions with a rudimentary introduction to TTCM and BICMI-ID in Section 2.2.3 and Section 2.2.4.2, respectively. Then in Section 2.2.5, we presented simulation results for 4PSK, 8PSK, 16QAM and 64QAM aided TTCM and BICM-ID schemes, when communicating over both AWGN and uncorrelated Rayleigh fading channels. It was found in Figure 2.14 and Figure 2.15 that the performance of the TTCM was 0.5 dB–2.5 dB better than that of BICM-ID, when transmitting over AWGN channels, while imposing the same complexity. All the 4PSK-TTCM, 8PSK-TTCM and 16QAM-TTCM systems had a better BER performance than that of BICM-ID, when communicating over uncorrelated Rayleigh fading channels at a given complexity, as shown in Figure 2.16 and Figure 2.17. Furthermore, the $E_b/N_0$ and $SNR$ values required for both the TTCM and BICM-ID schemes communicating over the AWGN and uncorrelated Rayleigh fading channels at BER = $10^{-5}$ and BER = $10^{-6}$ were listed in Table 2.5 and Table 2.7, respectively. These thresholds were then used as the mode-switching thresholds for our adaptive scheme

in Section 2.3.1.1. The performance of our near-instantaneously adaptive coded modulation scheme communicating over both quasi-static as well as over the shadow-and-fast Rayleigh fading channels defined in Section 2.3.2.1 were shown in Section 2.3.2. The higher-order modes were activated more frequently compared to their lower-order counterparts upon increasing the SNR, as demonstrated by Figures 2.25 and 2.27. Furthermore, the BPS throughput increased smoothly, while the BER was maintained below $10^{-6}$, when transmitting over the quasi-static as well as shadow-and-fast Rayleigh fading channels, as shown in Figures 2.26 and 2.28. As expected, the performance recorded for transmission over the quasi-static Rayleigh fading channel was better than that over the shadow-and-fast Rayleigh fading channel owing to the more benign characteristics of the quasi-static channel.

Following the investigation of coherent coded modulation in Chapter 2, we proposed novel soft-decision aided non-coherent coded modulation schemes in **Chapter 3**. The fixed mode performance of the soft-decision aided schemes was investigated in Section 3.2, where the concept of the soft-decision StQAM aided BICM-ID scheme was detailed in Section 3.2.1. The simulation results of Figure 3.4 show that the optimum ring ratio of the twin-ring StQAM was 0.2, which was then employed in our simulations. Figure 3.6 illustrated that the 16-DAPSK (2,8)-BICM scheme outperforms the 16DPSK-BICM scheme by approximately 12 dBs at a BER of $10^{-6}$. Furthermore, observe in Figure 3.6 that 16-DAPSK (2,8)-BICM-ID outperforms the non-iterative 16-DAPSK (2,8)-BICM by approximately 2 dB after the *second iteration* with the aid the extrinsic bit-probabilities of Equation (3.11) and Equation (3.12). The EXIT curve of the outer CC of the BICM-ID scheme does not match the shape of the soft decision aided 64-DAPSK (4,16) demapper, while that of the outer TC in the TuCM scheme does, as shown in Figure 3.13. Hence, the TuCM scheme was considered in our multi-ring DAPSK investigations conducted in Section 3.2.2. Furthermore, offset DAPSK is also considered in order to facilitate the employment of a less stringent linear power amplifier at the transmitter. Observe in Figure 3.14 that compared to the identical-throughput TuCM assisted 64-DPSK scheme, the 4-ring based TuCM assisted 64-ary DAPSK arrangement has a power-efficiency improvement of 4.2 dB at a bit error ratio of $10^{-5}$. Furthermore, when the TC block size is increased, the system operates closer to the channel capacity. The simulation results of Figure 3.15 showed that when using a TC block length of 400 modulated symbols, the 64 DAPSK (4, 16) scheme is 7.56 dB away from its capacity curve, while it had a reduced gap of 2.25 dB, when using a longer TC block length of 40 000 modulated symbols. Then, adaptive soft-decision aided non-coherent coded modulation schemes were proposed in Section 3.3 and their performance was investigated in Section 3.3.2, when communicating over both quasi-static as well as shadow-and-correlated Rayleigh fading channels.

In **Chapter 4**, we investigated the employment of coded modulation schemes for cooperative communications. Firstly, we proposed a hybrid technique of mitigating the effects of RN-induced error propagation in Section 4.2, which takes into consideration both the RN-BER (as detailed in Section 4.2.1.1) and the RN location (as detailed in Section 4.2.1.2) for mitigating the error propagation. The results shown in Figure 4.6 demonstrated that this technique is particularly beneficial,

when the BER at the RN is high, since transmit power reductions of up to 19 dB may be attained at a BER of $10^{-4}$. Secondly, relay aided ACM schemes were conceived in Section 4.3 for cooperative communications over the quasi-static and shadow-and-fast Rayleigh fading channels. The SNR switching thresholds were listed in Tables 3.4–3.6, while the related ACM performance of cooperative communications was characterized in Figures 4.16–4.23. Then in Section 4.4 we proposed the adaptive TTCM (ATTCM) aided Distributed Space-Time Trellis Coding (STTC) scheme of Figure 4.25 for cooperative communication over quasi-static Rayleigh fading channels. An ATTCM scheme is employed by the SN of Figure 4.25 during the first transmission period for reliably conveying the source bits to $N$ number of RNs by appropriately adjusting the code-rate and modulation mode according to the near-instantaneous channel conditions. The TTCM switching thresholds were carefully chosen for ensuring that the BER at each RN becomes lower than $10^{-6}$ in order to minimise the potential error propagation imposed by the RNs. During the second transmission period, an $N$-antenna assisted Distributed STTC (DSTTC) scheme is created with the aid of the aforementioned $N$ single-antenna relay nodes as portray in Figure 4.26. More specifically, $N$ relay nodes are utilised to form STTC codewords based on the re-encoded TTCM symbols of the relays for transmission to the DN. At the DN, iterative extrinsic information exchange is performed between the STTC and TTCM decoders for recovering the original source bits. It is shown in Figure 4.29 that the proposed ATTCM-DSTTC scheme requires 12 dBs less transmission power in comparison to a standard TTCM scheme, when aiming for a frame error ratio of $10^{-3}$.

Following the investigation of coherent coded modulation schemes designed for cooperative communications in Chapter 4, we focused our research efforts on their non-coherent coded modulation counterparts in **Chapter 5**. Firstly, based on the soft-decision aided DAPSK scheme of Chapter 3, we investigated a 16-StQAM-TC assisted NC scheme relying on the butterfly network topology of Figure 5.1 in Section 5.2. As expected, the achievable BER performance is affected by the location of the RN. More specifically, as seen in Figure 5.2, when the transmit power at the SNs and RN are identical, the RN located at the centre of the butterfly network topology achieves the best performance. However, when power sharing is invoked in Section 5.2.1.2, the optimum RN location was found to be closer to the DNs, where another dB of power gain can be attained, as evidenced by Figure 5.3. Then, the NC capacity was investigated in Section 5.2.1.3. Figure 5.5 showed that the achievable capacity of the NC aided scenario is higher compared to the single-link scenario. Secondly, the soft-decision M-DAPSK scheme of Section 5.3 was incorporated into an AF based cooperative communication system in Section 5.3. As demonstrated in Figure 5.7, an AF based cooperative communication system obtained about 4.5 dB SNR improvement for a TC block length of 40 000 modulated symbols, compared to that of the traditional point-to-point transmission. Finally, in Section 5.4 we proposed a low-complexity cooperative wireless and optical-fiber communication scheme for uplink communication in a FFR based multicell, multiuser system. More specifically, the FFR principle is invoked for improving the cell-edge performance without reducing the throughput of the cell-center. Each cell is illuminated with the aid of six Remote Antennas (RAs), which are connected to the central base-station with the aid of realistically modelled

imperfect optical-fiber links. When a Mobile Station (MS) is located at the cell-edge, the two nearest RAs can be invoked for detecting and forwarding the user's signal to the base-station, based on the Single-Input Multiple-Output (SIMO) principle. The FFR systems, basic philosophy was presented in Figure 5.8. Furthermore, we employed both the DFO and AROF of Section 5.4.1.1 for the optical fiber link, as detailed in Section 5.4.1. Furthermore, we designed a Turbo Coded (TC) 16-level Star-Quadrature Amplitude Modulation (StQAM) scheme for supporting optical-fiber-aided cooperative wireless transmission in Section 5.4.1.3, where the receiver does not have to estimate the channel state information. Hence, a lower detection complexity can be achieved, when compared to coherently detected schemes, albeit naturally, at a 3 dB power-loss. We also investigated the effect of phase-rotations imposed by imperfect optical-fiber links. The simulation results in Figure 5.14a and Figure5.14b showed that our non-coherent TC-StQAM scheme is robust to both wireless and optical-fiber imperfections. More explicitly, the proposed TC-StQAM-SIMO scheme is capable of removing 6 out of 12 BER peaks at the cell-edge, despite dispensing with CSI for both the wireless and optical-fiber links. Furthermore, we have also proposed an ATSDD scheme for AROF aided and RA-assisted uplink transmission in a FFR based multicell, multiuser system in Section 5.4.1.4. A combination of the wireless and optical-fiber channels was considered, which imposed different imperfections. We have demonstrated that our proposed ATSDD scheme was a practical, low complexity, energy efficient design in Figures 5.18–5.20.

## 6.2 Design Guidelines

In this section, we summarize the general design guidelines of coherent and non-coherent coded modulation schemes conceived for cooperative communications by examining the various schemes investigated throughout Chapters 1– 5.

1. Non-coherent Coded Modulation Design:

   (a) Differentially encoded and non-coherently detected modulation techniques have a low complexity, since they do not require any CSI. However, when channel coding is incorporated into M-DAPSK ($M_a$,$M_p$), its performance remains far from the corresponding detection-dependent DCMC's capacity owing to the employment of hard-decision based demodulation. *Hence, the family of soft-decision aided non-coherent demodulation may be recommended for low-complexity, near-capacity yet energy-efficient designs, bearing in mind that the closer the system is operated to its capacity, the higher its complexity and delay.*

   (b) The above-mentioned soft-decision aided non-coherent detector designs may involve several design aspects, such as the choice of separate amplitude and phase detection versus their joint detection, the determination of the optimal ring ratios for different M-DAPSK schemes, the interleaver length and the particular bit-to-symbol mapping methods employed, which fundamentally determine the properties our proposed soft-

decision aided M-DAPSK systems. *Hence these parameters have to be carefully chosen using the EXIT charts for designing near-capacity coded modulation schemes.*

(c) As another low-complexity, energy-efficient non-coherent coded modulation design, the family of near-instantaneous by adaptive schemes was conceived in Section 3.3, which were based on our fixed-mode soft-decision aided M-DAPSK schemes. More specifically, the transmitter extracts the coded modulation mode required by the receiver for achieving its target integrity from the reverse-link transmission burst in order to accommodate the channel-quality fluctuations. *As a design-lesson, the fixed CM-modes have to be incorporated into near-instantaneous adaptive transceivers for the sake of maintaining the target-BER, whist achieving the highest possible throughput.*

2. Coherent and Non-coherent Coded Modulation for Cooperative Communications Design:

(a) Cooperative communications has emerged recently as a strong candidate for improving the cell-edge coverage. While DF relaying is prone to RN-induced error propagation owing to decoding errors, AF techniques fails to improve the SNR, because both the signal and the noise are amplified together. Hence, the challenges of RN-induced error-propagation and the acquisition of CSI must be tackled before it wide-spread practical employment. Hence, we embarked on mitigating the RN-induced error-propagation in the context of coherent CM systems in the DF scenarios, while non-coherent coded modulation dispensing with CSI was conceived for AF scenarios. *Explicitly, for the more complex, but higher-performance DF schemes coherent detection may be recommenced, while the combination of AF relaying and non-coherent detection is ideal for low-cost designs.*

(b) Coherent Coded Modulation for Cooperative Communication Design:

- The RNSPA technique was designed for mitigating the RN-induced error propagation in Section 4.2. More specifically, the system selected the most appropriate relay based on the transmit power level required for guaranteeing reliable relaying, whilst also considering the RN-BER. As demonstrated in Figures 4.3−4.11, our RNSPA technique is particularly beneficial, when the BER at the RN is high. As a design-lesson, in addition to the careful choice of AF/DF relaying as well as coherent vs non-coherent detection, also relay-selection play a crucial role in determining the attainable performance.
- Both non-coherently and coherently detected adaptive coded modulation may also be invoked in cooperative systems as another improvement.
- In Section 4.4, we designed an ATTCM-DSTTC scheme for cooperative communications as another diversity-gain improvement for the sake of mitigating the RN-induced error propagation and ultimately for saving energy. More specifically, an ATTCM scheme was employed for the SR link for the sake of realising the full potential of various TTCM schemes, where the RN-induced error propagation was

minimised. This is because the ATTCM scheme is capable of counteracting the time-varying nature of the mobile radio channels. Explicitly, a higher-rate code and/or a higher-order modulation mode are employed, when the instantaneous estimated channel quality is high in order to increase the number of BPS transmitted. Conversely, a more robust lower-rate code and/or a lower-order modulation mode are employed, when the instantaneous channel quality is low, in order to improve the mean BER.

Furthermore, the DSTTC scheme of Section 4.4.2 was invoked for the RD links for the sake of achieving a spatial diversity gain for the RD links. *In conclusion, whilst the co-located antenna elements of classic STTC are prone to shadow-fading, this problem is circumvented by the distributed elements of cooperative/distributed STTCs.*

(c) Non-Coherent Coded Modulation for Network-Coded Cooperative Communications:

- In Section 5.2.1.1 first designed a soft-decision aided M-DAPSK aided TC based physical layer for a butterfly-structured NC system relying on the DF relaying protocol. The role of NC is that of improving both the achievable throughput and the diversity gain. More specifically, the butterfly-structured NC scheme allows a single RN to combine the information received from two different SNs, before broadcasting the information to two different DNs. Furthermore, an efficient power sharing mechanism was designed for further reducing the overall transmit power requirement of the network in Section 5.2.1.2. *In a nutshell, NC may be recommended for eliminating the half duplex throughput loss of conventional AF/DF relaying.*
- *Finally, non-coherent coded modulation schemes may be recommended as a sophisticated combination of wireless mobile systems and optical fiber links, as detailed in Section 5.4. Non-coherent by detected coded modulation schemes are particularly suitable for optical fiber links, where the employment of coherent detention still remains a research challenge to a large extent.*

## 6.3 Suggestions for Future Work

The research illustrated in this thesis can be extended in several directions. In this section, we highlight a number of potential future research ideas.

### 6.3.1 Optimization Analysis for Soft-Decision aided M-DAPSK

In Chapter 3, we derived new soft-decision demodulation formulas for M-DAPSK. We also determined the optimal ring ratios for our proposed soft-decision detector. The subject of constellation design has been an active research topic [59, 227–233] in context of conventional coherent trans-

mission. By contrast, the design of the optimal constellations for differential modulation schemes has failed to attract sufficient research efforts. As demonstrated in Chapter 3, the choice of bit-to-symbol mapping method substantially influences the performance of the soft-decision aided M-DAPSK system. Therefore, the optimisation of constellation labelling for the soft-decision aided M-DAPSK systems is of immediate interest. As a further improvement, *low-complexity, low-power* techniques have to be designed for the overall network context, when considering realistic multi-user, multi-cell scenarios instead of single-user links. More specifically, all performance improvements achieved by more sophisticated and more complex signal processing have to be justified in the light of the extra power-consumption in the above holistic design context. The whole system may also be optimised in terms of the choice of code-rates and puncturing-rates, the required memory and the iterative decoding performance achieved with the aid of exchanging extrinsic information.

### 6.3.2 Multiple-Symbol Detection Aided M-DPSK/DAPSK

Based on Chapter 3, a new soft-decision aided M-DPSK/DAPSK detection method was proposed in [104, 105], which achieved the optimum differential detection capability at a substantially reduced detection complexity. The conventional single-symbol M-DPSK/DAPSK detection philosophy can be extended to Multi-Symbol Differential Detection (MSDD), Multiple-Symbol Differential Sphere Detection (MSDSD), Decision-Feedback Differential Detection (DFDD) and Linear Prediction aided Differential Detection (LPDD). Let us briefly consider the hard-decision scenario. In the MSDD scheme, the determinant of the correlation matrix is a constant for M-DPSK [234–238], but it is not a constant for M-DAPSK. Hence, it is easier to invoke for an MSDSD M-DPSK scenario, but it deserves research efforts to solve this problem also for M-DAPSK. However, the transmit symbols of M-DAPSK do not have a constant amplitude value. We might circumvent this problem in tow different ways. On the one hand, we can dynamically update the determinant of the correlation matrix according to the tentative transmitted candidate symbol [239], which may involve a high complexity but it provides the optimal solution. On the other hand, separate amplitude and phase detection [240] may be employed at a reduced complexity, which might exhibit an error floor. The same problems exist for the soft-decision scenario.

### 6.3.3 Coded Modulation for the Uplink/Downlink of the Long-Term Evolution System

For the LTE downlink, Orthogonal Frequency Division Multiplexing (OFDM) [241] is relying on a large number of parallel, narrow-band subcarriers is used. For the uplink, where the available transmission power is significantly lower than for the downlink, the situation is somewhat different. One of the most important factors in the uplink design is to facilitate the employment of power-efficient amplifiers. Hence, single-carrier frequency-division multiple access (SC-FDMA) is used for the LTE uplink [242]. Employing channel coding for further improving the performance

of OFDM systems has also been studied in [243–247]. For example, LDPC codes combined with OFDM are capable of providing a significant performance improvement as compared to uncoded systems [246]. Furthermore, BICM and BICM-ID have also been investigated in the context of OFDM systems [243–245], while LDPC coded SC-FDMA was studied in [248]. As a further extension of the LTE uplink/downlink, we can employ the proposed soft-decision aided non-coherent CM schemes for reducing the complexity.

### 6.3.4 Space-Time-Coded Modulation for Combined Wireless and Optical Communications

Space-time codes have been proposed for wireless communications in order to exploit all the degrees of freedom available in a MIMO channel [249–252]. The space-time channel coding technique has been proposed for amalgamated wireless and optical channels in [253]. Space-Time Coded Modulation (STCM) was proposed as a further improvement for wireless communications, which jointly designed space-time coding and CM [250, 254]. As another further research idea, we might investigate a STCM system conceived for both the downlink and uplink in combined wireless and optical communications.

### 6.3.5 Space-Frequency-Time Coded Modulation for Broadband Wireless Communications

The application of space-frequency-time coding combined with OFDM was recently presented as attractive solution for future high data rate wireless communications [255, 256]. Reducing the energy consumption [214] in wireless communications has recently drawn increasing attention from the research community. Hence, we might investigate a joint spacial-domain, frequency-domain and time-domain coded modulation techniques conceived for future energy-efficient solutions.

### 6.3.6 Superposition-Based ACM for MIMO-OFDMA Systems

Orthogonal Frequency Division Multiple Access (OFDMA) has become the dominant multiple access scheme for next generation wireless networks, since both of the LTE system and the IEEE 802.16m system have adopted OFDMA as their multiple access technology [257]. In OFDMA systems, multi-user diversity can be exploited not only for increasing the achievable network capacity but also for reducing the energy consumption [258]. We might propose a superposition-based [164] ACM for MIMO-OFDMA networks. More specifically, we could select the optimal modulation corresponding to the near-instantaneous channel conditions by using superposition based modulation for increasing the achievable efficiency.

### 6.3.7 An Iterative Technique for Mitigating the RN-induced Error Propagation

In Section 4.2, a technique referred to as the Correcting the Relay's Decoding Errors at the Destination (CRDED) was employed for mitigating the RN-induced error propagation. However, as seen in Figure 4.2, the RN-BER $\triangle c_k^i$ was only taken into account by the symbol-to-bit demapper of the RD link. We might employ a joint iterative processing based on $y_{sd}$, $y_{rd}$ and $\triangle c_k^i$ for further improving the end-to-end performance. More specifically, an iterative decoding scheme exchanging extrinsic information between the SR-link's demapper, the RD-link's demapper and a CM decoder may be designed with the aid of EXIT charts for approaching the achieveable capacity.

# Appendix A

## A.1 Appendix to Chapter 2

Figure A.1 was obtained by transmitting 10 000 frames, each having a block length of 12 000 symbols. The number of iterations was $I_t = 4$ over the AWGN channel. Figure A.2 was generated for the 12 000 symbol block length and $I_t = 4$ iterations over the uncorrelated Rayleigh fading channel. It is worth noting that the value of $\text{SNR}_{min}$ varies with the number of iterations and block size.

## A.2 Appendix to Chapter 3

Figure A.3 shows the BER performance of the BICM-ID-64-DAPSK (4,16) scheme when communicating over the correlated Rayleigh fading channel associated with $f_d = 0.01$ and $f_d = 0.001$ using the parameters listed in Table 3.7. Figure A.4 presents the constellation diagrams of the 8-DAPSK (4, 2), 16-DAPSK (4, 4), 32-DAPSK (4, 8) and 64-DAPSK (4, 16) modulation schemes.

## A.3 Appendix to Chapter 5

### A.3.1 Peak Power and Average Power

The peak power of an optical pulse is the maximum occurring optical power. The peak power is often calculated from the full width at half-maximum pulse duration $T_{FWHM}$ and the pulse energy $E_p$. The conversion depends on the temporal shape of the pulse. For example, for Gaussian-shaped pulses, the peak power may be expressed as [259]:

$$P_{peak} \approx 0.94 \frac{E_p}{T_{FWHM}}. \tag{A.1}$$

The average power is the pulse energy averaged over the full period $T$, which might be formulated as:

$$P_{avg} \approx \frac{E_p}{T_{all}}. \tag{A.2}$$

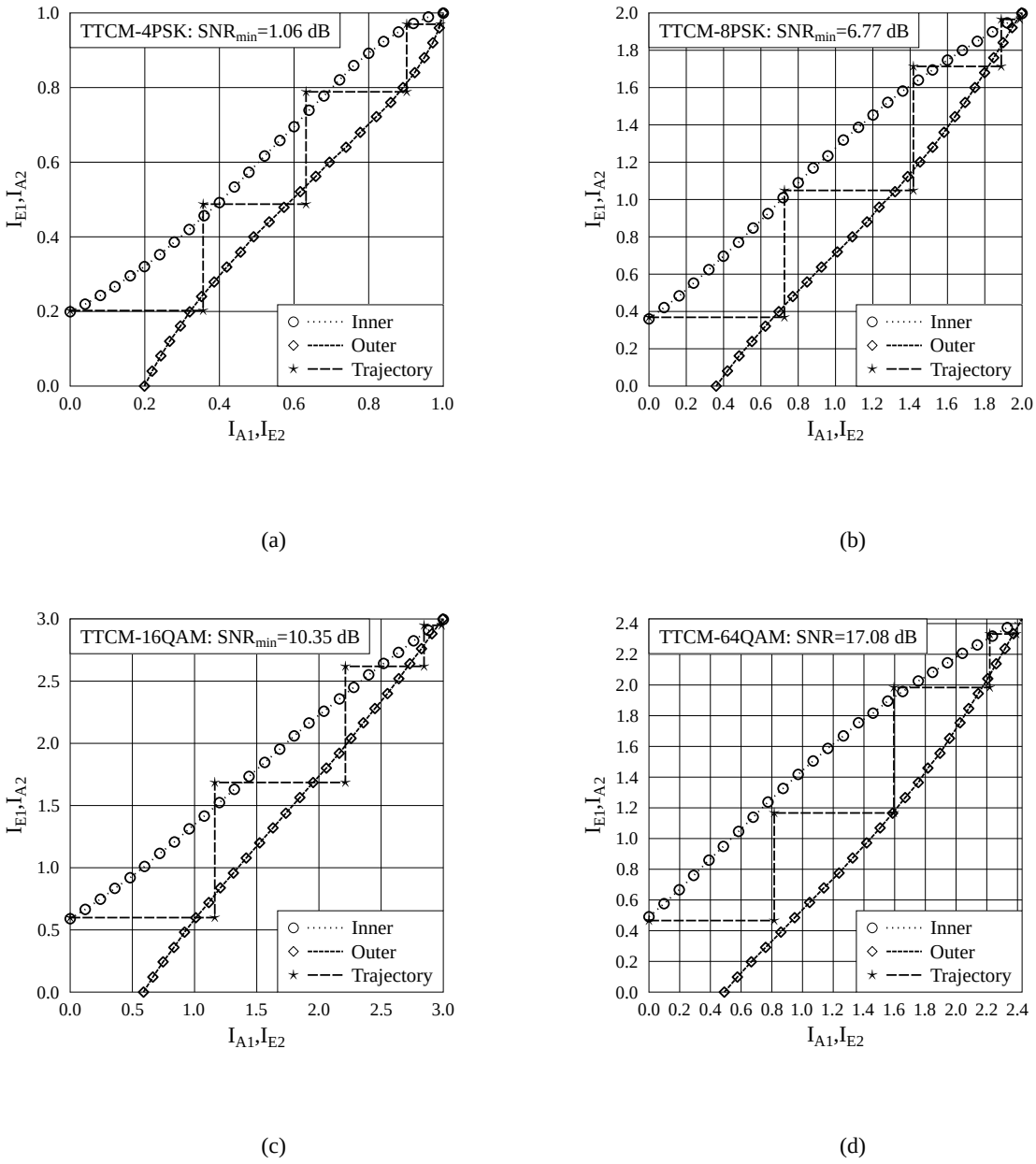


Figure A.1: EXIT charts of **4PSK, 8PSK, 16QAM and 64QAM** for **TTCM** when communicating over the **AWGN channel** with SNR$_{min}$.

Based on Equations (A.1)–(A.2), the conversion between the peak power and the average power may be written as [259]:

$$P_{peak} \approx 0.94 \frac{P_{avg} T_{all}}{T_{FWHM}} \tag{A.3}$$

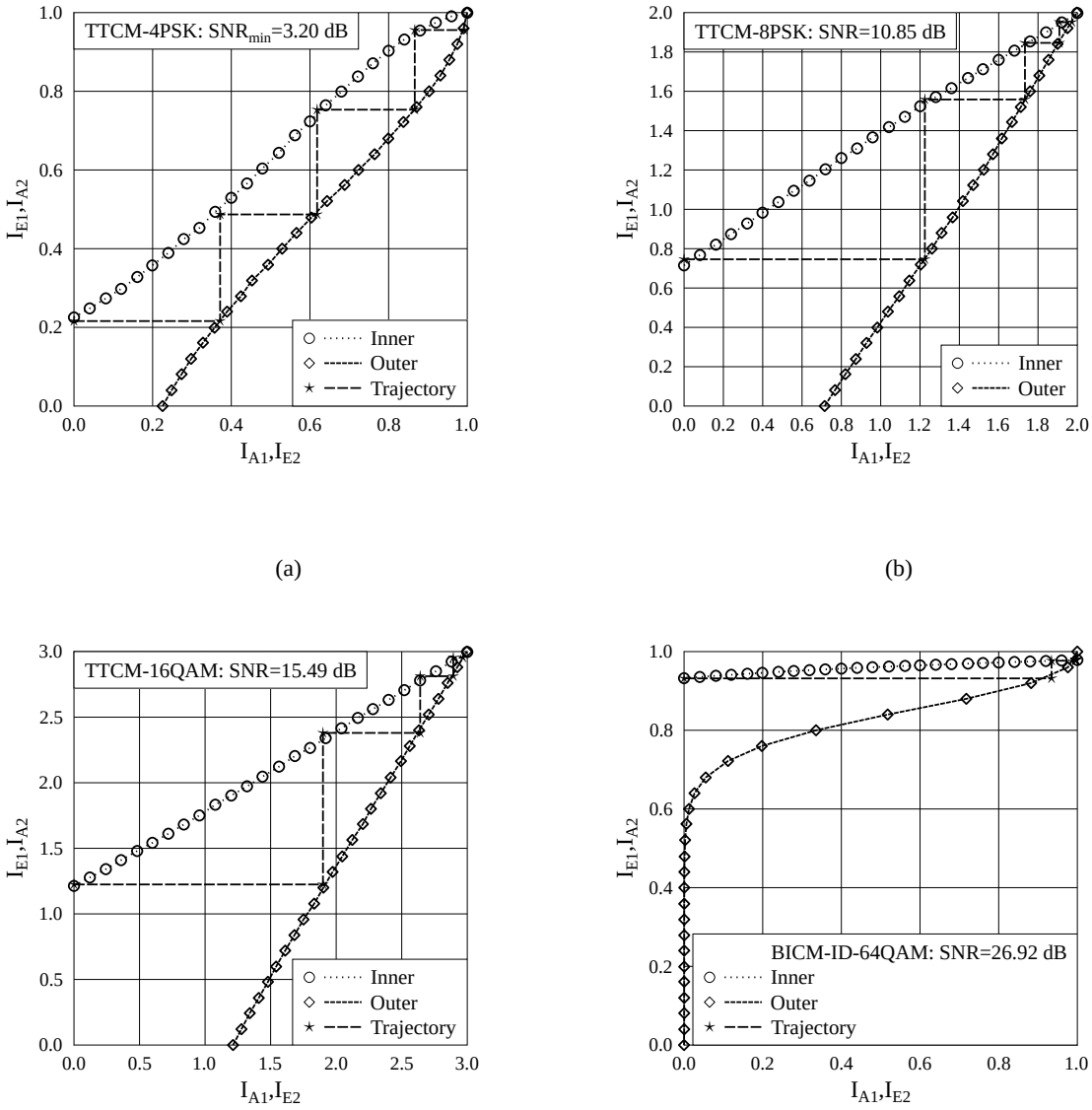


Figure A.2: EXIT charts performance of **4PSK, 8PSK, 16QAM and 64QAM** for **TTCM** when communicating over the **uncorrelated Rayleigh fading channel** with SNR$_{min}$.

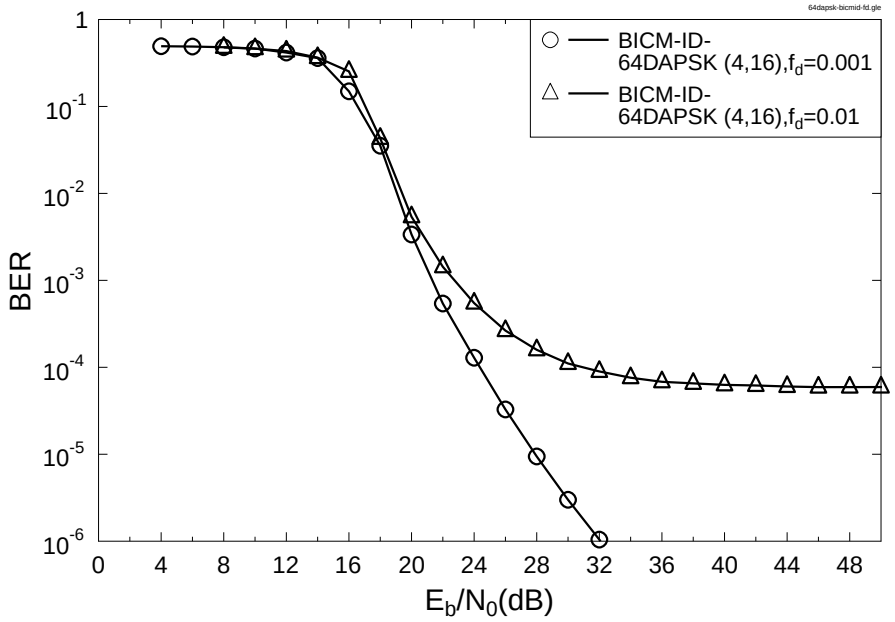


Figure A.3: BER performance of the BICM-ID aided 64-DAPSK (4,16) scheme when communicating over a **correlated Rayleigh fading channel** associated with $f_d = 0.01$ and $f_d = 0.001$. The simulation parameters are shown in Table 3.7.

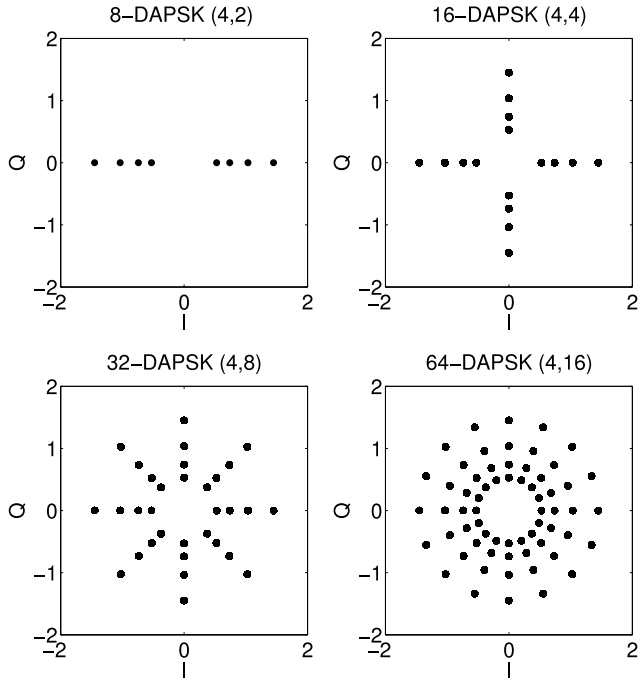


Figure A.4: Constellation diagrams of the M-DAPSK (4, $M_p$) modulation schemes.

# Bibliography


[1] C. E. Shannon, “A mathematical theory of communication,” *Bell System Technical Journal*, pp. 379–423 and 623–656, June and October 1948.

[2] T. M. Cover and J. A. Thomas, *Elements of information theory*. John Wiley Sons, Inc., 1991.

[3] G. Ungerböeck, “Channel coding with multilevel/phase signals,” *IEEE Transactions on Information Theory*, vol. 28, pp. 55 – 67, Jan. 1982.

[4] J. G. Proakis, *Digital communications*. New York: McGraw-Hill, 1995.

[5] R. Gallager, *Information theory and reliable communication*. John Wiley and Sons, 1968.

[6] L. Hanzo, S. X. Ng, T. Keller, and W. T. Webb, *Quadrature amplitude modulation: From basics to adaptive trellis-coded, turbo-equalised and space-time coded OFDM, CDMA and MC-CDMA systems*. Hardcover, Wiley-IEEE Press, 2004.

[7] E. Kreyszig, *Advanced engineering mathematics*. John Wiley and Sons, 1993.

[8] P. E. McIllree, *Channel capacity calculations for M-ary N-dimensional signal sets*. The University of South Australia: M. Eng thesis, 1995.

[9] P. E. McIllree, “Calculation of channel capacity for M-ary digital modulation signal sets,” in *Proceedings of IEEE International Conference on Information Engineering*, (Singapore), pp. 639–643, 1993.

[10] G. Ungerböck, *Channel coding with multilevel/phase signals*. IEEE Transactions on Information Theory, Vol. IT-28, pp. 55-67, January 1982.

[11] L. Hanzo, W. T. Webb, and T. Keller, *Signal-and multi-carrier quadrature amplitude modulation*. New York: IEEE Press-John Wiley, 2002.

[12] G. J. Foschini and M. J. Gans, “On limits of wireless communications in a fading environment when using multiple antennas,” *Wireless Personal Communications*, vol. 6, pp. 311–335, March 1998.

[13] I. S. Reed and R. A. Scholtz, "N-orthogonal phase modulated codes," *IEEE Transactions on Information Theory*, vol. 12, pp. 388–395, July 1966.

[14] W. C. Lindsey and M. K. Simon, "L-orthogonal signal transmission and detection," *IEEE Transactions on Communications*, vol. COM-20, pp. 953–960, October 1972.

[15] S. ten Brink, "Convergence behavior of iteratively decoded parallel concatenated codes," *IEEE Transactions on communications*, vol. 10, pp. 1721–1737, October 2001.

[16] S. X. Ng, J. Kliewer, O. R. Alamri, and L. Hanzo, "On the design of turbo trellis coded modulation schemes using symbol-based exit charts," *IEEE Vehicular Technology Conference*, pp. 25–28, September 2006.

[17] S. X. Ng, O. R. Alamri, Y. Li, J. Kliewer, and L. Hanzo, "Near-capacity turbo trellis coded modulation design based on EXIT charts and union bounds," *IEEE Transactions on Communications*, vol. 56, pp. 2030–2039, December 2008.

[18] J. Kliewer, S. X. Ng, and L. Hanzo, "Efficient computation of EXIT functions for nonbinary iterative decoding," *IEEE Transactions on Communications*, vol. 54, pp. 2133–2136, 2006.

[19] S. X. Ng, J. Wang, and L. Hanzo, "Unveiling near-capacity code design: the realization of Shannon's communication theory for MIMO channels," *IEEE ICC (Beijing, China)*, 2008.

[20] H. E. Gamal and A. R. Hammons, "Analyzing the turbo decoder using Gaussian approximation," *IEEE Transactions Information Theory*, vol. 47, pp. 671–686, 2001.

[21] D. Divsalar, S. Donlinar, and F. Pollara, "Iterative turbo decoder analysis based on density evolution," *IEEE Journal Select. Areas Commun*, vol. 19, pp. 891–907, 2001.

[22] S. X. Ng, T. H. Liew, L.-L. Yang, and L. Hanzo, "Comparative study of TCM, TTCM, BICM and BICM-ID schemes," in *IEEE Vehicular Technology Conference*, vol. 4, pp. 2450 –2454 vol.4, 2001.

[23] C. E. Shannon, "Communication in the presence of noise," *Proceedings of the IRE*, vol. 37, pp. 10 – 21, Jan. 1949.

[24] R. Hamming, "Error detecting and error correcting codes," *Bell System Technical Journal*, pp. 147–160, 1950.

[25] I. Reed, "A class of multiple-error-correcting codes and the decoding scheme," *IRE Professional Group on Information Theory*, vol. 4, pp. 38 –49, Sep. 1954.

[26] P. Elias, "Coding for noisy channels," *IRE Convention Record, pt.4*, pp. 37–47, 1955.

[27] R. Gallager, "Low-density parity-check codes," *IRE Transactions on Information Theory*, vol. 8, pp. 21 –28, Jan. 1962.

[28] G. J. Forney, R. Gallager, G. Lang, F. Longstaff, and S. Qureshi, "Efficient modulation for band-limited channels," *IEEE Journal on Selected Areas in Communications*, vol. 2, pp. 632 – 647, Sep. 1984.

[29] L. Bahl, C. Cullum, W. Frazer, and F. Jelinek, "An efficient algorithm for computing free distance (corresp.)," *IEEE Transactions on Information Theory*, vol. 18, pp. 437 – 439, May 1972.

[30] L. Bahl, J. Cocke, F. Jelinek, and J. Raviv, "Optimal decoding of linear codes for minimizing symbol error rate (corresp.)," *IEEE Transactions on Information Theory*, vol. 20, pp. 284 – 287, Mar. 1974.

[31] Y. Sugiyama, M. Kasahara, S. Hirasawa, and T. Namekawa, "A method for solving key equation for decoding Goppa codes," *Information and Control*, vol. 27, pp. 87–99, 1975.

[32] F. J. MacWilliam and J. A. Sloane, *The theory of error-correcting codes*. North-Holland Mathematical Library, 1977.

[33] H. Imai and S. Hirakawa, "A new multilevel coding method using error-correcting codes," *IEEE Transactions on Information Theory*, vol. 23, pp. 371 – 377, May 1977.

[34] J. Wolf, "Efficient maximum likelihood decoding of linear block codes using a trellis," *IEEE Transactions on Information Theory*, vol. 24, pp. 76 – 80, Jan. 1978.

[35] L.-F. Wei, "Trellis-coded modulation with multidimensional constellations," *IEEE Transactions on Information Theory*, vol. 33, pp. 483 – 501, July 1987.

[36] D. Divsalar and M. K. Simon, "Multiple trellis coded modulation (MTCM)," *IEEE Transactions on Communications*, vol. 36, pp. 410 –419, Apr. 1988.

[37] G. J. Pottie and D. P. Taylor, "Multilevel codes based on partitioning," *IEEE Transactions on Information Theory*, vol. 35, pp. 87 –98, Jan. 1989.

[38] A. R. Calderbank, "Multilevel codes and multistage decoding," *IEEE Transactions on Communications*, vol. 37, pp. 222 –229, Mar. 1989.

[39] J. Hagenauer and P. Hoeher, "A Viterbi algorithm with soft-decision outputs and its applications," in *IEEE Global Telecommunications Conference*, pp. 1680 –1686 vol.3, Nov. 1989.

[40] W. Koch and A. Baier, "Optimum and sub-optimum detection of coded data disturbed by time-varying intersymbol interference [applicable to digital mobile radio receivers]," in *IEEE Global Telecommunications Conference*, vol. 3, pp. 1679 –1684, Dec 1990.

[41] W. T. Webb, L. Hanzo, and R. Steele, "Bandwidth efficient QAM schemes for Rayleigh fading channels," *IEE Proceedings I, Communications, Speech and Vision*, vol. 138, pp. 169 –175, June 1991.

[42] E. Zehavi, "8-PSK trellis codes for a rayleigh channel," *IEEE Transactions on Communications*, vol. 40, pp. 873 –884, May 1992.

[43] C. Berrou, A. Glavieux, and P. Thitimajshima, "Near Shannon limit error-correcting coding and decoding: Turbo codes," in *Proceedings of the International Conference on Communications*, (Geneva, Switzerland), pp. 1064–1070, May 1993.

[44] Y. Kofman, E. Zehavi, and S. Shamai, "Performance analysis of a multilevel coded modulation system," *IEEE Transactions on Communications*, vol. 42, pp. 299 –312, Feb./Mar./Apr. 1994.

[45] J. Huber and U. Wachsmann, "Capacities of equivalent channels in multilevel coding schemes," *Electronics Letters*, vol. 30, pp. 557 –558, Mar 1994.

[46] S. L. Goff, A. Glavieux, and C. Berrou, "Turbo-codes and high spectral efficiency modulation," in *IEEE International Conference on Communications*, pp. 645 –649 vol.2, May 1994.

[47] P. Robertson, E. Villebrun, and P. Hoeher, "A comparison of optimal and sub-optimal map decoding algorithms operating in the log domain," in *IEEE International Conference on Communications*, vol. 2, pp. 1009 –1013 vol.2, Jun 1995.

[48] D. Raphaeli, "Noncoherent coded modulation," *IEEE Transactions on Communications*, vol. 44, pp. 172 –183, Feb. 1996.

[49] X. Li and J. A. Ritcey, "Bit-interleaved coded modulation with iterative decoding," *IEEE Communications Letters*, vol. 1, Nov. 1997.

[50] S. Chen and T. Fuja, "Soft-decision decoding metrics for DAPSK," in *IEEE International Symposium on Information Theory*, p. 304, June-July 1997.

[51] T. May, H. Rohling, and V. Engels, "Performance analysis of Viterbi decoding for 64-DAPSK and 64-QAM modulated OFDM signals," *IEEE Transactions on Communications,*, vol. 46, pp. 182 –190, Feb. 1998.

[52] P. Roberson and T. Wörz, "Bandwidth-efficient turbo trellis-coded modulation using punctured component codes," *IEEE Journal on Selected Areas in Communications*, vol. 16, pp. 206–218, 1998.

[53] G. Caire and G. Taricco and E. Biglieri, "Bit-interleaved coded modulation," *IEEE Transactions on Information Theory*, vol. 44, pp. 927–946, May 1998.

[54] S. ten Brink, J. Speidel, and R. H. Han, "Iterative demapping for QPSK modulation," *Electronics Letters*, vol. 34, pp. 1459 –1460, July 1998.

[55] S. ten Brink, J. Speidel, and R. Yan, "Iterative demapping and decoding for multilevel modulation," in *IEEE Global Telecommunications Conference*, vol. 1, pp. 579–584, Nov. 1998.

[56] X. Li and J. A. Ritcey, "Trellis-coded modulation with bit-interleavering and iterative decoding," *IEEE Journal on Selected Areas in Communications*, vol. 17, Apr. 1999.

[57] R. H. Morelos-Zaragoza, M. P. C. Fossorier, S. Lin, and H. Imai, "Multilevel coded modulation for unequal error protection and multistage decoding.I. Symmetric constellations," *IEEE Transactions on Communications*, vol. 48, pp. 204 –213, Feb. 2000.

[58] M. Isaka, M. P. C. Fossorier, R. H. Morelos-Zaragoza, S. Lin, and H. Imai, "Multilevel coded modulation for unequal error protection and multistage decoding. II. Asymmetric constellations," *IEEE Transactions on Communications*, vol. 48, pp. 774 –786, May 2000.

[59] A. Chindapol and J. A. Ritcey, "Design, analysis, and performance evaluation for BICM-ID with square QAM constellations in rayleigh fading channels," *IEEE Journal on Selected Areas in Communications*, vol. 19, pp. 944 –957, May 2001.

[60] P. Ormeci, X. Liu, D. L. Goeckel, and R. D. Wesel, "Adaptive bit-interleaved coded modulation," *IEEE Transactions on Communications*, vol. 49, pp. 1572 –1581, Sep. 2001.

[61] J. Hou and M. H. Lee, "Multilevel LDPC codes design for semi-BICM," *IEEE Communications Letters*, vol. 8, pp. 674 – 676, Nov. 2004.

[62] L. H. J. Lampe, R. F. H. Fischer, and R. Schober, "Multilevel coding for multiple-antenna transmission," in *2002 IEEE International Symposium on Information Theory*, p. 104, 2002.

[63] K. Ishibashi, H. Ochiai, and R. Kohno, "Low-complexity bit-interleaved coded DAPSK for Rayleigh-fading channels," *IEEE Journal on Selected Areas in Communications*, pp. 1728–1738, Sep. 2005.

[64] Y. Nana, E. Sharon, and S. Litsyn, "Improved decoding of LDPC coded modulations," *IEEE Communications Letters*, vol. 10, pp. 375 – 377, May 2006.

[65] S. X. Ng, Y. Li, and L. Hanzo, "Distributed turbo trellis coded modulation for cooperative communications," *in processing of IEEE ICC'09*, June 2009.

[66] Z. Yang, Q. Xie, K. Peng, and J. Song, "Labelling optimization for BICM-ID systems," *IEEE Communications Letters*, vol. 14, pp. 1047 –1049, Nov. 2010.

[67] T. T. Nguyen and L. Lampe, "Bit-interleaved coded modulation with mismatched decoding metrics," *IEEE Transactions on Communications*, vol. 59, no. 2, pp. 437–447, February.

[68] T. Islam, R. Schober, R. K. Mallik, and V. K. Bhargava, "Analysis and design of cooperative BICM-OFDM systems," *IEEE Transactions on Communications*, vol. 59, no. 6, pp. 1742–1751, June, 2011.

[69] T. Cheng, K. Peng, Z. Liu, and Z. Yang, "Improve the performance of LTE turbo coded modulation by irregular mapping," in *IEEE Wireless Communications and Networking Conference (WCNC)*, pp. 597–601, April, 2012.

[70] Z. Andalibi, H. H. Nguyen, and J. E. Salt, "Analysing bit-interleaved coded modulation in multiple-input multiple-output systems with channel estimation error," *IET Communications*, vol. 6, no. 11, pp. 1502–1510, 2012.

[71] N. Tran, L. Rodriguez, T. Le-Ngoc, and H. Bahrami, "Precoding and symbol grouping for NAF relaying in BICM systems," *IEEE Transactions on Vehicular Technology*, vol. PP, no. 99, 2013.

[72] L. Hanzo, W. T. Webb, and T. Keller, *Single- and multi-carrier quadrature amplitude modulation*. IEEE Press-John Wiley, 2004.

[73] L. Hanzo and C. H. Wong and M. S. Yee, *Adaptive Wireless Transceivers: Turbo-coded, Turbo-Equalized and Space-Time Coded TDMA, CDMA and OFDM Systems*. John Wiley Sons, Ltd, 2002.

[74] T. Alsedairy, M. A. Imran, and B. Evans, "Energy and spectrum efficient systems with adaptive modulation and spectrum sharing for cellular systems," in *IEEE 73rd Vehicular Technology Conference*, pp. 1–5, 2011.

[75] J. Hayes, "Adaptive feedback communications," *IEEE Transactions on Communication Technology*, vol. 16, pp. 29 –34, Feb. 1968.

[76] J. Cavers, "Variable-rate transmission for rayleigh fading channels," *IEEE Transactions on Communications*, vol. 20, pp. 15 – 22, Feb. 1972.

[77] V. Hentinen, "Error performance for adaptive transmission on fading channels," *IEEE Transactions on Communications*, vol. 22, pp. 1331 – 1337, Sep. 1974.

[78] R. Steele and W. T. Webb, "Variable rate QAM for data transmission over rayleigh fading channels," in *IEEE Wireless 1991,(Calgary, Alberta)*, pp. 1–14, 1991.

[79] S. Otsuki, S. Sampei, and N. Morinaga, "Square-QAM adaptive modulation/TDMA/TDD systems using modulation level estimation with Walsh function," *Electronics Letters*, vol. 31, pp. 169 –171, Feb. 1995.

[80] J. M. Torrance and L. Hanzo, "Optimisation of switching levels for adaptive modulation in slow rayleigh fading," *Electronics Letters*, vol. 32, pp. 1167 –1169, June 1996.

[81] A. J. Goldsmith and S. Chua, "Variable-rate variable-power mqam for fading channels," *IEEE Transactions on Communications*, vol. 45, pp. 1218 –1230, Oct. 1997.

[82] S. Chua and A. Goldsmith, "Adaptive coded modulation for fading channels," in *IEEE International Conference on Communications, Montreal*, vol. 3, pp. 1488 –1492 vol.3, June 1997.

[83] D. L. Goeckel, "Adaptive coding for fading channels using outdated channel estimates," in *48th IEEE Vehicular Technology Conference*, vol. 3, pp. 1925 –1929 vol.3, May 1998.

[84] C. H. Lim and J. K. Jeong, "Adaptive modulation using multipath fading compensation," *Electronics Letters*, vol. 34, pp. 940 –942, May 1998.

[85] M. S. Alouini and A. Goldsmith, "Capacity of rayleigh fading channels under different adaptive transmission and diversity-combining techniques," *IEEE Transactions on Vehicular Technology*, vol. 48, pp. 1165 –1181, Jul 1999.

[86] C. H. Wong and L. Hanzo, "Upper-bound performance of a wideband burst-by-burst adaptive modem," in *49th IEEE Vehicular Technology Conference*, vol. 3, pp. 1851 –1855, July 1999.

[87] A. Duel-Hallen, S. Hu, and H. Hallen, "Long-range prediction of fading signals," *IEEE Signal Processing Magazine*, vol. 17, pp. 62 –75, May 2000.

[88] K. L. Hole, H. Holm, and G. E. Oien, "Adaptive multidimensional coded modulation over flat fading channels," *IEEE Journal on Selected Areas in Communications*, vol. 18, pp. 1153 –1158, July 2000.

[89] V. K. N. Lau, "Design of adaptive bit interleaved TCM for rayleigh fading channels," in *IEEE International Conference on Communications*, vol. 3, pp. 1188 –1192 vol.3, 2000.

[90] B. Choi and L. Hanzo, "Optimum mode-switching-assisted constant-power single- and multicarrier adaptive modulation," *IEEE Transactions on Vehicular Technology*, vol. 52, no. 3, pp. 536–560, 2003.

[91] S. X. Ng, C. H. Wong, and L. Hanzo, "Burst-by-burst adaptive decision feedback equalized tcm, ttcm, bicm and bicm-id," in *IEEE International Conference on Communications*, vol. 10, pp. 3031 –3035 vol.10, 2001.

[92] X. Liu, P. Ormeci, R. D. Wesel, and D. L. Goeckel, "Bandwidth-efficient, low-latency adaptive coded modulation schemes for time-varying channels," in *IEEE International Conference on Communications*, vol. 7, pp. 2211 –2215 vol.7, 2001.

[93] Y. Zhang and K. B. Letaief, "Single- and multi-user adaptive pragmatic trellis coded modulation for OFDM systems," in *IEEE Wireless Communications and Networking*, vol. 1, pp. 9 –14 vol.1, March 2003.

[94] Z. Zhou, B. Vucetic, M. Dohler, and Y. Li, "MIMO systems with adaptive modulation," *IEEE Transactions on Vehicular Technology*, vol. 54, pp. 1828 – 1842, Sep. 2005.

[95] D. V. Duong, G. E. Oien, and K. J. Hole, "Adaptive coded modulation with receive antenna diversity and imperfect channel knowledge at receiver and transmitter," *IEEE Transactions on Vehicular Technology*, vol. 55, pp. 458 – 465, March 2006.

[96] G. Caire and K. R. Kumar, "Information theoretic foundations of adaptive coded modulation," *Proceedings of the IEEE*, vol. 95, pp. 2274 –2298, Dec. 2007.

[97] D. V. Duong, B. Holter, and G. E. Oien, "Analysis and optimization of adaptive coded modulation systems in spatially correlated SIMO rayleigh fading channels," *IEEE Transactions on Vehicular Technology*, vol. 57, pp. 1929 –1934, May 2008.

[98] J. D. Brown, J. Abouei, K. N. Plataniotis, and S. Pasupathy, "Adaptive demodulation in differentially coherent phase systems: Design and performance analysis," *IEEE Transactions on Communications*, vol. 59, pp. 1772 –1778, July 2011.

[99] M. C. Clemente, F. Ruiz-Vega, P. Otero, and J. F. Paris, "Closed-form analysis of adaptive coded modulation over rician shadowed fading channels," *Electronics Letters*, vol. 47, no. 3, pp. 217–218, 2011.

[100] T. Jia and A. Duel-Hallen, "Adaptive bit-iiterleaved coded modulation based on the expurgated bound for mobile radio OFDM systems aided by fading prediction," *IEEE Transactions on Communications*, vol. 60, no. 8, pp. 2059–2064, August 2012.

[101] S. X. Ng and C. Y. Qian and D. Liang and L. Hanzo, "Adaptive turbo trellis coded modulation aided distributed space-time trellis coding for cooperative communications," in *IEEE Vehicular Technology Conference*, (Taipei), Spring 2010.

[102] D. Liang, S. X. Ng, and L. Hanzo, "Relay-induced error propagation reduction for decode-and-forward cooperative communications," in *2010 IEEE Global Telecommunications Conference*, pp. 1–5, 2010.

[103] D. Liang, S. X. Ng, and L. Hanzo, "Soft-decision Star-QAM aided BICM-ID," *Signal Processing Letters, IEEE*, vol. 18, pp. 169 –172, March 2011.

[104] C. Xu, D. Liang, S. X. Ng, and L. Hanzo, "Reduced-complexity non-coherent soft-decision-aided M-DAPSK dispensing with channel estimation," *accepted by IEEE Transactions on Vehicular Technology*, 2013.

[105] C. Xu, D. Liang, S. Sugiura, S. X. Ng, and L. Hanzo, "Reduced-complexity soft-decision aided PSK detection," in *IEEE Vehicular Technology Conference (VTC Fall)*, pp. 1–5, Sept.

[106] D. Liang, M. Song, S. X. Ng, and L. Hanzo, "Turbo coded and cooperative network coded non-coherent soft-decision star-QAM dispensing with channel estimation," in *2011 IEEE Global Telecommunications Conference*, pp. 1–5, 2011.

[107] D. Liang, S. X. Ng, and L. Hanzo, "Near-capacity turbo coded soft-decision aided DAPSK/star-QAM," in *2011 IEEE Vehicular Technology Conference*, pp. 1–5, 2011.

[108] D. Liang, X. Xu, S. X. Ng, and L. Hanzo, "Turbo-coded star-QAM for cooperative wireless and optical-fiber communications," in *2012 IEEE 3rd International Conference on Photonics (ICP)*, pp. 267–271, 2012.

[109] D. Liang, V. A. Thomas, X. Xu, S. X. Ng, M. El-Hajjar, and L. Hanzo, "Adaptive soft-decision aided differential modulation for cooperative wireless and optical-fiber communications," *will submitted to IEEE Signal Processing Letter*.

[110] G. Ungerböck, *Trellis-coded modulation with redundant signal sets Part 1 and Part 2*, vol. 25. IEEE Communication Magazine, February 1987.

[111] C. H. Wong and L. Hanzo, "Upper-bound performance of a wide-band adaptive modem," *IEEE Transactions on Communications*, vol. 48, pp. 367 –369, Mar 2000.

[112] T. S. Rappaport, *Wireless communications: Principles and practice, second edition*. NJ:Prentice Hall, 1996.

[113] B. Sklar, "Rayleigh fading channels in mobile digital communication systems. I. Characterization," *IEEE Communications Magazine*, vol. 35, pp. 136 –146, Sep. 1997.

[114] B. Sklar, "Rayleigh fading channels in mobile digital communication systems part II: Mitigation," *IEEE Communications Magazine*, vol. 35, pp. 148 –155, Sep. 1997.

[115] S. X. Ng, *Coded modulation schemes for wireless channels*. PhD thesis, 2002.

[116] L. Hanzo, T. Liew, and B. Yeap, *Turbo coding, turbo equalisation and space time coding for Transmission over Wireless channels*. New York, USA: John Wiley IEEE Press, 2002.

[117] D. Divsalar and M. K. Simon, "The design of trellis coded MPSK for fading channels: performance criteria," *IEEE Transactions on communication*, vol. 36, pp. 1013–1021, 1988.

[118] G. D. Forney, "The viterbi algorithm," in *Proceedings of IEEE*, vol. 61, pp. 268–277, March 1973.

[119] P. Roberson, E. Villebrun, and P. Höher, "A comparison of optimal and sub-optimal MAP decoding algorithms operating in the log domain," in *Proceedings of the International Conference on Communications*, pp. 1009–1013, June 1995.

[120] K. Abend and B. D. Fritchman, "Statistical detection for communication channels with intersymbol interference," in *Proceedings of IEEE*, vol. 58, pp. 779–785, May 1970.

[121] P. Roberson, "A overview of bandwidth efficient turbo coding schemes," in *In International Symposium on Turbo Codes and related topics*, pp. 103–110, September 1997.

[122] J. K. Cavers and P. Ho, "Analysis of the error performance of trellis-coded modulations in rayleigh-fading channels," *IEEE Transactions on Communications*, vol. 40, pp. 74–83, 1992.

[123] S. Lin and D. Constello Jr., *Error control coding: fundamentals and applications*. Englewood Cliffs, NJ, USA: Prentice-Hall, October 1982. ISBN: 013283796X.

[124] J. Hagenauer, "Rate-compatible puncture convolutional codes (RCPC) and their application," *IEEE Transactions on Communications*, vol. 36, pp. 389–400, April 1988.

[125] L. Lee, "New rate-compatible puncture convolutional codes for Viterbi decoding," *IEEE Transactions on Communications*, vol. 42, pp. 3073–3079, December 1994.

[126] H. Chen and A. Haimovich, "Exit charts for turbo trellis-coded modulation," *IEEE Communications Letters*, vol. 8, pp. 668 – 670, Nov. 2004.

[127] A. Goldsmith, *Wireless communications*. Cambridge University Press, 2005.

[128] E. Issman and W. T. Webb, "Carrier recovery for 16-level QAM in mobile radio," *IEE colloquium on multi-level modulation*, pp. 9/1 – 9/8, March 1990.

[129] L. Chen, H. Kusaka, and W. Kominami, "Blind phase recovery in QAM communication systems using higher order statistics," *Signal Processing Letters, IEEE*, vol. 3, pp. 147 –149, may. 1996.

[130] Y. Wang and E. Serpedin, "A class of blind phase recovery techniques for higher order QAM modulations: Estimators and bounds," *Signal Processing Letters, IEEE*, vol. 9, pp. 301 – 304, Oct. 2002.

[131] W. T. Webb, L. Hanzo, and R. Steele, "Bandwidth-efficient QAM schemes for Rayleigh-fading channels," *IEE Proceedings*, vol. 138, pp. 169–175, June 1991.

[132] B. Eitel and J. Speidel, "Speed-optimized soft-decision demodulation of multilevel DAPSK," in *International Conference on Consumer Electronics, Technical Papers*, pp. 469 –470, Jan. 2006.

[133] K. Ishibashi, H. Ochiai, and R. Kohno, "Low-complexity bit-interleaved coded DAPSK for Rayleigh-fading channels," *IEEE Journal on Selected Areas in Communications*, vol. 23, pp. 1728 – 1738, Sept. 2005.

[134] C. Berrou and A. Glavieux, "Near optimum error correcting coding and decoding: Turbo-codes," *IEEE Transactions on Communications*, vol. 44, pp. 1261 –1271, Oct. 1996.

[135] L. Hanzo and T. H. Liew and B. L. Yeap, *Turbo coding, turbo equalisation and space-time coding for transmission over fading channels*. Wiley-IEEE Press, 2002.

[136] R. F. Pawula, "Offset DPSK and a comparison of conventional and symmetric DPSK with noise correlation and power imbalance," in *Military Communications Conference, 1983. MILCOM 1983. IEEE*, vol. 1, pp. 93 –98, Nov. 1983.

[137] T. S. Rappaport, *Wireless communications: Principles and practice (2nd Edition)*. Prentice Hall, Dec. 31, 2001.

[138] J. Proakis and M. Salehi, *Digital communications(5th Edition)*. McGraw-Hill Higher Education, Nov., 2007.

[139] L. Hanzo and O. Alamri and N. El-Hajjar and N. Wu, *Near-capacity multi functional MIMO systems*. John Wiley & Sons, Ltd, May 2009.

[140] M. Rohling, T. May, K. Bruninghaus, and R. Grunheid, "Broad-band OFDM radio transmission for multimedia applications," *Proceedings of the IEEE*, vol. 87, pp. 1778 –1789, Oct. 1999.

[141] S. Pasupathy, "Minimum shift keying: A spectrally efficient modulation," *IEEE Communications Magazine*, vol. 17, pp. 14 –22, July 1979.

[142] L. Hanzo and Y. Akhtman and L. Wang and M. Jiang, *MIMO-OFDM for LTE, WiFi and WiMAX: Coherent versus non-coherent and cooperative turbo transceivers*. John Wiley & Sons, Ltd, October 2010.

[143] K. J. R. Liu and A. K. Sadek and W. Su and A. Kwasinski, *Cooperative communications and networking*. Cambridge University Press, 2009.

[144] T. Cover and A. El Gamal, "Capacity theorems for the relay channel," *IEEE Transactions on Information Theory*, vol. 25, no. 5, pp. 572–584, 1979.

[145] N. Laneman and D. N. C. Tse and G. W. Wornell, "Cooperative diversity in wireless networks: efficient protocols and outage behavior," *IEEE Trans. on Information Theory*, vol. 50, no. 12, pp. 3062–3080, 2004.

[146] J. N. Laneman, G. W. Wornell, and D. N. C. Tse, "An efficient protocol for realizing cooperative diversity in wireless networks," in *2001 IEEE International Symposium on Information Theory*, p. 294, 2001.

[147] A. Sendonaris and E. Erkip and B. Aazhang, "User cooperation diversity part I: System description," *IEEE Transactions on Communications*, vol. 51(11), pp. 1927–1938, 2003.

[148] A. Sendonaris, E. Erkip, and B. Aazhang, "User cooperation diversity part II: Implementation aspects and performance analysis," *IEEE Transactions on Communications*, vol. 51, pp. 1939 – 1948, Nov. 2003.

[149] T.E. Hunter and A. Nosratinia, "Cooperation diversity through coding," in *IEEE International Symposium on Information Theory*, 2002.

[150] Y. Li and B. Vucetic, "On the performance of a simple adaptive relaying protocol for wireless relay networks," in *IEEE Vehicular Technology Conference*, pp. 2400 –2405, May 2008.

[151] E. C. van der Meulen, "Three-terminal communication channels," *Advanced Applied Probability*, vol. 3, no. 1, pp. 120–154, 1971.

[152] A. Sendonaris, E. Erkip, and B. Aazhang, "Increasing uplink capacity via user cooperation diversity," in *IEEE International Symposium on Information Theory*, p. 156, Aug 1998.

[153] M. Dohler, E. Lefranc, and H. Aghvami, "Space-time block codes for virtual antenna arrays," in *The 13th IEEE International Symposium on Personal, Indoor and Mobile Radio Communications*, vol. 1, pp. 414 – 417 vol.1, Sept. 2002.

[154] J. N. Laneman and G. W. Wornell, "Distributed space-time-coded protocols for exploiting cooperative diversity in wireless networks," *IEEE Transactions on Information Theory*, vol. 49, pp. 2415 – 2425, Oct. 2003.

[155] B. Zhao and M. C. Valenti, "Distributed turbo coded diversity for relay channel," *Electronics Letters*, vol. 39, pp. 786 – 787, May 2003.

[156] R.U. Nabar and H. Bolcskei and F.W. Kneubuhler, "Fading relay channels: performance limits and space-time signal design," *IEEE Journal on Selected Areas in Communications*, vol. 22, pp. 1099–1109, August 2004.

[157] A. Ribeiro, X. Cai, and G. B. Giannakis, "Symbol error probabilities for general cooperative links," in *IEEE International Conference on Communications*, vol. 6, pp. 3369 – 3373 Vol.6, June 2004.

[158] M. Janani and A. Hedayat and T. Hunter and A. Nosratinia, "Coded cooperation in wireless communications: space-time transmission and iterative decoding," *IEEE Transactions on Signal Processing*, vol. 52, pp. 362–371, February 2004.

[159] A. Stefanov and E. Erkip, "Cooperative coding for wireless networks," *IEEE Transactions on Communications*, vol. 52, pp. 1470–1476, September 2004.

[160] K. Azarian and H. El Gamal and P. Schniter, "On the achievable diversity-multiplexing tradeoff in half-duplex cooperative channels," *IEEE Transactions on Information Theory*, vol. 51, pp. 4152–4172, December 2005.

[161] H. H. Sneessens and L. Vandendorpe, "Soft decode and forward improves cooperative communications," in *6th IEE International Conference on 3G and Beyond*, (Washington, DC), pp. 1–4, November 2005.

[162] A. Host-Madsen and J. Zhang, "Capacity bounds and power allocation for wireless relay channels," *IEEE Transactions on Information Theory*, vol. 51, pp. 2020 –2040, June 2005.

[163] G. Kramer and M. Gastpar and P. Gupta, "Cooperative strategies and capacity theorems for relay networks," *IEEE Transactions on Information Theory*, vol. 51, pp. 3037–3063, September 2005.

[164] E. G. Larsson and B. R. Vojcic, "Cooperative transmit diversity based on superposition modulation," *IEEE Communications Letters*, vol. 9, pp. 778 – 780, Sep 2005.

[165] Y. Li and B. Vucetic and T.F. Wong and M. Dohler, "Distributed turbo coding with soft information relaying in multihop relay networks," *IEEE Journal on Selected Areas in Communications*, vol. 24, pp. 2040–2050, November 2006.

[166] L. Xiao, T. E. Fuja, J. Kliewer, and D. J. Costello, "Cooperative diversity based on code superposition," in *IEEE International Symposium on Information Theory*, pp. 2456 –2460, July 2006.

[167] A. Host-Madsen, "Capacity bounds for cooperative diversity," *IEEE Transactions on Information Theory*, vol. 52, pp. 1522 –1544, April 2006.

[168] D. Chen and J. N. Laneman, "Modulation and demodulation for cooperative diversity in wireless systems," *IEEE Transactions on Wireless Communications*, vol. 5, pp. 1785 –1794, July 2006.

[169] X. Bao and J. Li, "Efficient message relaying for wireless user cooperation: Decode-Amplify-Forward (DAF) and Hybrid DAF and coded-cooperation," *IEEE Transactions on Wireless Communications*, vol. 6, pp. 3975–3984, November 2007.

[170] L. Xiao and T. Fuja and J. Kliewer and D. Costello, "A network coding approach to cooperative diversity," *IEEE Transactions on Information Theory*, vol. 53, pp. 3714–3722, October 2007.

[171] Y. Zhao, R. Adve, and T. J. Lim, "Improving amplify-and-forward relay networks: optimal power allocation versus selection," *IEEE Transactions on Wireless Communications*, vol. 6, pp. 3114 –3123, August 2007.

[172] X. Bao and J. Li, "Adaptive network coded cooperation (ANCC) for wireless relay networks: matching code-on-graph with network-on-graph," *IEEE Transactions on Wireless Communications*, vol. 7, pp. 574 –583, February 2008.

[173] G. Yue and X. Wang and Z. Yang and A. Host-Madsen, "Coding schemes for user cooperation in low-power regimes," *IEEE Transactions on Signal Processing*, vol. 56, pp. 2035–2049, May 2008.

[174] K. B. Letaief and W. Zhang, "Cooperative communications for cognitive radio networks," *Proceedings of the IEEE*, vol. 97, pp. 878 –893, may 2009.

[175] K. Lee and L. Hanzo, "MIMO-assisted hard versus soft decoding-and-forwarding for network coding aided relaying systems," *IEEE Transactions on Wireless Communications*, vol. 8, pp. 376 –385, Jan. 2009.

[176] S. Chatzinotas, M. A. Imran, and C. Tzaras, "Capacity limits in cooperative cellular systems," *Zhang Y, Chen H-H, Guizani M (eds.), Cooperative Wireless Communications, Auerbach Publications, Taylor & Francis Group*, pp. 25–52, 2009.

[177] L. Kong, S. X. Ng, R. G. Maunder, and L. Hanzo, "Near-capacity cooperative space-time coding employing irregular design and successive relaying," *IEEE Transactions on Communications*, vol. 58, pp. 2232 –2241, August 2010.

[178] L. Dong, Z. Han, A. P. Petropulu, and H. V. Poor, "Improving wireless physical layer security via cooperating relays," *IEEE Transactions on Signal Processing*, vol. 58, pp. 1875 –1888, March 2010.

[179] X. Xu, M. F. Flanagan, N. Goertz, and J. Thompson, "Joint channel and network coding for cooperative diversity in a shared-relay environment," *IEEE Transactions on Wireless Communications*, vol. 9, pp. 2420 –2423, August 2010.

[180] S. W. Peters and R. W. Heath, "Cooperative algorithms for MIMO interference channels," *IEEE Transactions on Vehicular Technology*, vol. 60, pp. 206 –218, Jan. 2011.

[181] S. Talwar, Y. Jing, and S. ShahbazPanahi, "Joint relay selection and power allocation for two-way relay networks," *IEEE Signal Processing Letters*, vol. 18, pp. 91 –94, Feb. 2011.

[182] S. Sugiura, S. Chen, H. Haas, P. M. Grant, and L. Hanzo, "Coherent versus non-coherent decode-and-forward relaying aided cooperative space-time shift keying," *IEEE Transactions on Communications*, vol. 59, pp. 1707 –1719, June 2011.

[183] P. Clarke and R. C. de Lamare, "Transmit diversity and relay selection algorithms for multirelay cooperative MIMO systems," *IEEE Transactions on Vehicular Technology*, vol. 61, pp. 1084 –1098, March 2012.

[184] J. L. Rebelatto, B. F. Uchoa-Filho, Y. Li, and B. Vucetic, "Multiuser cooperative diversity through network coding based on classical coding theory," *IEEE Transactions on Signal Processing*, vol. 60, pp. 916 –926, Feb. 2012.

[185] M. F. U. Butt, S. X. Ng, and L. Hanzo, "Self-concatenated code design and its application in power-efficient cooperative communications," *IEEE Communications Surveys Tutorials*, vol. 14, pp. 858 –883, quarter 2012.

[186] Y. Qi, R. Hoshyar, M. A. Imran, and R. Tafazolli, "H2-ARQ-relaying: Spectrum and energy efficiency perspectives," *IEEE Journal on Selected Areas in Communications*, vol. 29, no. 8, pp. 1547–1558, 2011.

[187] A. Nasri, R. Schober, and M. Uysal, "Performance and optimization of network-coded cooperative diversity systems," *IEEE Transactions on Communications*, vol. PP, no. 99, pp. 1–12, 2013.

[188] R. Zhang, L. Wang, G. Parr, O. G. Aliu, B. Awoseyila, N. Azarmi, S. Bhatti, E. Bodanese, H. Chen, M. Dianati, A. Dutta, M. Fitch, K. Giridhar, S. Hailes, K. V. S. Hari, M. A. Imran, A. K. Jagannatham, A. Karandikar, S. Kawade, M. Z. A. Khan, S. C. Kompalli, P. Langdon, B. Narayanan, A. Mauthe, J. McGeehan, N. Mehta, K. Millet, K. Moessner, R. Rajashekar, B. Ramkumar, V. Ribeiro, K. Vasudevan, L. Hanzo, and J. Bigham, "Advances in base- and mobile-station aided cooperative wireless communications: An overview," *IEEE Vehicular Technology Magazine*, vol. 8, no. 1, pp. 57–69, 2013.

[189] R. Ahlswede, C. Ning, S. Y. R. Li, and R. W. Yeung, "Network information flow," *IEEE Transactions on Information Theory*, vol. 46, pp. 1204 –1216, July 2000.

[190] Y. Li and B. Vucetic, "Distributed turbo coding with soft information relaying in wireless sensor networks," in *The International Conference on Computer as a Tool*, pp. 29 –32, Nov. 2005.

[191] F. A. Onat, A. Adinoyi, Y. Fan, H. Yanikomeroglu, and J. S. Thompson, "Optimum threshold for SNR-based selective digital relaying schemes in cooperative wireless networks," in *IEEE Wireless Communications and Networking Conference*, pp. 969 –974, March 2007.

[192] K. Lee and L. Hanzo, "Iterative detection and decoding for hard-decision forwarding aided cooperative spatial multiplexing," in *IEEE ICC 2009*, (Dresden, Germany), pp. 1–5, 14-18 June 2009.

[193] S. X. Ng and Y. Wang and L. Hanzo, "Distributed convolutional-coded differential space-time block coding for cooperative communications," in *IEEE Vehicular Technology Conference*, (Taipei), Spring 2010.

[194] X. Li and J. A. Ritcey, "Bit-interleaved coded modulation with iterative decoding using soft feedback," *IEE Electronics Letters*, vol. 34, pp. 942–943, May 1998.

[195] H. Ochiai and P. Mitran and V. Tarokh, "Design and analysis of collaborative diversity protocols for wireless sensor networks," in *Proceedings of IEEE VTC Fall*, (Los Angeles, USA), pp. 4645 – 4649, 26-29 September 2004.

[196] V. Tarokh, N. Seshadri, and A. R. Calderbank, "Space-time codes for high data rate wireless communication: Performance criterion and code construction," *IEEE Transactions on Information Theory*, vol. 44, pp. 744–765, March 1998.

[197] Y. Li, "Distributed coding for cooperative wireless networks: An overview and recent advances," *IEEE Communications Magazine*, vol. 47, pp. 71–77, August 2009.

[198] E. Zimmermann and P. Herhold and G. Fettweis, "On the performance of cooperative relaying protocols in wireless networks," *European Transactions on Telecommunications*, vol. 16, no. 1, pp. 5–16, 2005.

[199] C. Wong and L. Hanzo, "Upper-bound performance of a wideband burst-by-burst adaptive modem," *IEEE Transactions on Communications*, vol. 48, pp. 367–369, March 2000.

[200] A.J. Goldsmith and S. Chua, "Adaptive coded modulation for fading channels," *IEEE Transactions on Communications*, vol. 46, pp. 595–602, May 1998.

[201] S. X. Ng and J. Y. Chung and P. Cherriman and L. Hanzo, "Burst-by-burst adaptive decision feedback equalised TCM, TTCM and BICM for H.263-assisted wireless video telephony," *IEEE Transactions on Circuits and Systems for Video Technology*, pp. 363–374, March 2006.

[202] C. Hausl and P. Dupraz, "Joint network-channel coding for the multiple-access relay channel," in *3rd Annual IEEE Communications Society on Sensor and Ad Hoc Communications and Networks*, vol. 3, pp. 817 –822, Sep. 2006.

[203] C.-D. Chung, "Differentially amplitude and phase-encoded QAM for the correlated Rayleigh-fading channel with diversity reception," *IEEE Transactions on Communications*, vol. 45, pp. 309 – 321, March 1997.

[204] Y. Ma and Q. T. Zhang and R. Schober and S. Pasupathy, "Diversity reception of DAPSK over generalized fading channels," *IEEE Transactions on Wireless Communications*, vol. 4, pp. 1834 – 1846, July 2005.

[205] J.-Y. Hwang, J. Oh, J. Kim, and Y. Han, "Utility-aware network coding in wireless butterfly networks," in *IEEE Vehicular Technology Conference*, pp. 1 –5, May 2010.

[206] D. Wu, Y. Tian, and C. Yang, "A cooperative three-time-slot transmission in asymmetric two-way relay channels," in *IEEE Vehicular Technology Conference Spring*, pp. 1 –5, May 2011.

[207] Q. Zhao and H. Li, "Differential modulation for cooperative wireless systems," *IEEE Transactions on Signal Processing*, vol. 55, pp. 2273 –2283, May 2007.

[208] T. Himsoon, W. P. Siriwongpairat, W. Su, and K. J. R. Liu, "Differential modulations for multinode cooperative communications," *IEEE Transactions on Signal Processing*, vol. 56, pp. 2941 –2956, July 2008.

[209] C. Huang and C. Chung, "Differentially amplitude- and phase-encoded QAM for amplify-and-forward multiple-relay systems," *IEEE Transactions on Vehicular Technology*, vol. 61, pp. 2054 –2066, June 2012.

[210] G. Kardaras, T. T. Pham, J. Soler, and L. Dittmann, "Analysis of control and management plane for hybrid fiber radio architectures," in *IEEE International Conference on Communication Technology (ICCT)*, pp. 281 –284, Nov. 2010.

[211] X. Xu, R. Zhang, S. Ghafoor, and L. Hanzo, "Imperfect digital-fiber-optic-link-based cooperative distributed antennas with fractional frequency reuse in multicell multiuser networks," *IEEE Transactions on Vehicular Technology*, vol. 60, pp. 4439 –4449, Nov. 2011.

[212] D. Wake, W. Webster, G. Wimpenny, K. Beacham, and L. Crawford, "Radio over fiber for mobile communications," in *IEEE International Topical Meeting on Microwave Photonics*, pp. 157 – 160, Oct. 2004.

[213] H. Ekstrom, A. Furuskar, J. Karlsson, and et al, "Technical solutions for the 3G long-term evolution," *IEEE Communications Magazine*, vol. 44, pp. 38– 45, March 2006.

[214] G. Auer, V. Giannini, C. Desset, I. Godor, P. Skillermark, M. Olsson, M. A. Imran, D. Sabella, M. J. Gonzalez, O. Blume, and A. Fehske, "How much energy is needed to run a wireless network?," *IEEE Wireless Communications*, vol. 18, no. 5, pp. 40–49, 2011.

[215] A. Ghosh, D. R. Wolter, J. G. Andrews, and R. Chen, "Broadband wireless access with WiMax/802.16: current performance benchmarks and future potential," *IEEE Communications Magazine*, vol. 43, pp. 129–136, Feb. 2005.

[216] L. Hanzo and T. H. Liew and B. L. Yeap and R. Y. S. Tee and S. X. Ng, *Turbo Coding, Turbo Equalisation and Space-Time Coding: EXIT-Chart-Aided Near-Capacity Designs for Wireless Channels*. Wiley-IEEE Press, 2011.

[217] C. H. C. III, E. I. Ackerman, G. E. Betts, and J. L. Prince, "Limits on the performance of rf-over-fiber links and their impact on device design," *IEEE Transactions on Microwave Theory and Techniques*, vol. 54, pp. 906 – 920, Feb. 2006.

[218] S. Ghafoor and L. Hanzo, "Reduced dispersion duplex DQPSK radio-over-fiber communications using single-laser-based multiple side-bands," in *IEEE International Conference on Communications (ICC)*, pp. 1 –5, June 2011.

[219] D. M. Fye, "Design of fiber optic antenna remoting links for cellular radio applications," in *IEEE 40th Vehicular Technology Conference*, pp. 622 –625, May 1990.

[220] K. Xu, X. Sun, J. Yin, H. Huang, J. Wu, X. Hong, and J. Lin, "Enabling ROF technologies and integration architectures for in-building optical wireless access networks," *IEEE Photonics Journal*, vol. 2, pp. 102 –112, April 2010.

[221] R. P. Merrett, A. J. Cooper, and I. C. Symington, "A cordless access system using radio-over-fibre techniques," in *IEEE Vehicular Technology Conference*, pp. 921 –924, May 1991.

[222] C. Harvey, I. C. Symington, and D. Kirsten, "Cordless communications utilising radio over fibre techniques for the local loop," in *IEEE International Conference on Communications*, pp. 1171 –1175 vol.3, June 1991.

[223] M. Shibutani, T. Kanai, K. Emura, and J. Namiki, "Feasibility studies on an optical fiber feeder system for microcellular mobile communication systems," in *IEEE International Conference on Communications*, pp. 1176 –1181 vol.3, June 1991.

[224] A. J. Cooper, "Fibre-radio: a new technique for delivering cordless access services," in *IEEE Global Telecommunications Conference*, pp. 999 –1005 vol.2, Dec. 1991.

[225] J.K.Shaw, *Mathematical principles of optical fiber communications*. Society for Industrial and Applied Mathematics, 2004.

[226] G. P. Agrawal, *Nonlinear fiber optics*. Academic Press, 4th ed., 2006.

[227] L. H. Lampe, R. F. H. Fischer, S. Calabro, and S. H. Muller-Weinfurtner, "Coded modulation DPSK on fading channels," in *IEEE Global Telecommunications Conference*, vol. 5, pp. 2540–2544, 1999.

[228] Y. Huang and J. A. Ritcey, "Optimal constellation labelling for iteratively decoded bit-interleaved space-time coded modulation," *IEEE Transactions on Information Theory*, vol. 51, no. 5, pp. 1865–1871, May.

[229] E. Agrell, J. Lassing, E. G. Strom, and T. Ottosson, "On the optimality of the binary reflected gray code," *IEEE Transactions on Information Theory*, vol. 50, no. 12, pp. 3170–3182, Dec.

[230] N. S. Muhammad and J. Speidel, "Joint optimization of signal constellation bit labelling for bit-interleaved coded modulation with iterative decoding," *IEEE Communications Letters*, vol. 9, no. 9, pp. 775–777, Sep.

[231] E. Agrell, J. Lassing, E. G. Strom, and T. Ottosson, "Gray coding for multilevel constellations in gaussian noise," *IEEE Transactions on Information Theory*, vol. 53, no. 1, pp. 224–235, Jan.

[232] D. Torrieri and M. C. Valenti, "Constellation labelling maps for low error floors," *IEEE Transactions on Wireless Communications*, vol. 7, no. 12, pp. 5401–5407, December.

[233] Q. Xie, Z. Yang, J. Song, and L. Hanzo, "EXIT-chart-matching-aided near-capacity coded modulation design and a BICM-ID design example for both gaussian and rayleigh channels," *IEEE Transactions on Vehicular Technology*, vol. 62, no. 3, pp. 1216–1227, March.

[234] L. Lampe, R. Schober, V. Pauli, and C. Windpassinger, "Multiple-symbol differential sphere decoding," *IEEE Transactions on Communications*, vol. 53, pp. 1981–1985, 2005.

[235] D. Divsalar and M. K. Simon, "Maximum-likelihood differential detection of uncoded and trellis coded amplitude phase modulation over AWGN and fading channels-metrics and performance," *IEEE Transactions on Communications*, vol. 42, pp. 76 –89, Jan. 1994.

[236] P. Ho and D. Fung, "Error performance of multiple-symbol differential detection of PSK signals transmitted over correlated Rayleigh fading channels," *IEEE Transactions on Communications*, vol. 40, pp. 1566 –1569, Oct. 1992.

[237] R. Schober, W. H. Gerstacker, and J. B. Huber, "Decision-feedback differential detection of MDPSK for flat Rayleigh fading channels," *IEEE Transactions on Communications*, vol. 47, pp. 1025–1035, July 1999.

[238] P. Hoeher and J. Lodge, ""Turbo DPSK": Iterative differential PSK demodulation and channel decoding," *IEEE Transactions on Communications*, vol. 47, no. 6, pp. 837–843, 1999.

[239] C. Xu, L. Wang, S. X. Ng, and L. Hanzo, "Multiple-symbol differential sphere detection aided differential space-time block codes using QAM constellations," *IEEE Signal Processing Letters*, vol. 18, no. 9, pp. 497–500, 2011.

[240] L. Wang, K. V. S. Hari, and L. Hanzo, "Iterative amplitude/phase multiple-symbol differential sphere detection for DAPSK modulated transmissions," in *IEEE International Conference on Communications (ICC)*, pp. 3466–3470, 2012.

[241] D. Astely, E. Dahlman, A. Furuskar, A. Kangas, M. Lindstrom, and S. Parkvall, "LTE: the evolution of mobile broadband," *IEEE Communications Magazine*, vol. 47, no. 4, pp. 44–51, 2009.

[242] Y. Zhu and K. B. Letaief, "Single carrier frequency domain equalization with time domain noise prediction for wideband wireless communications," *IEEE Transactions on Wireless Communications*, vol. 5, no. 12, pp. 3548–3557, 2006.

[243] I. Lee, A. M. Chan, and C. E. W. Sundberg, "Space-time bit-interleaved coded modulation for OFDM systems," *IEEE Transactions on Signal Processing*, vol. 52, no. 3, pp. 820–825, 2004.

[244] D. Rende and T. F. Wong, "Bit-interleaved space-frequency coded modulation for OFDM systems," *IEEE Transactions on Wireless Communications*, vol. 4, no. 5, pp. 2256–2266, 2005.

[245] Z. Hong and B. L. Hughes, "Robust space-time codes for broadband OFDM systems," in *IEEE Wireless Communications and Networking Conference*, vol. 1, pp. 105–108 vol.1, 2002.

[246] B. Lu, X. Wang, and K. R. Narayanan, "Ldpc-based space-time coded OFDM systems over correlated fading channels: Performance analysis and receiver design," *IEEE Transactions on Communications*, vol. 50, no. 1, pp. 74–88, 2002.

[247] S. H. Song and K. B. Letaief, "Diversity analysis for linear equalizers over ISI channels," *IEEE Transactions on Communications*, vol. 59, no. 9, pp. 2414–2423, 2011.

[248] S. Rosati, G. E. Corazza, and A. Vanelli-Coralli, "Coded SC-FDMA for broadband satellite return links," in *2012 6th Advanced Satellite Multimedia Systems Conference (ASMS) and 12th Signal Processing for Space Communications Workshop (SPSC)*, pp. 226–232, 2012.

[249] S. Alamouti, "A simple transmit diversity technique for wireless communications," *IEEE Journal on Selected Areas in Communications*, vol. 16, no. 8, pp. 1451–1458, 1998.

[250] V. Tarokh, A. Naguib, N. Seshadri, and A. R. Calderbank, "Space-time codes for high data rate wireless communication: performance criteria in the presence of channel estimation errors, mobility, and multiple paths," *IEEE Transactions on Communications*, vol. 47, no. 2, pp. 199–207, 1999.

[251] J. C. Belfiore, G. Rekaya, and E. Viterbo, "The golden code: a 2 times;2 full-rate space-time code with nonvanishing determinants," *IEEE Transactions on Information Theory*, vol. 51, no. 4, pp. 1432–1436, 2005.

[252] S. Chatzinotas, M. A. Imran, and R. Hoshyar, "On the multicell processing capacity of the cellular MIMO uplink channel in correlated Rayleigh fading environment," *IEEE Transactions on Wireless Communications*, vol. 8, no. 7, pp. 3704–3715, 2009.

[253] S. M. Haas, J. H. Shapiro, and V. Tarokh, "Space-time codes for wireless optical channels," in *IEEE International Symposium on Information Theory*, pp. 244–, 2001.

[254] D. Cui and A. M. Haimovich, "Design and performance of turbo space-time coded modulation," in *IEEE Global Telecommunications Conference*, vol. 3, pp. 1627–1631, 2000.

[255] D. Agrawal, V. Tarokh, A. Naguib, and N. Seshadri, "Space-time coded OFDM for high data-rate wireless communication over wideband channels," in *IEEE Vehicular Technology Conference*, vol. 3, pp. 2232–2236, 1998.

[256] D. Tujkovic, M. Juntti, and M. Latva-aho, "Space-frequency-time turbo coded modulation," *IEEE Communications Letters*, vol. 5, no. 12, pp. 480–482, 2001.

[257] M. Pischella and J. C. Belfiore, "Distributed margin adaptive resource allocation in MIMO OFDMA networks," *IEEE Transactions on Communications*, vol. 58, no. 8, pp. 2371–2380, 2010.

[258] S. Sezginer and P. Bianchi, "Asymptotically efficient reduced complexity frequency offset and channel estimators for uplink MIMO-OFDMA systems," *IEEE Transactions on Signal Processing*, vol. 56, no. 3, pp. 964–979, 2008.

[259] R. Paschotta, "Field guide to optical fiber technology," *SPIE Field Guide*, vol. FG16, 2010.

# Subject Index

# Author Index

**D**



**E**



**F**



**G**

## H

## I



## J



## K

**L**



**M**

**N**



**O**



**P**

## Q



## R



## S

## X



## Y



## Z